Multi-scale approaches for the vibration and energy flow through piezoelectric waveguides : simulation strategies, control mechanisms and circuits optimization

Yu Fan

Numéro d'ordre NNT: 2016LYSEC019 Année: 2016

ECOLE CENTRALE DE LYON

DOCTORAL SCHOOL MEGA

(Mécanique, Énergétique, Génie civil, Acoustique)

THESIS

Multi-scale approaches for the vibration and energy flow through piezoelectric waveguides: simulation strategies, control mechanisms and circuits optimization

defended on June 17, 2016 by

Yu FAN

to obtain the title of

Doctor

Specialty : Mechanics

Jury members

Reviewers :	Fabrizio	Scarpa	-	Professor, University of Bristol
	Claude	Richard	-	Professor, INSA de Lyon
Advisor :	Mohamed	Ichchou	-	Professor, ECL
Co-advisors :	Manuel	Collet	-	Research Director, CNRS
	Lin	Li	-	Professor, Beihang University
Examiners :	Michel	Massenzio	-	Professor, UCBL
	Zoran	Dimitrijevic	-	Doctor, PSA Peugeot Citroën
	Olivier	Bareille	-	Associate Professor, ECL
	Jean-Pierre	Laine	-	Associate Professor, ECL

To my wife Han Liujie.

Acknowledgments

This work has been done in the "Laboratoire de Tribologie et Dynamique des Systèmes" of "Ecole Centrale de Lyon", with the financial support from the company PSA Peugeot Citroën. Before I came to France to officially start the PhD research, some initial work (literature review, beam piezoelectric element etc.) had been done with the financial support from Beihang University. During the PhD study I was honored to visit the I-Deal technologies GmbH in Saarbrücken, Germany as secondary researcher for 3 months, funded through the Marie Curie EU project Smart-Nest. The overall work would not have been completed without the extraordinary support and management of PSA, ECL, BUAA and Smart-Nest. For this I would like to express my sincere acknowledgments to these organizations.

I would like to express my deepest gratitude to thesis advisor Prof. Ichchou for managing the whole complex project and for guiding me into the new world of waves. Great thanks go to CNRS senior researcher Dr. Collet, for his selfless sharing of expert insights; for his keen sense of innovation that inspires me to move forward; also for his rigorous internal review that polishes our publications. I would like to express my appreciation to Prof. Li for the support of the initial work and for the thorough discussions concerning the application of vibration control. I also want to thank Dr. Dimitrijevic for the precious remarks from the industrial point of view. I am grateful to other experienced researchers in our group: Dr. Lainé for the golden suggestions concerning the free-interface CMS methods; Dr. Bareille for the valuable discussions about the WFE method; Dr. Dessombz for technique support of the softwares. I also would like to acknowledge the thesis reviewers Prof. Scarpa and Prof. Richard for their time and insightful suggestions.

A particular acknowledgment has to be made to the Python community, especially to the selfless developers of the open-source scientific packages. All the numerical tools proposed in this work as well as most of the figures were developed and generated by Python programming language. Its intuitive grammar, compact style and diverse resources make working with Python very productive and pleasant. For this I should quote the famous words of Bruce Eckel to express my gratitude: "Life is short, you need Python."

Last but not least, I am very fortunate to meet many amazing colleagues among my contemporaries in ECL. Having them, I feel a quite transparent and friendly atmosphere in our lab. I am indebted to many of them: Zhou Changwei and Huang Xingrong for being my patient "French-Chinese translators"; Jean-Loup for the detailed English correction and also for letting me win a few Go games; Christophe, Yi Kaijun, Régis, Anna-Rita, Zakaria, Omar, Sun Xiangkun, Meng Han, Hui Yi and Chai Wenqi for many helpful discussions and suggestions. I would like to express my thankfulness to all of my friends, may our friendship last forever.

Abstract

This thesis describes analysis and control approaches for the vibration and energy flow through periodic structures. The wave description is mainly used to address the structural dynamic problems considered in the thesis: forced response is calculated as the superposition of the wave motions; natural modes are understood as standing waves induced by the propagating waves that recover to the same phase after traveling a whole circle of the finite structure.

One advantage of the wave description is that they can remarkably reduce the dimensions of structural dynamic problems. This feature is especially useful in mid- and high frequencies where directly computing the full Finite Element Method (FEM) model is rather time-consuming because of the enormous number of degree-of-freedoms. This thesis extends one widely used wave-based numerical tool termed Wave Finite Element Method (WFEM). The major improvements are the use of several Component Mode Synthesis (CMS) methods to accelerate the analysis for general waveguides with proportional damping or piezoelectric waveguides. The numerical error is reduced by using the proposed eigenvalue schemes, the left eigenvectors and the reduced wave basis. Another contribution is the multi-scale modeling approach for the built-up structures with both periodic and non-periodic parts. The main idea is to model the non-periodic parts by FEM, and model the periodic parts by WFEM. By interfacing different substructures as reflection coefficients or mechanical impedance, the response of the waveguide is calculated in terms of different scales. These two contributions extend WFEM to more complex structures and to more realistic models of the engineering applications.

Another benefit of the wave perception is that it leads to new ideas for vibration control. In this thesis periodically distributed piezoelectric materials and shunt circuit are used to artificially modify the wave properties by electric impedance. A novel metrics termed the Wave Electromechanical Coupling Factor (WEMCF) is proposed, to quantitatively evaluate the coupling strength between the electric and mechanical fields during the passage of a wave. This factor can be post-processed from the wave characteristics obtained from WFEM through an energy formula. We show that WEMCF is strongly correlated to the best performance of the piezoelectric waveguide. Hence the design for the geometric and electric parameters can be done separately. An application is given, concerning the vibration reduction of a cantilever beam. WEMCF is used as an optimization objective during the geometric design, when the overall mass of the piezoelectric materials is constrained. Then the negative capacitance is used with a stability consideration to enlarge the Bragg band gap. The vibration is localized and efficiently dissipated by few boundary dampers. The wave-based design process yields several broadband, stable, lightweight and boundary condition insensitive solutions. Therefore, it is promising at mid- and high frequencies where exact modal information is difficult to access.

Keywords: Multi-scale modeling, wave and finite element method, reduced model, piezoelectric shunt, wave electromechanical coupling factor, broadband vibration control, energy flow, periodic structure

Résumé

Cette thèse s'interesse au contrôle des flux d'énergie mécanique dans les structures périodiques. Les problèmes de dynamique des structures considérés dans cette thèse sont abordés sous l'angle d'une description ondulatoire : la réponse forcée d'un système est calculée comme une superposition d'ondes dans la structure, tandis que les modes propres sont interprétés comme des ondes stationnaires.

Un des avantages de l'approche ondulatoire est qu'elle permet de réduire de manière importante la taille des problèmes de dynamique. Ceci se révèle particulièrement utile dans le domaine des hautes et moyennes fréquences, où les calculs par éléments finis deviennent très coûteux en temps à cause du grand nombre de degrés de liberté nécessaire à la convergence du modèle. Afin de contourner ce problème, cette thèse s'appuie sur la méthode des éléments finis ondulatoires (WFEM). Une des principales améliorations proposées est l'utilisation de plusieurs méthodes de synthèses modales (Component Mode Synthesis (CMS)) pour accélérer l'analyse des guides d'ondes généraux en présence d'amortissement ou de matériaux piézo-électriques. Les erreurs numériques restent faibles du fait de l'utilisation d'une base de projection réduite constituée d'ondes propagatives. Une autre contribution est le procédé de modélisation multi-échelle pour les assemblages de structures périodiques et non-périodiques. L'idée principale est de modéliser les parties non-périodiques par éléments finis, et les parties périodiques par WFEM. Les interactions entre les différentes sous-structures sont modélisées par des coefficients de réflexion ou des impédances mécaniques. Ces travaux forment une extension de la WFEM à des structures plus complexes et plus proches des applications industrielles.

Un autre intérêt de la vision ondulatoire est qu'elle mène à de nouvelles idées pour le contrôle des vibrations. Dans cette thèse, des matériaux piézo-électriques shuntés disposés périodiquement sont utilisés afin de modifier artificiellement la propagation des ondes grâce au couplage électromécanique. Un nouveau critère, nommé Wave Electromechanical Coupling Factor (WEMCF), est proposé pour évaluer, en termes énergétiques, l'intensité du couplage entre le champ électrique et le champ mécanique lors du passage d'une onde. On montre que le WEMCF est fortement lié à l'atténuation dans le guide d'ondes piézo-électrique. La conception des paramètres géométriques et électriques peut être ainsi être effectuée séparément. Ce principe est appliqué à la réduction des vibrations d'une poutre encastrée. Le WEMCF est utilisé comme fonction objectif pour l'optimisation durant la conception géométrique, la masse totale de matériau piézo-électriques étant contrainte. Un circuit à capacité négative est utilisé pour élargir le band-gap de Bragg. La stabilité du système est prise en compte comme une contrainte sur la valeur de cette capacité. Les vibrations sont localisées et facilement dissipées par l'introduction d'absorbeurs sur la frontière. Ce procédé de conception basée sur une approche ondulatoire aboutit à des solutions stables, légères, et insensibles aux conditions aux limites dans une large gamme de fréquence. Par conséquent, il est prometteur pour analyser les structures en moyenne et haute fréquence où il est difficile d'accéder aux informations modales exactes.

Mots clés : modélisation multi-échelle, éléments finis ondulatoires, modèle réduit, piézo-électrique, facteur de couplage électromécanique ondulatoire, contrôle de vibration en large bande, flux d'énergie, structure périodique

Contents

List of Figures

List of Tables

List of Abbreviations

Short form	Signification
AC	Alternating Current
DC	Direct Current
DOF	Degree of Freedom
SDOF	Single Degree of Freedom
ABC	Artificial Boundary Condition
PML	Perfectly Matched Layer
FSDT	First-order Shear Deformation Theory
EMCF	Electromechanical Coupling Factor
MEMCF	Modal Electromechanical Coupling Factor
WEMCF	Wave Electromechanical Coupling Factor
MAC	Modal Assurance Criterion
NC	Negative Capacitance
CMS	Component Modal Synthesis
FEM	Finite Element Method
WFEM	Wave and Finite Element Method
FRF	Frequency Response Function
DSM	Dynamic Stiffness Matrix
DM	Diffusion Matrix
OC	Open Circuit
SC	Short Circuit
TMD	Tuned Mass Damper
PZT	Lead-Zirconate-Titanate
PVDF	Polyvinylidene Fluoride
PDE	Partial Differential Equation
SMA	Shape Memory Alloy
PEM	Piezo-electromechanical
LR	Local Resonance
DtN	Dirichlet-to-Neumann
SSD	Synchronized Switch Damping
SSDI	Synchronized Switch Damping on Inductor
SSDS	Synchronized Switch Damping on Short circuit
SSDNC	Synchronized Switch Damping on Negative Capacitance
SSDV	Synchronized Switch Damping on Voltage

Introduction

Scientific context

The research conducted in this thesis was aimed to explore the use of structural periodicity so as to achieve the goals of wave filtering, energy reflection/attenuation and vibration reduction. Piezoelectric materials and shunting circuits are considered as a mean to modify the wave characteristics in a desired manner. The work can be related to three main axes:

1) The efficient analysis methods for periodic structures/substructures. The underlying idea for applications of periodic structures is to artificially design certain characteristics for the guided waves. For structures with piezoelectric patches, electric circuits and complex geometries, the analytical solutions are difficult to access. Therefore an efficient numerical tool that can simulate the wave characteristics (free-wave analysis) of the periodic piezoelectric structures is needed. Moreover, in a more practical point of view, probably the designed periodic component will finally become a substructure in a bigger structural system. Thus a numerical tool that can analyze the energy flow and vibration (forced response) in such built-up structural systems are also required.

2) The understanding of mechanisms that link the wave characteristics with the energy flow and vibration. Analyzing a periodic structure in isolation, some conclusions have already been drawn. For instance: a single evanescent wave exists in semi-infinite/infinite structural systems can not carry energy; inside a frequency band gap, a finite periodic structure has lower modal density. But are these conclusions still hold when we integrate a periodic component into a larger structural system? For example, does a band gap in the periodic substructure directly link to a low vibration and low energy flow frequency range of the built-up structure? To answer these questions, we need to clarify the links between the wave characteristics of a infinite periodic substructure and the dynamic behavior of a finite periodic structure or a built-up structure with finite/infinite extent.

3) Design/optimization processes for the piezoelectric structures, for both geometric and electric parameters. To reduce the vibration and energy flow at mid- and high frequencies, a broadband performance is desired. In addition, this should be achieved for given frequencies and excitations. To do that, design processes are required. In terms of structural modes, generally the geometrics of are designed to obtain good electromechanical coupling; the electric parameter are designed to maximize damping, to tune a resonance, to minimize the energy density etc. Analogy to that, indicators that can also evaluate the electromechanical coupling strength for waves are required. It will be better if the indicators can be easily calculated from the existing or proposed numerical tools. So that we can used these indicators to design the geometrics of a waveguide. For the electric part, appropriate criteria should be used for different objectives. For example the criterion for the energy reflection might be different from the one for vibration reduction.

Outline of the thesis

The work related to the aforementioned point 1) is reflected in Chapters 2 and 3, the proposed methods are further applied for more realistic structures, shown in Chapter 6. Discussions related to the point 2) can be found in Chapters 3, 5 and 6. Solutions for the point 3) are summarized in Chapters 4 and 5. A brief outline of chapters and appendices are listed below.

- In Chapter 1, the results of conducted literature review are presented. The survey concerns existing work based on piezoelectric materials for dynamic modeling, wave analyzing, electromechanical coupling and vibration reduction. Remarks are given at the end of each part.

- In Chapter 2, an efficient numerical tool for the free-wave analysis are proposed. Based on the free-wave characteristics, the forced response can be computed once the boundary conditions and excitations are given. The main claim is the use of free-interface Component Modal Synthesis (CMS) methods into Wave and Finite Element Method (WFEM) to accelerate the calculation. A periodic open thin-wall structure is considered as an application, and aspects such as accuracy, efficiency and convergence are discussed and compared with several different modal reduction schemes. The influence of reduced wave basis for the accuracy of forced response results are discussed.

- In Chapter 3, a numerical tool is developed for the prediction of vibration and energy flow in built-up structure with both non-periodic and periodic parts. The non-periodic part is modeled by FEM while the periodic substructures are described by WFEM. Different parts are connected in a multi-scale manner such that the final dimension of the problem are largely reduced. A new reduced model is proposed for free-wave analysis of waveguides with piezoelectric shunts or local dampers. Through detailed validations, we show that whit FEM/WFEM hybrid method is an accurate and rapid tool for both finite and infinite structures.

- In Chapter 4, a criterion termed Wave Electromechanical Coupling Factor (WEMCF) is proposed. It quantitatively evaluates the coupling strength between the electric and mechanical fields during the passage of a wave. We show that the WEMCF can be calculated either by an energy formula or by frequency formula. The equivalence of these two formulas makes WEMCF consistent with the Modal Electromechanical Coupling Factor. WEMCF can be post-processed from the free-wave characteristics obtained from WFEM. The reduced unit cell model is recommended to accelerate the calculation. An application is given based on a built-up structure with periodic piezoelectric substructures, showing the strong correlation between WEMCF and the best energy transmission loss of the resistive PZT waveguide.

- In Chapter 5, a design process is proposed for periodic piezoelectric structures to achieve broadband vibration control. The idea is to reduce the modal density and concentrate the vibration to the dissipative boundaries. Band-gap resonances are effectively suppressed and the mechanisms for these unusual modes are discussed.

The WEMCF is used as the criterion to optimize the geometric configuration under a constrained amount of PZT material. Negative capacitance is used to create a wide band gap and its stability are considered as well. The design process yields several solutions for the control of multiple high-order modes of a cantilever beam. The proposed design process does not rely on any modal information and the vibration reduction performance is also proved to be insensitive to the boundary conditions.

- In Chapter 6, the developed numerical tools are applied to a thin-wall structure coupled with periodic piezoelectric patches. The aim is to (1) illustrate the industrial application of the numerical methods; and (2) re-examine the conclusions obtained by simpler structures. Resulting from the complexity of the thin-wall structure, we show that some proposed enhancements are not optional but imperative. Additionally, the two equivalent ways for WEMCF are confirmed by the both lower-order and high-order waves of the thin-wall structure.

- Concluding remarks and discussions concerning the perspective work can be found after Chapter 6.

- The first appendix gives the material coefficients of the PZT material used in the thesis. The second appendix gives the detailed derivation and validation of the triple-layered piezoelectric beam element used in Chapter 3 and 5. The third appendix gives the derivation and validation of the Artificial Boundary Conditions that are used in Chapter 3. The fourth appendix gives supplementary material for Chapter 2. The fifth appendix gives supplementary material for Chapter 3. The last appendix gives supplementary material for Chapter 5.

Chapter 1

Literature review

Abstract: In this chapter the existing work concerning the structures coupled with piezoelectric materials are reviewed. First we briefly introduce the piezoelectric effects and the commonly used materials. Dynamic models and the methods to obtain wave characteristics from the dynamic models are outlined. Once the piezoelectric materials and electric circuits are involved into the governing equations, these methods can be directly used to predict the wave characteristics in piezoelectric structures. Then the electromechanical couping factor which is of utmost importance for many applications is individually reviewed. Finally the applications for vibration control are summarized. Remarks are given at the end of each part. Several analogies and dualities can be found such as the wave-mode duality, the duality between the vibration control and energy harvesting and the analogy between SSD and dry friction. The analogy between electric networks and mechanical models inspires pure mechanical and electric replacement models for piezoelectric structures. It also underlies many vibration control strategies such as electromechanical TMD, piezoelectric network and PEM structures.

Contents

1.1 Piezoelectric materials

The concept of smart structure provides another promising possibility of solving a variety of engineering issues, such as vibration control, noise reduction, fault diagnose, wireless sensing, self powering and so on. Smart structures could be defined as 'the structures that can sense external disturbance and respond to that in a desired fashion' [1]. Generally a smart structure can be implemented by integrating some 'smart material' that couples at least another field to the mechanical field. This introduces new design variables (Degree-of-Freedoms, DOFs) to modify or measure the mechanical characteristics. An additional subsystem can then be designed regarding the new variables so as to have the coupled structural system work in a desired manner. These smart materials involve electrorheological (ER) or magnetorheological (MR) fluids, magnetostrictive materials, electrostrictive materials, shape memory alloys (SMA), piezoelectric materials and so on. Figure 1.1 lists various effects that are observed in materials in response to various inputs: mechanical, electrical, magnetic, thermal, light. The smart materials correspond to the non-diagonal cells.

Input \ Output	Strain	Electric charge	Magnetic flux	Temperature	Light
Stress	Elasticity	Piezo-electricity	Magneto-striction		Photo-elasticity
Electric field	Piezo-electricity	Permittivity			Electro-optic effect
Magnetic field	Magneto-striction	Magneto-electric effect	Permeability		Magneto-optic
Heat	Thermal expansion	Pyro-electricity		Specific heat	
Light	Photostriction	Photo-voltaic effect			Refractive index

Figure 1.1: Stimulus-response relations indicating various effects in materials [2]. The smart materials correspond to the non-diagonal cells.

Figure 1.2 shows the energy density by unit mass with respect to the maximum frequency; the diagonal lines indicate a constant power density per unit mass. Note that all the material characteristics vary by several orders of magnitude. Among them all, the piezoelectric materials have the advantages of light-weight, large working frequency range and high power density, therefore they are undoubtedly the most mature and those with the most applications.

The piezoelectric effect was first discovered by the bothers Pierre Curie and Jacques Curie [4], who demonstrated that when certain crystalline materials were stressed, an electric charge was produced on the material surface and the converse effect was also available [5]. So the piezoelectric effect exists in two aspects: one is the direct piezoelectric effect that describes the material's ability to transform mechanical strain into electrical charge; another is the converse effect, which indicates the ability to convert an applied electrical potential into mechanical strain energy.

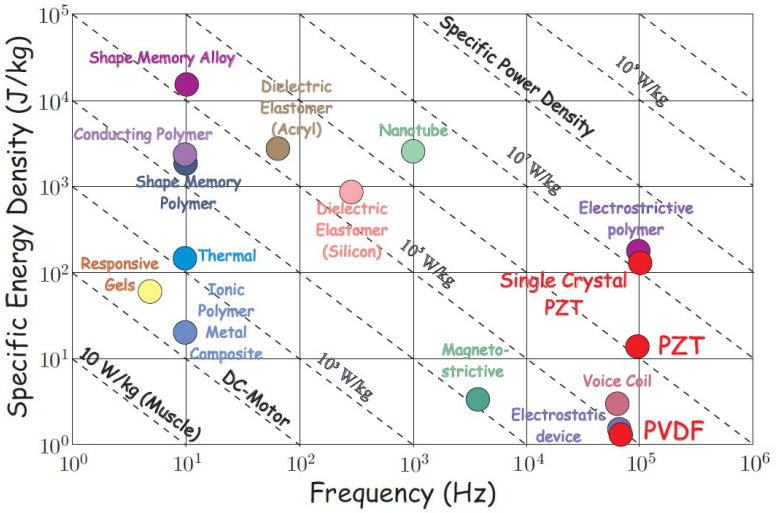

Figure 1.2: Specific energy density vs. maximum frequency for various smart material actuators [2].

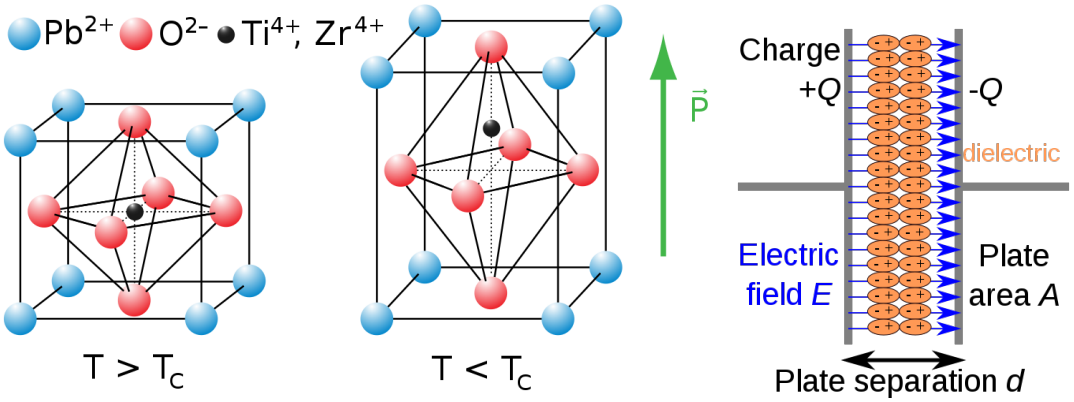

(a) (b)

Figure 1.3: Illustration of piezoelectric effects [3]: (a) Tetragonal unit cell of lead titanate before and after poling; (b) a piezoelectric patch behaves like a capacitance, the mechanical stress can also cause a charge separation.

Piezoelectric effect is closely related to the non-centrosymmetric crystalline structure in Piezoelectric materials. One of the defining traits is that the molecular structure is oriented such that the material exhibits a local charge separation, known as an electric dipole. Throughout the material composition the electric dipoles are orientated randomly, but when the material is heated above a certain point, i.e. the Curie temperature, and a very strong electric field is applied simultaneously, the electric dipoles reorient themselves relative to the electric field; this process is termed poling, shown in Figure 1.3a. Once the material is cooled, the dipoles maintain their orientation and the material is then said to be poled. After the poling process, the material will exhibit the piezoelectric effect.

When applying a mechanical stress, the dipole density field is subject to change. This might either be caused by a re-configuration of the dipole-inducing surrounding or by re-

orientation of molecular dipole moments under the influence of the external stress. The change appears as a variation of surface charge density upon the crystal faces, i.e. as a variation of the electric field extending between the faces caused by a change in dipole density in the bulk. In this regard, a piezoelectric patch behaves like a capacitance as shown in Figure 1.3b, mechanical stress, as well as an externally applied voltage, both cause the charge separation.

Mathematically, such electromechanical behavior of a piezoelectric material can be captured by two groups of linear equations [6]; the full 3D constitutive equations write

$$\{T\} = [c^E]\{S\} - [e]\{E\}$$
$$\{D\} = [e]^{\mathrm{T}}\{S\} + [\varepsilon^{\mathrm{S}}]\{E\}$$

where $\{T\}$ is the stress vector with 6 components, $\{S\}$ the strain vector with 6 components, $\{E\}$ the electric field vector with 3 components, $\{D\}$ the charge intensity vector with 3 components. The matrices,$[c^E]$, $[e]$, $[\varepsilon^S]$ are stiffness matrix evaluated at constant electric field, piezoelectric matrix, permittivity matrix evaluated at constant strain, respectively. Note that $[e]$ matrix sets the bridge between the structural stress and the applied electric field, representing the piezoelectric effect. The constitutive relation could also be written in other forms, giving the relationship between the chosen two terms among $\{T\}$, $\{S\}$, $\{D\}$ and $\{E\}$ and the rest two [6]. For example, one can also write the full 3D constitutive equations into

$$\{S\} = [s^E]\{T\} + [d]\{E\} \tag{1.1}$$
$$\{D\} = [d]^{\mathrm{T}}\{T\} + [\varepsilon^{\mathrm{T}}]\{E\} \tag{1.2}$$

The most popular piezoelectric materials are Lead-Zirconate-Titanate (PZT) which is a ceramic, and Polyvinylidene Fluoride (PVDF, see [7] for the detail) which is a polymer. PZT has an isotropic behavior in the plate, due to the fact that $d_{13} = d_{32}$; namely the electric field along the 3rd axis equally influences the stress in the 1st and 2nd axes. On the contrary, when PVDF is polarized under stress, its piezoelectric properties are highly anisotropic, with $d_{31} \approx 5d_{32}$. A PVDF is much lighter ($\sim 1800\,\mathrm{kg/m^3}$) than a PZT ($\sim 7800\,\mathrm{kg/m^3}$) but a PVDF is softer (Young's modulus $\sim 2.5\,\mathrm{GPa}$) than a PZT ($\sim 50\,\mathrm{GPa}$). Some new piezoelectric materials in the nanoscale can be found in [8]. There is no definitive answer as to which material is better. It depends on the restrictions and requirements of the application.

1.2 Dynamic models for piezoelectric structures

In conventional structural dynamics, the governing equations of a mechanical system could be established by means of the Hamilton's Principle, once the kinetic coenergy and potential energy of the system are written by a set of generalized coordinates compatible with the kinematic constraints [9]. To model a structural system with common materials, piezoelectric materials and electric networks, similar strategy exists. Preumont [2] provides a generalized variational indicator writes

$$\mathcal{V}.\mathcal{I}. = \int_{t_1}^{t_2} \left(\delta W_{\mathrm{m}}^* + \delta T^* - \delta W_{\mathrm{e}} - \delta V + \sum_k E_k \delta q_k + \sum_j F_j \delta x_j \right) \mathrm{d}t$$

where W_{m}^{*} is the magnetic coenergy; W_{e} is the electric energy; T^{*} is the kinetic coenergy; V is the elastic potential energy; q_k is the generalized charge coordinates; x_j is the generalized displacement coordinates; E_k is the applied electric potentials; F_j is the applied forces. It is proved that **the actual path is that which cancels the variational indicator $\mathcal{V}.\mathcal{I}.$ with respect to all admissible variations δx_k and δq_k of the path between two instants t_1 and t_2 at which $\delta x_j(t_1) = \delta x_j(t_2) = 0$ and $\delta q_k(t_1) = \delta q_k(t_2) = 0$.**

On this basis, the corresponding generalized Lagrange's equations follows

$$\frac{\mathrm{d}}{\mathrm{d}t}\left(\frac{\partial \mathcal{L}}{\partial \dot{q}_k}\right) - \frac{\partial \mathcal{L}}{\partial q_k} = E_k$$
$$\frac{\mathrm{d}}{\mathrm{d}t}\left(\frac{\partial \mathcal{L}}{\partial \dot{x}_j}\right) - \frac{\partial \mathcal{L}}{\partial x_j} = F_j$$

where $\mathcal{L}$ is the Lagrange indicator, given by

$$\mathcal{L} = W_{\mathrm{m}}^{*} + T^{*} - W_{\mathrm{e}}^{*} - V$$

Once the system configuration is determined, the energy and coenergy functions could be written in terms of the selected generalized coordinates. Accordingly the governing equations could be obtained using Lagrange's equations.

In practice, sometimes the piezoelectric materials are intensionally designed such that they work in a uniaxial strain/stress status. That is to say the applied electric field and external forces would only induce significant response in one direction, such as when designing torsional [10] or bending [11] transducers. Sometimes the mass of the piezoelectric materials can be neglected in comparison with the host structure. This often happens when designing a sensor [2]. When the piezoelectric materials are manufactured into bars, beams, rings or plates, for example in the applications of energy harvesting [12], the simplicity of geometries also leads to assumptions of the electric and mechanical fields. In all these situations, the full 3D constitutive and geometric equations can be simplified, leading to lumped parameter models or distributed models which can be analytically solved. For more complex situations, FEM can be used. These modeling strategies will be respectively discussed.

1.2.1 Lumped parameter models

The Lumped parameter approach simplifies the description of the behavior of spatially distributed physical systems into a topology consisting of discrete entities. For piezoelectric systems, this approach often leads to an approximative model with 2 DOFs, one for the mechanical displacement while another for the electric charge (or voltage). The corresponding model parameters, such as mass, damping and stiffness coefficients are obtained by equivalence.

In some applications this kind of equivalence is straightforward. Consider the piezoelectric stack transducer shown in Figure 1.4, if the inertia of the piezoelectric stack and the stiffness of the proof mass are neglected, it leads to a Lumped Parameter Model writing

$$\begin{pmatrix} V \\ -M\ddot{x} \end{pmatrix} = \frac{K_{\mathrm{a}}}{C_{\mathrm{p}}(1-k^2)} \begin{bmatrix} 1/K_{\mathrm{a}} & -nd_{33} \\ -nd_{33} & C_{\mathrm{p}} \end{bmatrix} \begin{pmatrix} Q \\ x \end{pmatrix}$$

where x is the mechanical displacement, V the voltage and Q the charge. For the detailed derivation please refer to [13]. With this rather simplified model one can understand many basic concepts of piezoelectric transducers, such as intrinsic capacitance, OC/SC statuses, electromechanical coupling factor and so on. In the work of Mokrani [13], this model is used to explore the damping performance of a nonlinear circuits. Similar strategies and 2DOF equations were considered to analysis piezoelectric bimorphs [14, 15], a thickness-stretch oscillator [16] and a torsional energy generator [10].

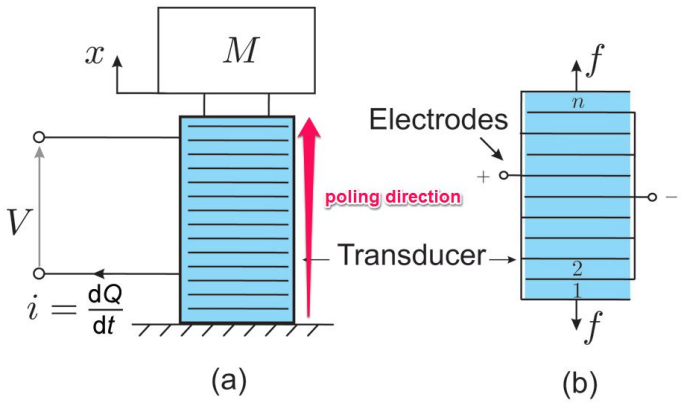

Figure 1.4: (a) Unidimensional spring-mass system. (b) Piezoelectric linear transducer made of n identical elements.

For a more complex situation as illustrated in Figure 1.5a, when a piezoelectric transducer is integrated into a host structure, the governing equations [17] write

$$\begin{bmatrix} m & 0 \\ c_{33}d_{33}L & C_{\mathrm{ps}}L \end{bmatrix} \begin{bmatrix} \ddot{x} \\ \ddot{u}_{\mathrm{p}} \end{bmatrix} + \begin{bmatrix} d_0 & 0 \\ c_{33}d_{33}R & C_{\mathrm{ps}}R \end{bmatrix} \begin{bmatrix} \dot{x} \\ \dot{u}_{\mathrm{p}} \end{bmatrix} + \begin{bmatrix} c_0 + c_{33} & -c_{33}d_{33} \\ \frac{c_{33}d_{33}}{C} & 1 + \frac{C_{\mathrm{ps}}}{C} \end{bmatrix} \begin{bmatrix} x \\ u_{\mathrm{p}} \end{bmatrix} = \begin{bmatrix} F(t) \\ 0 \end{bmatrix}$$

where the SDOF model is used for both the host structure and piezoelectric transducer. Owing to the external capacitance, non-diagonal terms appear in the mass and stiffness matrices. The governing equations can be rewritten into a simpler form

$$\begin{bmatrix} m & 0 \\ 0 & m_{\mathrm{p}} \end{bmatrix} \begin{bmatrix} \ddot{x}_1 \\ \ddot{x}_2 \end{bmatrix} + \begin{bmatrix} d_0 & 0 \\ 0 & d_{\mathrm{sd}} \end{bmatrix} \begin{bmatrix} \dot{x}_1 \\ \dot{x}_2 \end{bmatrix} + \begin{bmatrix} c_0 + c_{33} + c_{\mathrm{sd}} & -c_{\mathrm{sd}} \\ -c_{\mathrm{sd}} & c_{\mathrm{sd}} + c_\delta \end{bmatrix} \begin{bmatrix} x_1 \\ x_2 \end{bmatrix} = \begin{bmatrix} F(t) \\ 0 \end{bmatrix}$$

where $x_1 = x$ and $x_2 = x + u_{\mathrm{p}} C_{\mathrm{ps}} (c_{33} d_{33})^{-1}$. This means that the electromechanical system shown in Figure 1.5a can be represented by a pure mechanical model shown in Figure 1.5b. The shunted R-L-C circuit is equivalent to a spring-mass-damper system and the coupling mechanism is represented by a string linking the mass of the host structure and the 'electric' mass. This reveals the underlying mechanism of piezoelectric effect and the similarity between mechanical systems and electric systems. The equivalence allows us to firstly design a mechanical system and then implement it by piezoelectric materials and the shunted electric circuits. This idea is widely used for vibration control [18, 19], and more detailed information will be given in sections 1.5.

Alternatively, it is also possible to represent a piezoelectric structure by a pure electric replacement model, as shown in Figure 1.6. The mechanical mass, stiffness and damping are respectively transformed into electric inductor, capacitor and resistor. Mechanical

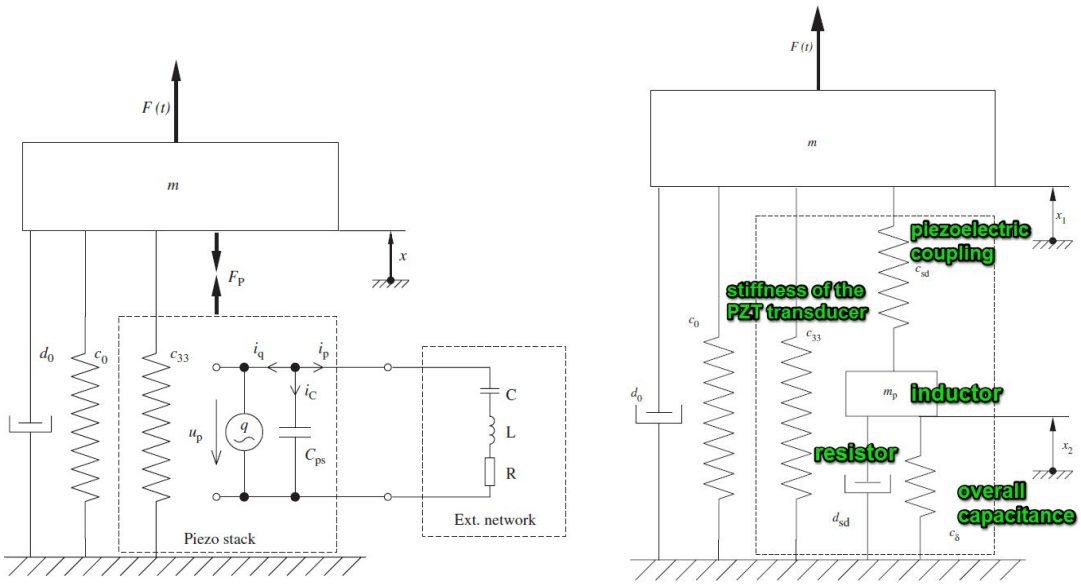

Figure 1.5: Lumped parameter models with 2 DOFs [17]: (a) Mechanical model with piezoelectric element connected to external LRC-network; (b) Mechanical replacement model.

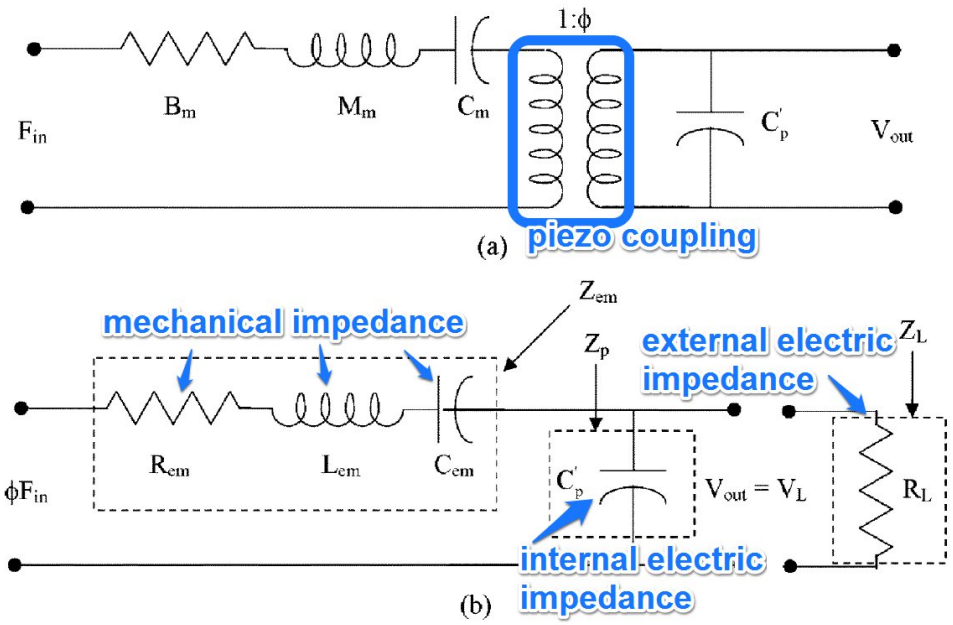

Figure 1.6: Two electric replacement models for SDOF mechanical system coupled with a SDOF piezoelectric system and an external circuit [16]: (a) represent piezoelectric coupling as a transducer, so that the variables' unit and value remain untransformed; (b) merge the coupling mechanism into the mechanical impedance, the mechanical variables are transformed into the equivalent electric variables.

force and displacement are equivalent to electric voltage and charge. This model allows one to implement an effective structural system with ease and can focus on the electric design. This idea has been used by Petit et al. [20] to preliminarily design a damping circuits, and Lossouarn et al. [21, 22] to design multi-mode dampers.

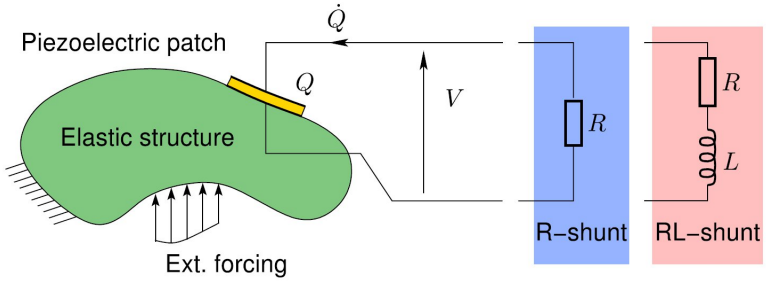

Figure 1.7: A general case for piezoelectric structure [23].

The mechanical parameters of the lumped parameter models can be intuitively obtained by assumptions and simplifications of the displacement and geometries, as previously discussed. Also the parameters can come from a complex structure/substructure for which we only interested in few modes. Consider a general case for piezoelectric structures as shown in 1.7, a reduced order model can be obtained by expanding the displacement field $\mathbf{U}(\mathbf{x}, t)$ onto N vibration modes

$$\mathbf{U}(\mathbf{x}, t) = \sum_{i=1}^{N} \phi_i(\mathbf{x}) q_i(t)$$

The electromechanical model of the problem is thus described by

$$\overbrace{\ddot{q}_i + 2\xi_i\omega_i\dot{q}_i + \omega_i^2 q_i}^{\text{mechanical}} - \overbrace{\chi_i V}^{\text{coupling}} = F_i, \forall i \in \{1...N\} \tag{1.3}$$

$$\underbrace{CV - Q}_{\text{electric}} + \sum_{i=1}^{N} \underbrace{\chi_i q_i}_{\text{coupling}} = 0 \tag{1.4}$$

in which N modal equations corresponding to the balance law of mechanical forces, and one electrical equation, associated with the balance of electric charges on the electrodes. With this strategy, one can reduce a distributed model or a refined Finite element model to a lumped parameter model. Generally, $\phi_i(\mathbf{x})$ is the ith open-circuit natural modal shape [2, 23, 24]. Note that the N modal coordinates are still coupled with each other through the electric voltage, which is different from the conventional modal reduction schemes. This will be further discussed in the following sections.

For complex structural systems, the lumped parameter models can also be employed [25–27]. For one sector in the bladed disc show in Figure 1.8, a 2DOF mechanical model can be used to describe the blade and a 2DOF electromechanical model is used for the disc coupled with piezoelectric patches. The overall governing equations are assembled by the equations of substructures.

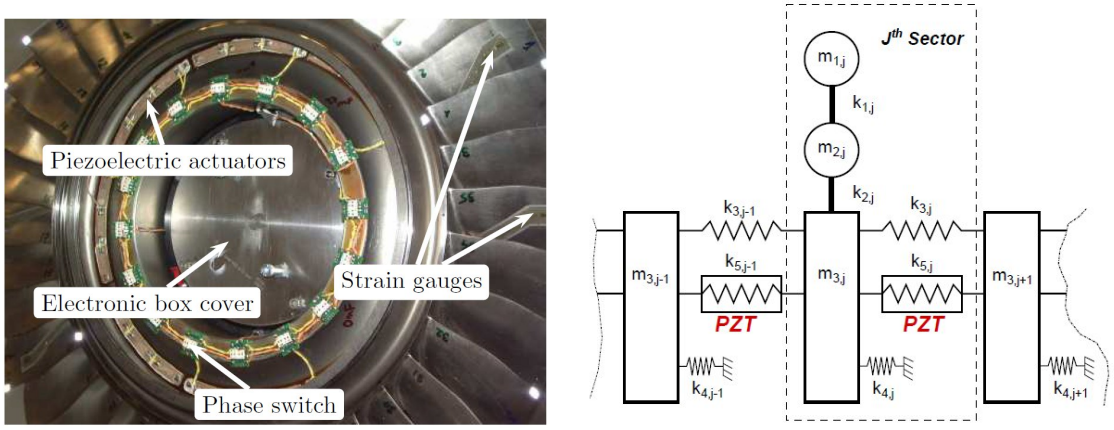

(a) (b)

Figure 1.8: Lumped parameter models for a bladed disc [25]: (a) real structure; (b) lumped parameter model.

1.2.2 Distributed parameter models

In principle, every piezoelectric system is governed by a group of partial differential equations (PDE) associated with specified boundary and initial conditions, forming a distributed parameter model. The analytical results could contribute to a deep understanding of the dynamics to structures coupled with piezoelectric materials. It becomes an active area of research since the early 1990s. At the beginning researchers focused on the modeling of piezoelectric stack actuators and bending actuators. By stacking the piezoelectric layers on top of one another, the cumulative volume of piezoceramics increases the energy delivered to a load. On the other hand, bending actuators [28] consist of multiple piezoceramics layers with greater length than the stacked type. Those layers can either be double mounted or single ended as a cantilever, as shown in Figure 1.9. When electric voltage is applied, one layer extends and the other contracts, shown in Figure 1.10, resulting a bending motion.

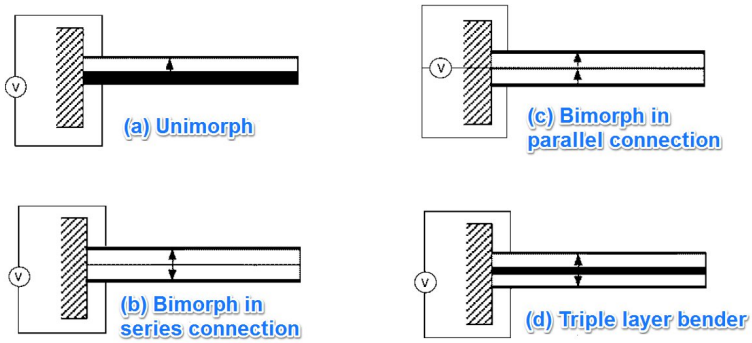

Figure 1.9: Illustrations of cantilever-mounted piezoelectric unimorph, bimorph, and triple layer morph benders [28].

In 1990, Smits et al. [30] derived a 4×4 static constitutive matrix for piezoelectric

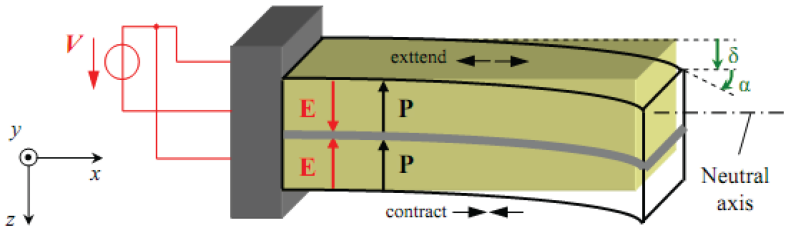

Figure 1.10: Basic intensive parameters of bimorph actuators after applying electric field [29].

bimorphs, relating the canonical conjugates: bending moment & tip rotation, transverse force & tip displacement, uniform pressure & volume displacement and voltage & charge. Later, Smits and Ballato [15] determined the dynamic constitutive equations of bimorphs. The starting point is the general solution of the Euler-Bernoulli beam theory. It has been shown that all elements in the constitutive matrix have a built-in resonance factor that causes the bimorphs to resonate at the mechanical resonance frequencies. A rather comprehensive literature review of piezoelectric bending mode devices and their applications has been given by Smits et al. [31]. For the triple layer bender, Wang et al. [28] systematically derived the constitutive equations. As a special case, if the thickness of the central elastic layer is set to 0, the constitutive equations become those for bimorph bender, and the results are consistent with those derived by Smits et al. [15]. Crawley et al. [32] compares the uniform strain model, Euler-Bernoulli model and FEM model for piezoelectric benders. Based on comparison with more detailed finite element models and experiments, the Bernoulli-Euler bending model was judged to accurately predict extensional and bending deformations, shown in Figure 1.11. The deviation in net displacement from the simple Bernoulli-Euler model was judged to be significant for shorter, thicker actuators and for thick beams, where the influence of material shear was greatest.

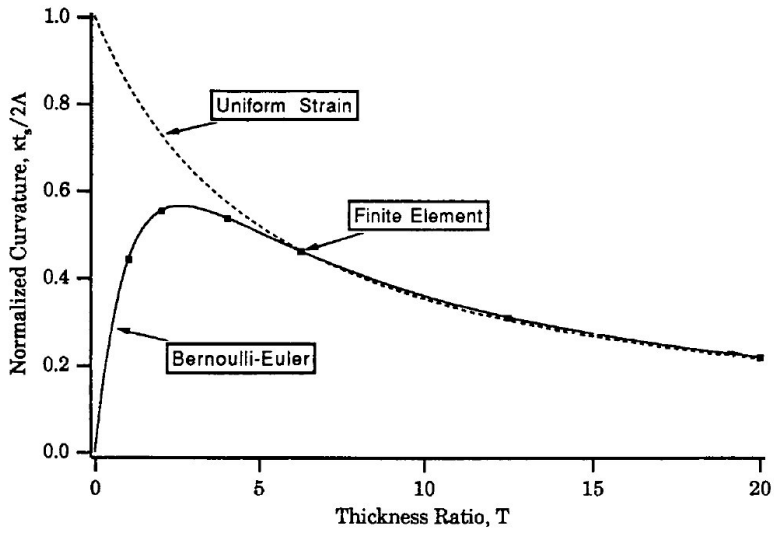

Figure 1.11: Comparison of induced bending strains from analytical and finite element models [32].

As discussed, there exists an equivalent electric representation of a lumped parameter model for the piezoelectric structures. Cho et al. [33] proposed an exact equivalent electric circuit representation for the piezoelectric bimorph beam. The electric network has one electrical and four mechanical ports. For an electromechanical system where other mechanical or electrical components are attached to the bimorph, an equivalent electric circuit of the system can be thus generated by connecting the electrically equivalent impedances to the circuit according to the mechanical boundary conditions or external mechanical components, as shown in Figure 1.12.

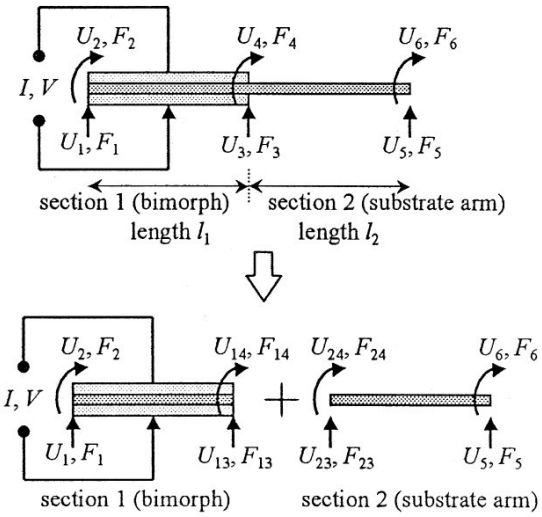

(a) flows (U_i, I) and efforts (F_i, V) of the segmented bimorph and substrate arm.

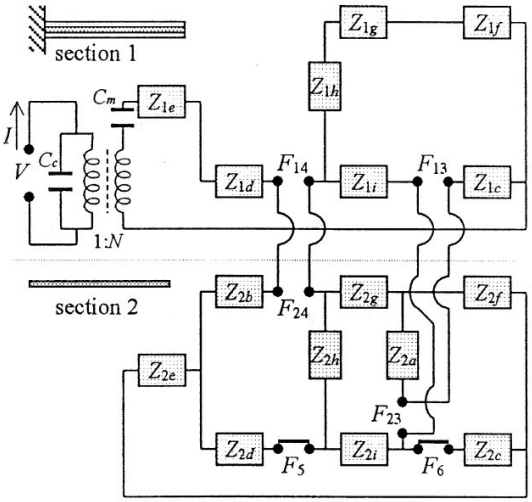

(b) series connections between the segmented bimorph and the substrate arm.

Figure 1.12: Equivalent electric circuit of the segmented piezoelectric bimorph and its substrate arm with clamped-free boundary conditions [33].

However, the shear deformation and the rotational inertia have not been taken into account in the work of Cho et al. Ha et al. [34] proposed another equivalent electric network through an eight-by-eight impedance matrix with thickness effects. This leads to an eight-port overall equivalent circuit. The effects of shear and rotational inertia and the circuit conditions on the resonance/ antiresonance frequencies for a wide range of thickness ratios have been studied using the circuit. These equivalent circuits can facilitate further analyses of the electromechanical system for probing the effects of connecting external systems, or of making modifications to the bimorph.

Erturk and Inman [35] presented an exact electromechanical solution of cantilevered piezoelectric beams with Euler–Bernoulli beam assumptions. In their work a piezoelectric beam is governed by

$$\frac{\partial^2 M(x,t)}{\partial x^2} + m\frac{\partial^2 w_{\mathrm{rel}}(x,t)}{\partial t^2} = p(x,t)$$

where

$$M(x,t) = YI\frac{\partial^2 w_{\mathrm{rel}}(x,t)}{\partial x^2} + \upsilon V(t)\overbrace{\left[\frac{\mathrm{d}\delta}{\mathrm{d}x}(x-x_1) - \frac{\mathrm{d}\delta}{\mathrm{d}x}(x-x_2)\right]}^{\text{the electrode is covered from } x_1 \text{ to } x_2}$$

is the internal bending moment caused by both transverse deformation w_{rel} and piezoelectric voltage V. The targeted applications are energy harvesters for transverse vibrations. Thus the dynamic behavior of the beam around certain natural modes is of interest. A modal superposition strategy is employed where the electrode-free eigenfunctions are used to form the coordinate transforming relation. The governing equation in the modal domain is similar to Equations (1.3) and (1.4). The same authors extended the analytical solution is to bimorph configurations with series and parallel connections of piezoceramic layers and experimentally validated [36]. This model allows us to conveniently analysis the dynamic response, equivalent parameters around few interested modes. It is promising for applications in energy harvesting and vibration control. Fau-Penella and Puig-Vidal [37] presented an equivalent circuit for the modal-superposition models, shown in Fig 1.13. This representation is more intuitive and general than the ones shown in Figure 1.12. The modal electromechanical coupling coefficients are represented by a set of transformers with different transforming ratios. It also shows that the structural 'modal' DOFs are coupled with each other through the voltage.

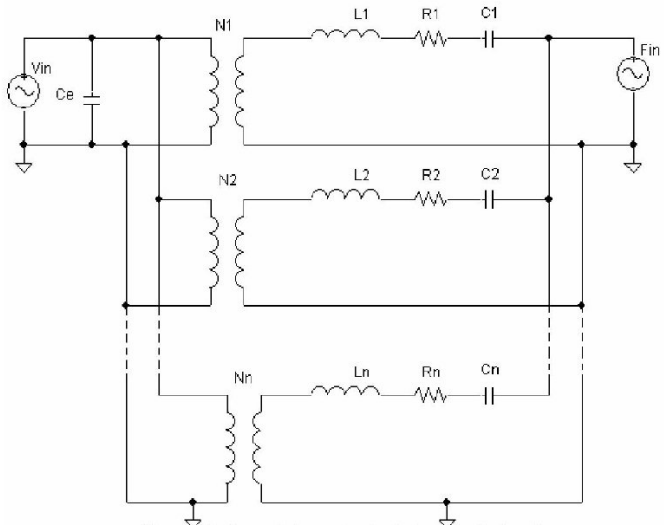

Figure 1.13: Complete equivalent electrical circuit for piezoelectric cantilever [37].

Moreover, studies can be found in the literature for stepped beams [38] and multilayer bending actuators [39]. The analysis of cantilevered piezoelectric beam with a mass on its top was studied in [1], and was extended to 2-mass case and validated experimentally [40]. It has been shown that the piezoelectric layer with an applied voltage equivalent to a distributed load proportional to second derivative of the width of the electrode. This leads us to design the shape of the electrode so as to design a modal actuator/ sensor [2].

There are also extensive studies concerning 2D structures such as a plate couples with piezoelectric materials. Benjeddou et al. [41] proposed an exact two-dimensional analytical solution for the free-vibration analysis of simply-supported piezoelectric adaptive plates. Layerwise first-order shear deformation theory (FSDT) kinematics, and quadratic non-uniform electric potential, are assumed in the study. They compared the results to available (exact) three-dimensional elasticity and finite-element solutions, showing that the results were the closest to the exact coupled three-dimensional ones. This model

was extended by Deü and Benjeddou [42] to show the influence of the electric boundary conditions, plate side-to-thickness ratio and piezoceramic lamina thickness and position on the electromechanical coupling of both in-plane and thickness modes. Preumont et al. [2] studied the equivalent loads created by a voltage applied to the piezoelectric patch bonded to the plate. They found that the piezoelectric loads consist of an in-plane force normal to the contour of the electrode, and a constant moment acting on the contour of the electrode.

Concerning the beams and plates with piezoelectric materials and electric circuits, another important analytical modeling strategy is proposed by Dell'Isola and co-authors [43, 44]. Their approaches are not for general cases but for beam/ plates with distributed piezoelectric materials and with periodic electric interconnections, termed Piezoelectromechanical (PEM) structures, as shown in Figures 1.14 and 1.15.

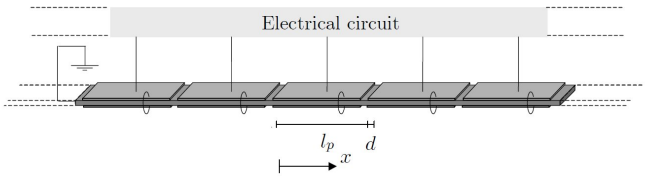

Figure 1.14: Illustration of a PEM beam [45].

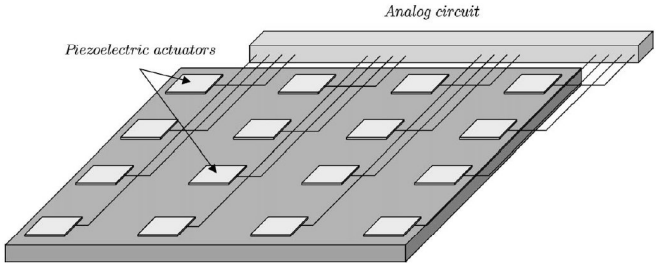

Figure 1.15: Illustration of a PEM plate [44].

One of the underlying ideas of their methods is the mechanical-electric analogies. The periodic interconnection of the piezoelectric patches (see Figure 1.16 for some examples), can be regarded as a finite difference approximation to the electric voltage field. The electric network can then be directly replaced by the spatial differential operator. The mechanical field is also treated by a homogenization process, leading to a distributed model. This way the PEM structures can be modeled by two groups of PDE, one for the mechanical field and another for the electric field. For instance, the PEM beam with the (S,S)-Network [46] shown in Figure 1.16 is modeled by the following distributed equations if the electric network and **disconnected**

$$U^{(4)}(X,t) + \frac{1}{c_{\mathrm{b}}^2}\ddot{U}(X,t) = 0$$
$$\ddot{\psi}(X,t) - \delta_2\dot{\psi}^{(2)}(X,t) - \beta_2\psi^{(2)}(X,t) = 0$$

where U is the transverse displacement and ψ is the electric flux-linkage (defined as the time primitive of the electric potential). Once the network is **connected** to the

piezoelectric patches, the governing equations of the mechanical and electric fields are coupling together, leading to complex PDEs. Let us see another example concerning plates. The free motion of the PEM plate with a membrane-like network [47] shown in Figure 1.17 is model by

$$\begin{aligned} \overbrace{\ddot{\upsilon} + \alpha\Delta\Delta\upsilon}^{\text{mechanical}} - \overbrace{\gamma\Delta\dot{\phi}}^{\text{coupling}} &= 0 \\ \underbrace{\ddot{\phi} + \delta\dot{\phi} - \beta\Delta\phi}_{\text{electric}} + \underbrace{\gamma\Delta\dot{\upsilon} + \delta\gamma\Delta\upsilon}_{\text{coupling}} &= 0 \end{aligned}$$

where υ is the out-of-plane displacement and ϕ the electric flux-linkage. With these distributed models, the wave and modal characteristics can be calculated with ease. Their specific applications will be presented in sections 1.5.

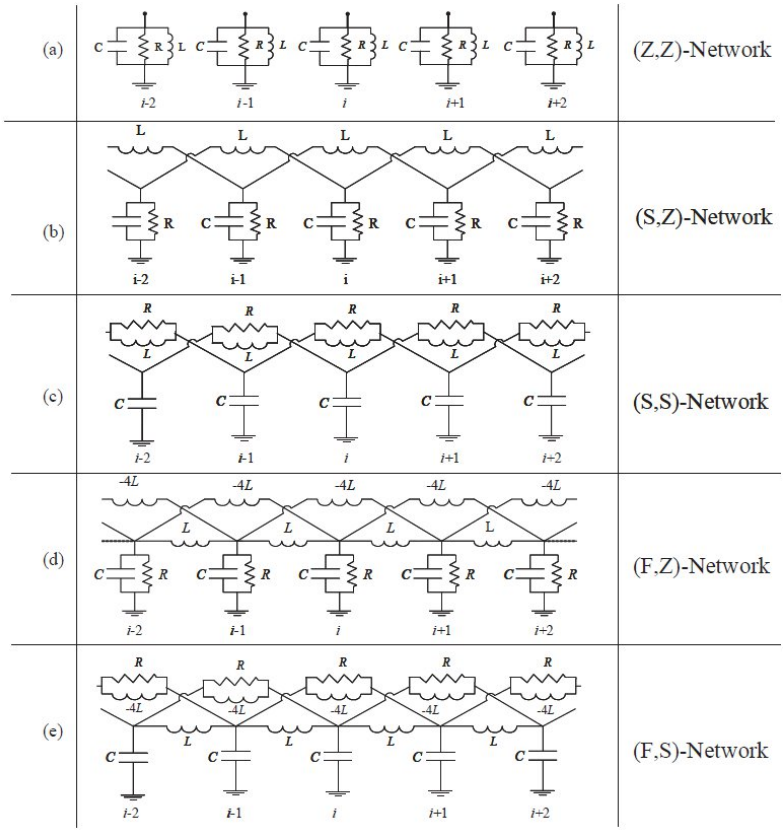

Figure 1.16: Circuit schemes of the modular lumped electric networks [46].

Note that one main aim of PEM is to use a passive electric network to modify the vibration and wave characteristics of the host structure. One can first design a electric network and use the aforementioned methodologies to see what is the equivalent elastic media of such a network and how it influences the structural system. Alternatively, one can also first design the attached elastic media such that the desired characteristics can be achieved. In this case we have to find an implementation of such elastic media by means of electric networks [48].

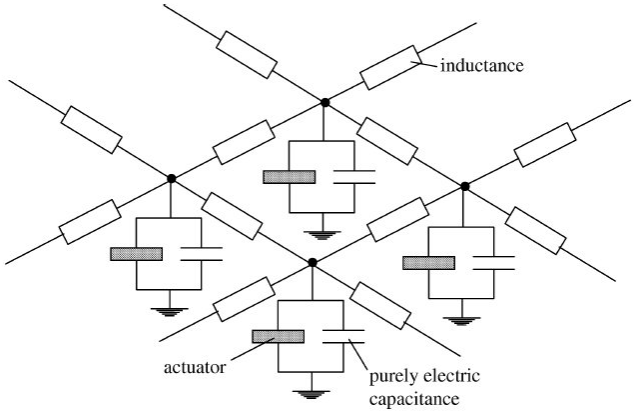

Figure 1.17: Electrical connection scheme for the PEM plate considered in [47].

1.2.3 Finite element models

Finite Element Method (FEM) is a well-developed numerical technique in common use for finding approximate solution to boundary value problems. It uses variational methods to minimize an error function and produce a stable solution. FEM encompasses all the methods for connecting many simple element equations over many small subdomains, named finite elements, to approximate a more complex equation over a larger domain. The idea of using FEM to analysis piezoelectric systems started in early 1970s, and nowadays many kinds of element with different shape (like shell, beam, rod and solid elements) and order are proposed. A comprehensive review can be found in [49]. Elements with no electric DOF and those are capable to capture the 'induced voltage' are of special interest.

One concern of the FEM is that the model dimension (number of DOFs) are enormous if the geometric or material configurations are complex, especially in mid- and high frequencies. Model reduction strategies are accordingly proposed. Lazarus et al. [50, 51] proposed a reduced model in which the system's electrical state is fully described by only a couple of variables per piezoelectric patches, namely the electric charge contained in the electrodes and the voltage between the electrodes. The reduction is achieved by a modal truncation based on short-circuit natural modes. Collet and Cunefare [52] proposed a modified Craig-Bampton condensation able to take into account the entire piezoelectric coupling as far as it is accurately introduced in the basic model employed. Two additional displacement fields are introduced to the basis: 1) A set of the dual displacement fields adjoint to the piezoelectric applied forces computed with homogeneous connecting Dirichlet condition; and 2) A set of fields that are the inner normal modes with homogeneous Dirichlet connecting conditions, orthogonal to the piezoelectric applied forces. The model was experimentally validated in their study.

With its advantages, FEM has already been used to many applications of piezoelectric structures. Pagani Jr et al. [53] used a full FEM model to determine the optimal weighted array of a piezoelectric modal filter and so does in [54]. Complex interconnection of patches or material blocks are required in such application, which is very difficult to model by analytical methods. Kim et al. [55] used a FEM model to find the best location for piezoelectric patches in a plate with only one edge clamped, to achieve the best vibration

control performance. Bareille et al. [56] used a FEM model to design a torsional actuator; designs with different number of patches and different ways of locating the patches are compared. Applications can also be seen for rotor-machinery blades or bladed discs coupled with piezoelectric patches [57, 58].

1.2.4 Remarks

Knowing the governing equations is the starting point towards piezoelectric actuating, sensing, energy harvesting, vibration control, wave filtering and so on. Choosing an appropriate modeling strategy is a trade-off between efficiency and accuracy. In applications for energy harvesting, if the task is to design/optimize the electric circuits, the lumped parameter models can be used. It is similar in applications for vibration reduction when only one patch is used to control one mode. In applications for spatial sensing and actuating, the distributed models are required. It is also the case for multi-mode vibration control in beam-like or plate-like structures. The analogy between the mechanical properties and electric elements are well studied in the literature, leading to pure mechanical and pure electric representation of piezoelectric systems. These replacement models provide insights into the mechanism to understand and utilize the piezoelectric effects. It underlies the PEM beams and plates proposed for broadband vibration control and noise isolation. With the increase of complexity, FEM becomes a reliable numerical tool. Reduced models can be used to mitigate the issue regarding matrix size.

It is worth to note that each models has its own assumptions. Lumped parameter models are valid only in low frequencies or around certain natural modes. Distributed parameter models has assumptions on the geometrics and on the stress & strain. The distributed models used for PEM structures rely on the homogenization on both mechanical and electric fields. This makes the models only valid when the wavelength is much smaller than the patch dimension. In FEM the element type and mesh density need to be carefully chosen to control the discretization error.

1.3 Electromechanical coupling factors

1.3.1 Definitions

Piezoelectric effect is the corner stone of all the piezoelectric based smart structures. It naturally comes into a question that how do we quantitatively describe the 'strength' of the electromechanical coupling for a piezoelectric material. The criteria that can measure the 'converting capability' are termed Electromechanical Coupling Factors (EMCF). Moreover, there are two scales regarding EMCF. The first on is **the material scale**. EMCF in this scale is used to describe the couping strength or converting capability of a piezoelectric material. EMCF in this scale is directly related to the material parameters. It allows one to choose an appropriate piezoelectric material before it is manufactured into certain components. The second one is **the structure scale**. EMCF in this scale is expected to include the coupling strength of the whole structure, taking into account the geometrics and the locations of piezoelectric material, as well as the frequency and structural deformations (see [59] for an example). It allows one to design or optimize a smart structure.

Summarizing earlier studies [60–63], the last IEEE standard on piezoelectric materials and transducers [6] uses two EMCF, one for the material scale [61] and another for the structure scale [60].

For the material scale, the internal energy in a piezoelectric material writes

$$U = \frac{1}{2}\int_v \left(\{T\}^{\mathrm{T}}\{S\} + \{E\}^{\mathrm{T}}\{D\}\right) \mathrm{d}v$$

Introducing the constitutive equations (1.1) and (1.2), leading to

$$U = U_{\mathrm{e}} + 2U_{\mathrm{m}} + U_{\mathrm{d}} \tag{1.5}$$

where U_{e} , U_{m}, U_{d} are the elastic energy, electric energy and mutual energy respectively. Specifically, they are

$$U_{\mathrm{e}} = \frac{1}{2}\int_v \left(\{T\}^{\mathrm{T}}\ [s^E]\{T\}\right) \mathrm{d}v$$
$$U_{\mathrm{m}} = \frac{1}{2}\int_v \left(\{T\}^{\mathrm{T}}\ [d]\{E\}\right) \mathrm{d}v$$
$$U_{\mathrm{d}} = \frac{1}{2}\int_v \left(\{E\}^{\mathrm{T}}\ [\varepsilon^{\mathrm{T}}]\{E\}\right) \mathrm{d}v$$

The EMCF k_{s} defined in [61] writes

$$k_{\mathrm{s}}^2 = \frac{U_{\mathrm{m}}^2}{U_{\mathrm{e}}U_{\mathrm{d}}} \tag{1.6}$$

and it is used in IEEE standard [6] for uniform electro-elastic states. For instance for a '13' thickness stretch mode, where the only T_1 and E_3 are non-zero, it leads to

$$k_{31}^2 = \frac{d_{13}^2}{\varepsilon_{33}^{\mathrm{T}} c_{11}^{\mathrm{D}}} \tag{1.7}$$

only depended on the material parameters. Similarly, terms k_{33}^2, k_{51}^2 etc. can also be obtained in the similar manner. These terms are also called static coupling factors. They are especially useful in actuating and sensing where the deformation of piezoelectric materials can be assumed.

For a host structure coupled with a piezoelectric transducer, i.e. the structure scale, the EMCF can be obtained at each natural modes [60], by

$$k_{\mathrm{d}}^2 = \frac{\omega_{\mathrm{r}}^2 - \omega_{\mathrm{a}}^2}{\omega_{\mathrm{r}}^2} \tag{1.8}$$

where ω_{r} is the resonance frequency in the FRF of V/Q, and ω_{a} is the anti-resonance frequency. In fact, ω_{r} corresponds to the open-circuit frequency of the mode and ω_{r} to the short-circuit modal frequency [2]. Term k_{d} is also called Modal Electromechanical Coupling Factor (MEMCF) [23]. Equation (1.8) also gives a convenient way to experimentally measure the WEMCF and it is widely used in practice. The MEMCF can also be calculated from a energy-based formula [64]

$$k_{\mathrm{d}}^2 = \frac{U_{\mathrm{OC}} - U_{\mathrm{SC}}}{U_{\mathrm{OC}}} \tag{1.9}$$

where U_{OC} is the internal energy of the structure when the electrodes are open and U_{SC} is the internal energy for short-circuit electrodes.

To understand the equivalence between Equations (1.9) and (1.8), Preumont [2] provided an intuitive interpretation. Consider a longitudinal piezoelectric transducer subjected to the following mechanical cycle: first, it is loaded with a force F with short-circuited electrodes; the resulting extension is $\Delta = F/K_{\mathrm{sc}}$. The stored energy is $W_1 = F^2/(2K_{\mathrm{sc}})$. At this point, if we disconnect the electrodes and the transfer is unloaded according to a path of slope $K_{\mathrm{oc}} = K_{\mathrm{sc}}/(1-k^2)$, the stored energy now becomes $W_2 = F^2(1-k^2)/(2K_{\mathrm{sc}})$, leaving $W_1 - W_2$ stored in the transducer. The ratio between the remaining stored energy and the initial stored energy is $(W_1 - W_2)/W_1 = k^2$, which is the MEMCF.

Equations (1.8) and (1.9) are proposed for modes where the structure has finite extend. For open structural structures, the coupling mechanism is associated to waves. Various definitions can be found for different cases. Chen et al. [65] calculated EMCF by

$$k = \frac{V_{\mathrm{oc}} - V_{\mathrm{sc}}}{V_{\mathrm{sc}}}$$

for Rayleigh-type surface acoustic waves in a semi-infinite with alternating piezoelectric and non-piezoelectric super-lattices, where V_{oc} and V_{sc} are the group velocity in open-circuit and short-circuit situation respectively. Fan et al. [66] used the Green's function method to calculate the electromechanical coupling coefficient of a Lamb wave in a multi-layered plate. To the writer's knowledge, no research efforts has been devoted to evaluate the EMCF for the guided waves in 1D and 2D uniform or periodic structures.

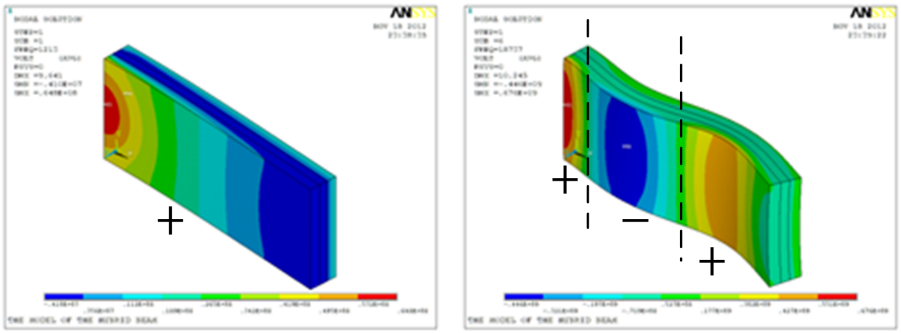

(a) (b)

Figure 1.18: Charge distribution of a cantilever beam with uniform piezoelectric materials in the electrode-free situation (a) the first mode; (b) the third mode.

1.3.2 Optimization and enhancements

In practice a larger electromechanical coupling factor is always desired, corresponding to an optimization problem. MEMCF can be used as a criterion for the design of geometric parameters. To illustrate this, let us consider an electrode-free piezoelectric cantilever beam. The first mode produces the same kind of charge on the surface of piezoelectric materials. When a uniform electrode is attached, no generated charge is canceled as

shown in Figure 1.18a, leading to a good coupling. However, the third mode generates different kind of charges on the surface shown in Figure 1.18b. If a uniform electrode is still used, charge with different signs would cancel each other out, leading to a very low coupling factor. There are several ways to improve the MEMCF by modifying the geometric parameters.

First, one can use shaped electrodes over a uniform piezoelectric material. Vasques [67] suggested the using of a shaped electrode to optimize the MEMCF for certain mode while filtering out the other modes, leading to a spatial modal filter. This filter can be used to sense, actuate or dampen the modal vibration without influencing other modes. Vasques demonstrated that the optimized shape function for the width $S(x)$ should be proportional to the second order spatial derivation of the modal shape ϕ, namely

$$S(x) \propto \frac{\mathrm{d}^2\phi(x)}{\mathrm{d}x^2}$$

and the optimized results are illustrated in Figure 1.19. Note that the width is required to be vary in a continuous way, this may causes manufacturing difficulties in practice.

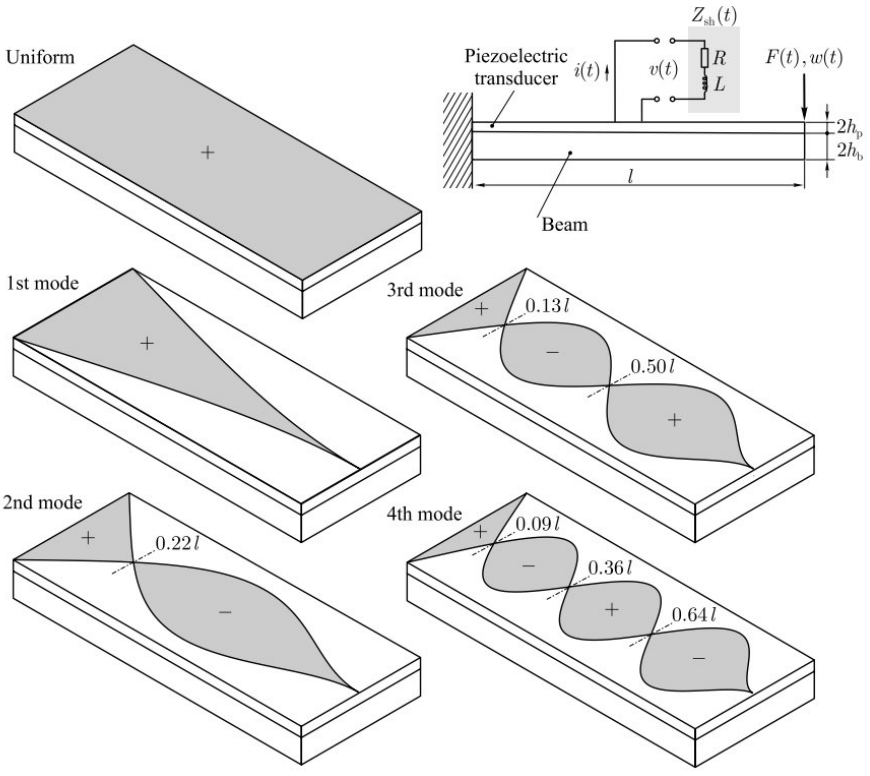

Figure 1.19: Schematics for uniform and modal electrode configurations [67].

Alternatively, one can still use a number of simple rectangular piezoelectric patches which are easy to be purchased. The aim is to find proper locations for them so as to achieve acceptable MEMCF for the targeted mode. Ducarne et al. [68] optimized the placement, length and thickness of piezoelectric patches for two different configurations of beam, shown in Figure 1.20. Note that the length of the patches and width are in many cases chosen in priori to minimize the added mass of the patches, or simply because the

area covered by the patches has to be limited. In such cases additional constrains have to be considered.

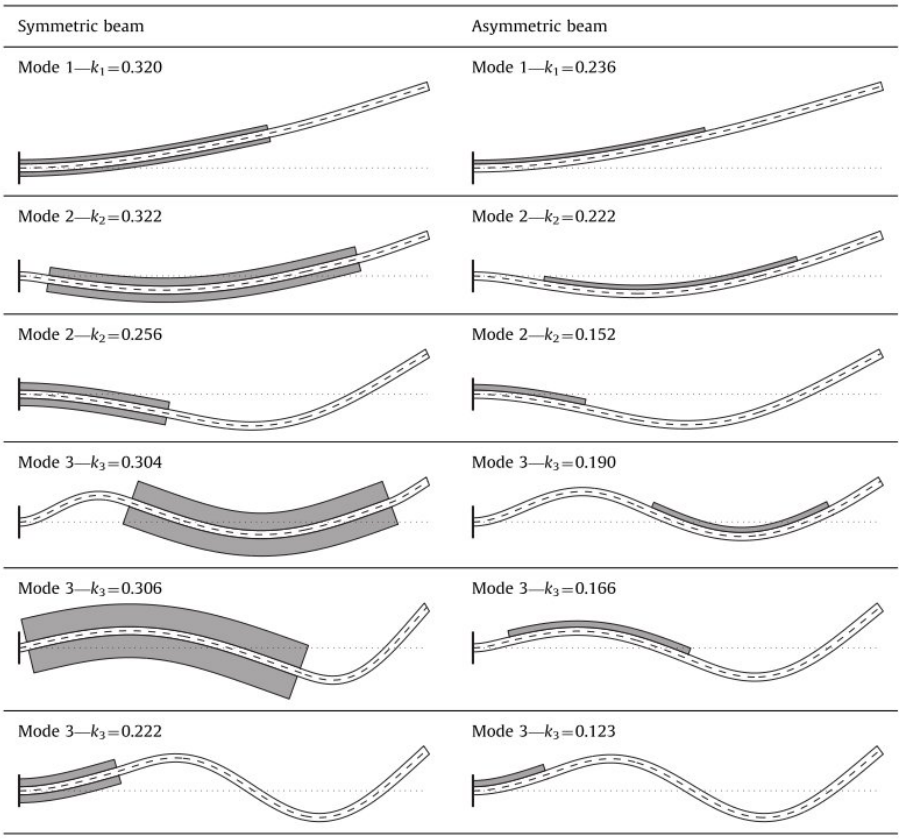

Figure 1.20: Deformed shapes of the optimal configurations for an aluminum/PIC151 beam [68].

We can see that the optimal geometric parameters for MEMCF vary dramatically for different modes. To have a piezoelectric structure with good MEMCF for multiple modes, Li et al. [59] designed a cantilever beam with distributed electrodes and a electric network whose connection is frequency-dependent, shown in Figure 1.21. It is based on the fact that the MEMCF for a single mode is determined by two factors: material-structure coupling factor and modal position coupling function. The former is only related to material properties and structure dimensions and the latter is related to position of the electrode. Accordingly, they first distributed the electrodes into several small pieces and design the connection patten of the electrodes for each mode. Then a 'current flow' network is used to decide the 'weight' of the connection pattens at a given frequency. The strategy ensures electrodes with same kind of charge always being connected therefore achieves best MEMCF for multiple modes.

Once the geometric parameters are decided, a semi-active circuit termed Negative Capacitance (NC) can be used to further enhanced the coupling strength. Its applications can be seen in extensive studies [69–72]. Commonly a NC is implemented by the synthesis electrical circuit shown in Figure 1.22 leading to $Q_C/V_C = -C_n$. The equivalent

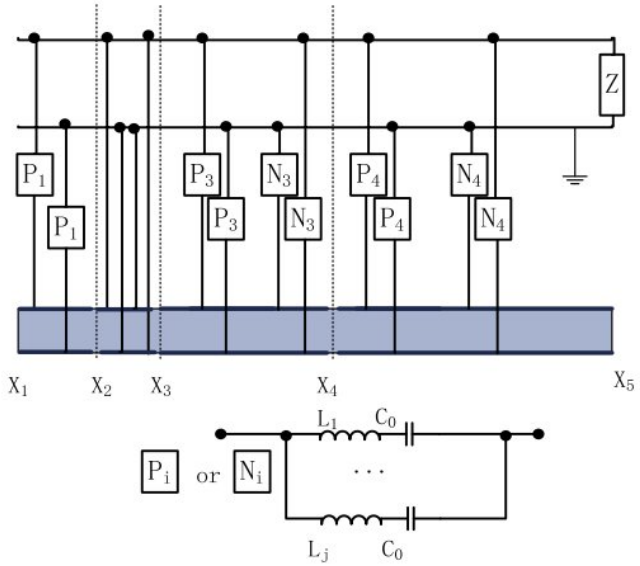

Figure 1.21: The layout of electrodes and electric networks to optimize MEMCF for the first three modes of a cantilever beam [59].

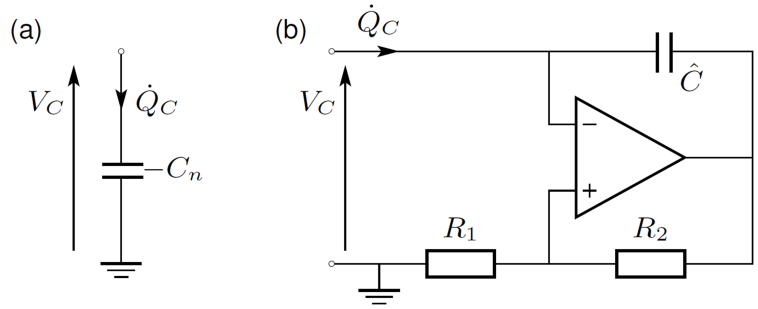

Figure 1.22: Synthesis electrical circuit as a NC commonly used in the literature.

capacitance can be determined by

$$C_{\text{neg}} = \frac{R_1}{R_2}\hat{C}$$

where R_1, R_2 and $\hat{C}$ are the resistances and capacitance shown in the figure; C_{n} is the absolute value of the negative capacitance. Commonly there are two configurations in the literature to introduce one NC into the shunt circuit, namely the parallel and the series configurations, shown in Figure 1.23. According to the work of Marneffe and Preumont [73], for the parallel configuration, the OC natural frequency $\hat{\omega}_{\text{oc}}$ for the transducer becomes

$$\hat{\omega}_{\text{oc}}^2 = \omega_{\text{oc}}^2 + \frac{\chi_i^2}{C_{\text{p}} - C_{\text{n}}}$$

while the SC natural frequency remains unchanged, namely $\hat{\omega}_{\text{sc}}^2 = \omega_{\text{sc}}$. This leads to the change of MEMCF for each mode

$$\hat{k}_i^2 = \frac{C_{\text{p}}}{C_{\text{p}} - C_{\text{n}}} k_i^2$$

according to Equation (1.8), where k is MEMCF without NC and $\hat{k}$ is MEMCF with parallel NC. If $C_{\mathrm{n}} < C_{\mathrm{p}}$, an increase of the MEMCF can be achieved.

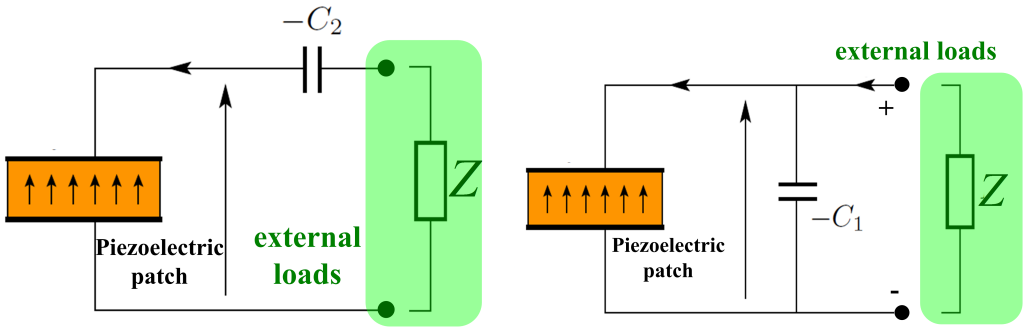

(a) (b)

Figure 1.23: Illustration of a piezoelectric transducer connected to a negative in series (a) and in parallel (b).

For the series configuration, the SC natural frequency $\tilde{\omega}_{\mathrm{sc}}$ for the transducer becomes

$$\tilde{\omega}_{\mathrm{sc}}^2 = \omega_{\mathrm{sc}}^2 - \frac{\chi_i^2}{C_{\mathrm{n}} - C_{\mathrm{p}}}$$

while the OC natural frequency remains unchanged, namely $\tilde{\omega}_{\mathrm{oc}}^2 = \omega_{\mathrm{oc}}$. This also induce a change of MEMCF for each mode

$$\tilde{k}_i^2 = \frac{C_{\mathrm{n}}}{C_{\mathrm{n}} - (1 - k_i^2)C_{\mathrm{p}}} k_i^2$$

according to Equation (1.8), where $\tilde{k}$ is MEMCF with series NC. If $(1-k_i^2)C_{\mathrm{p}} < C_{\mathrm{n}} < C_{\mathrm{p}}$, an increase of the MEMCF can also be achieved.

A comparison between series and parallel NC can be found in [73] and the stability study reveals that the series configuration is better than the parallel one. Moreover, the series configuration increases the equivalent capacitance (in contrast to the parallel case), which further reduces the optimal value the inductance in a RL shunt and thus makes it easier to implement electronically.

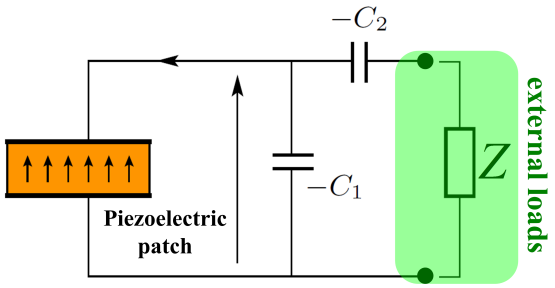

Figure 1.24: The new configuration of using two NCs proposed by Berardengo et al. [74].

Note that a parallel NC only changes the OC natural frequencies, while a series NC only changes the SC natural frequencies. A new configuration of using two NCs has been

proposed by Berardengo et al. [74], shown in Figure 1.24. This changes at the same time the short and open circuit resonance frequencies of the electromechanical system. Consequently a better MEMCF and a wider stability zone can be achieved.

1.4 Analysis methods for wave characteristics

Wave propagation characteristics underlie the vibration and acoustic performance of structures. First, we can use wave characteristics to predict the vibration and acoustic performances of structures [75]. Theoretically the wave-based methods can give the same answer to a same structural dynamic problem as the mode-based methods, and this equivalence is termed 'wave-mode duality' in the literature [76–78]. The wave-based methods can analyze open structural systems and can also remarkably reduce the dimension of problems. These features are especially useful in mid- and high frequencies. Secondly, another important application is the structural health monitoring [79, 80], the wave-based methods involve high frequency excitation and thereby can detect minute damages unlike low-frequency vibration technique. Moreover, one can achieve some unusual dynamic features by designing the wave characteristics, such as low modal density, negative refraction and negative group velocity. These are related to the rising research field concerning the periodic structures or the so-called 'phononic structures' [81].

With regard to these applications, the obtaining of the wave characteristics is essential. This section gives a brief review of the existing tools that yield wave characteristics of a given structure. Generally each of these methods is based on the governing equations of the whole or part of the structure. By the approaches that have been mentioned in section 1.2, the piezoelectric materials can be included in the governing equations. In this regard, here we only presents the methods in a general sense. Whether a method is applicable for certain piezoelectric structures depend on whether the piezoelectric structures can fit into the governing equations that underlies the method.

1.4.1 Analytical methods

Simple structures, for example a uniform rod and a uniform beam, are amenable to exact analysis. For such waveguides the analytical solutions are available for the wavenumber, the group velocity, and wave shapes [82]. As an example, for a thin beam where the Euler-Bernoulli theory holds, the governing equation for free vibration is given in form

$$\rho A \frac{\partial^2 u(x,t)}{\partial t^2} + EI \frac{\partial^4 u(x,t)}{\partial x^4} = 0$$

where ρ, E, A, I are density, young's modulus, area and second moment of area respectively. Assuming time- and space-harmonic motion, the displacement is written as

$$u(x,t) = e^{-jkx+j\omega t}$$

where $j = \sqrt{-1}$, k is the wavenumber and ω the angular frequency. Substituting to the governing equation, it yields four wave numbers

$$\begin{aligned} k_1 &= +\sqrt{\omega}C \\ k_2 &= -\sqrt{\omega}C \\ k_3 &= +j\sqrt{\omega}C \\ k_4 &= -j\sqrt{\omega}C \end{aligned}$$

where $C = (\rho A/(EI))^{1/4}$. The positive real and negative imaginary wavenumbers are associated with the positive-going waves so that the waves propagate in the positive direction of the beam and the other wavenumbers are associated with the negative-going waves. So k_1 represents the positive-going propagating wave; k_2 represents the negative-going propagating wave; k_3 represents the negative-going evanescent wave; k_4 represents the positive-going evanescent wave. Note each wavenumber is a function of the frequency, this is termed dispersion equation/curves. Once the dispersion equations are obtained the group velocity $\partial\omega/\partial k$ and phase velocity ω/k can be calculated.

A dispersion curve describes the relationship between the 'frequency' in space (k) and in time (ω). But the deformation and stress caused by the passage of the wave is not given by dispersion relations. To express that we need to calculate the 'wave modes' or 'wave shapes'. According to Euler-Bernoulli theory, the rotational deformation $\theta(x)$, internal bending moment $m(x)$ and internal transverse force $f(x)$ can be known once the displacement $u(x)$ is given. Assembling them in a vector, we have

$$\phi = \begin{pmatrix} u \\ \theta \\ f \\ m \end{pmatrix} = \begin{pmatrix} 1 \\ \partial u/\partial x \\ EI\partial^3 u/\partial x^3 \\ -EI\partial^2 u \partial x^2 \end{pmatrix}$$

By considering each wavenumber we obtain the corresponding wave shapes, ϕ_1, ϕ_2, ϕ_3, ϕ_4. The wave numbers $k_{1,2,3,4}$ and waveshapes $\phi_{1,2,3,4}$ in combine is termed the 'wave basis' [83]. The wave basis is the starting point of all the wave-based applications.

There are many useful properties of the wave basis [84, 85]. For instance, using the wave shapes we can transform the physical state-vector $\mathbf{S}$ into the wave domain, as

$$\mathbf{S} = \begin{pmatrix} u \\ \theta \\ f \\ m \end{pmatrix} = \sum_{i=0}^{4} a_i \phi_i = \Phi \mathbf{a} \tag{1.10}$$

In physical domain, the state-vector at two different locations, say $x = x_0$ and $x = x_1$, are related by a transfer matrix, namely

$$\mathbf{S}(x_0) = \mathbf{T}\mathbf{S}(x_1)$$

It is not difficult to check that $\mathbf{T}$ is a full matrix. However, by transforming the $\mathbf{S}$ into $\mathbf{a}$, it can be proved [83] that

$$\mathbf{a}(x_0) = \Lambda \mathbf{a}(x_1) \tag{1.11}$$

where Λ is a diagonal matrix only links to the wavenumbers and the distance between two points $x_0 - x_1$. More importantly, we have

$$\Lambda = \Phi^{-1}\mathbf{T}\Phi \tag{1.12}$$

These conclusions, shown in Equations (1.11) and (1.12), are very important as we will see later.

Note that during the analysis towards wave basis, we do not consider any boundary conditions, which means the waves we are searching for can be understood as the free deformations that can happen in the unbounded media. This does not mean that wave basis can only be used for infinite structures. For a finite structure, a boundary condition only constrains the relationship between the injected wave and the reflected waves and such a relation can be calculated by the wave basis. Let us still use the Euler-Bernoulli beam as an example, if a free boundary condition is imposed at $x = x_0$, namely $f(x_0) = 0$ and $m(x_0) = 0$. Introducing these constrains to Equation 1.10, leading to

$$\begin{pmatrix} a_1(x_0) \\ a_4(x_0) \end{pmatrix} = \mathbf{R} \begin{pmatrix} a_2(x_0) \\ a_3(x_0) \end{pmatrix}$$

where $\mathbf{R}$ is a 2×2 reflection matrix. This way the finite boundary conditions have been considered and with that natural modes [78] and forced response [84] can be calculated.

The approach described above can be applied to other cases where the equation of motion can be analytically expressed, such as plate and stiffened plate [86].

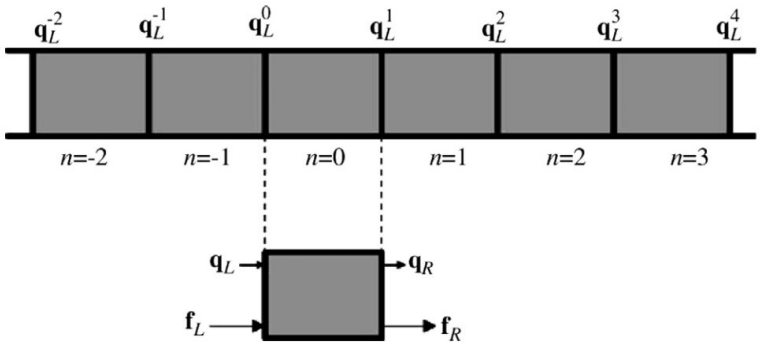

Figure 1.25: Illustration of a uniform waveguide and the state vector of a unit cell [87].

1.4.2 Transfer matrix method

Equations (1.11) and (1.12) actually indicate that the wave characteristics are related to the eigendecomposition of transfer matrix. So if the homogeneous problem of the governing equations is difficult to search, one can try to first express the transfer relation between two state vectors at the ends of one segment of the structure, as

$$\begin{pmatrix} \mathbf{q}_n \\ \mathbf{f}_n \end{pmatrix} = \mathbf{T} \begin{pmatrix} \mathbf{q}_{n+1} \\ \mathbf{f}_{n+1} \end{pmatrix} \tag{1.13}$$

where $\mathbf{T}$ is the transfer matrix. For uniform structures, the segment length Δ can be arbitrary (Figure 1.25) while for the periodic structures (Figure 1.26), a smallest repetitive

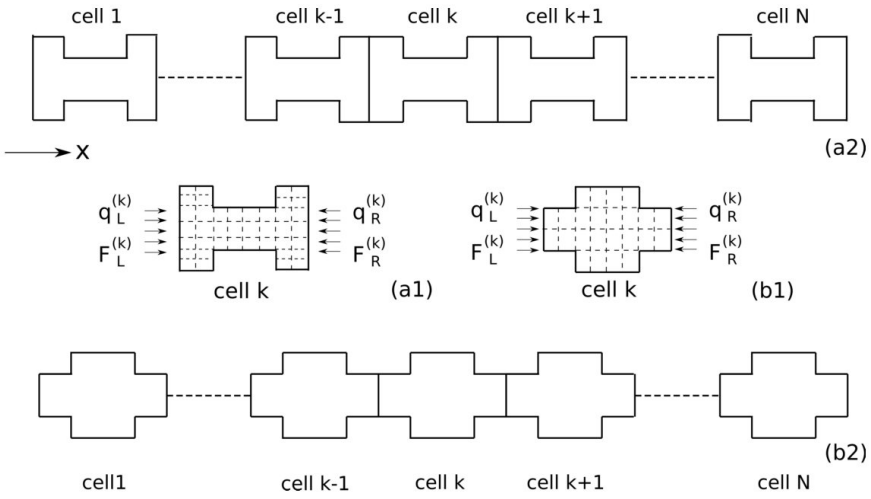

Figure 1.26: Illustration of a periodic waveguide. The choosing of the unit cell is not unique: (a1) 1st choice of unit cell (a2) Periodic structure considering a1 as unit cell. (b1) 2nd choice of unit cell (b2) Same periodic structure as a2 considering b1 as unit cell [88].

segment should be used. Then a 1D periodic condition derived from the Bloch theory is applied

$$\begin{pmatrix} \mathbf{q}_{n+1} \\ \mathbf{f}_{n+1} \end{pmatrix} = \lambda \begin{pmatrix} \mathbf{q}_n \\ \mathbf{f}_n \end{pmatrix} \tag{1.14}$$

leading to the following eigenvalue problem

$$(\mathbf{T} - \lambda \mathbf{I}) \begin{pmatrix} \mathbf{q}_n \\ \mathbf{f}_n \end{pmatrix} = \mathbf{0} \tag{1.15}$$

The eigenvalue is linking to the wavenumber $\lambda = e^{-jk\Delta}$ and the associated eigenvector is the corresponding waveshape.

This method has been applied to analyze the wave characteristics of periodic Timoshenko beam [89], nonsymmetrical axially loaded thin-walled Bernoulli–Euler beam [90] and periodic structures with local resonators [91, 92]. It should be noted that the transfer matrix method can suffer from numerical ill-conditioning when solutions are to be found numerically [75, 93].

Similarly, one can also started from the equation of motion using the receptance matrix [94] i.e. reciprocal of the dynamic stiffness matrix, formed by

$$\begin{pmatrix} \mathbf{f}_\mathrm{L} \\ \mathbf{f}_\mathrm{R} \end{pmatrix} = \begin{bmatrix} \alpha_\mathrm{LL} & \alpha_\mathrm{LR} \\ \alpha_\mathrm{RL} & \alpha_\mathrm{RR} \end{bmatrix} \begin{pmatrix} \mathbf{q}_\mathrm{L} \\ \mathbf{q}_\mathrm{R} \end{pmatrix}$$

Applying the 1D periodic periodic condition, it leads to the polynomial eigenvalue problem

$$\{\lambda^2 \alpha_\mathrm{LR}(\omega) - \lambda[\alpha_\mathrm{LL}(\omega) + \alpha_\mathrm{RR}(\omega)] + \alpha_\mathrm{RL}(\omega)\}\mathbf{f}_\mathrm{L} = \mathbf{0}$$

The receptance method hs been used to analyze waves in periodic structures for mono-coupled systems [95] and for multi-coupled systems [96] where the complex conjugate

wavenumbers are described. Many general conclusions have been drawn in their studies. The receptance method has also been used to analyze a periodic structure with local resonance [97] as well.

1.4.3 Wave and finite element method

The Wave and Finite Element Method (WFEM) is an alternative to investigate wave motion in general complicated waveguides. Free wave propagation in one-, two- and three-dimensions can be analyzed for periodic structures using an FE model of a single periodic section. The method starts from modeling a short section of a waveguide using conventional FEs such that the equation of motion is given in terms of a discrete finite number of DOFs, for time-harmonic motion it gives the form of dynamic stiffness matrix. The transfer matrix and receptance matrix can be formed using elements of the dynamic stiffness matrix by eliminating the internal DOFs. Then still applying a periodicity condition (1.14) gives the eigenvalue problem for 1D structures. The eigenvalues and eigenvectors represent the free wave propagation characteristics such as the wavenumbers and wave modes.

However, it is not necessary for WFEM to use same eigenvalue schemes as the transfer matrix method or the receptance method. A series of eigenvalue schemes have been proposed, the main idea is the use generalized eigenvalue problem to replace the standard eigenvalue problem (1.15). For example the zhong's method [98] and the scheme used by [24]. The main aim is to improve the numerical accuracy and reduce the ill-conditioning. Using FEM to model a unit cell allows WFEM to be used for periodic structures with complex geometric and material configurations. But a drawback is that the DOFs may be enormous, inducing numerical errors and slowing the calculation. To address this, reduced models for the unit cells can be used. The reduced model can be built from modes of the unit cells [99–101] or waves of other frequencies [102–104], or both [105]. This thesis concerns the WFE method for 1D waveguides and it is specifically reviewed in chapter 2.

For 2D periodic structures as illustrated in Figure 1.27, waves can propagate in two directions x and y, represented by two wavenumbers k_x and k_y. The periodic conditions write

$$\begin{aligned}
\mathbf{q}_2 &= \lambda_\mathrm{x}\mathbf{q}_1 \\
\mathbf{q}_3 &= \lambda_\mathrm{y}\mathbf{q}_1 \\
\mathbf{q}_4 &= \lambda_\mathrm{x}\lambda_\mathrm{y}\mathbf{q}_1 \\
\mathbf{q}_\mathrm{R} &= \lambda_\mathrm{x}\mathbf{q}_\mathrm{L} \\
\mathbf{q}_\mathrm{T} &= \lambda_\mathrm{y}\mathbf{q}_\mathrm{B}
\end{aligned}$$

and

$$\begin{aligned}
&\mathbf{f}_1 + \lambda_\mathrm{x}^{-1}\mathbf{f}_2 + \lambda_\mathrm{y}^{-1}\mathbf{f}_3 + \lambda_\mathrm{x}^{-1}\lambda_\mathrm{y}^{-1}\mathbf{q}_4 = \mathbf{0} \\
&\mathbf{f}_\mathrm{L} + \lambda_\mathrm{x}^{-1}\mathbf{q}_\mathrm{R} = \mathbf{0} \\
&\mathbf{f}_\mathrm{B} + \lambda_\mathrm{y}^{-1}\mathbf{q}_\mathrm{T} = \mathbf{0}
\end{aligned}$$

Considering them when solving the homogeneous problem of the unit cell, the wavenumbers and waveshapes can be obtained. The unknown variables are k_x, k_y and ω, one can fix a frequency and one of the wavenumber (say k_x) and search for the other wavenumber

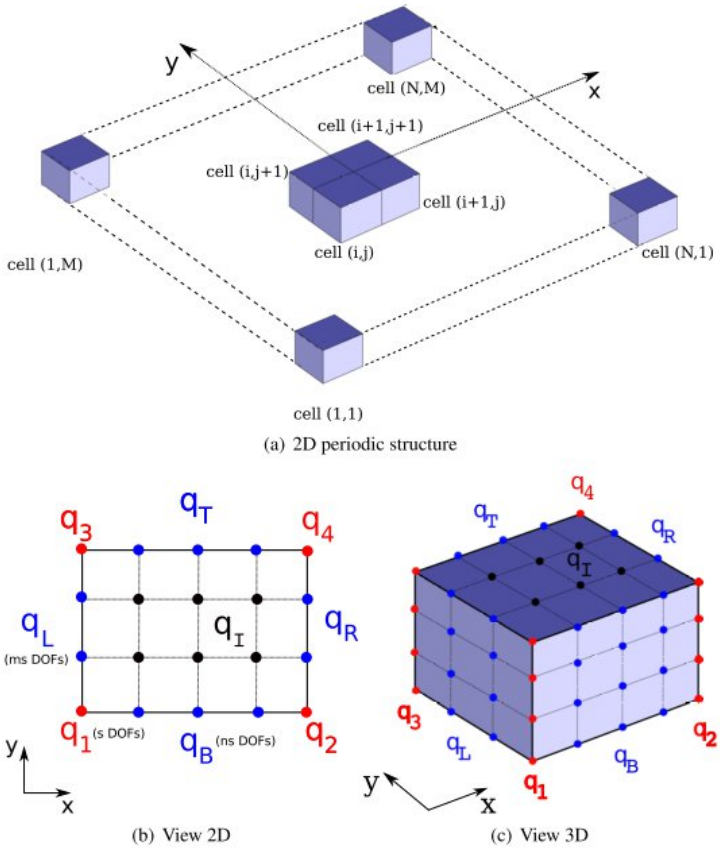

Figure 1.27: Illustration of a 2D periodic waveguide and a unit cell [101].

k_y, termed the 'inverse form'. Alternatively one can fix both wavenumbers and searching for the propagating frequencies, termed the 'direct form'. Different forms leads to different way to present the results. A typical results obtained from the inverse form is shown in Figure 1.28 which is similar to the 1D case. Results of the direct form are often presented by the phase constant surfaces as shown in Figure 1.29.

For simple waveguides, Mace et al. [106] showed free wave propagation in a rod, a beam and a plate strip with simply-supported edges using the WFE method. They also presented the free wave propagation in a layered sandwich beam. Applications of the WFE method to more complicated waveguides are reviewed. Houillon et al. [107] analysed free wave propagation in thin-walled structures in which an approach of evaluating the same wave modes at two different discretised frequencies is proposed. Mencik and Ichchou [108] investigated free wave propagation in a fluid-filled pipe considering acoustical-structural coupling. They also predicted the coupling power between two different waveguides using the WFE method [109]. This work was latter extended by Huang et al. [110–112] by considering piezoelectric elements between two waveguides. Free wave propagation in a fluid-filled pipe was also presented by Bocquillet et al [113]. They formulated an eigenvalue problem using elements of the transfer matrix and numerical solutions were found with initial estimates.

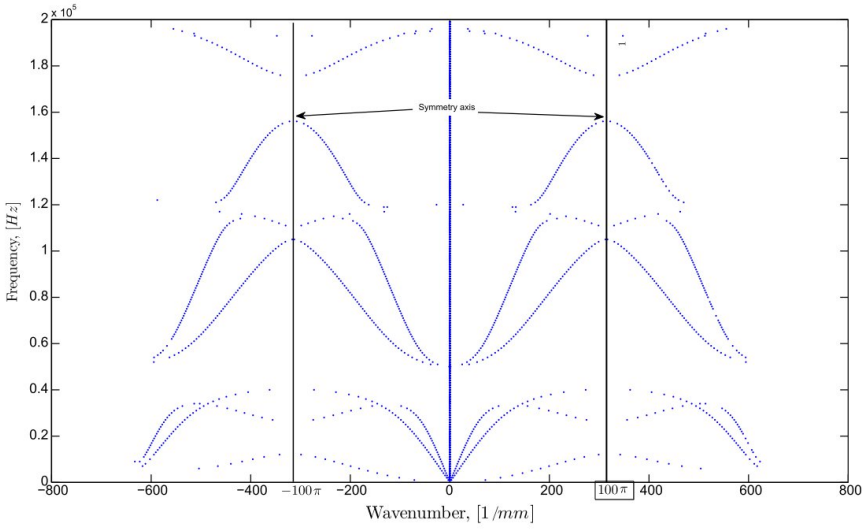

Figure 1.28: Illustration of results presentation for the inverse form [85].

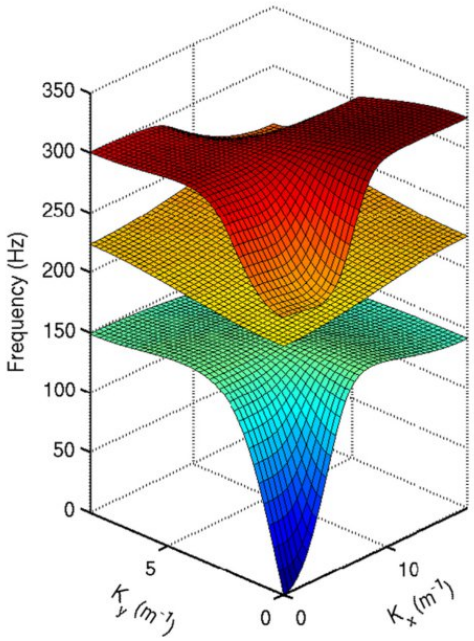

Figure 1.29: Illustration of results presentation for the direct form [105].

1.4.4 Artificial boundary conditions

All the previously mentioned methods require the analyzed structures or substructures to be periodic or uniform. Sometimes the analysis of complex non-periodic structures in a unbounded situation is required, such as to analyze a building's reaction when an earthquake wave is coming [114]. In such a situation, the earth can be regarded as infinitely large, and the waves can transmit through the interface between the building and the earth. This is also useful in structural vibration analysis at mid and high frequencies because the boundaries are no longer 'ideal' at such frequencies so the energy-exchange be-

tween near-field and far-field should be taken into account [82]. To simulate this 'infinite' boundary condition. there are many techniques such as Boundary Element Method [115], Infinite Element Method [116] and Artificial Boundary Conditions (ABC) [114, 117–119]. Among them the ABC is most convenient to be introduced into FE model of the nearfield. It is also considered in the thesis as a reference.

The general ideal of ABC is to firstly model the near-field using conventional FEM and leave all boundaries free, then introduce certain constrain equations on the boundary nodes so as to simulate the interaction of the far field which is not modeled in FEM. The ABC has two major branches: the transmission boundary [114, 118] and the elastic-viscous boundary [117–119].

Transmission boundary simulate the behavior of wave propagating out of the near-field by artificially constrains the displacement and velocity of the boundary nodes using the historic response data of near nodes, the 2nd-order transmission boundary shown in Figure 1.30 writes

$$U(x_\mathrm{b}, t+\Delta t) = 2U(x_\mathrm{b} - C_\mathrm{g}\Delta t, t) - U(x_\mathrm{b} - 2C_\mathrm{g}\Delta t, t-\Delta t)$$

where C_g is the group velocity. Elastic-viscous ABC simulates the behavior of far filed by representing the stress-displacement and stress-velocity relation with a set of dampers and spring in parallel, as shown in Figure 1.31. For instance, if the farfield is a uniform rod, the equivalent transfer function for the ABC writes

$$H_u = \frac{f(x_\mathrm{b}, t)}{u(x_\mathrm{b}, t)} = j\omega A\sqrt{E\rho}$$

where A is the cross-section area, ρ the mass density and E the Young's modulus. The derivation of elastic-viscous ABC for rods and beams are given in Appendix C.

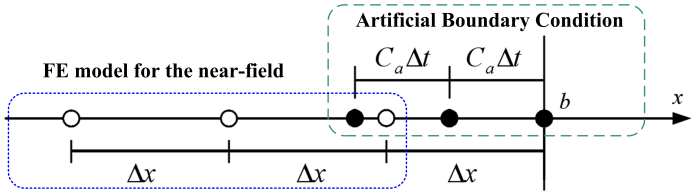

Figure 1.30: Schematic of the 2nd-order transmission boundary used in 1-D problem.

A comparison between these two kinds of ABC has been reported by Zhao [118], it is shown that the elastic-viscous type is more stable and accurate. For transmission ABC, it suffering stability issues, and to conquer it an extra damping should be introduced to the near filed. Here two questions rise: 1) the introduced damping would affect the simulation accuracy and 2) the value of introduced damping lacks a decided rule. Moreover, when dispersive wave happens, the parameter of wave speed should be approximated. New methods like Dirichlet-to-Neumann (DtN) ABC [117] seem to be a good direction solving this problem, but by now there is no ABC that is suitable and precise for all kind of situations.

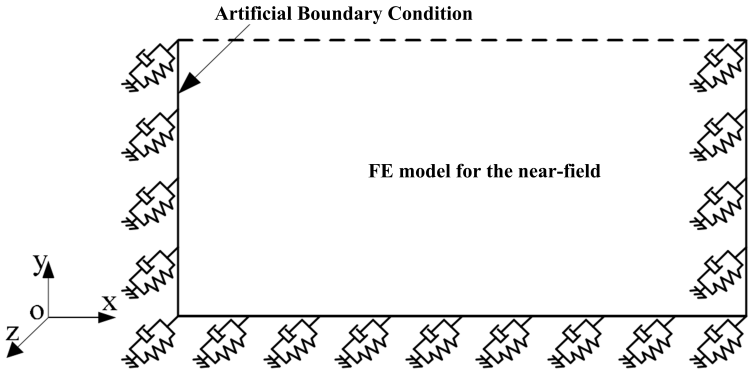

Figure 1.31: Schematic of elastic-viscous ABC used in 2-D problem.

1.4.5 Remarks

Considering the complexity of engineering practice, WFEM seems to be a good choice for the prediction of wave basis, but the numerical issues should be resolved and strategies to reduce the size of matrices are necessary. Another interesting direction might be using WFEM as a substructure technique to model a built-up structure having (1) both periodic and non-periodic parts [110–112] or (2) multiple periodic parts [120–122].

To analyze free-wave characteristics along a given direction (angle) for a 2D periodic structure, the WFEM leads to a transcendental eigenvalue problem, which cannot be solved by conventional eigenvalue searching approaches [123]. Alternatively, treatment of harmonic wave propagation through the setting up of a quadratic eigenvalue problem has been considered for both 1D models [124] and multi-dimensional models [85]. The advantages of the quadratic eigenvalue problem route are twofold: (1) it easily enables the incorporation of frequency dependency in the material properties and (2) it readily provides the wave solution for both spatially propagating and spatially decaying modes. However, some of the required matrices in these methods can not be directly obtained from the conventional FEM. That may increase the complexity and difficulty of the analyzing process.

1.5 Piezoelectric strategies for vibration control

The application of piezoelectric-based structure for vibration control can be dated back to 1980s when Forward [125] carried out a preliminary experimental demonstration of using external electronic circuits to dampen mechanical vibrations in optical systems. In that work both passive and active strategies were considered. In **active** vibration control, piezoelectric transducers mounted in the host structure are performed as sensors or actuators. A feedback loop is established with certain control laws so as to apply active forces according to the sensor signal, as shown in Figure 1.32. Active control has advantages such as high performance, modal selective and adaptive. Piezoelectric-based active vibration strategies has been applied in many engineering cases, such as a civil structure [126], a aircraft vertical tail [127] and a aeronautic blade suffering flutter [128]. Comprehensive literature reviews regarding active vibration control can be found

in [129, 130]. It can also be applied in combine with viscoelastic damping treatments to enhance the performance, leading to hybrid active-passive damping treatments [131].

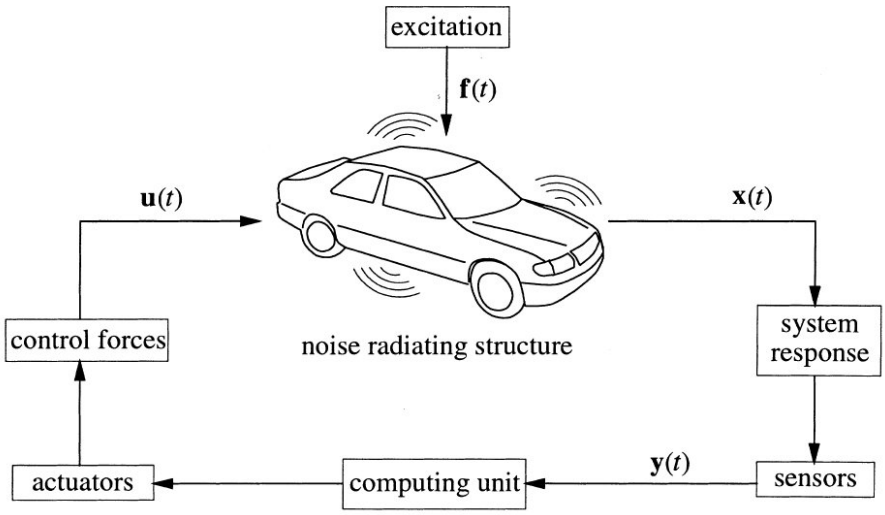

Figure 1.32: Illustration of the active vibration and noise control [132].

One concern of the active control strategies is the requirements of external equipments such as power sources, amplifiers and AC/DC converters and computers. On the other hand, **passive** vibration control strategies directly connect dissipative electric circuits to the transducers. Part of the electric energy converted from the mechanical field is then dissipated, leading to structural damping. This strategy does not need external power and generally the circuits are much simpler than the active strategies.

However, as it will be shown hereafter, passive strategies may not adaptive to the environment changes, and they have difficulties to achieve a broadband performance. External energy sources can be introduced to drive some electric circuits with special features that are impossible to be achieved by passive circuits. Generally the external energy is used to maintain a negative capacitance or status shifting circuits, rather than driving actuators in active control methods. So these approaches are termed **semi-active** strategies. Generally the energy consumption in a semi-active approach is relatively low, so it is feasible to be powered by an energy-harvesting circuit generating energy from the same host structure. This leads to self-powered vibration control systems. Though there is no 'external' energy source in such a system, we still classify self-powered ones into the semi-active category.

In this section we focus the review on passive and semi-active strategies for they are more relevant to the thesis subject.

1.5.1 Passive strategies for single mode

A systematic research concerning the vibration control using passive circuits can be found in 1990s by Hagood and Flotow [18]. Two shunting circuits, namely the resistive shunt (a resistor alone) and the resonance shunt (RL series, see Figure 1.33) were discussed numerically and experimentally with a cantilever beam. They found that both two circuits

can be used to reduce the vibration of a single mode. The resistive shunt is equivalent to a viscoelastic damping and there exists an optimal value for the resistor. The resonance shunt can be tuned to the structural mode, performing as a lightweight mechanical vibration absorber. The best performances of the resonance shunt is better than the resistive shunt while they are both determined by the MEMCF.

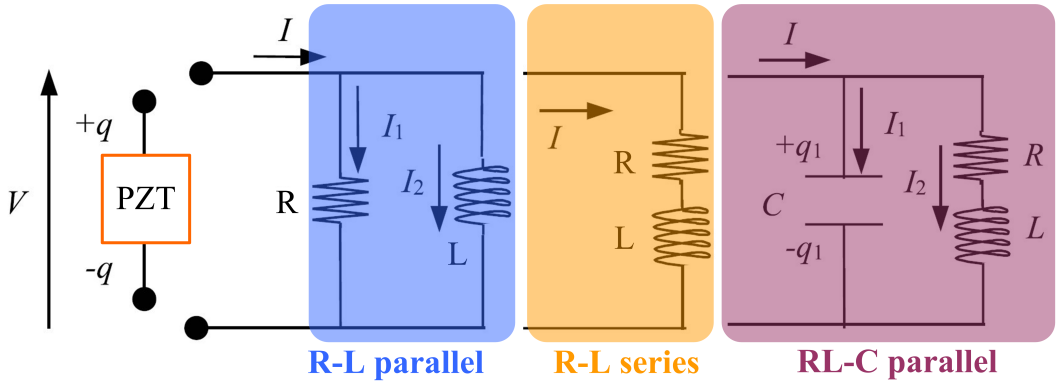

Figure 1.33: Illustration of some single-mode shunts.

Other configuration of circuits, such as the RL parallel circuit proposed by Wu [133] and the RL-C parallel circuit [134, 135] can also reduce the vibration of a single mode, shown in Figure 1.33. The additional capacitor in RL-C parallel circuit allows the reduction of the optimal value of the inductance by a factor $1+\alpha$, where α is the ratio between the external capacity and the capacity of the piezoelectric transducer. Caruso [136] studied the optimal values of the electric components belonging to three shunts shown in Figure 1.33 by pole placement technique, taking into account the inherent structural damping. The analysis showed that the RL series shunt circuit is the most effective one, shown in Figure 1.34. The RL parallel shunt circuit performs very close to the RL series circuit. But the optimal value of the tuning parameter for the RL parallel circuit does not depend on the mechanical inherent damping and the piezoelectric coupling coefficient, implying an easier tuning procedure. For the RL–C parallel circuit the value of the external capacitance cannot be chosen too large in order to have an effective damping system, and this implies a limitation on the reduction of the tuning inductance achievable with this circuit.

New results regarding these simple circuits can still be seen recently, Thomas et al. [23] found closed-form expressions for the optimization of the resistive and RL series circuits. The vibration reduction brought by the shunt is measured with two indicators: an added damping factor for the free vibration case and a gain reduction in the forced vibration case. It is shown (Figure 1.35) that those indicators depend only on two parameters: the MEMCF and the structural damping. A new turning strategy for RL series circuit based on the exact solutions is proposed by Soltani et al. [137]. Their solution imposes exactly two equal peaks in the receptance function that are associated with the smallest possible vibration amplitude of the host structure. Results show that the performance is superior to all previous tuning rules for resonant circuit, but the improvement may be marginal for small electromechanical coupling parameters.

The basic idea of the RL series, RL parallel and RL-C parallel shunts is to implement

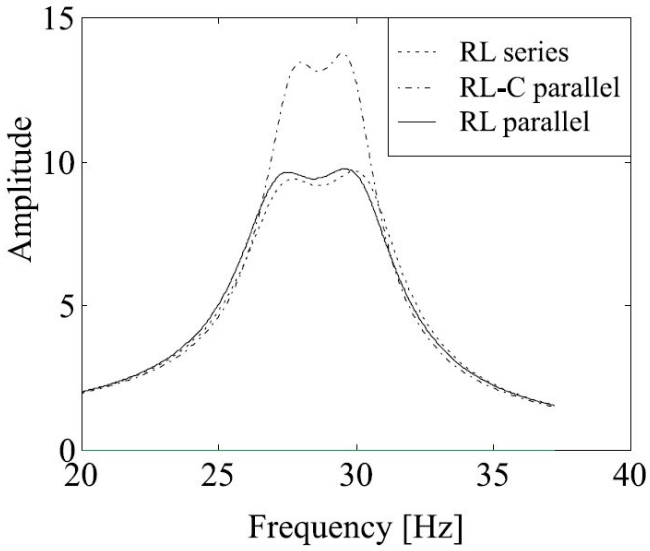

Figure 1.34: Dimensionless amplitude relevant to the three shunts optimized according to the transfer function optimization technique [136].

		Free response Pole placement criterion	Forced response Transfer function criterion
Resistive shunt	Opt. resistance	$R = \frac{1}{C\omega_j(1+k_j^2/2)}$	$R = \frac{1}{C\omega_j\sqrt{1+k_j^2/2}}$
	Performances	$\xi_{\text{add}}^{\text{R}} = \frac{k_j^2}{4\sqrt{1+k_j^2/2-k_j^4/16}} \simeq \frac{k_j^2}{4}$	$A_{\text{dB}}^{\text{R}} = 20\log\frac{k_j^2+2\sqrt{2}\xi_j\sqrt{2+k_j^2}}{4\xi_j\sqrt{1-\xi_j^2}}$
Resonant shunt	Opt. resistance	$R = \frac{2k_j}{C\omega_j(1+k_j^2)^{3/2}}$	$R = \sqrt{\frac{3}{2}}\frac{k_j}{C\omega_j\sqrt{1+k_j^2}}$
	Opt. inductance	$L = \frac{1}{C\omega_j^2(1+k_j^2)^2}$	$L = \frac{1}{C\omega_j^2(1+k_j^2)}$
	Performances	$\xi_{\text{add}}^{\text{RL}} = \frac{\lvert k_j\rvert}{\sqrt{4-k_j^2}} \simeq \frac{\lvert k_j\rvert}{2}$	$A_{\text{dB}}^{\text{RL}} = A_{\text{dB}}^{\text{RL}}(k_j, \xi_j),$

Figure 1.35: Optimal electrical parameter values for the tuned resistive and resonant shunt and associated performances [23] where k_j is the MEMCF.

an Tuned Mass Damper (TMD), as shown in Figure 1.6. However, enhanced performance of vibration control can be achieved by putting another reaction mass in series with the existing TMD [138]. The total mass of a series TMD can be much smaller than a classic TMD to achieve the same effectiveness of vibration suppression but at the cost of several times of larger motion stroke. Zou and Cui [19] used a resonance piezoelectric shunt to implement the secondary oscillator in such double-mass series TMD, as shown in Figure 1.36. By tuning both the resonances of the mechanical TMD and secondary piezoelectric TMD close to that of the host structure, an enhanced performance is achieved as shown in Figure 1.37. Moreover, the electromechanical series TMD does not suffer from large motion stroke as in the mechanical double-mass series TMD.

Interestingly, a series TMD implemented by piezoelectric shunts for vibration reduction is similar to a generator for energy harvesting [1], as it is shown in Figure 1.38.

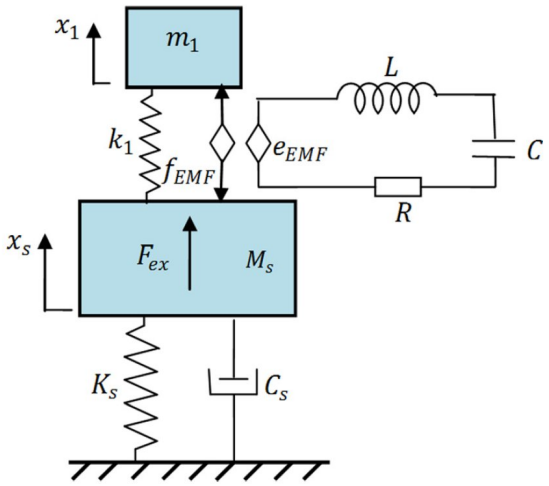

Figure 1.36: Series TMD with electromagnetic resonant shunt [19].

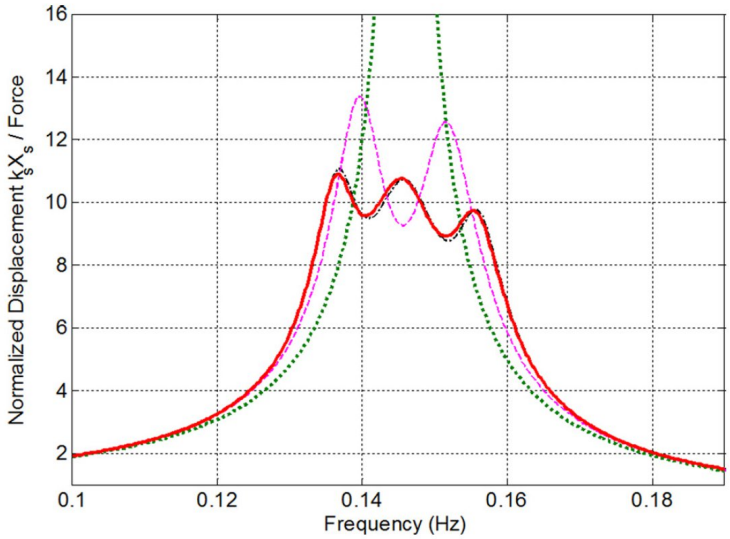

Figure 1.37: The frequency responses of electromagnetic shunt series TMD for Taipei 101 Tower (solid) in comparison with double-mass TMD (dashed-dotted), classic TMD (dash), and system without TMD (dot), where all parameters are optimized to minimize the H2 norm from external force to the displacement of the primary system [19].

Suppose we have a host structure, if the target is to reduce the vibration, according the idea of series TMD, we can design a mechanical structure (which is a beam in the figure) to implement the first TMD and integrate piezoelectric subsystem to realize the secondary TMD. On the other hand for the energy harvesting, the beam is designed to create a large strain on the piezoelectric patches when the host structure vibrates. The electric circuit is then designed to store the converted energy rather than dissipate them. These also require the beam and the electric circuit to be tuned to the interested frequency. That is to say, the series TMD shown in Figure 1.36 can also be used as a energy harvester just by changing the dissipative circuit into energy storage one [19].

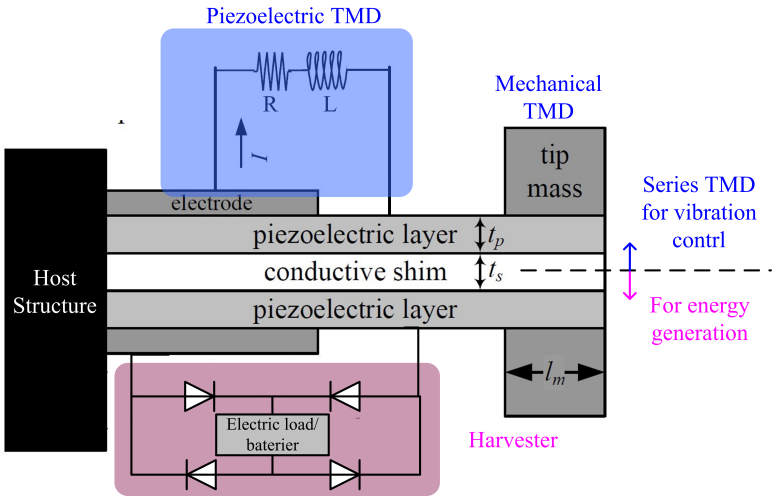

Figure 1.38: The similarity between a series TMD and an energy harvester, both realized by piezoelectric strategies.

To store the electric energy, it is better to convert the alternating current (AC) to the direct current (DC). A typical electric circuit for that is the bridge rectifier shown in Figure 1.38, which is an arrangement of four diodes in a bridge circuit configuration. Warkentin and Hagood [139] firstly examined the use of such nonlinear shunting circuit to attain effective damping. Lesieutre et al. [140] addresses the damping associated with a harvester that consists of a full-bridge rectifier, a filter capacitor, a switching DC–DC step-down converter, and a battery. They show that the best induced loss factor depends only on the MEMCF. Specifically they use a system with MEMCF of 26% to yield a modal loss factor of 2.2%. According to Figure 1.35, this performance is better than the resistive shunt where $\xi^{\mathrm{R}}_{\mathrm{add}}(26\%) = 1.69\%$ but worse than the resonance circuit where $\xi^{\mathrm{R}}_{\mathrm{add}}(26\%) = 13\%$.

Energy harvesting itself is another important research branch concerning the application of piezoelectric materials. The efficiency of piezoelectric-based energy harvesting has been proved in comparison with other electrostatic generators [141]. It has been brought on by the modern advances to wireless technology and low-power electronics such as microelectromechanical systems [12]. Relating to vibration control, energy harvesting can be used as a nonlinear passive strategy as introduced. It can also be used to drive the low-power semi-active circuits as it will be presented in section 1.5.3.

1.5.2 Passive strategies for multiple modes

At mid- and high frequencies, the modal density and overlap of a structure are high [142]. At a given frequency band there might be several modes, their contributions to the vibration can not be effectively reduced by a single resistive or resonance circuit. Electric shunting circuit with multiple tuning frequencies were proposed, where each electric resonant is turned to a structural modal frequency. Hollkamp [143] directly shunted several resonance circuits in parallel to the piezoelectric patch, as shown in Figure 1.39. The reduction of vibration was experimentally observed in multiple modes.

However, tuning of the inductor in one branch in such circuit would interfere with

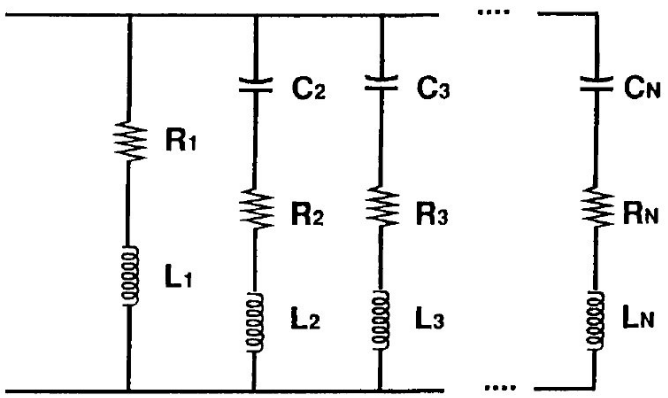

Figure 1.39: Multi-mode vibration resonator circuits proposed by Hollkamp [143].

or caused de-tuning of the other branches, or even the entire shunt circuit. That is why the design of circuit in [143] is not achieved by individually tuning each branch but by directly optimizing the vibration behavior of on many unknown electric parameters. Wu [144] reported a circuit consists of a 'current blocker' at each branch. The current blocker is comprising of one parallel capacitor-inductor circuit that is placed in series with each parallel RL circuit. Depending on the number of structural modes to be damped simultaneously, a different number of blocker circuits are needed for each branch, as shown in Figure 1.40 for a 3 modes case. This allows one to separately design each branch by single-mode rules and integrate them together to get a multi-mode performance. Behrens and Moheimani [145] further simplified the circuits such that less electric elements are required, as shown in Figure 1.41. In stead of preventing the current from flowing at a specific frequency, they allow the current to flow, by using a series capacitor-inductor circuit. One current flow component is needed for each branch regardless of the number of modes to be damped. Note that Figure 1.41 is similar with Figure 1.39, so maybe we can remark that Behrens and Moheimani [145] actually proposed a way to design the original circuit used by Hollkamp [143].

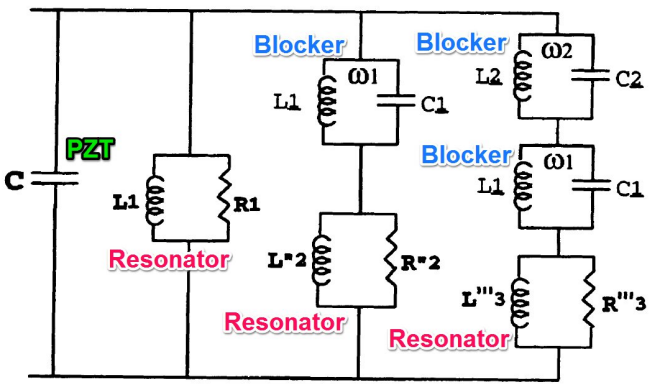

Figure 1.40: Multi-mode vibration resonator circuits proposed by Wu [144] for 3 modes: using current blockers plus parallel RL resonators.

As discussed in the previous section, for a mode with low MEMCF even if a electric

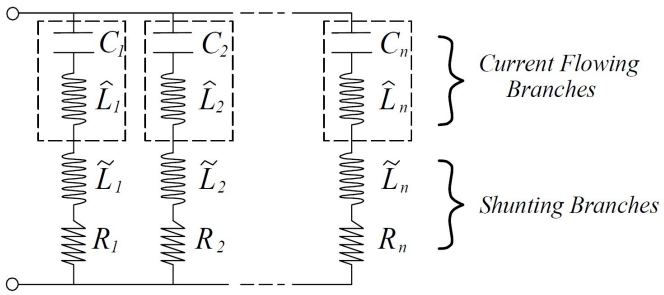

Figure 1.41: Multi-mode vibration resonator circuits proposed by Behrens and Moheimani [145]: using current-flow branches plus series RL resonator.

circuit with multi-mode damping ability is shunted, the vibration around the modal frequencies could not be significantly reduced. So it is also important to attain reasonable MEMCF for multiple modes so as to achieve significant broadband damping performance. This can be done by the geometric designs shown in Section 1.3.2. Alternatively, other criteria can be found in the literature to obtain the best design for multi-mode vibration control. Kim er al. [55] used two piezoelectric patches for multi-mode control of a plate and the criterion is to maximize the modal voltages associated with the considered modes. Ip and Tse [146] also optimized the spatial orientation of PZT patches to control a plate structure. The criterion in their study is to optimize the modal displacement induced by the voltage applied on the patch. Giorgio et al. [147] propose a strategy for controlling n structural modes by n piezoelectric transducers shunted with a multi-terminal electric network, as shown in Figure 1.42a. By introducing a proper transformation of electric coordinates, a one to one correspondence between the modal mechanical and new electric DOF is approximately attained. Further, the distribution of the piezoelectric transducers is improved to maximize the damping performance. In their work a double clamped beam and a fully clamped plate were developed to validate the technique and the multi-mode vibration control performance is achieved, as shown in Figure 1.42b.

In the work of [55, 59, 146, 147], the distribution patten for the piezoelectric materials, the electrodes and the geometric parameters are determined by optimization processes. Then a multi-mode electric circuit is connected to the terminals so as to dissipate the structural vibration. These two steps (geometric and electric design) are directly related to the modes chosen to be reduced. For different modes the final configuration might be rather different. The concept of Piezoelectric electromechanical (PEM) structure enables one to tune all the modes at once [45, 148, 149] with a preselected configuration. A PEM structure comprises of periodically distributed piezoelectric patches interconnected by a periodic electric network. Examples of PEM structures can be seen in Figures 1.15 and 1.17 for a PEM plate and Figure 1.14 and 1.16 for PEM beams. The electric network is designed to be resonant at all the structural characteristic frequencies and so that its modal shapes may piezoelectrically interact with those of the host structure. These design specifications allow one to control simultaneously all the modes, dispensing with the use of either active elements or heavy inductors. The synergic behavior of the piezoelectric patches leads to a very high perfomance in terms of energy transduction efficiency over a frequency bandwidth in principle infinite.

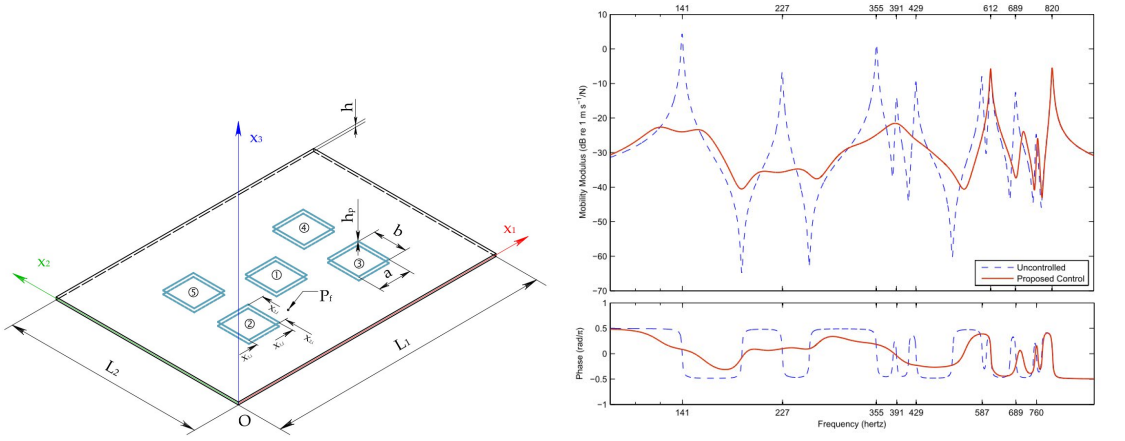

(a) (b)

Figure 1.42: The distributed piezoelectric strategy proposed by Giorgio et al. [147]: (a) optimizing five patches for five modes; (b) comparison between mobility of the controlled and uncontrolled beam: the first five modes considered.

Dell'Isola and co-authors are among the major contributors are of PEM structures. In 2001, they [47] introduced the PEM plate shown in Figures 1.14 and 1.16. Such a PEM plate is modeled as a coupled system of the Kirchhoff–Love plate and a membrane. It is proven that a criterion exists assuring electromechanical coupling of by creating self-resonance between the membrane modes and plate modes. This criterion allows for the determination of the net-impedances maximizing the electromechanical energy exchange. The modal shapes are shown in Figure 1.43, in a fully clamped case. The coincidence of the electric (membrane) and mechanical (plate) modes happens not only in frequencies but also in spatial distributions. In 2002, they [48] showed a another methodology to design a PEM structure, new circuital analogs for the uniformly damped elastica and Kirchhoff–Love plate are found. In 2004 they [150] experimentally validated the effectiveness of a PEM beam prototype obtained by interconnecting distributed piezoelectric elements either by RL impedances (RL network), or R impedances (R network). They showed that the PEM beams have smaller optimal inductance compared to classical piezoelectric shunting, and the optimal inductance can be further reduced by increasing the number of piezoelectric elements. Improved modeling and electric designing strategies are proposed in [44, 151]. The performance of different circuit topologies for the interconnection of the piezoelectric transducers were compared in [46].

Two homogenization processes are performed during the modeling of PEM, converting 1) the periodic piezoelectric structure into a uniform media and 2) the discrete electric network to a continuous media. These all depend on the long wave-length assumption hence only valid for lower order modes. In the work of Lossouarn et al. for rods [21] and beams [22] , the network is kept discrete to get closer to real applications with a finite number of piezoelectric patches. Two novel models based on a transfer matrix formulation are presented. Both take into account a discrete electrical network but the first model considers a discrete mechanical medium while the second keeps the continuity of the beam. The first experimental validation of a multi-modal damping strategy involving a

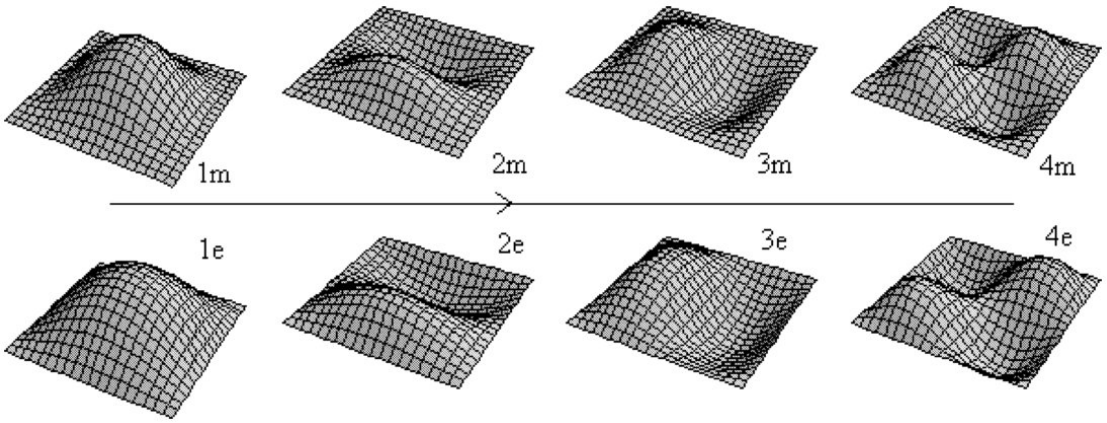

Figure 1.43: Modal basis for the clamped PEM plate [47], 'm' refers to the mechanical modes and 'e' to the electric (membrane) modes.

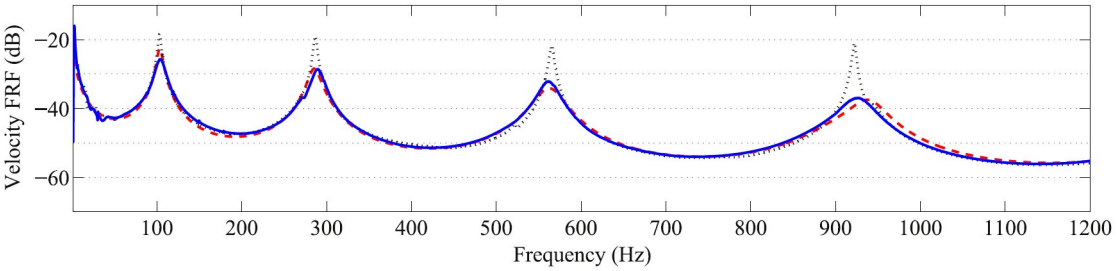

Figure 1.44: Mechanical frequency response functions [22]. The dotted line denotes the experiment with open-circuited patches, the dashed line denotes the transfer matrix model with a tuned network, and the solid line denotes the experiment with a tuned network.

beam/rod coupled to its discrete electrical analogue is presented, as shown in Figure 1.44.

In some engineering applications the host structure itself is periodic or near-periodic, and the most apparent examples are components used in rotor machineries such as bladed discs and circular shells, shown in Figure 1.45. Fan and Li [27] proposed two kinds of piezoelectric network which construct a structure-electric-structure energy transfer path, shown in Figure 1.46. The interaction forces are expected to perform like active force among the network-connected structures when they are excited. Modal and response analysis were conducted theoretically showing the network-connection introduces: 1) an additional resonance frequency point and 2) an additional part in response proportion to the average excitation over all components. Once the external forces applied on each substructure are fixed, the key point of this idea is to construct a piezoelectric network with appropriate Parameter study (the form of connection, the dimensions and content of network as well as the value of electric components, etc.) that makes the additional term of excitation caused by network connection and the external forces cancel each other out. It is illustrated in Figure 1.47 that this technique is excitation sensitive. The optimized performance is better than that of pure passive piezoelectric shunts. This idea was then extended by Li et al [26] considering the mechanical coupling between periodic sectors. The obtained result shows a parallel network is effective for nodal-diameter vibration

while a series network is effective for the zero-nodal-diameter vibration.

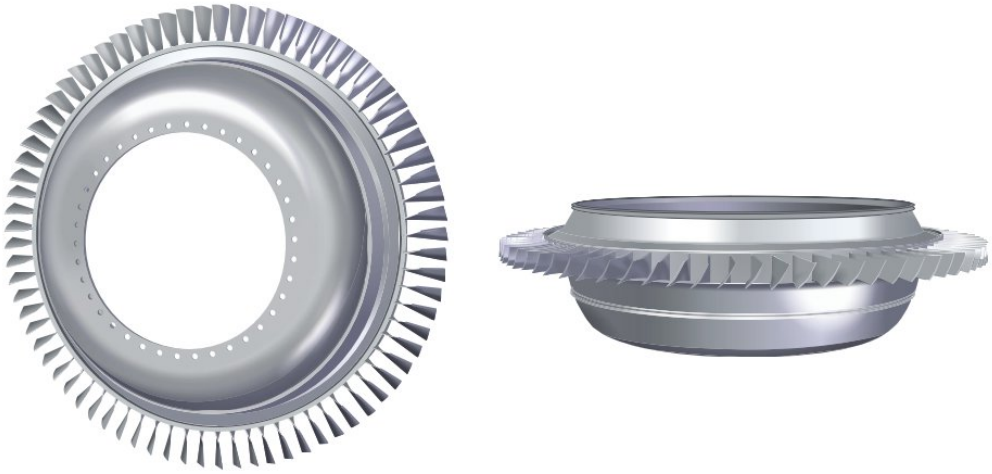

Figure 1.45: An example of periodic structures originally existing in engineering applications: bladed disc [152].

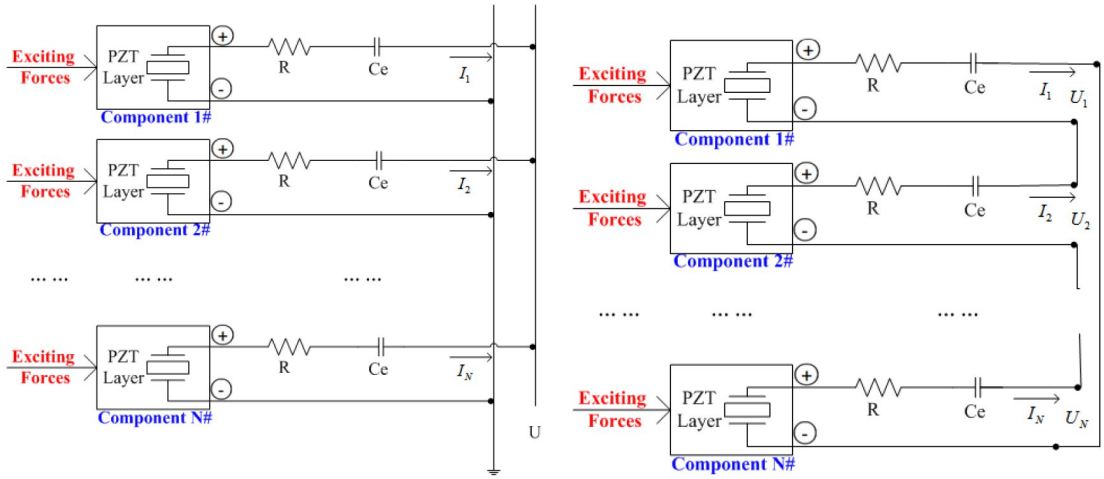

Figure 1.46: Piezoelectric networks proposed by Ref [26, 27]: (a) parallel network; (b) series network.

However, in a more realistic situation there will be slight differences between substructures, hereafter referred to as mistuning, such as the blade-to-blade differences in geometry and material properties due to manufacturing tolerances or in-service degradations. The structure then becomes nearly periodic or called mistuned and vibration localization could occur under certain circumstances [154, 155]. This phenomenon could lead to large vibration in certain regions of the structure and could be very harmful to the system. The occurrence of localization may also significantly reduce the effectiveness of structural modeling, and henceforth deteriorate design/control performance.

Tang and Wang [156] have demonstrated the use of piezoelectric networks for the vi-

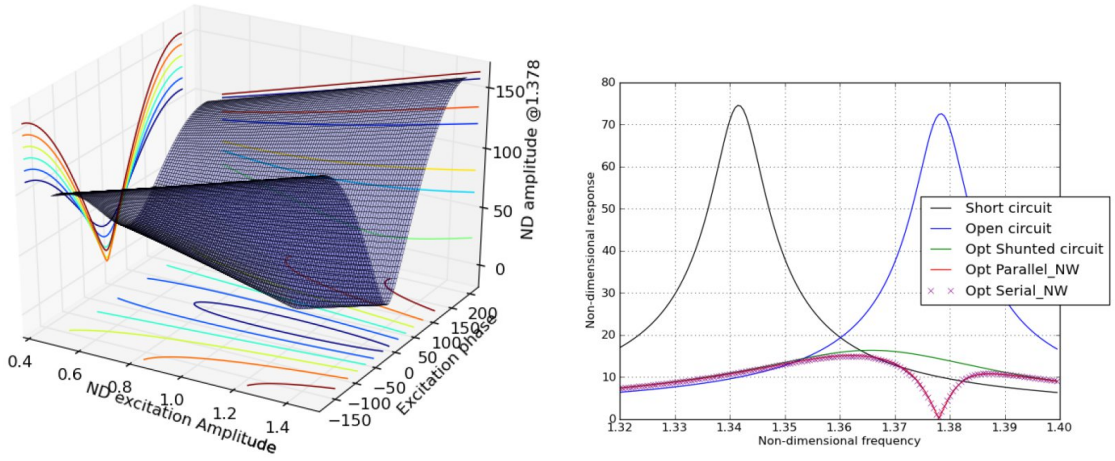

(a) (b)

Figure 1.47: Major results obtained in Ref [27]: (a) amplitude of the 1st component at resonance frequency based on Parallel Network under varying amplitude and phase of average excitation; and (b) The response curve of short-circuit, open-circuit and optimized piezoelectric shunts of single, non-connected component, compared with the optimized curves of piezoelectric networks.

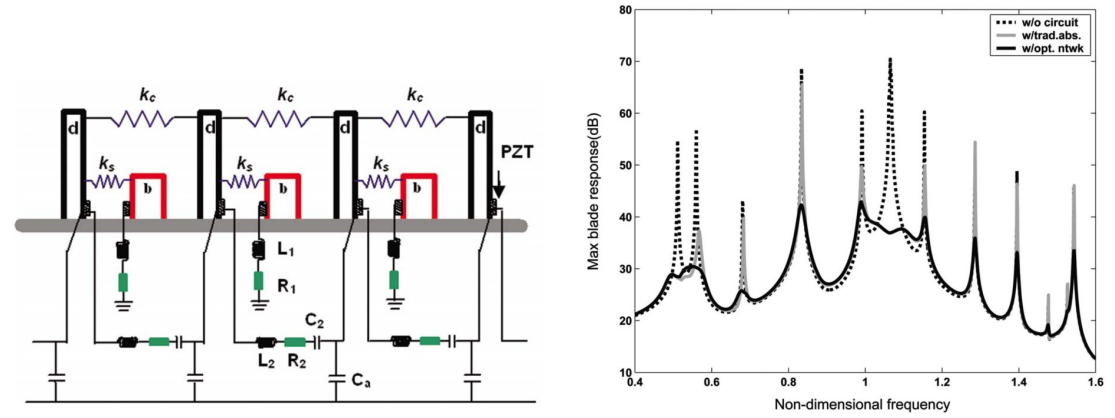

(a) (b)

Figure 1.48: Research highlights of Ref [153]: (a) the proposed piezoelectric network and individual circuits; (b) maximum response of the blade-model beams versus frequency for without circuit case, with traditional absorber case, and with the new optimal network case.

bration reduction of mistuned periodic structures where piezoelectric materials distribute onto both the blade and disk. Identical inductive piezoelectric circuits are applied to all substructures to absorb the vibration energy, and the shunt circuits are connected to each other with capacitive elements. With this design, the otherwise localized vibration energy can be transferred into electrical form and stored in the inductors and piezoelectric capacitors, and this part of energy can propagate throughout the integral system by way of the strong electrical coupling. A parameter study and experimental validation are further

presented by Yu et al. [69]. Using a more convening dynamic model of the bladed disc, the same authors [153] extended the electric design. They showed that (in Figure 1.48) as compared to the traditional absorber, the optimal network is much more effective in suppressing multiple harmonics simultaneously, and as a result, the maximum responses are much lower throughout the frequency range.

Multiple network on a same bladed disc has recently been proposed [152]. By organizing $4n$ piezoelectric transducers (PZT patches) in two parallel loops of $2n$ patches each, the demand on the inductors may be reduced by $4n^2$ as compared to independent loops, allowing the use of passive components.

1.5.3 Semi-active strategies

One of the most commonly considered semi-active strategies is the negative capacitance circuit. As presented in Section 1.3.2, it can enhance the MEMCF and consequently improve the performance of a existing passive circuit. By using NC one should also pay attention to its stabilities [157, 158].

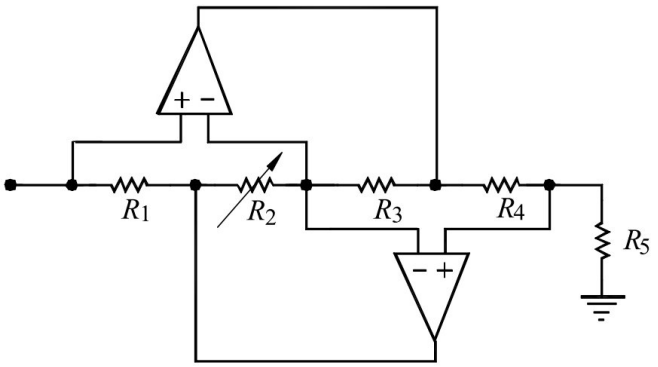

Figure 1.49: Circuit diagram of a synthetic inductor.

Another popular semi-active strategy is the synthesis circuit used to analogy a inductor. As presented, many passive strategies involve large inductances so as to tune the circuits or filter the current flow. Yet the required inductance are often very large, making them very difficult be realized in practice. As reported by Hagood et al. [18], the optimal inductance is around 142H to tune a PZT patch at 33 Hz. The RL-C series circuit can reduce the requirement of inductance but worsen the performance as well. By using the Gyrator circuits shown in Figure 1.49, a circuit behaves like a inductor can be realized. The circuit requires two operational amplifiers per inductor, creating an inductance $L = R_1R_3R_5/R_2 \times C$. By changing the variable resistor R_2, various inductance values could be obtained. However, the gyrator circuit is not a pure inductor, it creates a resistive component which is not desirable for designing the optimal resistance in the shunt branch circuit [134]. This circuit has been applied in many studies [71, 134, 136, 152] as an implementation of large inductances.

The control strategies proposed by Tang et al. [159], Morgan et al. [160], Davis et al. [161] and Hollkamp et al. [162] can also be regarded as semi-active ones. But the most important branch of semi-active strategies might be the ones based on switching

circuit. Clark [163] proposed the State Switch Damping to open the electrode when the structure starts moving away from its equilibrium position and to close when the structure starts moving in the opposite direction. The shifting of piezoelectric transducer from the OC status (high-stiffness) to the SC status (low-stiffness) creates a variable-stiffness. Consequently, energy stored in the actuator from the structure while the actuator is in its high-stiffness state, and the energy is dissipated (not returned to the structure) by switching the actuator to its low-stiffness state. The Further work of the same author [164] show that a better performance can be achieved if switching from OC to a resistive shunts. In comparison with the tuned R-L shunt, the state-switched approach only works better for off-resonance (particularly low-frequency) frequencies, and is less sensitive to changes in system parameters.

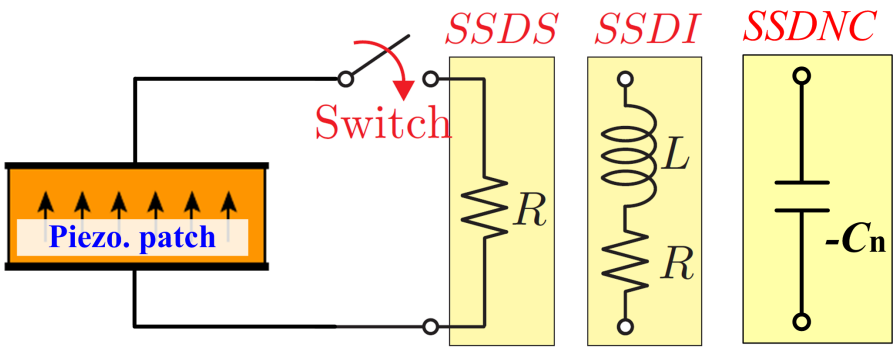

Figure 1.50: Illustrations of the circuits for SSDS, SSDI, SSDNC techniques.

Alternatively, the Synchronized Switch Damping on Short circuit (SSDS) technique was firstly proposed Richard et al. [165] in 1999, as illustrated in Figure 1.50. Different from the State Switch Damping, they proposed to close the electrodes during a very short period of time because shortest time for the SC status led to the best damping efficiency. They show that the best results are obtained for a threshold corresponding to a maximum and a minimum of the considered signal (displacement or voltage). The damping efficiency appears to be twice what is obtained with pure resistive damping and is equivalent to what is achievable with a tuned inductor damper. It can work at any frequency without the need for large inductor especially for low frequency applications. The principle of SSD consists of keeping the sign of the electric charge in the piezoelectric transducer opposed to the sign of velocity (see Figure 1.51), producing an effect equivalent to dry friction [166].

Richard et al. [166] proposed to close the circuit on an inductor, termed Synchronized Switch Damping on Inductor (SSDI), as illustrated in Figure 1.50. The inductor forms a resonator with the intrinsic capacitance of the piezoelectric material. Hence opening the circuit after half-circle of the electric resonance leads to a voltage which is 90 degrees out of phase with the motion, enhancing the damping mechanism shown in Figure 1.52. Usually the electric oscillating frequency is at least ten times higher than those of the mechanical modes of interest to ensure the generated charge remains approximately constant during switching process [168]. This makes the inductors for SSDI can be orders of magnitude smaller than those of RL shunt. In [166] an inductor of 80 mH was used, making a remarkable increase of the damping performance than the SSDS. The comparison studied

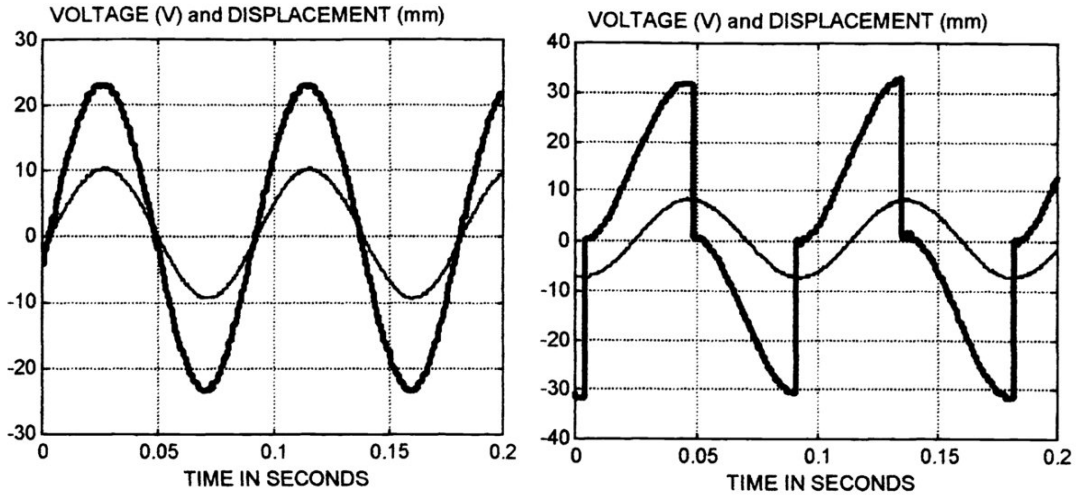

(a) (b)

Figure 1.51: The piezovoltage (in Volts, thick line) and the deflection of beam (in mm, thin line) are plotted as a function of time. (a) Open circuit case and (b) the proposed switching configuration [165].

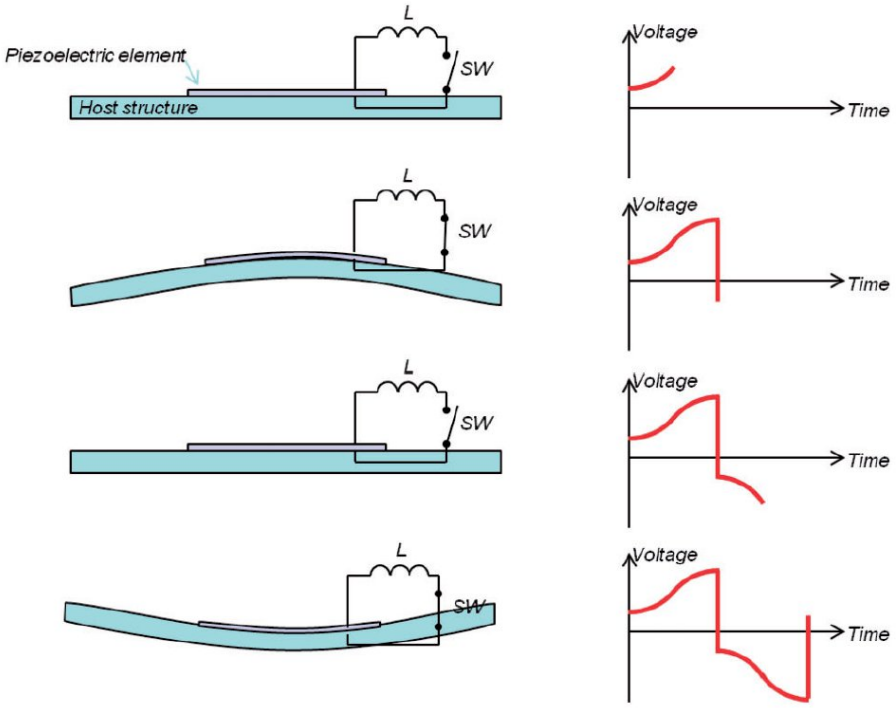

Figure 1.52: Illustration of the voltage waveforms of the SSDI technique [167].

conducted by Corr and Clark [169] confirms the superior damping performance of SSDI, shown in Figure 1.53. The work also indicated that SSDI has a lower sensitivity to environmental changes than the resonant shunt technique, and it is easier to be tuned.

In the study of Petit [20], it is shown that the performance of SSDI and SSDS is

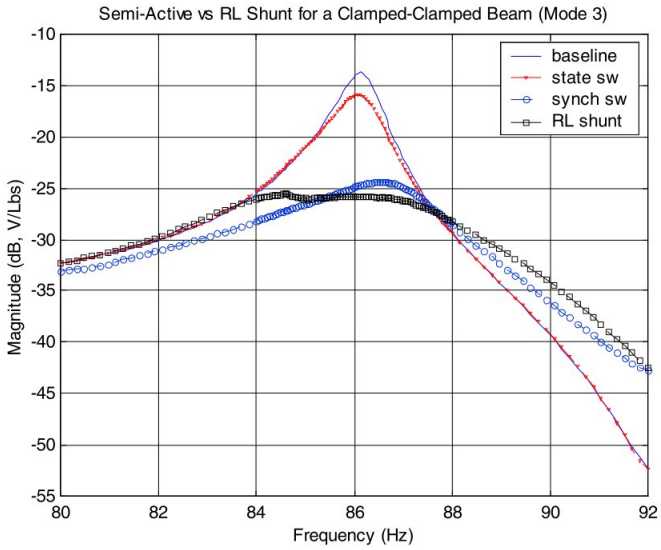

Figure 1.53: Experimental comparison of resonant shunting, state switching, and pulse switching for a clamped–clamped aluminum beam [169].

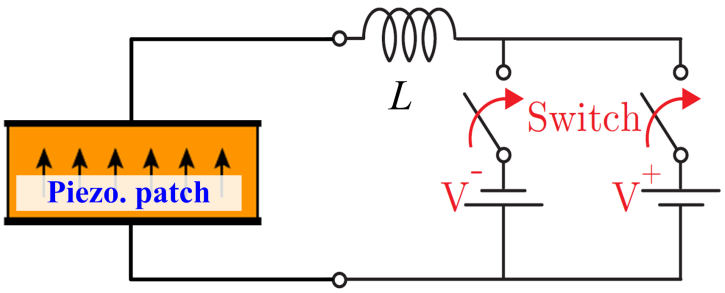

Figure 1.54: Illustration of the SSDV technique.

strongly dependent to the MEMCF. Ji et al. [170] proposed to replace the short-circuit to a negative capacitor, illustrated in Figure 1.50, termed Synchronized Switch Damping on Negative Capacitance (SSDNC). However, in the absence of an inductor, the high current resulting from closing the switch produces saturations of the synthetic negative capacitor. Petit [20] show that switching the electrodes on to a voltage source (SSDV, illustrated in Figure 1.54) can compensate the low MEMCF by artificially increasing the piezoelements voltage and thus reinforcing the damping. However when the mechanical energy is dissipated, the transducer continues to recharge and inject energy into the system. An improvement to SSDV was proposed by Badel et al. [171], which consisted of adapting the voltage source to the amplitude of vibration; this technique is rather complex.

SSD-based techniques can also be used to enhance the series piezoelectric TMD [19] (Figure 1.37) as proposed by Lallart et al. [172]. According to the dual function of the series TMD, it can both be used to dampen the structure or to generate energy for other systems. Due to the low power requirement feature, it is promising to design self-powered vibration control systems [173–176].

The aforementioned work have fully demonstrated the use of SSD as effective damping techniques for single mode vibration control. However, it has also been proven that switching at each extremum of the reference signal (piezovoltage/displacement) is not an optimal algorithm of SSD techniques in multimodal vibration control case, since its principle only focuses on the highest detectable mode [177].

Many strategies aiming at improving the multi-modal damping effectiveness of the SSD techniques are proposed [177–179]. Most of the enhanced strategies are based on threshold detections, below which the control process is disabled. Moreover, these threshold criteria are obtained by time domain signal process according to the history of dynamical response in a given time window. For instance Corr and Clark [177] suggested that the switch timing is determined according to the rate of energy change. When the product of the applied voltage and the sum of the voltage rates for the controlled modes is less than zero, the shunt switch will be shut for removing the energy from mechanical system. Cherif et al. [180] used another control algorithm for triggering the switch named SSDI max. In this method, both the modal displacement extrema and the sign of voltage and its derivative are considered. If the voltage is positive and its derivative is negative when maximum modal displacement occurs, the switch is triggered immediately, or it should wait until this condition is fulfilled. Symmetric algorithm is used for the minimum modal displacement detection. By implementing this algorithm, control voltage for a targeted mode is artificially increased using the electric energy obtained from higher modes. Improvement in the damping for targeted mode was numerically demonstrated under bimodal and pulse excitations.

1.5.4 Remarks

The context of multi-mode vibration control is often related to mid- and high frequencies, therefore the desired strategies should also be insensitive with the change of modal frequencies induced by the changing of boundary conditions etc. In this regard, the passive strategies are facing challenges because the designed locations for piezoelectric patches may no longer be the best place for certain high-order mode under a small perturbation of the boundary conditions. PEM plates may be a promising solution but the implementation requires an electric analogy of the mechanical fields; this may be difficult for complex structures.

Concerning the semi-active strategies, multi-mode vibration control still remains an open field for SSD techniques. Various studies suggest the use of observers to estimate the modes and thus optimize the synchronization with a multi-mode structure. However, these model-based solutions may bring more complexity to the system, which makes their physical implementation even more complex than active techniques. Also the transfer and subsequent dissipation of the mechanical energy into electrical form is distributed on the frequency of the vibration and on its odd harmonics. This phenomenon can be harmful if the resonance frequency of one of these harmonics is in coincidence with a structural resonant mode [20].

Chapter 2

Model reduction schemes for the wave and finite element method using free modes of the unit cell

Abstract: In this chapter we introduce free-interface Component Modal Synthesis (CMS) methods into WFEM to reduce the unit cell model. The aim is to accelerate the calculation while maintain the accuracy. Several free-interface CMS methods with different approximations of the residual effects are implemented and compared. Adapting to the reduced methods, a new eigenvalue scheme based on the compliance matrix is proposed. We show that it is equivalent to the existing eigenvalue formulas. A periodic open thin-wall structure is considered as an application where both free-wave characteristics and forced response are computed. Aspects such as accuracy, efficiency and convergence are discussed and compared with the Craig-Bampton's fix-interface CMS method. Among the implemented models, the minimum model size is achieved by the exact CMS method, which only requires the modes below the maximum analyzing frequency, reducing the model size from 4416 to 16. The most numerically efficient model for WFEM is built by MacNeal's CMS method, where the CPU time of free-wave analysis can be reduced by 97%.

Contents

2.1 Introduction

The center of WFEM is the wave basis formed by the eigenvalues and eigenvectors of the transfer matrix of one unit cell. However, there are several numerical issues to obtain the wave basis as reported by Waki et al.[93]. One of these is the ill-conditioning of the standard eigenvalue scheme of the transfer matrix, especially when the Degree-of-Freedoms (DOFs) of the unit cell are enormous. Generalized eigenvalue schemes with better numerical stability are proposed, such as the one replacing force terms by displacement ones [93] or Zhong's method [98]. As a second issue, a big proportion of the waves are strong evanescent waves whose eigenvalues are either very large or small. Negative- and positive-going evanescent waves might not exactly coherent due to the numerical dispersion, even though the generalized eigenvalue schemes are used. This would induce significant errors in to the forced response calculation [181]. One idea is to use a reduced wave basis including all the propagating waves and some less-decaying waves to express the cross-section deformation, due to the fact that strong evanescent waves do not contribute much to the overall response. Left eigenvectors of the transfer matrix should be calculated to avoid the inverting of the reduced basis. This idea is used and validated in several applications [24, 102, 104, 182].

Since a FEM unit cell model is used, a refined mesh is necessary to have good prediction of the wave characteristics, as reported by Droz et al. [87]. However, the use of large-size FEM model would worsen the aforementioned numerical issues. All these eigenvalue schemes are based on the condensed Dynamic Stiffness Matrix (DSM), obtained by eliminating all the inner DOFs of the unit cell. A large sparse matrix corresponding to the inner DOFs is inverted, and it may induce numerical errors into the condensed DSM which can not be reduced by using an appropriate eigenvalue scheme. Moreover, the condense DSM is frequency-dependent, which means the inverse of a big sparse matrix is required at each frequency. This could dramatically increase the computational cost when a large FE model is used. On the other hand, the size of the eigenvalue problem is directly related to the number of DOFs at the boundaries. The use of a large FE model with more boundary DOFs will also increase the computational cost for solving the eigenvalue problem.

To accelerate the calculation of wave basis and mitigate the numerical error, reduced models have been proposed. In the literature, there are two main strategies to reduce the unit cell model for WFEM. Here we label them as wave-based [87, 102] and mode-based models [24, 88, 101]. The wave-based strategy uses a set of wave shapes selected at some preselected frequencies to express the cross-section deformation at the present frequency. Not all the waves are kept and the selection of waves depends on the application. Duhamel et al. [102] employed this strategy to compute the forced response, so the evanescent waves should be selected and kept. [87] used similar idea to accelerate the calculation of dispersion curves for propagating waves, hence only near-orthogonal propagating waves at those frequencies are kept. By this strategy, the DOFs at the boundaries can be reduced and so as the size of eigenvalue problem. To start this method, one needs to compute the wave solutions at the preselected frequencies using the full FE unit cell model, which increases the implementation difficulty.

Alternatively for the mode-based strategy, the unit cell model is reconstructed by CMS methods before the WFEM procedure. Zhou et al. [88] apply the Craig-Bampton's

CMS method [183] to the unit cell model, where the DOFs at left and right boundaries are kept in physical domain and all the inner DOFs are reduced to modal domain. This way the inner DOFs are reduced and the calculation of the condensed DSM is highly accepted. Later, the same authors applied the method into two dimensional structures and experimentally validated the results [100, 101]. Fan et al. [24] extended this method to structures with local dampers or piezoelectric shunts and applied to the periodic substructures in an open built-up structural system. The accuracy of this strategy is ensured by the principle of modal superposition and can be improved by retain more modes. It is intuitive to combine Craig-Bampton's method with WFEM because the boundaries DOFs at which the periodic boundary conditions apply are kept in the physical domain. Nonetheless, this convenience also constrains the size of the reduced model. Additionally, for uniform structures whose unit cell does not necessarily have inner DOFs, this method is not applicable. It remains a question whether free-interface CMS methods can be applied, where all the DOFs are transformed into modal domain. If applicable, it has the potential to be applied for uniform structures and to obtain a smaller reduced model for periodic structures. Besides, it is easier to include experimental data into the reduced model.

In general, we can summarize that in WFEM, there are two time-consuming tasks repetitively calculated at each frequency:

1. The inverse of a sparse matrix, whose size equals to the size of inner DOFs.

2. The solutions of a generalized eigenvalue problem, whose size equals to the size of boundary DOFs.

As discussed, the wave-based strategy reduces the size of eigenvalue problem, while the mode-based strategy reduces the size of matrix to be inverted. They both accelerate the calculation, but in different stages of the WFEM calculation. The former is more applicable for uniform structures with complex cross-section profile while the latter is more suitable for periodic structures with a lot of inner DOFs. It is feasible to combine these two strategies to analyze structures with numerous boundary and inner DOFs, as it is shown by [105]. For most of the applications, using either strategy can achieve a satisfying acceleration.

In this chapter, we explore the use of the free-interface CMS methods with the WFEM as alternatives. The basic idea of free-interface CMS methods is to use low-oder free modes plus residual effects to approximate the compliance matrix. Adapting to that, a new eigenvalue scheme based on the force vector is proposed (section 2.3.3), and the results can be easily recovered to the eigen-solutions of the transfer matrix. Free-interface methods proposed by Hou [184], MacNeal [185], Rubin [186] and Qiu et al. [187] are considered and implemented (section 2.3.1 and 2.3.2). They have different order of accuracy for the residual effects from zero order to infinite order. As references, the full WFEM (section 2.2.1) and WFEM with Craig-Bampton's method (section 2.2.2) are also implemented. A periodic thin-wall structure with complex wave characteristics is considered as the application (section 2.4). Comparison are made among the free-wave results obtained by the implemented methods to illustrate the efficiency, convergence and accuracy issues (section 2.5.1). For the forced response analysis, the accuracy on the strong evanescent waves and their influences are discussed (section 2.5.2).

2.2 The framework of the wave and finite element method

For the sake of clarity, we briefly review the WFEM for the free wave and forced response analysis. Two models of the unit cell are presented: 1) full finite element model [107, 182] and 2) the reduced model based on Craig-Bampton's CMS method [88]. A unit cell is the smallest repetitive substructure of the periodic structure, as shown in Figure 2.1. Obtaining the finite element description of a single unit cell is the starting point of WFEM. Imposing the periodic boundary conditions derived from the Bloch theorem, the homogeneous problem in the periodic structure leads to an eigenvalue problem, whose scheme can be formulated in many different ways. The solutions give wavenumbers and associated wave shapes at each frequency, revealing how free waves can travel in the structure. Additionally, the obtained left and right eigenvectors define the wave basis [85]. The wave basis has many useful properties which enable itself to diagonalize the transfer matrix by a reduced set of left and right eigenvectors [122, 188]. The forced response of the structure subject to external forces can then be obtained by wave decomposition and superposition [93, 182].

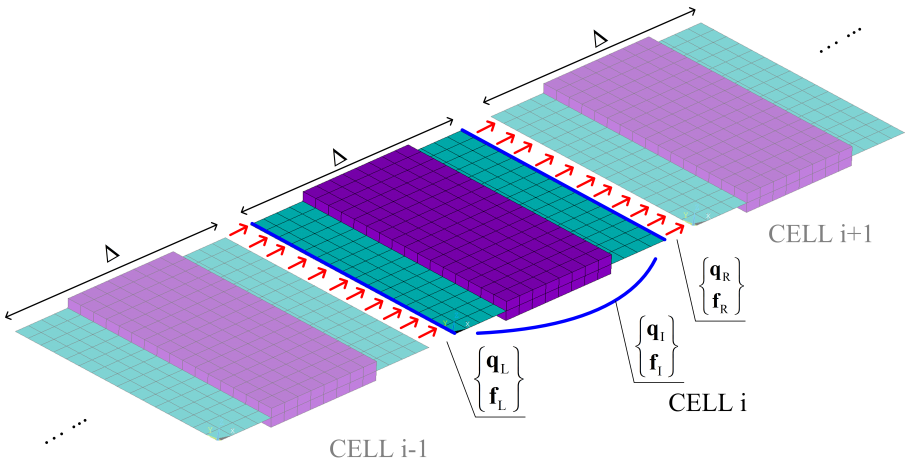

Figure 2.1: Illustration of the unit cells in a periodic structure.

2.2.1 WFEM with full FE model of the unit cell

In the context of free-wave analysis, external loads are not considered. Isolating a unit cell from the periodic structure and the discrete governing equations can be obtained by existing FE tools:

$$\mathbf{M}\begin{pmatrix}\ddot{\mathbf{q}}_L\\ \ddot{\mathbf{q}}_R\\ \ddot{\mathbf{q}}_I\end{pmatrix}+\mathbf{C}\begin{pmatrix}\dot{\mathbf{q}}_L\\ \dot{\mathbf{q}}_R\\ \dot{\mathbf{q}}_I\end{pmatrix}+\mathbf{K}\begin{pmatrix}\mathbf{q}_L\\ \mathbf{q}_R\\ \mathbf{q}_I\end{pmatrix}=\begin{pmatrix}\mathbf{f}_L\\ \mathbf{f}_R\\ \mathbf{0}\end{pmatrix} \tag{2.1}$$

where $\mathbf{q}$ is the displacement vector; $\mathbf{f}$ is the internal force vector; a superimposed dot denotes derivative with respect to time; $\mathbf{M}$, $\mathbf{C}$ and $\mathbf{K}$ refer to the mass, damping and stiffness matrices respectively. Subscripts L, R and I respectively denote the left-side, right-side and internal DOFs as illustrated in Figure 2.1. In the context of harmonic

motions, the dynamic equations of a unit cell at frequency ω are given by

$$\tilde{\mathbf{D}}\mathbf{q} = \left(-\omega^2\mathbf{M} + j\omega\mathbf{C} + \mathbf{K}\right)\mathbf{q} = \mathbf{f} \tag{2.2}$$

where $\tilde{\mathbf{D}}$ is the dynamic stiffness matrix.

According to the Bloch theorem, when a free wave travels in the periodic structure, the following conditions should be satisfied:

$$\mathbf{q}_\mathrm{R} = \lambda\mathbf{q}_\mathrm{L} \tag{2.3}$$

$$\mathbf{f}_\mathrm{R} = -\lambda\mathbf{f}_\mathrm{L} \tag{2.4}$$

where $\lambda = e^{-jk\Delta}$ describes the amplitude and phase changes when the wave travels from the left side to the right side of a unit cell. k is the wavenumber and Δ is the length of the unit cell. The minus sign appears in Equation (2.4) is induced by the equilibrium of the internal forces.

The objective of the free wave analysis is to find deformation vector $\mathbf{q}$ associated with a wavenumber k at frequency ω to satisfy Equations (2.1), (2.3) and (2.4). Two strategies are available in the literature. The first one is to fix a frequency ω, and search for all the k and $\mathbf{q}$, termed the 'direct form' [75]. Alternatively, it is also possible to fix a wavenumber k, and search for all ω and $\mathbf{q}$, termed the 'inverse form' [99]. The inverse form is convenient to calculate the propagating waves and it is often applied on two-dimensional structures [101]. The direct form can yield both propagating and evanescent waves, and it is obligatory when the next step is a forced response analysis [106]. It is more frequently used when analyzing one dimensional structures [88, 107, 122, 182, 188].

To have a coherent context, only the direct form is described here. Eliminating all the internal DOFs $\mathbf{q}_\mathrm{I}$ from Equation (2.1) at frequency ω, the condensed dynamic stiffness matrix of the unit cell writes

$$\begin{bmatrix}\mathbf{D}_\mathrm{LL} & \mathbf{D}_\mathrm{LR}\\ \mathbf{D}_\mathrm{RL} & \mathbf{D}_\mathrm{RR}\end{bmatrix}\begin{pmatrix}\mathbf{q}_\mathrm{L}\\ \mathbf{q}_\mathrm{R}\end{pmatrix} = \begin{pmatrix}\mathbf{f}_\mathrm{L}\\ \mathbf{f}_\mathrm{R}\end{pmatrix} \tag{2.5}$$

where

$$\begin{bmatrix}\mathbf{D}_\mathrm{LL} & \mathbf{D}_\mathrm{LR}\\ \mathbf{D}_\mathrm{RL} & \mathbf{D}_\mathrm{RR}\end{bmatrix} = \begin{bmatrix}\tilde{\mathbf{D}}_\mathrm{LL} & \tilde{\mathbf{D}}_\mathrm{LR}\\ \tilde{\mathbf{D}}_\mathrm{RL} & \tilde{\mathbf{D}}_\mathrm{RR}\end{bmatrix} - \begin{bmatrix}\tilde{\mathbf{D}}_\mathrm{LI}\\ \tilde{\mathbf{D}}_\mathrm{RI}\end{bmatrix}\tilde{\mathbf{D}}_\mathrm{II}^{-1}\begin{bmatrix}\tilde{\mathbf{D}}_\mathrm{IL} & \tilde{\mathbf{D}}_\mathrm{IR}\end{bmatrix} \tag{2.6}$$

Substituting condition (2.3) into Equation (2.5) to eliminate $\mathbf{f}_\mathrm{L}$ and $\mathbf{f}_\mathrm{R}$, and considering Equation (2.4), it comes to the eigenvalue problem

$$\left(\begin{bmatrix}\mathbf{0} & \mathbf{I}\\ -\mathbf{D}_\mathrm{RL} & -\mathbf{D}_\mathrm{RR}\end{bmatrix} - \lambda\begin{bmatrix}\mathbf{I} & \mathbf{0}\\ \mathbf{D}_\mathrm{LL} & \mathbf{D}_\mathrm{LR}\end{bmatrix}\right)\begin{pmatrix}\mathbf{q}_\mathrm{L}\\ \mathbf{q}_\mathrm{R}\end{pmatrix} = \mathbf{0} \tag{2.7}$$

Equation (2.7) provides a better conditioned way to calculate the eigenvalues of the transfer matrix

$$\left(\mathbf{T} - \lambda\mathbf{I}\right)\begin{pmatrix}\mathbf{q}_\mathrm{L}\\ \mathbf{f}_\mathrm{L}\end{pmatrix} = \mathbf{0} \tag{2.8}$$

where

$$\mathbf{T} = \begin{bmatrix}-\mathbf{D}_\mathrm{LR}^{-1}\mathbf{D}_\mathrm{LL} & \mathbf{D}_\mathrm{LR}^{-1}\\ -\mathbf{D}_\mathrm{RL} + \mathbf{D}_\mathrm{RR}\mathbf{D}_\mathrm{LR}^{-1}\mathbf{D}_\mathrm{LL} & -\mathbf{D}_\mathrm{RR}\mathbf{D}_\mathrm{LR}^{-1}\end{bmatrix} \tag{2.9}$$

is the transfer matrix. It links the displacement and force at the left and right boundaries

$$\begin{pmatrix} \mathbf{q}_{\mathrm{R}} \\ -\mathbf{f}_{\mathrm{R}} \end{pmatrix} = \mathbf{T} \begin{pmatrix} \mathbf{q}_{\mathrm{L}} \\ \mathbf{f}_{\mathrm{L}} \end{pmatrix} \tag{2.10}$$

However, the eigenvector given by Equation (2.7) is in the form of $\begin{pmatrix} \phi_{\mathrm{q}}^{\mathrm{T}} & \lambda\phi_{\mathrm{q}}^{\mathrm{T}} \end{pmatrix}^{\mathrm{T}}$. By the statement

$$\phi_{\mathrm{f}} = \mathbf{D}_{\mathrm{LL}}\phi_{\mathrm{q}} + \lambda\mathbf{D}_{\mathrm{LR}}\phi_{\mathrm{q}} \tag{2.11}$$

included in Equation (2.5), the eigenvector of Equation (2.7) can be post-processed into the form $\phi = \begin{pmatrix} \phi_{\mathrm{q}}^{\mathrm{T}} & \phi_{\mathrm{f}}^{\mathrm{T}} \end{pmatrix}^{\mathrm{T}}$ which is also the eigenvector of the transfer matrix $\mathbf{T}$ associated with the same eigenvalue. The eigenvector ϕ corresponds to a wave shape that exists in the structure at the given frequency, where ϕ_{q} is the nodal displacement and ϕ_{f} the internal forces at the cell interface under the passage of the wave.

Overall $2N$ eigenvalues can be found, by solving Equation (2.8) or (2.7). The eigenvalues appear in pairs of $(\lambda, 1/\lambda)$, each pair representing a positive- and a negative- going wave along the propagating direction. This is caused by the fact that $\mathbf{D}$ and $\tilde{\mathbf{D}}$ are symmetric (Hermitian) matrices [84]. If there is no damping mechanism, which means $\mathbf{T} \in \mathbb{R}^{2N\times 2N}$, an eigenvalue λ is either a complex number with $|\lambda| = 1$ or a real number greater or lower than 1. Therefore the corresponding wavenumber k is purely real or imaginary, associated with a propagating or an evanescent wave respectively. If damping mechanism is presented, namely $\mathbf{T} \in \mathbb{C}^{2N\times 2N}$, the eigenvalues can be complex numbers and wavenumbers k are also complex numbers and all these waves are decaying. The positive waves are those for which $|\lambda| < 1$, namely the amplitude decrease along the propagative direction. For the waves satisfying $|\lambda| = 1$, the positive going ones are those with a positive-going power flow, namely $\Re(j\omega\phi_{\mathrm{q}} \cdot \bar{\phi}_{\mathrm{f}}) > 0$. These discussions concerning the distinguishing of waves can be summarized as

- **propagating waves**: $|\lambda| = 1$, namely $\Im(k) = 0$
  - positive-going: $\Re(j\omega\phi_{\mathrm{q}} \cdot \bar{\phi}_{\mathrm{f}}) > 0$, namely $\Re(k) > 0$
  - negative-going: $\Re(j\omega\phi_{\mathrm{q}} \cdot \bar{\phi}_{\mathrm{f}}) < 0$, namely $\Re(k) < 0$
- **oscillating-decaying or evanescent waves**: $|\lambda| \neq 1$, namely $\Im(k) \neq 0$
  - positive-going: $|\lambda| < 1$, namely $\Im(k) < 0$
  - negative-going: $|\lambda| > 1$, namely $\Im(k) > 0$

Assembling eigenvectors by columns, we have matrix Φ :

$$\Phi = \begin{bmatrix} \Phi_{\mathrm{q}}^{+} & \Phi_{\mathrm{q}}^{-} \\ \Phi_{\mathrm{f}}^{+} & \Phi_{\mathrm{f}}^{-} \end{bmatrix} \tag{2.12}$$

where

$$\Phi_{\mathrm{q}}^{+} = \begin{bmatrix} \phi_{\mathrm{q},1}^{+} & \phi_{\mathrm{q},2}^{+} & \cdots & \phi_{\mathrm{q},N}^{+} \end{bmatrix}$$
$$\Phi_{\mathrm{q}}^{-} = \begin{bmatrix} \phi_{\mathrm{q},1}^{-} & \phi_{\mathrm{q},2}^{-} & \cdots & \phi_{\mathrm{q},N}^{-} \end{bmatrix}$$
$$\Phi_{\mathrm{f}}^{+} = \begin{bmatrix} \phi_{\mathrm{f},1}^{+} & \phi_{\mathrm{f},2}^{+} & \cdots & \phi_{\mathrm{f},N}^{+} \end{bmatrix}$$
$$\Phi_{\mathrm{f}}^{-} = \begin{bmatrix} \phi_{\mathrm{f},1}^{-} & \phi_{\mathrm{f},2}^{-} & \cdots & \phi_{\mathrm{f},N}^{-} \end{bmatrix}$$

and superscript + and − refer to the data belonging to positive and negative going waves respectively.

To establish the eigen-decomposition of matrix $\mathbf{T}$, left eigenvectors of $\mathbf{T}$ are required. If a row vector $\begin{pmatrix} \hat{\theta}_{\mathrm{q}}^{\mathrm{T}} & \hat{\theta}_{\mathrm{f}}^{\mathrm{T}} \end{pmatrix}$ is the left eigenvector obtained from Equation (2.7), then it is also the left eigenvector of $\mathbf{T}$ corresponding to the same eigenvalue. We also assemble the left eigenvectors by rows to form a matrix

$$\Theta = \begin{bmatrix} \Theta_{\mathrm{q}}^{+} & \Theta_{\mathrm{f}}^{+} \\ \Theta_{\mathrm{q}}^{-} & \Theta_{\mathrm{f}}^{-} \end{bmatrix} \tag{2.13}$$

where the left eigenvector in the ith row has the same eigenvalue as the right eigenvector in the ith column in matrix Φ. At a given frequency, matrices Φ, Θ and Λ define the wave basis and they have the following orthogonal relationships

$$\Theta\mathbf{T}\Phi = \Lambda = \begin{bmatrix} {}^{+}\Lambda & \\ & {}^{-}\Lambda \end{bmatrix} = \begin{bmatrix} \ddots & & \\ & \lambda_i & \\ & & \ddots \end{bmatrix} \tag{2.14}$$

when eigenvectors are normalized by

$$\Theta\Phi = \mathbf{I} \tag{2.15}$$

It is worth to note that Equations (2.14) and (2.15) still hold when a reduced set of associated left and right eigenvectors are kept in matrices Θ and Φ. This property allows us to use a reduced set of waves in the forced response analysis, and to avoid the searching of the pseudo inverse of matrix Φ.

2.2.2 WFEM with Craig-Bampton modal synthesis method

Searching for the inverse of $\tilde{\mathbf{D}}_{\mathrm{II}}$ in Equation (2.6) is time-consuming if the internal DOFs of the unit cell are numerous. The computational time becomes an issue especially when repetitive calculations are required with several groups of parameters to design a periodic structure. To accelerate the calculation, a reduced model of the unit cell is proposed by Zhou et al. [88, 101] based on the Craig-Bampton's method.

First perform a modal analysis on the unit cell with all the boundary DOFs fixed. Imposing $\mathbf{q}_{\mathrm{L}} = \mathbf{q}_{\mathrm{R}} = \mathbf{0}$, the ith natural frequency ω_i and modal shape ψ_i can be obtained by solving the eigenvalue problem

$$\left(-\omega_i^2\mathbf{M}_{\mathrm{II}} + \mathbf{K}_{\mathrm{II}}\right)\psi_i = \mathbf{0} \tag{2.16}$$

Assembling modal shapes by columns, we obtain matrix $\Psi = \begin{bmatrix} \psi_1 & \psi_2 & \cdots & \psi_{l_{\mathrm{rm}}} \end{bmatrix}$. Only the first l_{rm} modes are used to form Ψ, and $l_{\mathrm{rm}} < (w - 2N)$ where w is the overall number of DOFs of the unit cell and $2N$ is the number of DOFs at the boundaries. The criterion used to select the retained modes is

$$\omega_i < \alpha_{\mathrm{f}}\omega_{\mathrm{m}}, i \in [1, 2, ..., l_{\mathrm{rm}}] \tag{2.17}$$

where ω_{m} is the upper bound of the preselected frequencies to be analyzed. Factor α_{f} controls the number of the retained modes therefore affects the accuracy of the reduced

model as well. To have good prediction of the dispersion curves associated with the propagating waves, $\alpha_f = 3$ is suggested and numerically validated by Zhou et al. [88, 101].

A coordinate transformation is then defined

$$\begin{pmatrix} \mathbf{q}_L \\ \mathbf{q}_R \\ \mathbf{q}_I \end{pmatrix} = \begin{bmatrix} \mathbf{I} & \mathbf{0} & \mathbf{0} \\ \mathbf{0} & \mathbf{I} & \mathbf{0} \\ -\mathbf{K}_{II}^{-1}\mathbf{K}_{IL} & -\mathbf{K}_{II}^{-1}\mathbf{K}_{IR} & \Psi \end{bmatrix} \begin{pmatrix} \mathbf{q}_L \\ \mathbf{q}_R \\ \mathbf{y} \end{pmatrix} = \mathbf{B} \begin{pmatrix} \mathbf{q}_L \\ \mathbf{q}_R \\ \mathbf{y} \end{pmatrix} \tag{2.18}$$

Introducing this transformation into (2.1) and (2.2), and left-multiply matrix $\mathbf{B}^T$ at both sides of the equations, the dynamic stiffness matrix $\tilde{\mathbf{D}}^*$ writes

$$\tilde{\mathbf{D}}^* = -\omega^2 \mathbf{B}^T \mathbf{M} \mathbf{B} + j\omega \mathbf{B}^T \mathbf{C} \mathbf{B} + \mathbf{B}^T \mathbf{K} \mathbf{B} \tag{2.19}$$

Matrix $\tilde{\mathbf{D}}^*$ has a much smaller size than $\tilde{\mathbf{D}}$ in Equation (2.2). Then eliminating the modal coordinates $\mathbf{y}$ by introducing Equation (2.19) into (2.6) will also lead to Equation (2.5). But the calculation in Equation (2.6) is significantly accelerated because

$$\tilde{\mathbf{D}}_{II}^* = \ \mathrm{diag}(-\omega^2 + 2j\xi_i\omega_i\omega + \omega_i^2) \tag{2.20}$$

is a diagonal matrix due to the orthogonal relations

$$\begin{aligned} \Psi^T \mathbf{C}_{II} \Psi &= \ \mathrm{diag}\,(2\xi_i\omega_i) \\ \Psi^T \mathbf{M}_{II} \Psi &= \mathbf{I} \\ \Psi^T \mathbf{K}_{II} \Psi &= \ \mathrm{diag}\,(\omega_i^2) \end{aligned}$$

where j is the imaginary unit and ξ_i is the modal damping coefficient. One only needs to construct the reduced stiffness, mass and damping matrices in Equation (2.19) once, then the the free wave analysis at each frequency can be performed on the reduced model.

2.2.3 Forced response analysis using wave amplitudes

The forced response analysis based on WFEM can be understood as an accelerated transfer matrix method. Owing to the orthogonal properties of the wave basis, calculating the transferring of state vectors in wave domain is much quicker than in physical domain. Once the wave basis (Φ, Θ and Λ) is obtained (by full unit cell model or any other reduced models), the process of forced response remains the same.

The displacements and forces at a cross-section (say cross-section 0) between two unit cells can be represented by a linear combination of the wave shapes

$$\begin{pmatrix} \mathbf{q}_0 \\ \mathbf{f}_0 \end{pmatrix} = \Phi \begin{pmatrix} \mathbf{p}^+ \\ \mathbf{p}^- \end{pmatrix} \tag{2.21}$$

where $\mathbf{p}^+$ and $\mathbf{p}^-$ are the amplitudes of the positive-going and negative-going waves at this cross-section. Similarly, at the cross-section across i unit cells in the positive direction, there is

$$\begin{pmatrix} \mathbf{q}_i \\ \mathbf{f}_i \end{pmatrix} = \Phi \begin{pmatrix} \mathbf{r}^+ \\ \mathbf{r}^- \end{pmatrix} \tag{2.22}$$

If no external forces applied in-between, we have

$$\begin{pmatrix} \mathbf{q}_i \\ \mathbf{f}_i \end{pmatrix} = \mathbf{T}^i \begin{pmatrix} \mathbf{q}_0 \\ \mathbf{f}_0 \end{pmatrix} \tag{2.23}$$

Introducing Equations (2.22) and (2.21) to (2.23), and using the orthogonal relations (2.14) and (2.15), it can be proved that

$$\begin{pmatrix} \mathbf{r}^+ \\ \mathbf{r}^- \end{pmatrix} = \Lambda^i \begin{pmatrix} \mathbf{p}^+ \\ \mathbf{p}^- \end{pmatrix} \tag{2.24}$$

This is actually the transfer relation in wave domain.

Practically, it is not necessary to consider the full wave basis of $2N$ waves, because the strong evanescent waves might have very minor contribution to the overall response [189]. On the contrary, including all the waves even caused significant numerical errors [182]. The $2l_{\mathrm{rw}}$ kept waves (l_{rw} positive-going and l_{rw} negative-going) are the propagating and less decaying ones, namely the ones satisfying

$$\lambda_{\mathrm{CR}} \leq |\lambda| \leq 1/\lambda_{\mathrm{CR}} \tag{2.25}$$

where λ_{CR} is the factor which controls the maximum and minimum propagating constant of the retained waves.

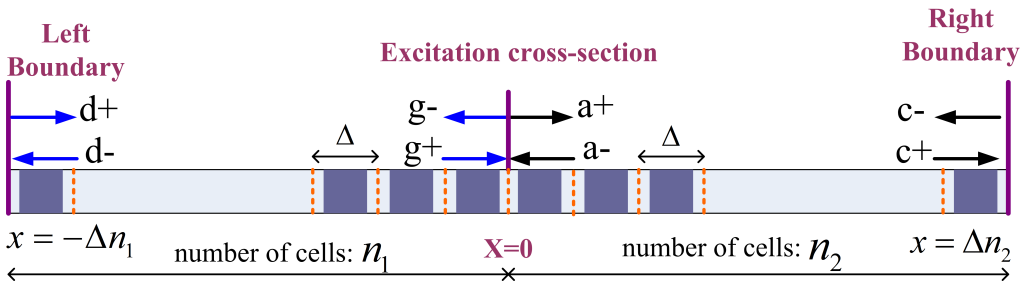

Figure 2.2: Illustration of the wave amplitudes in a periodic structure.

Suppose we have a finite periodic structure subject to excitation at one cross-section as shown in Figure 2.2. We can set the origin point to the excitation cross-section, and it has n_1 unit cells at the negative-x side and n_2 at the positive-x side. At the excitation cross-section, the boundary condition writes

$$\mathbf{f}_{\mathrm{left}} - \mathbf{f}_{\mathrm{right}} + \mathbf{f}_{\mathrm{ex}} = \mathbf{0} \tag{2.26}$$

$$\mathbf{q}_{\mathrm{left}} - \mathbf{q}_{\mathrm{right}} = \mathbf{0} \tag{2.27}$$

where subscript 'left' (respectively 'right') denotes the cross-section with infinitely small distance to the left (respectively right) side of the excitation cross-section. The wave amplitudes are $\mathbf{g}^+$ and $\mathbf{g}^-$ associated with the 'left' cross-section and $\mathbf{a}^+$ and $\mathbf{a}^-$ for the 'right' one, as illustrated in Figure 2.2. Introducing Equation (2.21) to Equation (2.27) and applying the orthogonal relation shown in (2.15), the force boundary condition can be written in terms of wave amplitudes

$$\begin{pmatrix} \mathbf{a}^+ \\ \mathbf{a}^- \end{pmatrix} - \begin{pmatrix} \mathbf{g}^+ \\ \mathbf{g}^- \end{pmatrix} = \Theta \begin{pmatrix} \mathbf{0} \\ \mathbf{f}_{\mathrm{ex}} \end{pmatrix} \tag{2.28}$$

This also indicates that the wave amplitudes are not continuous at the cross-section where external forces apply.

Tracing the traveling of waves at the left part, we have

$$\mathbf{d}^{+} = ({}^{+}\Lambda)^{-n_1}\mathbf{g}^{+} \tag{2.29}$$

$$\mathbf{d}^{-} = ({}^{-}\Lambda)^{-n_1}\mathbf{g}^{-} \tag{2.30}$$

and

$$\mathbf{d}^{+} = \mathbf{R}_{\mathrm{L}}\mathbf{d}^{-} \tag{2.31}$$

where $\mathbf{R}_{\mathrm{L}}$ is the reflection matrix at the left boundary of the structure, and $\mathbf{d}$ is the wave amplitude at the left boundary. Introducing Equations (2.29) and (2.30) into (2.31) to eliminate $\mathbf{d}$, the wave amplitudes $\mathbf{g}^{+}$ and $\mathbf{g}^{-}$ are related by

$$\mathbf{g}^{+} = ({}^{+}\Lambda)^{n_1}\mathbf{R}_{\mathrm{L}}({}^{-}\Lambda)^{-n_1}\mathbf{g}^{-} \tag{2.32}$$

Note that $[({}^{+}\Lambda)^{-n_1}]^{-1} = ({}^{+}\Lambda)^{n_1}$.

Similarly, for the right part, there is

$$\mathbf{c}^{+} = ({}^{+}\Lambda)^{n_2}\mathbf{a}^{+} \tag{2.33}$$

$$\mathbf{c}^{-} = ({}^{-}\Lambda)^{n_2}\mathbf{a}^{-} \tag{2.34}$$

and

$$\mathbf{c}^{-} = \mathbf{R}_{\mathrm{R}}\mathbf{c}^{+} \tag{2.35}$$

where $\mathbf{R}_{\mathrm{R}}$ is the reflection matrix at the right boundary of the structure, and $\mathbf{c}$ is the wave amplitude at the right boundary. Introducing Equations (2.33) and (2.34) into (2.35) to eliminate $\mathbf{c}$, the wave amplitudes $\mathbf{a}^{+}$ and $\mathbf{a}^{-}$ are related by

$$\mathbf{a}^{-} = ({}^{-}\Lambda)^{-n_2}\mathbf{R}_{\mathrm{R}}({}^{+}\Lambda)^{n_2}\mathbf{a}^{+} \tag{2.36}$$

The reflection matrix links the injected and reflected wave amplitudes at a boundary [24, 182]. It can be determined once the boundary condition is known. Let us express the boundary condition in a general way, as

$$\mathbf{A}\mathbf{f} + \mathbf{B}\mathbf{q} = \mathbf{0} \tag{2.37}$$

Again we express the forces and displacement by wave amplitudes, so that the reflection matrix becomes

$$\mathbf{R} = \left(\mathbf{A}\Phi_{\mathrm{f}}^{\mathrm{ref}} + \mathbf{B}\Phi_{\mathrm{q}}^{\mathrm{ref}}\right)^{-1}\left(\mathbf{A}\Phi_{\mathrm{f}}^{\mathrm{inc}} + \mathbf{B}\Phi_{\mathrm{q}}^{\mathrm{inc}}\right) \tag{2.38}$$

where superscript ref and inc refer to the reflected and injected waves respectively. For the left boundary, superscript ref can be replaced by + and inc by -. When the reduced wave basis is used, the calculation of $\mathbf{R}$ will pseudo-inversion. Equation (2.37) can be premultiplied by left eigenvectors (e.g. Θ_{q}^{+}), yielding

$$\mathbf{R} = \left(\Theta_{\mathrm{q}}^{+}\mathbf{A}\Phi_{\mathrm{f}}^{\mathrm{ref}} + \Theta_{\mathrm{q}}^{+}\mathbf{B}\Phi_{\mathrm{q}}^{\mathrm{ref}}\right)^{-1}\left(\Theta_{\mathrm{q}}^{+}\mathbf{A}\Phi_{\mathrm{f}}^{\mathrm{inc}} + \Theta_{\mathrm{q}}^{+}\mathbf{B}\Phi_{\mathrm{q}}^{\mathrm{inc}}\right) \tag{2.39}$$

This way the numerical errors can be reduced.

If the structure has infinite extent, then

$$\mathbf{R}_{\mathrm{inf}} = \mathbf{0} \tag{2.40}$$

. If the left side of the structure is free, the reflection matrix writes

$$\mathbf{R}_{\mathrm{L,free}} = -\left(\Theta_{\mathrm{f}}^{+}\Phi_{\mathrm{f}}^{-}\right)^{-1}\left(\Theta_{\mathrm{f}}^{+}\Phi_{\mathrm{f}}^{+}\right) \tag{2.41}$$

If right side of the structure is fully constrained, the reflection matrix is

$$\mathbf{R}_{\mathrm{R,fix}} = -\left(\Theta_{\mathrm{q}}^{+}\Phi_{\mathrm{q}}^{+}\right)^{-1}\left(\Theta_{\mathrm{q}}^{+}\Phi_{\mathrm{q}}^{-}\right) \tag{2.42}$$

For more complex situations, such as several periodic substructures connected together, or a periodic structure connected to a non-periodic components, the WFEM framework need to be extended, which will be discussed in the next Chapter.

Solving the linear Equations (2.28), (2.32) and (2.36), waves amplitudes $\mathbf{g}^{+}$, $\mathbf{g}^{-}$, $\mathbf{a}^{+}$ and $\mathbf{a}^{-}$ are obtained. The wave amplitudes $\mathbf{r}$ of any other cross-section at $x \leq 0$ can be obtained by introducing $\mathbf{p} = \mathbf{g}$ in Equation (2.24). If the cross-section locates at $x \geq 0$, then we introduce $\mathbf{p} = \mathbf{a}$ in Equation (2.24). The displacement and force vectors at the cross-section can then be recovered by Equation (2.21).

Having more unit cells in the structure only leads us to calculate a higher power of matrix Λ in Equations (2.32) and (2.36). Since matrix Λ is diagonal, this only induces minor computation increase. This is one of the major advantages of WFEM.

2.3 WFEM with free-interface modal synthesis method

Different with Craig-Bampton's method, when free-interface CMS methods are used, all the DOFs will be transformed into the modal domain. Only few low-order modes are kept. The the contribution of the truncated high-order modes, termed the residual flexibility, can be approximated and integrated to the overall compliance matrix of the unit cell. The condensed compliance matrix can be easily obtained because there are no external forces applied on the inner DOFs of the unit cell. This motivates us to use the internal forces at the boundaries as the unknown variables, leading to a new eigenvalue problem. We further demonstrate that this eigenvalue scheme is equivalent to the existing ones. Considering the fact that in most applications of WFEM the unit cell is statically indeterminate, the techniques to calculate the residual flexibility in such a case is given.

2.3.1 Reduced models of the unit cell

First we calculate the natural frequencies and modal shapes when the left and right boundaries of the unit cell are free. The ith natural frequency ω_i and eigenvector $\hat{\psi}_i$ are obtained by solving

$$\left(-\omega_i^2\mathbf{M} + \mathbf{K}\right)\hat{\psi}_i = \mathbf{0} \tag{2.43}$$

where matrices $\mathbf{K}$ and $\mathbf{M}$ come from Equation (2.1) with size $w \times w$. Assembling all the modal shapes by columns we get matrix $\hat{\Psi} = \begin{bmatrix} \hat{\psi}_1 & \hat{\psi}_2 & \cdots & \hat{\psi}_w \end{bmatrix}$ where the vectors are ranked by the associated natural frequencies in ascending order. The modes are normalized such that

$$\hat{\Psi}^{\mathrm{T}}\mathbf{M}\hat{\Psi} = \mathbf{I} \tag{2.44}$$

$$\hat{\Psi}^{\mathrm{T}}\mathbf{K}\hat{\Psi} = \Omega = \ \mathrm{diag}(\omega_i^2) \tag{2.45}$$

The physical displacement can then be expressed as a linear superposition of the modal shapes

$$\mathbf{q} = \hat{\Psi}\hat{\mathbf{y}} = \begin{bmatrix} \hat{\Psi}_{\text{low}} & \hat{\Psi}_{\text{high}} \end{bmatrix} \begin{pmatrix} \hat{\mathbf{y}}_{\text{low}} \\ \hat{\mathbf{y}}_{\text{high}} \end{pmatrix} \tag{2.46}$$

where $\hat{\mathbf{y}}$ is the modal coordinate vector. Subscript 'low' refers to the retained low-order modes while 'high' refers to high-order modes that will be truncated.

Using coordinate transformation (2.46) and Equations (2.44) and (2.45), Equation (2.1) can be solved [190]. The relationship between the displacement vector and the force vector writes

$$\mathbf{q} = \mathbf{H}\mathbf{f} = (\mathbf{H}_{\text{low}} + \mathbf{H}_{\text{high}})\,\mathbf{f} \tag{2.47}$$

where $\mathbf{H}$ is compliance matrix. The contribution of the low-order modes and high-order modes in the compliance matrix are

$$\mathbf{H}_{\text{low}} = \hat{\Psi}_{\text{low}} \left(\Omega_{\text{low}} - \omega^2\mathbf{I}\right)^{-1} \hat{\Psi}_{\text{low}}^{\text{T}} \tag{2.48}$$

and

$$\mathbf{H}_{\text{high}} = \hat{\Psi}_{\text{high}} \left(\Omega_{\text{high}} - \omega^2\mathbf{I}\right)^{-1} \hat{\Psi}_{\text{high}}^{\text{T}} \tag{2.49}$$

respectively.

The criterion used to determine the retained modes is the same as that was used in the reduced model based on Craig-Beampton's method (see section 2.2.2). The first l_{rm} modes that will be calculated should satisfy

$$\omega_i < \alpha_{\text{f}}\omega_{\text{m}}, i \in [1, 2, ..., l_{\text{rm}}] \tag{2.50}$$

where ω_{m} is the upper bound of the frequencies to be analyzed. Factor α_{f} controls the number of the retained modes.

Knowing only $\hat{\Omega}_{\text{low}}$ and $\hat{\Psi}_{\text{low}}$, the $\mathbf{H}_{\text{high}}$ is termed 'residual flexibility', representing the contribution of the high-order modes to the compliance matrix at low frequencies. It is shown by [187] that the exact residual flexibility can be divided into three parts

$$\mathbf{H}_{\text{high}} = \mathbf{H}_{\text{h1}} + \omega^2\mathbf{H}_{\text{h2}} + \omega^4\mathbf{H}_{\text{h3}} \tag{2.51}$$

where

$$\mathbf{H}_{\text{h1}} = \hat{\Psi}_{\text{high}}\Omega_{\text{high}}^{-1}\hat{\Psi}_{\text{high}}^{\text{T}} \tag{2.52}$$

$$\mathbf{H}_{\text{h2}} = \mathbf{H}_{\text{h1}}\mathbf{M}\mathbf{H}_{\text{h1}}^{\text{T}} \tag{2.53}$$

$$\mathbf{H}_{\text{h3}} = \mathbf{H}_{\text{high}}\mathbf{M}\mathbf{H}_{\text{h2}} \tag{2.54}$$

In practice, if the stiffness matrix $\mathbf{K}$ is nonsingular, namely it is invertible, we can use statement

$$\mathbf{K}^{-1} = \hat{\Psi}\Omega^{-1}\hat{\Psi}^{\text{T}} = \hat{\Psi}_{\text{low}}\Omega_{\text{low}}^{-1}\hat{\Psi}_{\text{low}}^{\text{T}} + \hat{\Psi}_{\text{high}}\Omega_{\text{high}}^{-1}\hat{\Psi}_{\text{high}}^{\text{T}} \tag{2.55}$$

to calculate the $\mathbf{H}_{\text{h1}}$ matrix by the known low-order modal information

$$\mathbf{H}_{\text{h1}} = \mathbf{K}^{-1} - \hat{\Psi}_{\text{low}}\Omega_{\text{low}}^{-1}\hat{\Psi}_{\text{low}}^{\text{T}} \tag{2.56}$$

Introducing Equation (2.56) to (2.53), matrix $\mathbf{H}_{\text{h2}}$ can be obtained. To obtain $\mathbf{H}_{\text{h3}}$, iteration is needed because $\mathbf{H}_{\text{high}}$ which depends on $\mathbf{H}_{\text{h3}}$ also appears at the right-hand-side of Equation (2.54). It is suggested by [191] that we can initially guess $\mathbf{H}_{\text{high}}^{(0)} =$

$\mathbf{H}_{\mathrm{h1}}+\omega^2\mathbf{H}_{\mathrm{h2}}$ and substitute it to Equation (2.54) to obtain $\mathbf{H}_{\mathrm{h3}}^{(0)}$. We substitute $\mathbf{H}_{\mathrm{h3}}^{(0)}$ into Equation (2.51) to get the updated $\mathbf{H}_{\mathrm{high}}^{(1)}$ which starts the next iteration. The iteration stops when $\mathbf{H}_{\mathrm{high}}^{(i)}$ is close enough to $\mathbf{H}_{\mathrm{high}}^{(i-1)}$ and the convergence can be achieved within few iterations [191].

Different approximation of the residual flexibility $\mathbf{H}_{\mathrm{high}}$ induces different accuracy and computational cost. In this chapter we consider five different approximations of $\mathbf{H}_{\mathrm{high}}$ and compare their performance when they are used with WFEM. The considered reduced models are

1. Reduced model without residual flexibility. Namely only $\mathbf{H}_{\mathrm{low}}$ is retained in Equation (2.47). The high-order modes and their residual are completely neglected, hence the accuracy in terms of the prediction of the residual terms is zero-order. In the remaining part of the chapter, this reduced model will be referred to as 'Free (0th)'. It is also known as Hou's method [184].

2. Reduced model with first-order approximation of residual flexibility. The residual flexibility $\mathbf{H}_{\mathrm{high}}$ is approximated by $\mathbf{H}_{\mathrm{high}} \approx \mathbf{H}_{\mathrm{h1}}$. It means that the static contribution of the high-order modes is retained. It is also known as MacNeal's method [185]. In the remaining part of the chapter, this reduced model will be referred to as 'Free (1st)'.

3. Reduced model with second-order approximation of residual flexibility. The residual flexibility $\mathbf{H}_{\mathrm{high}}$ is approximated by $\hat{\mathbf{H}}_{\mathrm{high}} \approx \mathbf{H}_{\mathrm{h1}} + \omega^2\mathbf{H}_{\mathrm{h2}}$. It is also known as Rubin's method [186]. In the remaining part of the chapter, this reduced model will be referred to as 'Free (2nd)'.

4. Reduced model with exact residual flexibility. The residual flexibility $\mathbf{H}_{\mathrm{high}}$ is calculated by the exact formula shown in Equation (2.51). Iteration is needed as presented before. It is also known as the exact substructure method proposed by [187]. It is supposed to provide an accurate prediction of the residual matrix, at least in principle. However due to the numerical error it might not be able to have infinite order of accuracy as expected. In the remaining part of the chapter, this reduced model will be referred to as 'Free (4th+)' (means at least better than fourth order accuracy).

5. Reduced model with fourth-order approximation of residual flexibility. The residual matrix $\mathbf{H}_{\mathrm{high}}$ is approximated by $\mathbf{H}_{\mathrm{high}} \approx \mathbf{H}_{\mathrm{h1}} + \omega^2\mathbf{H}_{\mathrm{h2}} + \omega^4\mathbf{H}_{\mathrm{h3}}^{(0)}$ where $\mathbf{H}_{\mathrm{h3}}^{(0)}$ is calculated by introducing $\mathbf{H}_{\mathrm{high}}^{(0)} = \mathbf{H}_{\mathrm{h1}} + \omega^2\mathbf{H}_{\mathrm{h2}}$ into Equation (2.54). It can be regarded as the aforementioned exact substructure method without iteration. In the remaining part of the chapter, this reduced model will be referred to as 'Free (4th)'.

Among these reduced models, 'Free (0th)' is straightforward and it is also the simplest one in terms of implementation, while its accuracy is the lowest. With the increase of order, the implementation complexity increases. 'Free (1st)' and 'Free (2nd)' have similar complexity because matrices $\mathbf{H}_{\mathrm{h1}}$ and $\mathbf{H}_{\mathrm{h2}}$ are frequency-independent therefore can be calculated once the modal truncation are made. For 'Free (4th+)', we need to converge the iteration at each frequency. Observing Equation (2.54), the sizes of matrices are nearly

the same as the full stiffness matrix. The iteration is likely to slow down the calculation. Using 'Free (4th)', we can illustrate the improvement of the accuracy and the extra time consuming by the iteration in 'Free (4th+)'.

2.3.2 Treatments for the singular stiffness matrix

Obtaining the first order term $\mathbf{H}_{1\mathrm{h}}$ is important to recover the residual flexibility, but in Equation (2.56) matrix $\mathbf{K}$ should be nonsingular. Yet in most of the applications of WFEM, the unit cell has rigid-body modes when the left and right boundaries are free. Consequently Equations (2.55) and (2.56) are no longer applicable because matrix $\mathbf{K}$ is singular. To solve this problem, we follow the method proposed in Ref [186, 191, 192], and the main steps are summarized in this section.

Suppose the unit cell has r rigid body modes ($r \leq 6$) when the left and right boundaries are free. Splitting $\hat{\Psi}_{\mathrm{low}} = \begin{bmatrix} \hat{\Psi}_{\mathrm{lr}} & \hat{\Psi}_{\mathrm{le}} \end{bmatrix}$, where the columns of $\hat{\Psi}_{\mathrm{lr}}$ are the r rigid body modal shapes and columns of $\hat{\Psi}_{\mathrm{le}}$ are the $(l_{\mathrm{rm}} - r)$ low-order elastic modal shapes. Equation (2.46) can then be rewritten as

$$\mathbf{q} = \begin{bmatrix} \hat{\Psi}_{\mathrm{lr}} & \hat{\Psi}_{\mathrm{e}} \end{bmatrix} \begin{pmatrix} \hat{\mathbf{y}}_{\mathrm{lr}} \\ \hat{\mathbf{y}}_{\mathrm{e}} \end{pmatrix} \tag{2.57}$$

where $\hat{\Psi}_{\mathrm{e}} = \begin{bmatrix} \hat{\Psi}_{\mathrm{le}} & \hat{\Psi}_{\mathrm{high}} \end{bmatrix}$. Same as the case where $\mathbf{K}$ is nonsingular, only the first l_{rm} modes will be retained. To find the first order term $\mathbf{H}_{\mathrm{h1}}$, we first find the overall static flexibility of all the elastic modes

$$\mathbf{K}_{\mathrm{e}}^{-1} = \hat{\Psi}_{\mathrm{e}} \Omega_{\mathrm{e}}^{-1} \hat{\Psi}_{\mathrm{e}}^{\mathrm{T}} \tag{2.58}$$

and remove the contribution of the low-order modes; it gives

$$\mathbf{H}_{\mathrm{h1}} = \mathbf{K}_{\mathrm{e}}^{-1} - \hat{\Psi}_{\mathrm{le}} \Omega_{\mathrm{le}}^{-1} \hat{\Psi}_{\mathrm{le}}^{\mathrm{T}} \tag{2.59}$$

where

$$\mathbf{K}_{\mathrm{e}}^{-1} = \mathbf{P} \bar{\mathbf{K}}^{-1} \mathbf{P}^{\mathrm{T}} \tag{2.60}$$

$$\bar{\mathbf{K}} = \mathbf{P}^{\mathrm{T}} \mathbf{K} \mathbf{P} \tag{2.61}$$

$$\mathbf{P} = \mathbf{B}^{\mathrm{T}} \mathbf{Q} \tag{2.62}$$

$$\mathbf{B} = \mathbf{I} - \mathbf{M} \hat{\Psi}_{\mathrm{lr}} \hat{\Psi}_{\mathrm{lr}}^{\mathrm{T}} \tag{2.63}$$

Matrix $\mathbf{Q}$ is the constrain matrix used to make the unit cell statically determinate. Imposing $\mathbf{q} = \mathbf{Q}\mathbf{q}_{\mathrm{c}}$ on Equation (2.1), the unit cell should have zero rigid body modes. The rank of matrix $\mathbf{Q}$ has to be $(w-r)$ and the size is $w \times (w-r)$. We have to appropriately choose r DOFs in $\mathbf{q}$ to constrain so as to cancel r rigid body modes. In this chapter we constrain the first r DOFs in $\mathbf{q}$ as suggested by [191]. Specifically, the constrain matrix is

$$\mathbf{Q} = \begin{bmatrix} \mathbf{0}_{r \times (w-r)} \\ \mathbf{I}_{(w-r) \times (w-r)} \end{bmatrix} \tag{2.64}$$

Note that Equation (2.1) is modeled by FEM and generally the DOFs linked to a same node will be arranged by continuous indexes. For instance, suppose the unit cell has 6

rigid body modes and constraining the first 6 DOFs (say '1UX', '1UY', '1UZ', '2UX', '2UY', '2UZ' for solid elements and '1UX', '1UY', '1UZ', '1THXY', '1THYZ', '1THZX' for shell elements) will be constrained.

Matrix $\mathbf{P}$ defines the transformation from the elastic deformation of the free-boundary unit cell $\mathbf{q}_\mathrm{e}$ to the elastic deformation of the constrained unit cell $\mathbf{q}_\mathrm{c}$; the transformation writes

$$\mathbf{q}_\mathrm{c} = \mathbf{P}\mathbf{q}_\mathrm{e} \tag{2.65}$$

where the size of $\mathbf{q}_\mathrm{e}$ is $w \times 1$ and $\mathbf{q}_\mathrm{c}$ is $(w-r) \times 1$. Elastic deformation $\mathbf{q}_\mathrm{e}$ is governed by

$$\mathbf{M}\ddot{\mathbf{q}}_\mathrm{e} + \mathbf{K}\mathbf{q}_\mathrm{e} = \mathbf{B}\mathbf{f} \tag{2.66}$$

where vector $\mathbf{Bf}$ represents the combination of the external and inertial forces induces by the rigid body motions. Introducing Equation (2.65) to (2.66), and left multiplying $\mathbf{P}^\mathrm{T}$, it gives

$$\bar{\mathbf{M}}\ddot{\mathbf{q}}_\mathrm{c} + \bar{\mathbf{K}}\mathbf{q}_\mathrm{c} = \mathbf{P}^\mathrm{T}\mathbf{B}\mathbf{f} \tag{2.67}$$

where $\bar{\mathbf{M}} = \mathbf{P}^\mathrm{T}\mathbf{M}\mathbf{P}$. It can be proved that

$$\hat{\Psi}_\mathrm{e} = \mathbf{P}\bar{\Psi}_\mathrm{c} \tag{2.68}$$

where $\bar{\Psi}_\mathrm{c}$ is the eigenvector matrix of Equation (2.67). Moreover

$$\bar{\Psi}_\mathrm{c}^\mathrm{T}\bar{\mathbf{K}}\bar{\Psi}_\mathrm{c} = \Omega_\mathrm{e} = \ \mathrm{diag}\,(\Omega_\mathrm{le}, \Omega_\mathrm{high}) \tag{2.69}$$

if $\bar{\Psi}_\mathrm{c}^\mathrm{T}\mathbf{M}\bar{\Psi}_\mathrm{c} = \mathbf{I}$. This indicates that models (2.66) and (2.67) have the same non-zero natural frequencies. Remind that our goal here it to find $\mathbf{K}_\mathrm{e}^{-1} = \hat{\Psi}_\mathrm{e}\Omega_\mathrm{e}^{-1}\hat{\Psi}_\mathrm{e}^\mathrm{T}$, by using Equation (2.68) and (2.69), it writes

$$\hat{\Psi}_\mathrm{e}\Omega_\mathrm{e}^{-1}\hat{\Psi}_\mathrm{e}^\mathrm{T} = \mathbf{P}\bar{\Psi}_\mathrm{c}\Omega_\mathrm{e}^{-1}\bar{\Psi}_\mathrm{c}^\mathrm{T}\mathbf{P}^\mathrm{T} = \mathbf{P}\bar{\mathbf{K}}^{-1}\mathbf{P}^\mathrm{T} \tag{2.70}$$

where $\bar{\mathbf{K}}$ is a nonsingular matrix with size $(w-r) \times (w-r)$. Removing the contribution of the low-order elastic modes from $\mathbf{K}_\mathrm{e}^{-1}$, as shown Equation (2.59), we obtain the first order residual flexibility $\mathbf{H}_\mathrm{h1}$. Subsequently, higher order residual terms $\mathbf{H}_\mathrm{h2}$, $\mathbf{H}_\mathrm{h3}$ and $\mathbf{H}_\mathrm{high}$ can be obtained in the same way when $\mathbf{K}$ is nonsingular.

2.3.3 Eigenvalue scheme for the wave characteristics

Once the compliance matrix $\mathbf{H}$ in Equation (2.47) is determined by one of the five considered models based on free modes plus residual effects, we can write the boundary DOFs in terms of internal forces at the boundaries

$$\begin{pmatrix} \mathbf{q}_\mathrm{L} \\ \mathbf{q}_\mathrm{R} \end{pmatrix} = \begin{bmatrix} \mathbf{H}_\mathrm{LL} & \mathbf{H}_\mathrm{LR} \\ \mathbf{H}_\mathrm{RL} & \mathbf{H}_\mathrm{RR} \end{bmatrix} \begin{pmatrix} \mathbf{f}_\mathrm{L} \\ \mathbf{f}_\mathrm{R} \end{pmatrix} \tag{2.71}$$

Introducing Equation (2.3) into (2.71) to eliminate $\mathbf{q}_\mathrm{L}$ and $\mathbf{q}_\mathrm{R}$ and considering Equation (2.4); it gives the following eigenvalue problem

$$\left(\begin{bmatrix} \mathbf{H}_\mathrm{RL} & \mathbf{H}_\mathrm{RR} \\ \mathbf{0} & \bar{\sigma}\mathbf{I} \end{bmatrix} - \lambda \begin{bmatrix} \mathbf{H}_\mathrm{LL} & \mathbf{H}_\mathrm{LR} \\ -\bar{\sigma}\mathbf{I} & \mathbf{0} \end{bmatrix} \right) \begin{pmatrix} \mathbf{f}_\mathrm{L} \\ \mathbf{f}_\mathrm{R} \end{pmatrix} = \mathbf{0} \tag{2.72}$$

where

$$\bar{\sigma} = \sqrt{\frac{\|\mathbf{H}_{\mathrm{LL}}\|_{\mathbf{2}}}{N}} \tag{2.73}$$

is introduced to balance the magnitudes of the compliance matrix and the identical matrix $\mathbf{I}$.

Eigenvalues obtained by scheme (2.72) are the same as the eigenvalues of the transfer matrix $\mathbf{T}$ Equations (2.7). It is due to the fact that they all search for the solutions of Equation (2.1) under boundary conditions (2.3) and (2.4). The scheme suggested in Equation (2.71) differs from the previous ones in the choice of unknown variables. An eigenvector given by Equation (2.72) is in the form of $\begin{pmatrix} \phi_{\mathrm{f}}^{\mathrm{T}} & -\lambda\phi_{\mathrm{f}}^{\mathrm{T}} \end{pmatrix}^{\mathrm{T}}$ and it can be recovered to the form

$$\begin{pmatrix} \phi_{\mathrm{q}} \\ \phi_{\mathrm{f}} \end{pmatrix} = \begin{bmatrix} \mathbf{H}_{\mathrm{LL}} & \mathbf{H}_{\mathrm{LR}} \\ \mathbf{I} & \mathbf{0} \end{bmatrix} \begin{pmatrix} \phi_{\mathrm{f}} \\ -\lambda\phi_{\mathrm{f}} \end{pmatrix} \tag{2.74}$$

which is the eigenvector of the transfer matrix $\mathbf{T}$ associated with the same eigenvalue λ. It can be proved (see E) that if a row vector $\begin{pmatrix} \mathbf{x}_{\mathrm{q}}^{\mathrm{T}} & \mathbf{x}_{\mathrm{f}}^{\mathrm{T}} \end{pmatrix}$ is a left eigenvector obtained from Equation (2.72), then

$$\begin{pmatrix} \theta_{\mathrm{q}}^{\mathrm{T}} & \theta_{\mathrm{f}}^{\mathrm{T}} \end{pmatrix} = \begin{pmatrix} \mathbf{x}_{\mathrm{q}}^{\mathrm{T}} & \bar{\sigma}\mathbf{x}_{\mathrm{f}}^{\mathrm{T}} \end{pmatrix} \tag{2.75}$$

is the left eigenvector of $\mathbf{T}$ associated with the same eigenvalue.

Once the eigenvalues and eigenvectors of $\mathbf{T}$ are obtained and organized in a same way as mentioned in section 2.2.1 to form the wave basis (Λ, Φ and Θ). The process for forced response analysis remains the same as it was outlined in section 2.2.3.

2.3.4 Remarks

The proposed eigenvalue scheme is based on the compliance matrix which can be obtained directly by the employed free-interface CMS methods. Theoretically, we can still obtain the condensed dynamic stiffness matrix by

$$\begin{bmatrix} \mathbf{D}_{\mathrm{LL}} & \mathbf{D}_{\mathrm{LR}} \\ \mathbf{D}_{\mathrm{RL}} & \mathbf{D}_{\mathrm{RR}} \end{bmatrix} = \begin{bmatrix} \mathbf{H}_{\mathrm{LL}} & \mathbf{H}_{\mathrm{LR}} \\ \mathbf{H}_{\mathrm{RL}} & \mathbf{H}_{\mathrm{RR}} \end{bmatrix}^{-1} \tag{2.76}$$

In that way we can still use eigenvalue scheme (2.7). However, an additional matrix inverse is required. It may cause unexpected numerical errors and additional computational cost. For these reasons we recommend Equation (2.72) to analysis the free wave characteristics when free-interface CMS methods are employed.

When full FE model of the unit cell is used, a time-consuming matrix inverse is needed at each frequency to generate matrices for the eigenvalue problem (2.7). While using the proposed reduced models, the matrix inverse is avoided by using Equations (2.48) and (2.51) to calculate the compliance matrix. The retained low-order modes are frequency independent, and so as the terms $\mathbf{H}_{\mathrm{h1}}$ and $\mathbf{H}_{\mathrm{h2}}$ used in the residual calculation. We only need to calculate them once for the free-wave analysis at several frequency points. For these reasons we expect an accelerated calculation of the dispersion relations and the wave basis.

Compared with the reduced model with Craig-Bampton's method, the proposed models with free modes yield same number of waves because the eigenvalue schemes have the

same size. However, the retained number of DOFs with Craig-Bampton's method could not be smaller than the number of DOFs at boundaries. If we built the reduced model by free modes plus the residual effects, the number of retained DOFs have no such restriction. By using more accurate approximation of the residual effects, it is promising to further reduce the size of the retained DOFs.

Higher order of accuracy leads to a smaller size of retained modes (DOFs) but more CPU time is required to recover the higher order residual effects. Compromise has to be made among these factors. This will be discussed in the next section with the application.

2.4 Application: an asymmetrical thin-walled structure

The flow chart of WFEM with the proposed reduced models is outlined in Figure 2.3. It starts from a modal analysis on the full FE model of the unit cell. Few low-order modes of the free unit cell are calculated. The retained modes are determined by the preselected frequency range to be analyzed. The next phase is the recovering of residual flexibility from the retained low-order modes. To do that several techniques can be used and their complexity increases with order of the accuracy. The next step is to solve the eigenvalue problem based on the compliance matrix. Right eigenvalues and eigenvectors are sufficient if the task is to obtain the dispersion curves of the waves. If the task is a forced response analysis then we also need to calculate the left eigenvectors to mitigate numerical error.

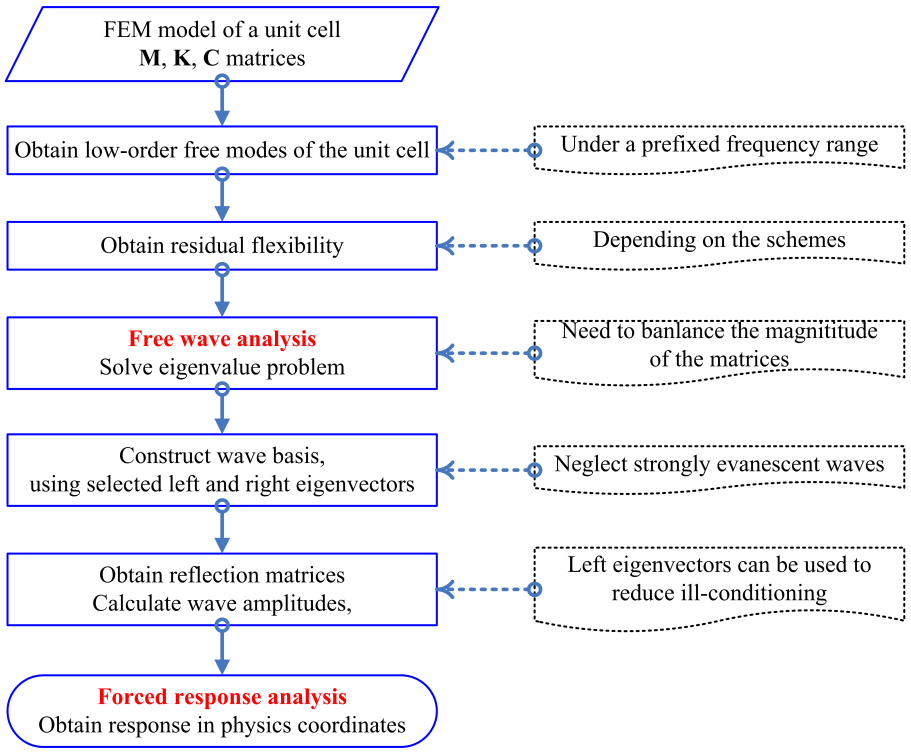

Figure 2.3: Flow chart of the free wave and forced response analysis by WFEM with the proposed reduced model.

The accuracy of the wave basis is mainly determined by two factors concerning the

reduced model. The first one is the number of retained modes and the second one is the accuracy of the approximated residual flexibility. When the analyst is predicting the modal density or designing a spatial signal filter and so on. Dispersion curves of the propagating waves are required, while strong evanescent waves are not of interest. In other cases, for example when the analyst is predicting the power flow injected by the excitation or checking the vibration reduction performance of the periodic structure, forced response analysis in required. Then some strong evanescent waves have to be kept in the wave basis and their accuracy becomes a concern. It remains a question that how the reduced model affects the accuracy of the propagating and evanescent waves respectively. It is also important to discuss how the accuracy of the evanescent waves affects the forced response results.

To verify the proposed reduced models and compare their performances, the binary periodic thin-wall structure studied by [90] is considered here, as shown in Figure 2.4. In their work the dispersion curves of the structure were studied by a Transfer Matrix Method performed on the Euler-Bernoulli beam model including warping effect. The shear center are not coincident to geometric center of the cross-section, so the flexural vibration is coupled with torsional deformation. The structure features complex dispersion curves and it was considered by [88] to test the performance of the reduced model using Craig-Bampton's CMS method.

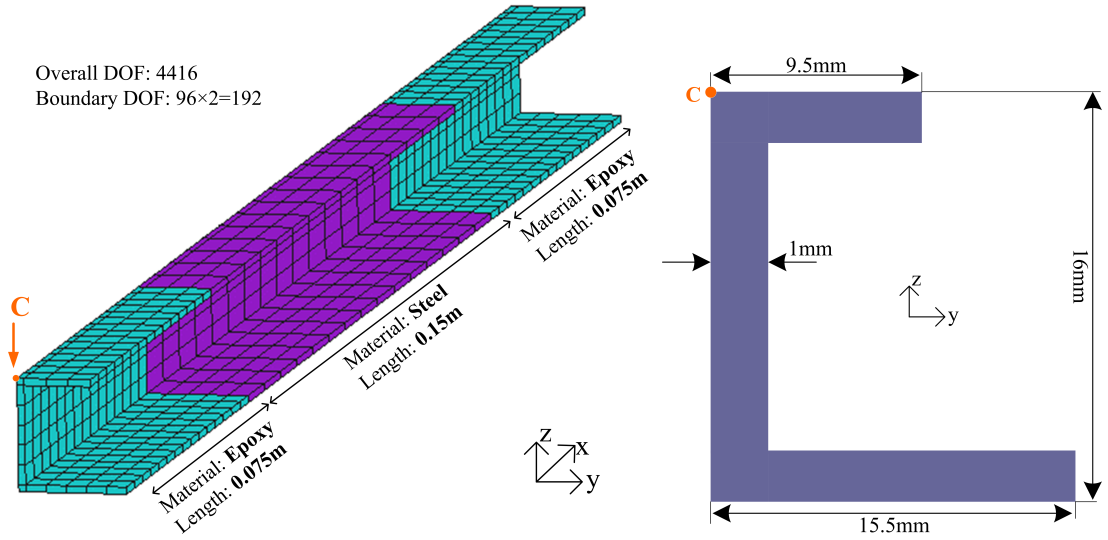

Figure 2.4: The considered thin-wall structure: (a) FE mesh of the unit cell, (b) geometric parameters of the cross-section. Point 'C' refers to the location where the forced response results are compared.

The periodicity is caused by the alternating appearance of two materials (Epoxy and Steel). The Epoxy material used here has Young's Modulus $4.35 \times 10^9\,\mathrm{N/m^2}$, Poisson ratio 0.368 and density $1180\,\mathrm{kg/m^3}$. The steel has Young's Modulus $2.106 \times 10^{10}\,\mathrm{N/m^2}$, Poisson ratio 0.3 and density $7780\,\mathrm{kg/m^3}$. Commercial FE software ANSYS is used to model the unit cell where SOLID185 element is employed. The unit cell has 4416 DOFs

where $2N = 192$ of them locate on the left and right boundaries.

2.5 Results and discussions

2.5.1 Free wave characteristics

The dispersion curves are calculated from 0 Hz to 2000 Hz by the WFEM using full unit cell model (referred to as 'full WFEM' hereafter). Positive-going waves with $0.1 \leq |\lambda| \leq 1$ are selected, including all the propagating waves as well as the evanescent waves in the band gaps. The dispersion curves of the positive and negative- going waves are symmetric to the x-axis, and here we only present the results of positive-going waves. Waves at different frequencies are recognized as several 'types' of wave by Modal Assurance Criterion (MAC) [24]. As shown in Figure 2.5, 4 types of wave are identified and a number was assigned to each of them as shown in Figure 2.5. Several band gaps for certain waves and one band gap (between 1500 Hz and 2000 Hz) for all the waves are observed. Some wave shapes (real part) are shown in Figure 2.6. The results indicate that waves 0, 1, 2, 3 are respectively z-axis flexural, y-axis flexural, torsional and longitudinal waves. From 500 Hz to 1000 Hz, a bifurcation phenomenon occurs between the dispersion curves of the flexural (0) and torsional (2) waves. It is due to the coupling effects between the two deformations. The waves have similar wave shapes around the bifurcation area, as shown in Figure 2.6b and 2.6e.

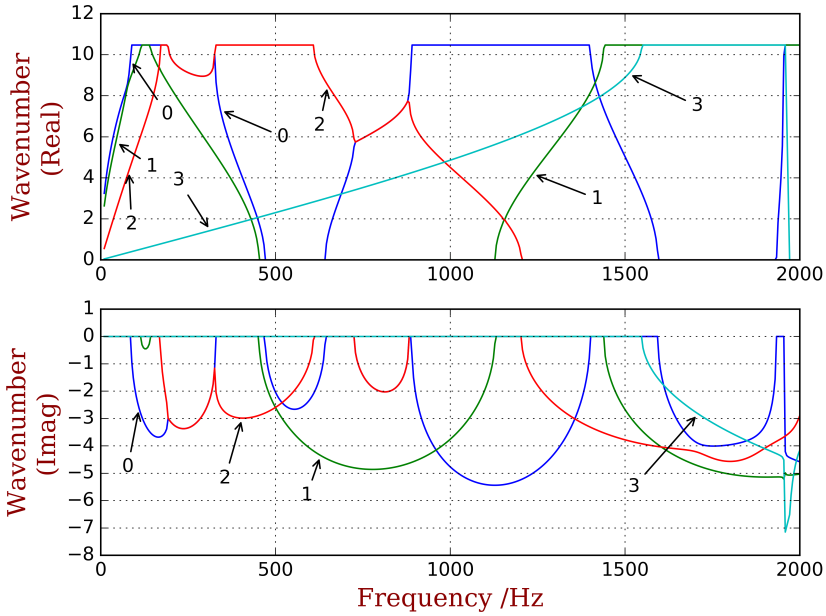

Figure 2.5: Dispersion curves of the waves with $0.1 \leq |\lambda| \leq 1$.

The results in Figure 2.5 are regarded as the benchmark. If the error of the results obtained by a reduced model is lower than 1%, we will regard it as converged (acceptable) results. Let us firstly use reduced model 'Free (0th)' to analyze the structure at same frequency range. Note that 'Free (0th)' is simplest model among the five considered ones.

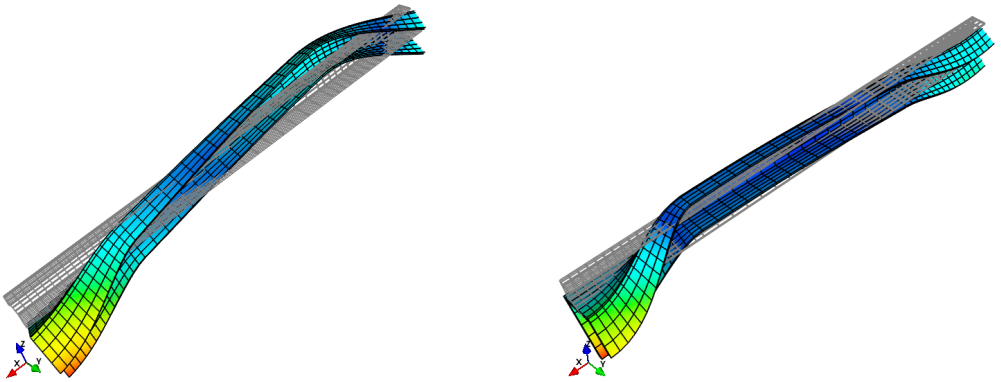

(a) (b)

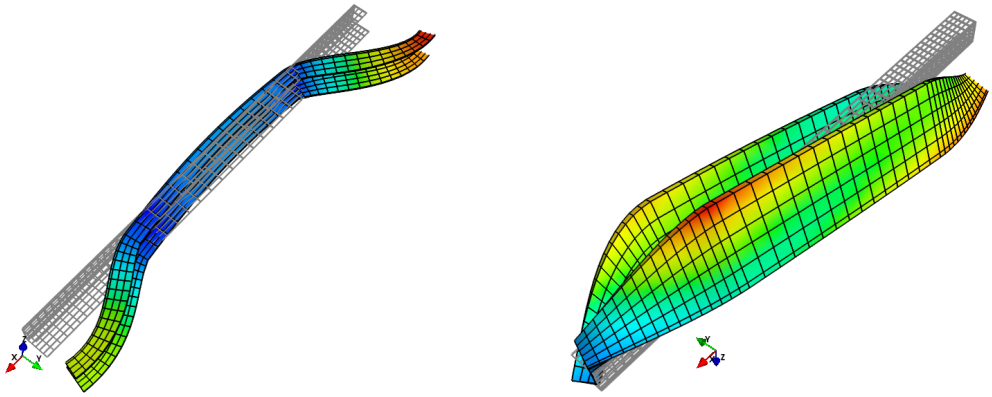

(c) (d)

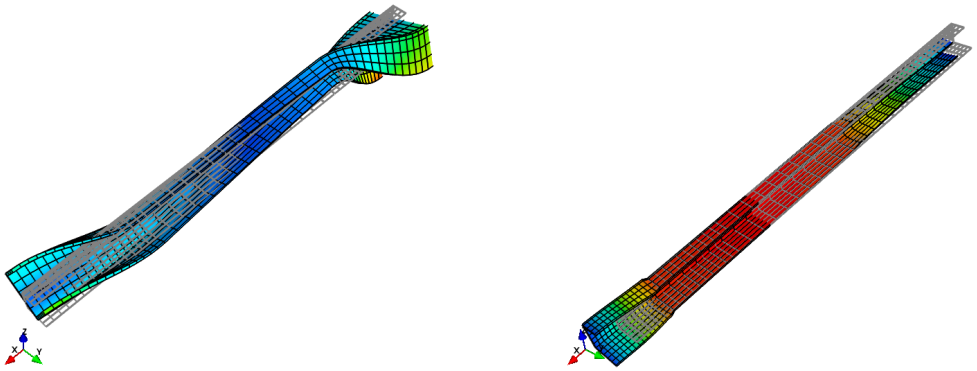

(e) (f)

Figure 2.6: Some propagating wave shapes (real parts) extended to the unit cell: (a) wave 0 at 383 Hz, flexural deformation along z-axis; (b) wave 0 at 703 Hz, coupled flexural-tortional deformation; (c) wave 1 at 1264 Hz, flexural deformation along y-axis; (d) wave 2 at 151 Hz, torsional deformation; (e) wave 2 at 703 Hz, coupled flexural-tortional deformation; (f) wave 3 at 1289 Hz, longitudinal deformation.

However it has the lowest order of accuracy because the residual effects are completely neglected. Figure 2.7 shows the trend of convergence, where the proportions of retained modes in the overall DOFs are 10%, 40%, 80% respectively. It can be seen that when 10% of the modes are retained, the results have significant error all over the frequency range. Even when 40% of the modes are used, it still gives incorrect prediction at many frequencies. The calculation converges when 80% DOFs are kept, namely we need to calculate 3532 modes out of the 4416×4416 eigenvalue problem (Equation (2.43)). The CPU time to obtained the acceptable dispersion curves is given in Figure 2.8. Comparing the 'Free (0th)' and full WFEM, the calculation is approximately accelerated by 60%, and a large proportion of time was spent to calculate the required modes.

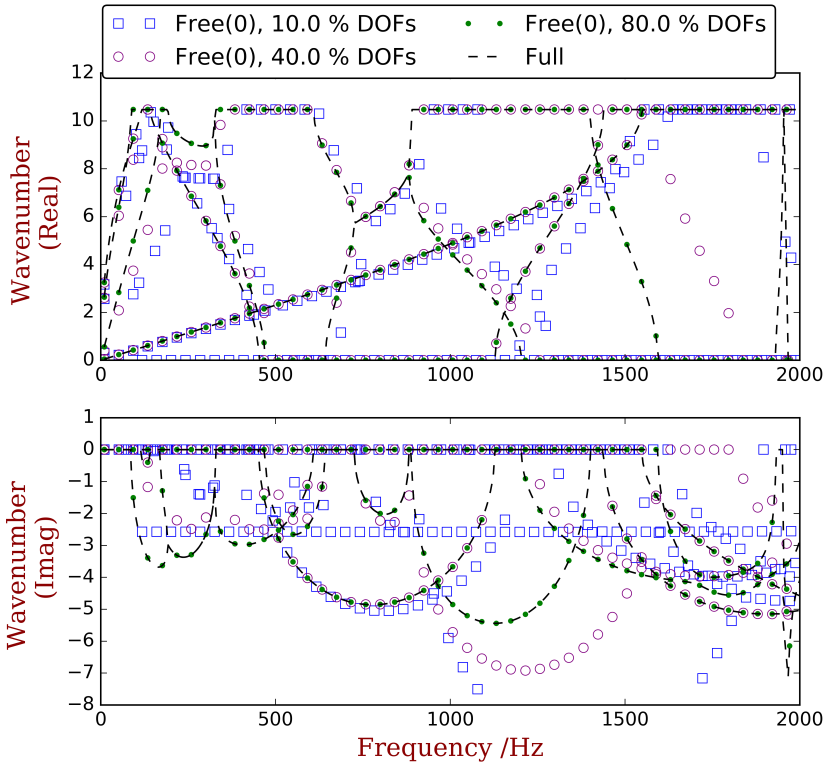

Figure 2.7: Dispersion curves of the waves with $0.1 \leq |\lambda| \leq 1$ when reduced model 'Free (0th)' is employed. The retained DOFs are given by percentage of the overall DOFs of the unit cell.

When the reduced models with residual effects are used, the number of retained modes to converge the calculation are dramatically reduced, as shown in Figure 2.8. Note that the natural frequencies and modal shapes can be partly solved for symmetric real eigenvalue problem shown in Equation (2.43). The reduction of kept modes leads to a saving of computing. Only 51 modes are needed when using 'Free (1st)'. This means the static contribution of the high-order modes is important for the wave characteristics. The trend of convergence of 'Free (1st)' is shown in Figure 2.9a where α_{f} controls the maximum natural frequency of the modes to be kept. Comparing 'Free (0th)' and 'Free (1st)', a large proportion of time is saved when the needed modes are reduced from 3532 to 51. The analysis time of 'Free (1st)' model is less than 10% of 'Free (0th)' model. That is to

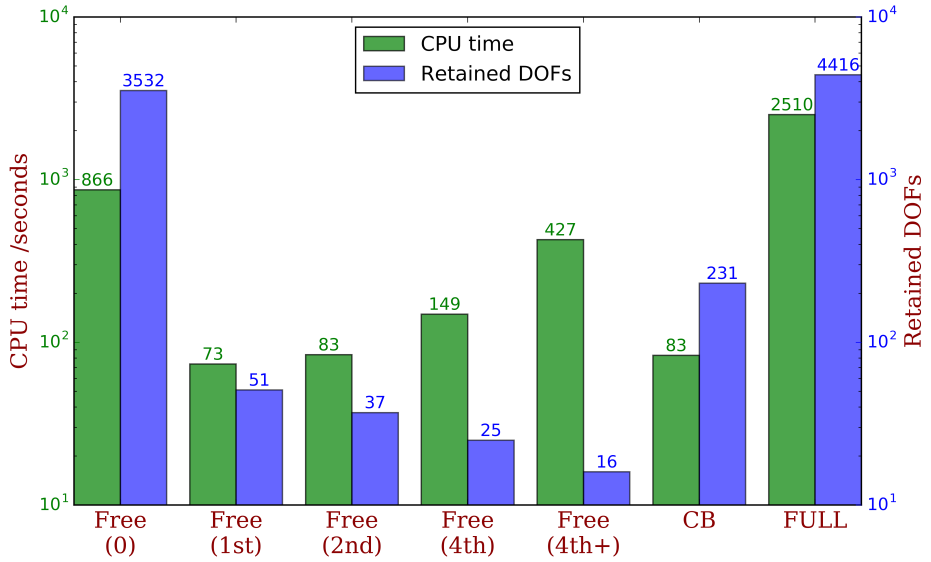

Figure 2.8: CPU time and retained DOFs for different models to obtain the converged results. The data was represented in log scale. The benchmark is the waves with $0.1 \leq |\lambda| \leq 1$ calculated by full WFEM (Figure 2.5), and the error torlerance is 1%.

say, the extra CPU time for the first order residual $\mathbf{H}_{\mathrm{h1}}$ is much shorter than the time saved from the size reduction.

The accuracy increases when using higher order models. Figure 2.9b compares 'Free (1st)', 'Free (2nd)', 'Free (4th)' and 'Free (4th+)' where the retained number of modes are the same. The results tend to converge towards the benchmark. It is interesting to see that a converged result can be achieved by using 'Free (4th+)', with only 16 modes whose natural frequencies are inside the analysis frequency range ($\alpha_{\mathrm{f}} = 1$). This might be useful if one wants to built the unit cell model by experimental data. The 'Free (2nd)' and 'Free (4th)' are not yet converged when $\alpha_{\mathrm{f}} = 1$, but by increasing α_{f} they also approach towards the benchmark. The CPU time and model dimensions are summarized in Figure 2.8 as well. As expected, the model size decreases with the increase of the order of accuracy. When higher order terms of residual effects are considered, additional computation is required. The CPU time increases when using 'Free (2nd)', 'Free (4th)' and 'Free (4th+)' models, because the extra CPU time is greater than the time saved by using less modes.

The differences between the 'Free (4th)' and 'Free (4th+)' depict the gain of accuracy and the extra time consuming caused by the iteration at each frequency point. As a reference, we also employ the reduced model using Craig-Bampton's CMS method (referred to as 'CB' in the figure). Because of the 192 boundary DOFs that are obligatory to be kept, the size is larger than the models built by free modes. In terms of the efficiency, WFEM with Craig-Bampton's CMS method is equivalent to 'Free (2nd)' and slightly slower than 'Free (1st)'.

'Free (1st)' with $\alpha_{\mathrm{f}} = 5$ and 'Free (4th)' with $\alpha_{\mathrm{f}} = 1$ both return converged results for the waves with $0.1 \leq |\lambda| \leq 1$ as shown in Figure 2.9a and 2.9b respectively. However for the strong evanescent waves, none of them matches at all the points with the full

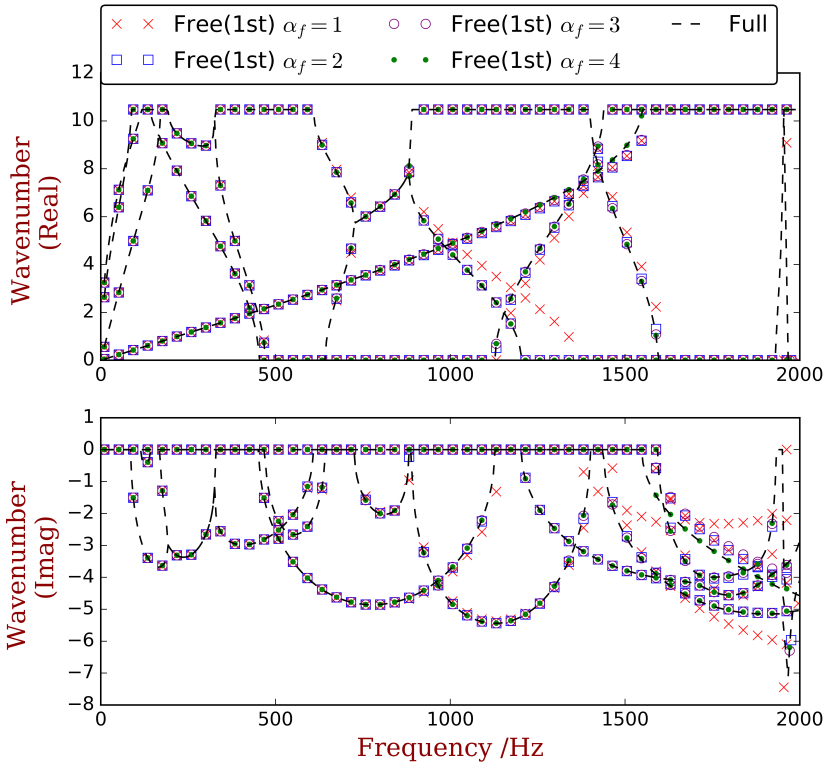

(a)

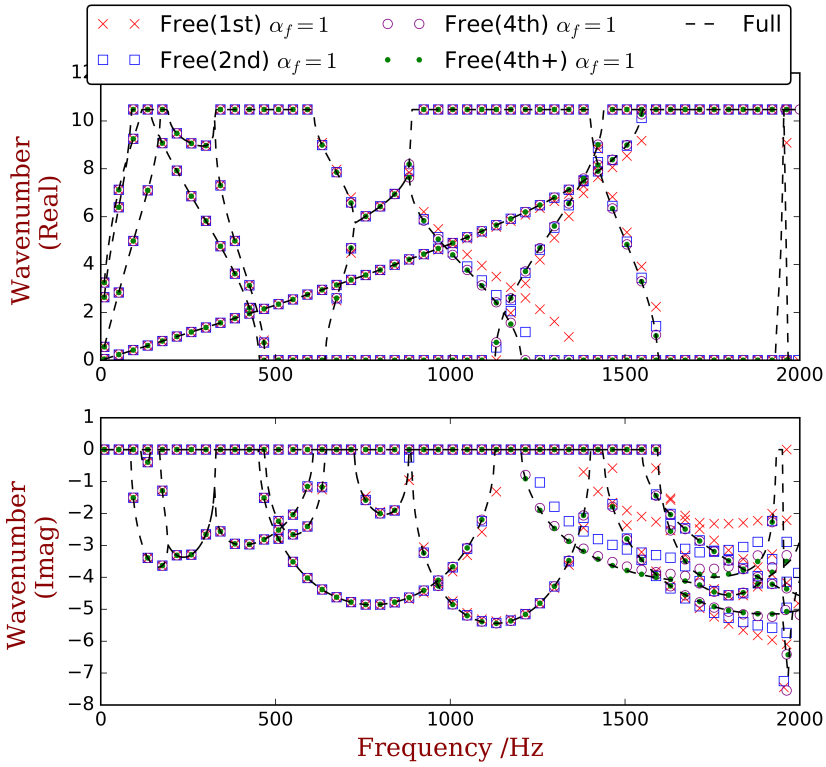

(b)

Figure 2.9: The convergence of the reduced models for the waves with $0.1 \leq |\lambda| \leq 1$: (a) use 'Free (1st)' model while changes the number of retained modes; (b) fix the number of the retained modes and use different models.

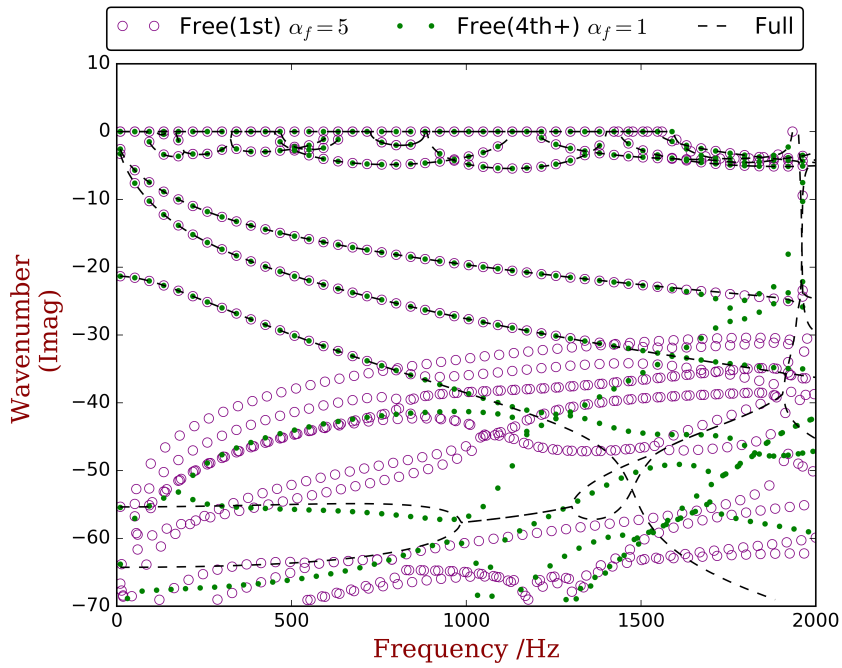

(a)

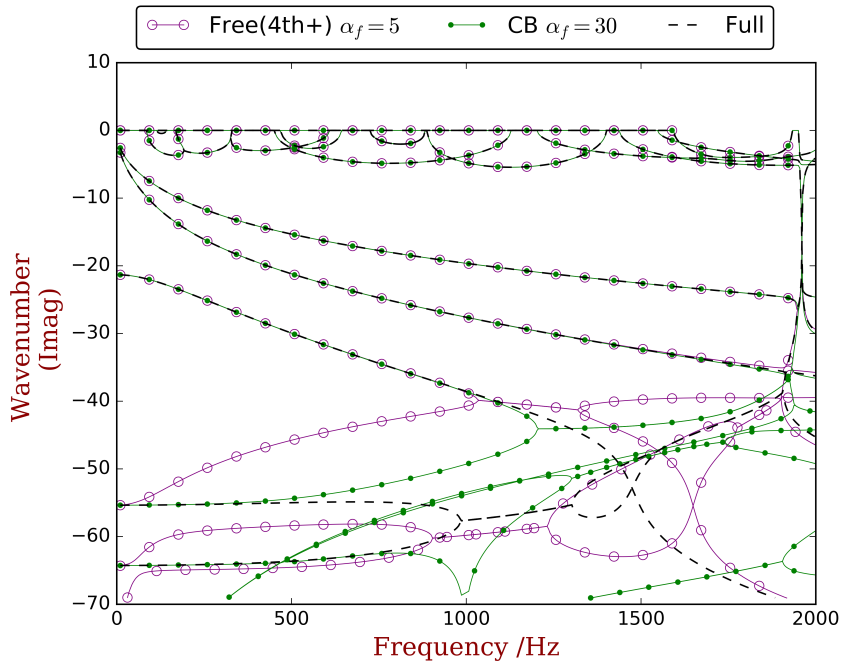

(b)

Figure 2.10: Wavenumbers (Imaginary part) of the waves with $10^{-9} \leq |\lambda| \leq 1$ where strong evanescent waves are included: (a) results obtained by 'Free (1st)' and 'Free (4th+)' which provide converged results for the waves with $0.1 \leq |\lambda| \leq 1$. (b) the converged results achieved by free-interface CMS models and fix-interface CMS models.

WFEM as shown in Figure 2.10a. Waves with $10^{-9} \leq |\lambda| \leq 1$ are selected so that some strong evanescent waves are included. By increasing the retained modes we establish the converged results for the waves with $10^{-9} \leq |\lambda| \leq 1$, as shown in Figure 2.10b. All the reduced models with free modes converge at the same results so we only present 'Free (4th+)' model. The converged results obtained by Craig-Bampton's method are also calculated for comparison. It can be seen that for the waves with $k > -40$, i.e. $10^{-5} \leq |\lambda| \leq 1$, the converged results have good agreements to the full WFEM. While for the waves with stronger spatial attenuation $k < -40$, i.e. $|\lambda| < 10^{-5}$, the converged results are different from each other and neither of them matches with the full WFEM.

Theoretically, the free-interface, fix-interface and the full model should match with each other at any waves by retaining more modes. However, the observed differences at the strong evanescent waves indicate the existence of systematic numerical errors. It is due to the fact that different framework of methods are implemented by different programing codes. As mentioned by [93, 193], the eigenvalue problem itself is prone to ill-conditioning when analyzing strong evanescent waves because their λ is either very large or small. For the strong evanescent waves, it is doubtful that whether we can still regard the results of full WFEM as the most accurate one. Because in full WFEM, the inverse of a large sparse matrix is directly solved as shown in Equation (2.6). Technically, none of the methods can be regarded as the reference for strong evanescent waves since they are sensitive to the numerical error. Nevertheless, we show that for the waves with smaller magnitude of λ, which are generally of interest, the results are not sensitive with this numerical error.

According to Figure 2.10, the differences concerning the wavenumber are apparent. Despite of that, the wave shapes of strong evanescent waves seem to be similar to the wave shapes of full WFEM as shown in Figure 2.11. Figures 2.11a and 2.11c show two strong evanescent wave shapes in Figure 2.10b at 500 Hz obtained by the 'Free (4th+)' model, and Figures 2.11b and 2.11d are obtained from the full WFEM. Visually wave 2.11a ($\Im(k) = -64.6\,\mathrm{m}^{-1}$) is similar to wave 2.11b ($\Im(k) = -63.6\,\mathrm{m}^{-1}$) ; and wave 2.11c ($\Im(k) = -45.7\,\mathrm{m}^{-1}$) is similar to wave 2.11d ($\Im(k) = -55.0\,\mathrm{m}^{-1}$). The MAC between wave 2.11a and wave 2.11b is 0.92; and the MAC between wave 2.11c and wave 2.11d is 0.81. The MAC results verify the visual similarity of the shapes. The accuracy issues of the strong evanescent waves will be further discussed in the next section where the forced response of a periodic structure is analyzed.

2.5.2 Forced response analysis

The considered finite periodic structure has five unit cells as shown in Figure 2.12. The left end is free and the right end is fully clamped. The reflection matrices at the boundaries are shown in Equation (2.41) and Equation (2.41). The harmonic excitation is applied at cross-section 2 on the 'UY' DOF of all the nodes. Full FE model of the whole periodic structure is analyzed in ANSYS and results are used as the benchmark here. The comparisons are made on the Frequency Response Function (FRF) at the C point on the free end, shown also in Figure 2.4. The reduced wave basis is formed by $\lambda_{\mathrm{CR}} = 10^9$ which means that all the waves presented in Figure 2.10b and their negative-going counterparts are included.

Figure 2.13 compares the FRF at 'UY' DOF obtained by 'Free (4th)' and CB model which yield converged results for the retained waves. Structural response is expected also

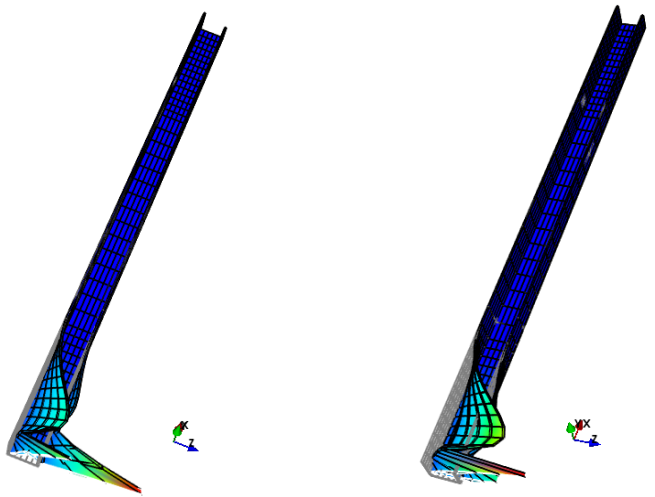

(a) (b)

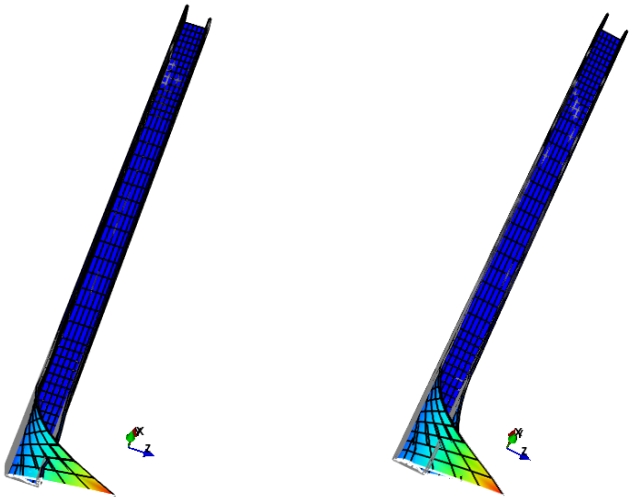

(c) (d)

Figure 2.11: Waveshapes (norm) of some strong evanescent waves in Figure 2.10b at 500 Hz, (a) and (c) are obtained by the converged 'Free (4th+)' model and (b) and (d) are obtained from full unit cell model. The deformation is extended to a unit cell.

at 'UZ' DOF due to the coupling between torsional and flexural deformations, and the results are compared in Figure 2.14. Good agreements can be observed among the methods at both DOFs, despite that the 'Free (4th)' and CB models give different predictions to some strong evanescent waves ($10^{-9} \leq |\lambda| \leq 10^{-5}$) as shown in Figure 2.10.

To explore the contribution of those strong evanescent waves, we run another forced response analysis by 'Free (4th)' model, threshold $\lambda_{\mathrm{CR}} = 10^5$ is used to filter out all

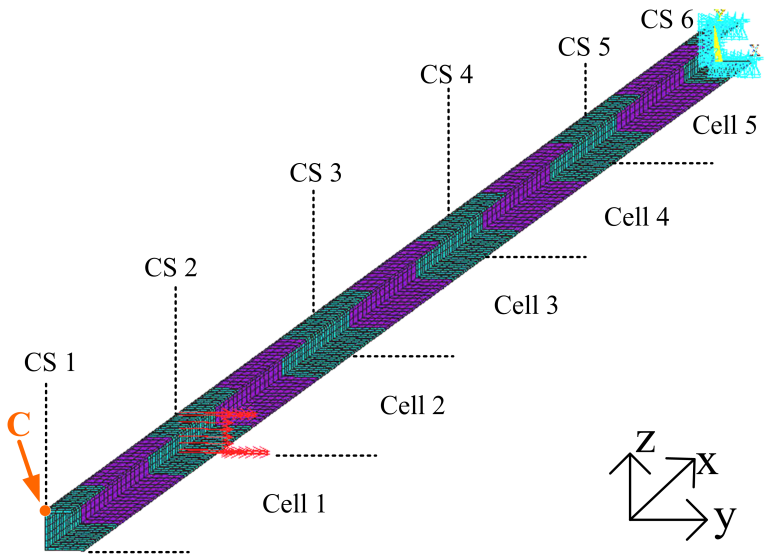

Figure 2.12: Finite element mesh of the periodic strucuture. Point 'C' refers to the location where results are observed.

the 'incorrect' evanescent waves in Figure 2.13. The results are shown in Figure 2.15. Significant errors can be seen, especially around 600 Hz and after 1200 Hz. This indicates that we have to keep some strong evanescent waves even though there are subject to numerical errors.

Evanescent waves appear around the discontinuous points of the structure, such as the excitation points and boundaries. An evanescent wave decays exponentially in space as shown in Figure 2.11, so it has localized influence. The imaginary part of wavenumber defines the speed it vanishes in space. For a positive evanescent wave, let us assume that the deformation inside a unit cell is $u(x) = e^{kx}$, where $k = \ln(\lambda)/\Delta$. It means that a unit deformation becomes $\lambda \ll 1$ at the other end of the cell where $x = \Delta$. The location where the deformation remains 10% is $x_{0.1}(\lambda) = \ln(0.1)/ln(\lambda)\Delta$. For the strong evanescent wave with $\lambda = 10^{-8}$, $x_{0.1}(10^{-8}) = 0.125\Delta$, if we multiply factor 5, then $x_{0.1}(5\times10^{-8}) = 0.137\Delta$, with error less than 10 percent. For a less-decaying evanescent wave, say with $\lambda = 10^{-1}$, $x_{0.1}(10^{-1}) = 1.0\Delta$, but $x_{0.1}(5 \times 10^{-1}) = 3.32\Delta$ indicating an unacceptable error. These rough calculation illustrate that for a strong evanescent wave, whose λ is either very big or small, a relatively big error in λ would not significantly affect the localization of vibration and the wave shape. This remark can be verified by Figure 2.11. On the contrary this conclusion does not stand for less-decaying evanescent waves.

On the other hand, to satisfy the continuous and equilibrium conditions at the singularity points (excitation and boundaries), the wave shapes of those evanescent waves are important because they are created at the singularity points. An insufficient wave basis would then induce an unexpected energy dissipation effects as shown in Figure 2.15 where several vibration peaks are suppressed. This can be understood by the fact that evanescent waves do carry energy [194]. This happens when there is a pair of incident and a reflected evanescent waves.

As discussed, there are some tolerance for strong evanescent waves. With inaccurate

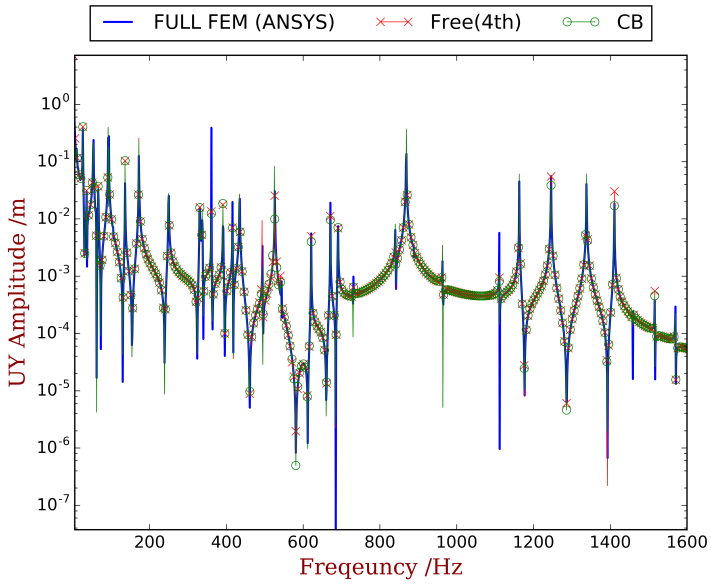

(a)

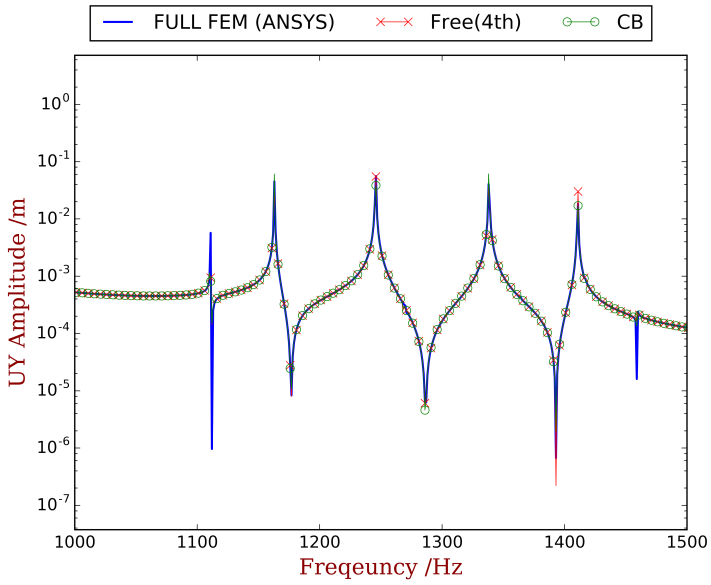

(b)

Figure 2.13: FRF of the 'UY' DOF at point C: (a) from 0 Hz to 1600 Hz; (b) zoom-in. Threshold $\lambda_{\mathrm{CR}} = 10^9$ is used to form the reduced wave basis.

evanescent waves we can still accurately predict forced response. There should exist a critical level, above which the waves should be correct so as to have reasonable results. Figure 2.16 compares the results obtained by 'Free (1st)' model with $\alpha_{\mathrm{f}} = 1$ and $\alpha_{\mathrm{f}} = 5$. As shown in Figure 2.9a, 'Free (1st)' with $\alpha_{\mathrm{f}} = 1$ does not give accurate predictions for waves with $0.1 \leq |\lambda| \leq 1$. While $\alpha_{\mathrm{f}} = 5$ is used, the waves with $0.1 \leq |\lambda| \leq 1$ are converged but a lot of strong evanescent waves still have significant errors, shown in Figure 2.10a. The FRF shown in Figure 2.16 presents a significant error from 1000 Hz when $\alpha_{\mathrm{f}} = 1$ is used. But the results with $\alpha_{\mathrm{f}} = 5$ matches very well. That is to say, once

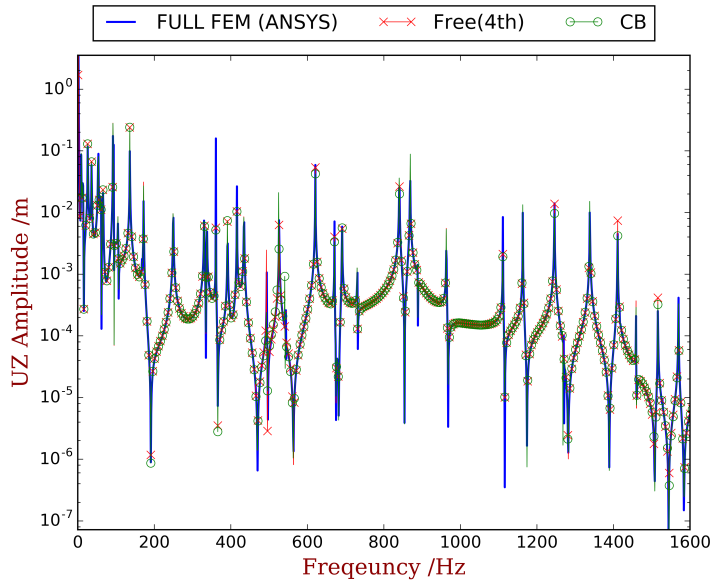

(a)

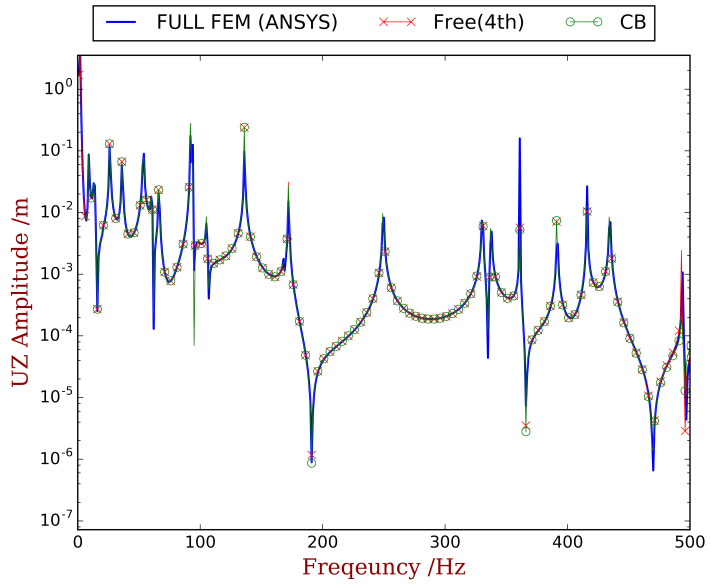

(b)

Figure 2.14: FRF of the 'UZ' DOF at point C: (a) from 0 Hz to 1600 Hz; (b) zoom-in. Threshold $\lambda_{CR} = 10^9$ is used to form the reduced wave basis.

the reduced models can provide converged results concerning the propagating waves and the evanescent waves in the band gap, they can be used to calculate the forced response.

2.6 Conclusions

In this chapter, we demonstrate the use of reduced unit cell models built by free modes plus residual effects with the Wave and Finite Element Method. It can be applied for both

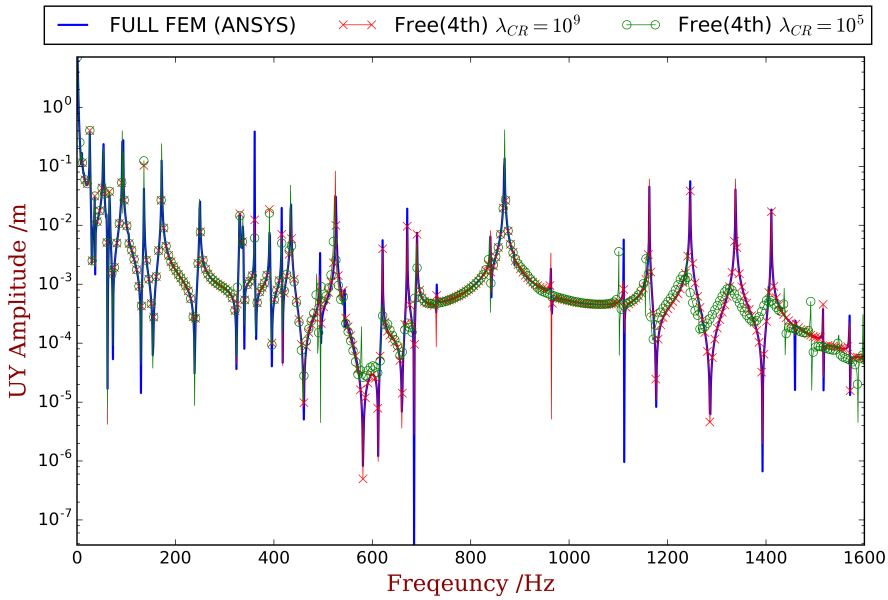

Figure 2.15: Comprasiron of FRF obtained by different number of retained waves to construct the wave basis.

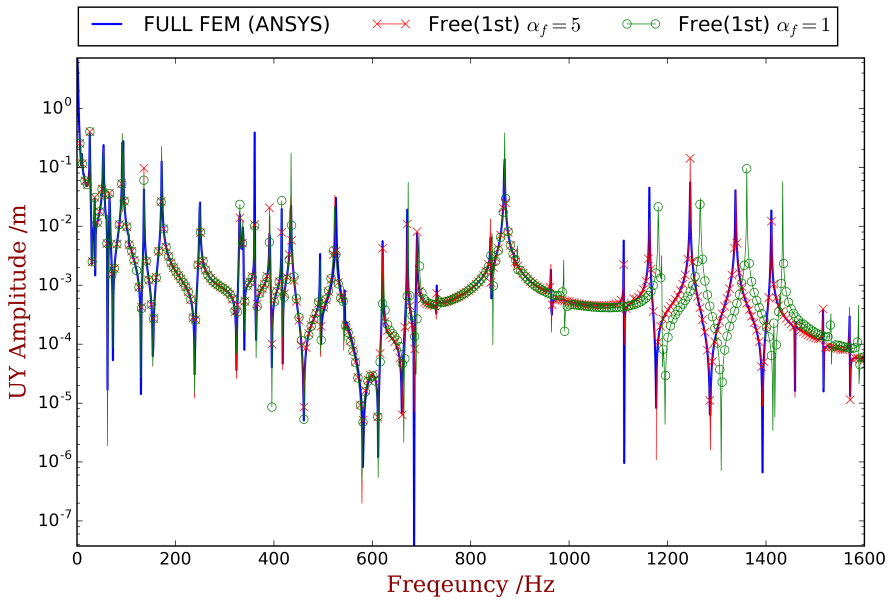

Figure 2.16: Comprasiron of FRF obtained by different number of retained modes in the reduced model.

free-wave and forced response analysis. A new eigenvalue scheme based on the compliance matrix is proposed to obtain the wavenumbers and the left and right wave shapes.

An asymmetric thin-wall structure is considered as the application. Several existing free-interface substructure strategies are implemented and compared. Good agreements with the full WFEM can be achieved when the parameters of the reduced models are appropriately chosen. We show that residual effects plays an important role concerning

the retained DOFs and CPU time. Without considering the residual flexibility (Hou's method [184]), a large proportion of the modes (80%) has to be kept though the calculation is accelerated to some extent (reduced by 60%). When residual effects are taking into account, the retained DOFs are dramatically reduced. For example when Rubin's method [186] is applied, 37 modes are retained to have the results with same accuracy. Especially when the exact substructure method [187] is used, only 16 modes are required. The natural frequencies of these 16 modes are lower than the maximum analyzing frequency. This can be an advantage when the model is built from the experimental data. In terms of the CPU time, the most efficient model is the one using MacNeal's method [185], in comparison with the full WFEM model, only 3% of the CPU time is required. As a reference, the reduced model using Craig-Bampton's fix-interface substructure method [183] is also implemented, and the efficiency is equivalent to Rubin's method. Due to the fact that all the boundary DOFs have to be kept, the Craig-Bampton's method retains more DOFs than most of the free-interface methods.

For the propagating and less-decaying waves ($10^{-5} < |\lambda| < 10^{5}$ for the considered case), the WFEM with a reduced model converges to the full WFEM method when more modes are retained. For reduced model with higher order of accuracy, the convergence can be achieved by using less modes. For the strong evanescent waves, the reduced models will also converge. Owing to some systematic numerical errors, the final results concerning strong evanescent waves of free-interface methods, the Craig-Bampton's method and the full WFEM are different. We show that the errors do not have significant influence of the localization of vibration and the wave shapes.

Forced response of the periodic thin-wall structure is analyzed by WFEM with reduced models. The reduced wave basis is used to mitigate numerical errors. We show that some strong evanescent waves have to be kept even though there are some inaccuracies in the wavenumbers, and the results still have good agreements to the full finite element model. Directly truncating those strong evanescent waves induces significant errors. This is due to the fact that sufficient wave shapes has to be kept in the wave basis so as to approximately satisfy the constrains on the boundaries.

Overall, for the free-wave analysis we recommend MacNeal's reduction method 'Free (1st)' in terms of efficiency, and the exact substructure method 'Free (4th+)' in terms of the extent of reduction. The use of reduced models should provide converged propagating and band gap waves in the reduced wave basis, so as to have a acceptable prediction for the forced response.

Chapter 3

A hybrid FEM-WFEM approach for energy flow prediction in built-up structures

Abstract: A periodic structure can be designed to have the desired dynamic features for vibration control or wave filtering. In practice the designed periodic structure is more likely to be used as a substructure. It will be assembled into an existing complex structural system which is not necessarily periodic. The built-up structure therefore has both non-periodic parts and periodic parts. It remains a question *whether the designed substructure can still perform as it was analyzed in isolation.* For example, *does a band gap in the periodic substructure directly link to a low-vibration and low-energy-flow frequency range of the built-up structure?* To answer these questions, in this chapter we present a rapid and accurate numerical tool to explore the vibration and energy flow for such built-up structures. The non-periodic part is modeled by FEM while the periodic substructures are described by WFEM. Different parts are connected in a multi-scale manner such that the final dimension of the problem are largely reduced. Since piezoelectric shunts are often used in the periodic substructures to obtain the desired wave characteristics, a new reduced model is proposed to accelerate the WFEM analysis. Some preliminary discussions concerning the energy flow in built-up structures are presented.

Contents

3.1 Introduction

It is well known that periodic structures feature the frequency band gaps in which certain propagating waves become evanescent. A periodic structure tends to have less natural modes in the band gaps, therefore it probably would have lower response [195]. This inspires the idea of building a periodic substructure such that the frequency locations of band gaps cover the excitation frequencies. This idea has been examined in numerous literature, as reported by Ref. [123, 196] on plate-like structures and Ref. [197, 198] on 1D waveguides. In most of the literature [110, 123, 196, 199] where band gaps are used, finite periodic structures were considered in isolation. They have shown that the structural response inside the band gaps are lower than in the propagating.

However, from a more practical point of view, the study needs to be further extended for the following reasons:

1. It might be very hard to have pure periodic structures in practice due to the unavoidable non-periodic geometric or material complexity. Let us consider integrating a periodic substructure in a car chassis to control the energy injected from the engine, shown in figure 3.1. The geometric and material properties near the excitation (the engine) are non-periodic and can not be largely modified. Though periodic substructure can be designed on the subsequent frame, but the overall system (the chassis) is not pure periodic.

2. 'how many unit cells are sufficient for the vibration reduction of the host system?' remains a question which could not be directly answered by the free wave characteristics summarized in the dispersion curves. Instead, the question can be addressed more intuitively by evaluating the forced response and energy flow in the built-up structure.

3. It is more appropriate to examine the performance of periodic waveguide in an open system context in terms of energy flow. It is due to the fact that the Bragg band gaps are generally mid- and high frequency phenomena where the waves and energy can be transmitted through the boundaries.

The mechanical model considered in this chapter can be used to target these problems. As shown in figure 3.2, the considered structural system consists of: 1) **near-field** part which is subject to external excitation; 2) **far-field** part which is located after the intentionally designed periodic substructure, and at mid- and high frequencies can be regarded as an infinite and uniform media; and 3) **periodic substructure** located between near-field and far-field (with several unit cells).

The proposed assembled model is not only for a more realistic representation of the engineering applications, but also for the full investigation of the performance of the designed periodic substructure in terms of wave and power diffusion. In the proposed model, the designed periodic substructure can be evaluated in a situation that it works as a part of an overall system, rather than to be individually evaluated. The designed periodic substructure changes the nature of the whole system, hence modifies the input impedance as well. Then the interaction between near-field part and the periodic substructure should be fully considered rather than to be simplified as injected waves or applied forces. Similarly,

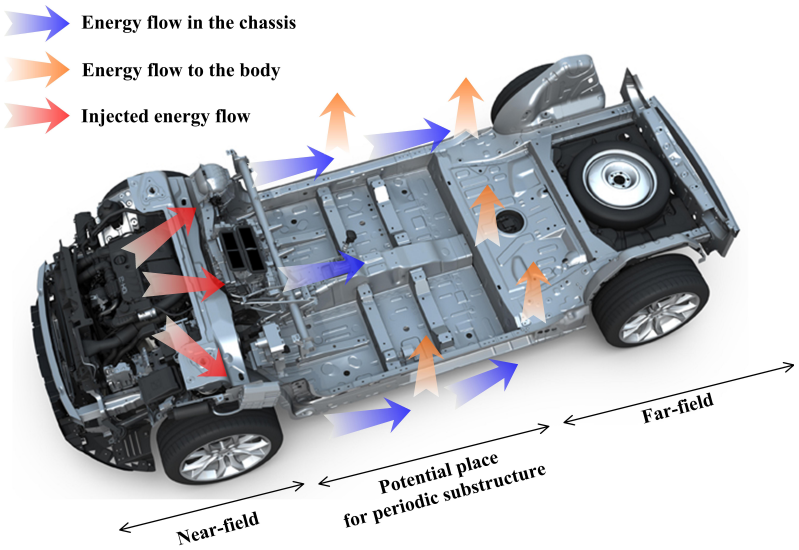

Figure 3.1: Illustration of energy flow in a car chassis.

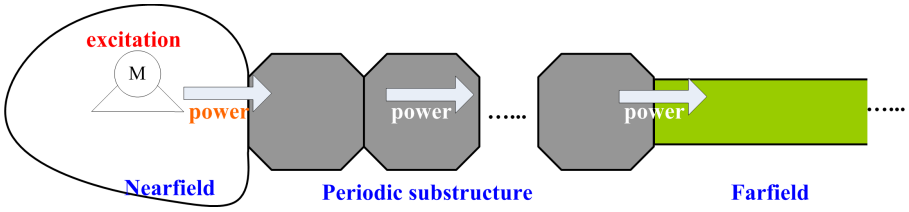

Figure 3.2: The proposed mechanical model for evaluating a periodic substructure.

the far-field also affects the overall dynamics indirectly. For instance, damping in either the periodic substructure or the far-field part will lead some dissipation to the near-field.

In this chapter, a FEM-WFEM hybrid method is developed to determine the forced response and energy flow in the proposed assembled structures. The periodic substructure and far-field part in figure 3.2 are regarded as waveguides that are sequentially connected to the near-field part, as shown in figure 3.3. The near-field part is modeled by FEM to handle the non-periodic complexity, while the waveguides are modeled by WFEM to speed up the computation. Contrarily to the aforementioned studies, the DOFs of the FE modeled near-field part will be kept while the DOFs of waveguides will be eliminated eventually. The response and energy flow of waveguides can be obtained by post-processing. Though considering several few waveguides are enough for the model discussed here, the method itself has the ability to handle the structures with an arbitrary number of waveguides.

Note that the idea of using WFEM and FEM in combine under a substructure framework has been explored by others as well. Duhamel [102] applied WFEM to simulate the forced response of structures with multiple periodic substructures rigidly jointed. Each substructure was modeled individually by WFEM so as to write the DSM in terms of the interconnected Degree-of-freedom (DOF). Then their DSM can be assembled to generate the overall DSM. Huang et al. [110, 111] considered the structures made by two uniform waveguides connected with a single piezoelectric scatterer, where the scatterer

was modeled by FEM so as to evaluate the corresponding diffusion and reflection matrices. Zhou et al. [200] studied the wave propagation in cylindrical pipes with local inhomogeneities, where FEM was used to model the inhomogeneous parts and WFEM was used to model the homogeneous parts. A more general situation was considered by Renno et al. [121, 122] by which the forced response of an arbitrary number of periodic substructures connected by elastic joints can be simulated. In their work the joints were firstly modeled by FEM, then deduced into the constrained relations relating the wave amplitudes of adjacent waveguides. However non of these strategies can be directly used in our case.

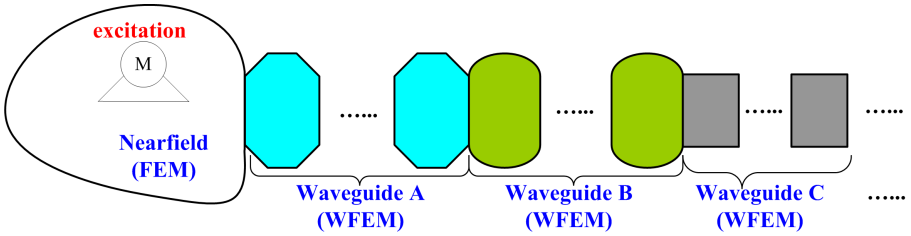

Figure 3.3: Illustration of the proposed modeling strategy.

The FEM-WFEM approach itself has no limitations on the configuration of periodic substructures, nor on the implementation of WFEM. Giving the complexity of the overall structure, it would be helpful to employ reduced models to the WFEM so as to accelerate the calculation and mitigate the ill-conditioning. However, the reduced models mentions in Chapter 2 are not applicable when there are local dampers or piezoelectric patches with electric circuits in the unit cell. In such cases the damping matrix or the dynamic stiffness matrix can not be diagonalized by the undamped modal shapes.

In this chapter, a new reduced model of WFEM is proposed for unit cell with local damper or piezoelectric shunts. This, hence, accelerates the computation of the wave basis. Then the FEM-WFEM hybrid method is presented. It is firstly validated by analytical solutions of an infinite beam. The results show that the wave propagation and the energy flow characteristics of the infinite structure are precisely captured. Then it is validated by a finite assembled piezoelectric structure in a wide frequency band. Finally an application of the proposed method is given, where a built-up structure incorporating piezoelectric composite between the excited substructure and the external parts is considered. The results reveal the complexity of such systems therefore attest the idea of considering a more complete model.

3.2 WFEM for piezoelectric structures

When piezoelectric materials and shunted circuits are involved in the unit cell, the electric DOFs can be treated as part of the internal DOFs, so that the procedure described in section 2.2.1 can still be applied. However the problem arises only when one applies the reduced models mentioned in chapter 2. Here we propose a new reduced model for WFEM to analyze structures with periodically distributed piezoelectric materials shunted with identical electric circuits. First we briefly outline the WFEM procedure specifically for piezoelectric substructures. Then the reduced model is presented and discussed.

3.2.1 Using full unit cell model

For a periodic piezoelectric structure as it is shown in Figure 3.4, we firstly take a unit cell and model it by any existed FEM package by using adaptive piezoelectric elements [49]. When analyzing the free waves, external loads are not considered, and the dynamic equations of the ith unit cell write

$$\mathbf{M}\begin{pmatrix}\ddot{\mathbf{q}}_{\mathrm{L}}\\ \ddot{\mathbf{q}}_{\mathrm{R}}\\ \ddot{\mathbf{q}}_{\mathrm{I}}\\ \ddot{\mathbf{q}}_{\mathrm{E}}\end{pmatrix}+\mathbf{C}\begin{pmatrix}\dot{\mathbf{q}}_{\mathrm{L}}\\ \dot{\mathbf{q}}_{\mathrm{R}}\\ \dot{\mathbf{q}}_{\mathrm{I}}\\ \dot{\mathbf{q}}_{\mathrm{E}}\end{pmatrix}+\mathbf{K}\begin{pmatrix}\mathbf{q}_{\mathrm{L}}\\ \mathbf{q}_{\mathrm{R}}\\ \mathbf{q}_{\mathrm{I}}\\ \mathbf{q}_{\mathrm{E}}\end{pmatrix}=\begin{pmatrix}\mathbf{f}_{\mathrm{L}}\\ \mathbf{f}_{\mathrm{R}}\\ \mathbf{0}\\ \mathbf{f}_{\mathrm{E}}\end{pmatrix} \tag{3.1}$$

where $\mathbf{q}$ is the generalized displacement array; $\mathbf{f}$ is the generalized force array; $\mathbf{M}$, $\mathbf{C}$ and $\mathbf{K}$ refer to the mass, damping and generalized stiffness matrices respectively. Subscripts L, R, I and E respectively denote the left-side, right-side, internal mechanical and the electric voltage DOFs as illustrated in Figure 3.4. Note that $\mathbf{f}_{\mathrm{E}}$ refers to the charges stored at the electrodes and $\mathbf{q}_{\mathrm{E}}$ refers to the voltage between electrodes. An additional equation should be given to describe the shunted electric circuits, it writes

$$\mathbf{f}_{\mathrm{E}}=-\mathbf{Y}\mathbf{q}_{\mathrm{E}} \tag{3.2}$$

where $\mathbf{Y}$ is the external electric admittance between voltages and charges. If the piezoelectric patches are not inter-connected in a unit cell, the admittance is a diagonal matrix, namely $\mathbf{Y}=\mathrm{diag}(Y_i)$. If an electrode is open, then $Y_i=0$; if an electrode is shorted, then $Y_i=+\infty$. Note that $\mathbf{Y}$ is likely frequency-dependent, for example when a Resistor-Inductor-Capacitor circuit is shunted, $Y_i=\left(-\omega^2 L_{\mathrm{E}}+j\omega R_{\mathrm{E}}+1/C_{\mathrm{E}}\right)^{-1}$. For this reason we denote it as $\mathbf{Y}(\omega)$ as well.

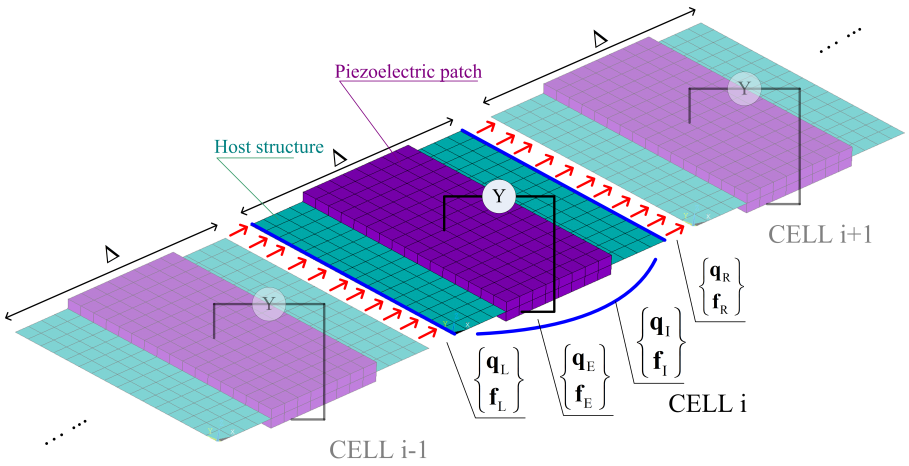

Figure 3.4: Illustration of the unit cells in a piezoelectric periodic structure.

Specifically, the generalized stiffness matrix writes

$$\mathbf{K}=\begin{bmatrix}\mathbf{K}_{\mathrm{LL}} & \mathbf{K}_{\mathrm{LR}} & \mathbf{K}_{\mathrm{LI}} & \mathbf{H}_{\mathrm{LE}}\\ \mathbf{K}_{\mathrm{LR}}^{\mathrm{T}} & \mathbf{K}_{\mathrm{RR}} & \mathbf{K}_{\mathrm{RI}} & \mathbf{H}_{\mathrm{RE}}\\ \mathbf{K}_{\mathrm{LI}}^{\mathrm{T}} & \mathbf{K}_{\mathrm{RI}}^{\mathrm{T}} & \mathbf{K}_{\mathrm{II}} & \mathbf{H}_{\mathrm{IE}}\\ \mathbf{H}_{\mathrm{LE}}^{\mathrm{T}} & \mathbf{H}_{\mathrm{RE}}^{\mathrm{T}} & \mathbf{H}_{\mathrm{IE}}^{\mathrm{T}} & \mathbf{C}_{\mathrm{p}}\end{bmatrix} \tag{3.3}$$

where $\mathbf{H}$ refers the piezoelectric terms and $\mathbf{C}_\mathrm{p}$ is the intrinsic capacitance matrix. The generalized mass matrix writes

$$\mathbf{M} = \begin{bmatrix} \mathbf{M}_{\mathrm{LL}} & \mathbf{M}_{\mathrm{LR}} & \mathbf{M}_{\mathrm{LI}} & \mathbf{0} \\ \mathbf{M}_{\mathrm{LR}}^{\mathrm{T}} & \mathbf{M}_{\mathrm{RR}} & \mathbf{M}_{\mathrm{RI}} & \mathbf{0} \\ \mathbf{M}_{\mathrm{LI}}^{\mathrm{T}} & \mathbf{M}_{\mathrm{RI}}^{\mathrm{T}} & \mathbf{M}_{\mathrm{II}} & \mathbf{0} \\ \mathbf{0} & \mathbf{0} & \mathbf{0} & \mathbf{0} \end{bmatrix} \tag{3.4}$$

Introducing Equation (3.2) into (3.1) and consider the harmonic motion. The dynamic stiffness matrix at frequency ω writes

$$\tilde{\mathbf{D}} = -\omega^2\mathbf{M} + j\omega\mathbf{C} + \mathbf{K} + \mathbf{Y}_\mathrm{g}(\omega) \tag{3.5}$$

where

$$\mathbf{Y}_\mathrm{g} = \begin{bmatrix} \mathbf{0} & \mathbf{0} & \mathbf{0} & \mathbf{0} \\ \mathbf{0} & \mathbf{0} & \mathbf{0} & \mathbf{0} \\ \mathbf{0} & \mathbf{0} & \mathbf{0} & \mathbf{0} \\ \mathbf{0} & \mathbf{0} & \mathbf{0} & \mathbf{Y} \end{bmatrix} \tag{3.6}$$

Eliminating all the internal DOFs ($\mathbf{q}_\mathrm{E}$ and $\mathbf{q}_\mathrm{I}$); it gives the condensed dynamic stiffness matrix of the unit cell

$$\begin{bmatrix} \mathbf{D}_{\mathrm{LL}} & \mathbf{D}_{\mathrm{LR}} \\ \mathbf{D}_{\mathrm{RL}} & \mathbf{D}_{\mathrm{RR}} \end{bmatrix} \begin{pmatrix} \mathbf{q}_\mathrm{L} \\ \mathbf{q}_\mathrm{R} \end{pmatrix} = \begin{pmatrix} \mathbf{f}_\mathrm{L} \\ \mathbf{f}_\mathrm{R} \end{pmatrix} \tag{3.7}$$

where

$$\begin{bmatrix} \mathbf{D}_{\mathrm{LL}} & \mathbf{D}_{\mathrm{LR}} \\ \mathbf{D}_{\mathrm{RL}} & \mathbf{D}_{\mathrm{RR}} \end{bmatrix} = \begin{bmatrix} \tilde{\mathbf{D}}_{\mathrm{LL}} & \tilde{\mathbf{D}}_{\mathrm{LR}} \\ \tilde{\mathbf{D}}_{\mathrm{RL}} & \tilde{\mathbf{D}}_{\mathrm{RR}} \end{bmatrix} + \begin{bmatrix} \tilde{\mathbf{D}}_{\mathrm{LI}} & \tilde{\mathbf{D}}_{\mathrm{LE}} \\ \tilde{\mathbf{D}}_{\mathrm{RI}} & \tilde{\mathbf{D}}_{\mathrm{RE}} \end{bmatrix} \begin{bmatrix} \tilde{\mathbf{D}}_{\mathrm{II}} & \tilde{\mathbf{D}}_{\mathrm{IE}} \\ \tilde{\mathbf{D}}_{\mathrm{EI}} & \tilde{\mathbf{D}}_{\mathrm{EE}} \end{bmatrix}^{-1} \begin{bmatrix} \tilde{\mathbf{D}}_{\mathrm{IL}} & \tilde{\mathbf{D}}_{\mathrm{IR}} \\ \tilde{\mathbf{D}}_{\mathrm{EL}} & \tilde{\mathbf{D}}_{\mathrm{ER}} \end{bmatrix} \tag{3.8}$$

Introducing the periodic boundary conditions (Equations (2.4) and (2.3)) into Equation (3.7), and eliminating $\mathbf{f}_\mathrm{L}$ and $\mathbf{f}_\mathrm{R}$, it comes to the eigenvalue problem

$$\left(\begin{bmatrix} \mathbf{0} & \sigma\mathbf{I} \\ -\mathbf{D}_{\mathrm{RL}} & -\mathbf{D}_{\mathrm{RR}} \end{bmatrix} - \lambda \begin{bmatrix} \sigma\mathbf{I} & \mathbf{0} \\ \mathbf{D}_{\mathrm{LL}} & \mathbf{D}_{\mathrm{LR}} \end{bmatrix} \right) \begin{pmatrix} \mathbf{q}_\mathrm{L} \\ \mathbf{q}_\mathrm{R} \end{pmatrix} = \mathbf{0} \tag{3.9}$$

Factor σ is then determined by the 2nd norm of the $\mathbf{D}_{\mathrm{RR}}$ matrix

$$\sigma = \frac{\|\mathbf{D}_{\mathrm{RR}}\|_\mathbf{2}}{N^2} \tag{3.10}$$

where N is the count of columns of matrix $\mathbf{D}_{\mathrm{RR}}$ and also the count of DOFs at the left or right cross-section. Having introduced the factor σ, the conditioning number of matrices becomes smaller. Hence the eigensolutions are more efficiently and accurately computed.

Equation (3.9) yield the same eigenvalues of the transfer matrix. However, the eigenvectors given by Equation (3.9) are in the form of $\begin{pmatrix} \phi_\mathrm{q}^\mathrm{T} & \lambda\phi_\mathrm{q}^\mathrm{T} \end{pmatrix}^\mathrm{T}$. By the statement

$$\phi_\mathrm{f} = \mathbf{D}_{\mathrm{LL}}\phi_\mathrm{q} + \lambda\mathbf{D}_{\mathrm{LR}}\phi_\mathrm{q} \tag{3.11}$$

included in Equation (3.7), the eigenvectors of Equation (3.9) can be post-processed to the form $\phi = \begin{pmatrix} \phi_\mathrm{q}^\mathrm{T} & \phi_\mathrm{f}^\mathrm{T} \end{pmatrix}^\mathrm{T}$ which are also the eigenvectors of the transfer matrix.

Concerning the left eigenvectors, while scheme (3.9) is applied, an adjustment is needed. If a row array $\begin{pmatrix} \hat{\theta}_{\mathrm{q},i} & \hat{\theta}_{\mathrm{f},i} \end{pmatrix}$ is the left eigenvector obtained from Equation (3.9), then

$$\begin{pmatrix} \theta_{\mathrm{q},i} & \theta_{\mathrm{f},i} \end{pmatrix} = \begin{pmatrix} \sigma\hat{\theta}_{\mathrm{q},i} & \hat{\theta}_{\mathrm{f},i} \end{pmatrix} \tag{3.12}$$

is the left eigenvector of the transfer matrix (see Appendix D for the demonstration). Equation (3.9) is applicable for WFEM for all the applications, and it can be used to replace (2.7).

3.2.2 Reduced model

Note that the reduce model proposed by Zhou et al. [88] (see section 2.2.2) is not applicable in this situation. In their work, the Craig-Bampton method for modal reduction was employed on all the internal DOFs. The admittance matrix $\mathbf{Y}_{\mathrm{g}}$ in Equation (3.5) can not be diagonalized by the undamped modal shapes. Consequently the modal coordinates are coupled with each other, then simply truncating the modes with higher natural frequencies might induce unexpected errors.

For these reasons, we modify the reduced model using Craig-Bampton method such that only $\mathbf{q}_{\mathrm{I}}$ is transformed into the modal space. The coordinates transformation is defined by

$$\begin{pmatrix} \mathbf{q}_{\mathrm{L}} \\ \mathbf{q}_{\mathrm{R}} \\ \mathbf{q}_{\mathrm{I}} \\ \mathbf{q}_{\mathrm{E}} \end{pmatrix} = \begin{bmatrix} \mathbf{I} & \mathbf{0} & \mathbf{0} & \mathbf{0} \\ \mathbf{0} & \mathbf{I} & \mathbf{0} & \mathbf{0} \\ -\mathbf{K}_{\mathrm{II}}^{-1}\mathbf{K}_{\mathrm{IL}} & -\mathbf{K}_{\mathrm{II}}^{-1}\mathbf{K}_{\mathrm{IR}} & \Psi & -\mathbf{K}_{\mathrm{II}}^{-1}\mathbf{H}_{\mathrm{IE}} \\ \mathbf{0} & \mathbf{0} & \mathbf{0} & \mathbf{I} \end{bmatrix} \begin{pmatrix} \mathbf{q}_{\mathrm{L}} \\ \mathbf{q}_{\mathrm{R}} \\ \mathbf{y} \\ \mathbf{q}_{\mathrm{E}} \end{pmatrix} = \mathbf{B} \begin{pmatrix} \mathbf{q}_{\mathrm{L}} \\ \mathbf{q}_{\mathrm{R}} \\ \mathbf{y} \\ \mathbf{q}_{\mathrm{E}} \end{pmatrix} \tag{3.13}$$

where $\Psi = \begin{bmatrix} \psi_1 & \psi_2 & \cdots & \psi_{l_m} \end{bmatrix}$. ψ_i is the ith natural mode of the unit cell with $\mathbf{q}_{\mathrm{L}} = \mathbf{q}_{\mathrm{R}} = \mathbf{q}_{\mathrm{E}} = \mathbf{0}$ and the corresponding natural frequencies is ω_i. Namely, ψ_i and ω_i satisfies

$$\left(-\omega_i^2\mathbf{M}_{\mathrm{II}} + \mathbf{K}_{\mathrm{II}}\right)\psi_i = \mathbf{0} \tag{3.14}$$

Only l_m modes are kept to form Ψ, and the number is less than that of $\mathbf{q}_{\mathrm{I}}$. The criterion used to select the retained modes is

$$\omega_i < \alpha_{\mathrm{f}}\omega_{\mathrm{m}}, i \in [1, 2, ..., l_{\mathrm{m}}] \tag{3.15}$$

where ω_{m} is the upper bound of the frequencies to be analyzed. By choosing different values of factor α_{f}, the number of the retained modes can be controlled. Introducing transformation (3.13) into (3.1) and (3.5), the dynamic stiffness matrix $\tilde{}$ is redefined by

$$\tilde{\mathbf{D}} = -\omega^2\tilde{\mathbf{M}} + j\omega\tilde{\mathbf{C}} + \tilde{\mathbf{K}} + \tilde{\mathbf{Y}}_{\mathrm{g}}(\omega) \tag{3.16}$$

where

$$\begin{aligned} \tilde{\mathbf{M}} &= \mathbf{B}^{\mathrm{T}}\mathbf{M}\mathbf{B} \\ \tilde{\mathbf{C}} &= \mathbf{B}^{\mathrm{T}}\mathbf{C}\mathbf{B} \\ \tilde{\mathbf{K}} &= \mathbf{B}^{\mathrm{T}}\mathbf{K}\mathbf{B} \\ \tilde{\mathbf{Y}}_{\mathrm{g}} &= \mathbf{B}^{\mathrm{T}}\mathbf{Y}_{\mathrm{g}}\mathbf{B} \end{aligned}$$

Matrix $\tilde{\mathbf{D}}$ obtained from Equation (3.16) has a much smaller size in comparison to the one obtained from Equation (3.5). Then eliminating $\mathbf{y}$ and $\mathbf{q}_{\mathrm{E}}$ by introducing Equation (3.16) into (3.8) will also lead to Equation (3.7). But the calculation in Equation (3.8) is significantly accelerated due to the reduced matrix size of $\mathbf{D}_{\mathrm{II}}$.

In the reduced model developed by Ref. [87, 102], the wave shapes at other frequencies are chosen to form the transformation matrix. Hence theoretically their methods can be applied. However, during the design process of the piezoelectric substructure, the electric admittance will be set to different values so as to evaluate the performance [123, 201]. The coordinate transformation needs to be performed once again, after each modification of the admittance.

By transforming and reducing only the internal mechanical DOFs while keeping the electric DOFs, the proposed method leads to a more reasonable reduced model for the piezoelectric structures. Especially, when the admittance is changed, there is no need to re-calculate the reduced matrices $\tilde{\mathbf{M}}$, $\tilde{\mathbf{K}}$ and $\tilde{\mathbf{C}}$.

3.3 Analysis of the assembled structure

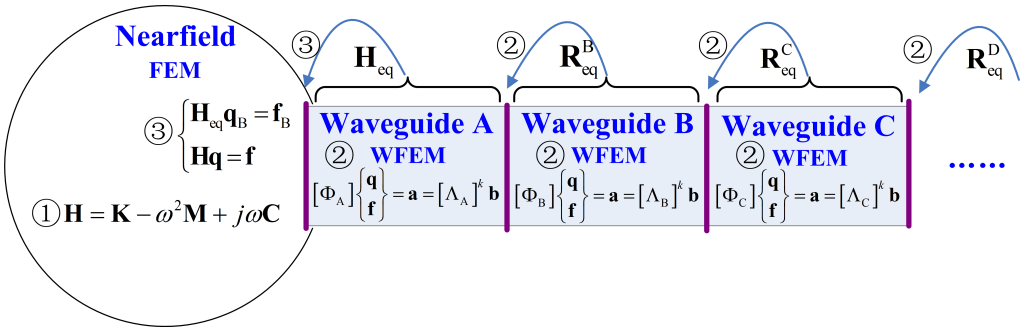

Figure 3.5: Illustration of the modeling process of the proposed method, where the numbers indicate the modeling order.

Remind that the considered structural system is divided into the 1) **near-field** part which is subject to external excitation and several 2) **periodic substructures** connected subsequently to the near-field. The analysis of such built-up structure can be made by three major steps, as illustrated in figure 3.5:

1. Model the near-field part by FEM;
2. Determine the wave basis of periodic substructures by WFEM. Calculate the equivalent reflection matrix of each waveguide;
3. Determine the equivalent impedance of the waveguide that are directly connected to the nearfield. To do this, the equivalent reflection matrices obtained in the second step will be used.

The first step can be done by means of any existing FEM software. In this section the second and third steps are described in detail. After these steps, all waveguides DOFs are eliminated and the dynamics of the waveguides are into the near-field. To recover their response, a post-processing procedure is needed, and it is reported at the end.

3.3.1 Equivalent reflection matrix

Consider two waveguides (B and C) connected together, as shown in figure 3.6. Waveguide B is regarded as the 'host' substructure because it is closer to the near-field than waveguide C. The objective is to represent waveguide C as the reflection matrix applied at its interface with waveguide B.

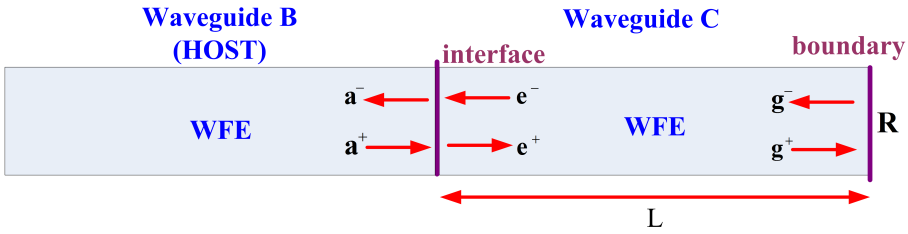

Figure 3.6: Illustration of two connected waveguides.

By WFEM the wave basis of waveguide B and C can be obtained by analyzing a unit cell of them. The enhanced approaches for WFEM developed in this thesis can be applied, as shown in chapter 2 for general cases and in the previous section for the piezoelectric case. Suppose the wave basis for substructure B is composed of right eigenvector matrix Φ, Left eigenvector matrix Θ and eigenvalue matrix Λ_b; and the wave basis for substructure C is composed of right eigenvector matrix Υ, Left eigenvector matrix $\bar{\Theta}$ and eigenvalue matrix Λ_c.

The displacement $\mathbf{q}_\mathrm{t}$ and internal force $\mathbf{f}_\mathrm{t}$ at the interface can be written in terms of the wave amplitudes associated with the wave basis Φ of waveguide B. Alternatively, they and also expressed in terms of basis Υ of waveguide C:

$$\begin{pmatrix} \mathbf{q}_\mathrm{t} \\ \mathbf{f}_\mathrm{t} \end{pmatrix} = \begin{bmatrix} \Phi_\mathrm{q}^+ & \Phi_\mathrm{q}^- \\ \Phi_\mathrm{f}^+ & \Phi_\mathrm{f}^- \end{bmatrix} \begin{pmatrix} \mathbf{a}^+ \\ \mathbf{a}^- \end{pmatrix} = \begin{bmatrix} \Upsilon_\mathrm{q}^+ & \Upsilon_\mathrm{q}^- \\ \Upsilon_\mathrm{f}^+ & \Upsilon_\mathrm{f}^- \end{bmatrix} \begin{pmatrix} \mathbf{e}^+ \\ \mathbf{e}^- \end{pmatrix} \tag{3.17}$$

At the other side of waveguide B, the wave amplitudes satisfy

$$\mathbf{g}^- = \mathbf{R}\mathbf{g}^+ \tag{3.18}$$

where $\mathbf{R}$ is the reflection matrix of the boundary, $\mathbf{g}^+$ and $\mathbf{g}^-$ are the amplitude array of the positive and negative going waves at the cross-section respectively. If waveguide C is infinite then $\mathbf{R} = \mathbf{0}$; if the boundary condition is given (Neumann, Dirichlet or mixed) then $\mathbf{R}$ can be calculated by transforming the specified displacement and force in wave domain as shown in section 2.2.3. If waveguide C has a subsequent waveguide, then $\mathbf{R}$ is calculated by setting C as host waveguide and calculate the equivalent reflection matrix of the subsequent waveguide.

The wave amplitudes in waveguide C must also satisfy the transfer relation in wave domain as shown in section (2.2.3); it writes

$$\begin{pmatrix} \mathbf{g}^+ \\ \mathbf{g}^- \end{pmatrix} = \begin{bmatrix} {}^+\Lambda_\mathrm{c}^{L_\mathrm{c}/\Delta_\mathrm{c}} & \\ & {}^-\Lambda_\mathrm{c}^{L_\mathrm{c}/\Delta_\mathrm{c}} \end{bmatrix} \begin{pmatrix} \mathbf{e}^+ \\ \mathbf{e}^- \end{pmatrix} \tag{3.19}$$

where ${}^+\Lambda_\mathrm{c}$ and ${}^-\Lambda_\mathrm{c}$ are the diagonal matrices consisting of positive and negative eigenvalues for waveguide C, L_c the overall length and Δ_c the unit cell length.

Introducing equation (3.18) in (3.19) gives

$$\mathbf{e}^- = \left({}^-\Lambda_c^{-L_c/\Delta_c} \cdot \mathbf{R} \cdot {}^+\Lambda_c^{L_c/\Delta_c}\right) \mathbf{e}^+ \tag{3.20}$$

$$= \mathbf{R}_c \mathbf{e}^+ \tag{3.21}$$

Eliminate $\mathbf{e}^+$ and $\mathbf{e}^-$ in Equation (3.17) by introducing (3.21) and after some algebra; it yields

$$\mathbf{a}^- = \mathbf{R}_{eq} \mathbf{a}^+ \tag{3.22}$$

where

$$\mathbf{R}_{eq} = -\left(\Phi_q^- - \mathbf{Y}\Phi_f^-\right)^{-1} \left(\Phi_q^+ - \mathbf{Y}\Phi_f^+\right) \tag{3.23}$$

and

$$\mathbf{Y} = \left[\Upsilon_q^+ + \Upsilon_q^- \mathbf{R}_c\right] \left[\Upsilon_f^+ + \Upsilon_f^- \mathbf{R}_c\right]^{-1} \tag{3.24}$$

Matrix $\mathbf{R}_{eq}$ is the searched equivalent reflection coefficients of waveguide C applied to waveguide B. Note that if reduced wave bases are used for the waveguides, which is recommended by the authors, pseudo inverse will be involved in Equations (3.24) and (3.23). To improve the numerical conditioning, the orthogonal relation of the left and right eigenvectors can be used. Premultiplying left eigenvector matrix Θ at both sides of Equation (3.17), inducing

$$\begin{pmatrix} \mathbf{a}^+ \\ \mathbf{a}^- \end{pmatrix} = \begin{bmatrix} \Theta_q^+ & \Theta_f^+ \\ \Theta_q^- & \Theta_f^- \end{bmatrix} \begin{bmatrix} \Upsilon_q^+ & \Upsilon_q^- \\ \Upsilon_f^+ & \Upsilon_f^- \end{bmatrix} \begin{pmatrix} \mathbf{e}^+ \\ \mathbf{e}^- \end{pmatrix} \tag{3.25}$$

which means

$$\begin{pmatrix} \mathbf{a}^+ \\ \mathbf{a}^- \end{pmatrix} = \begin{bmatrix} \mathbf{Y}_{pp} & \mathbf{Y}_{pn} \\ \mathbf{Y}_{np} & \mathbf{Y}_{nn} \end{bmatrix} \begin{pmatrix} \mathbf{e}^+ \\ \mathbf{e}^- \end{pmatrix} \tag{3.26}$$

where

$$\mathbf{Y}_{pp} = \Theta_q^+ \Upsilon_q^+ + \Theta_f^+ \Upsilon_f^+ \tag{3.27}$$

$$\mathbf{Y}_{pn} = \Theta_q^+ \Upsilon_q^- + \Theta_f^+ \Upsilon_f^- \tag{3.28}$$

$$\mathbf{Y}_{np} = \Theta_q^- \Upsilon_q^+ + \Theta_f^- \Upsilon_f^+ \tag{3.29}$$

and

$$\mathbf{Y}_{nn} = \Theta_q^- \Upsilon_q^- + \Theta_f^- \Upsilon_f^- \tag{3.30}$$

Introducing Equation (3.21) into Equation (3.26) to eliminate $\mathbf{e}^+$ and $\mathbf{e}^-$, we can still achieve (3.22) but the $\mathbf{R}_{eq}$ is give by

$$\mathbf{R}_{eq} = -\left(\mathbf{Y}_{np} + \mathbf{Y}_{nn}\mathbf{R}_c\right) \left(\mathbf{Y}_{pp} + \mathbf{Y}_{pn}\mathbf{R}_c\right)^{-1} \tag{3.31}$$

Once $\mathbf{R}_{eq}$ is given, the reflection matrix of waveguide B can also be determined and introduced in its previous waveguide. If waveguide B is directly connected to the near-field part, its dynamic features will be deduced into mechanical impedance and merged into the near-field part, as presented in the following subsection.

3.3.2 Equivalent impedance matrix

Consider the waveguide (A) that is directly connected to the near-field part at one end, and at the other end the reflection matrix $\mathbf{R}$ has already been determined as described in the previous subsection. The right eigenvalue matrix is Φ, the left eigenvalue matrix is Θ and the eigenvalue matrix is Λ_a. The objective here is to connect the dynamic behavior of the waveguide to the near-field part as shown in figure 3.7. Note that the near-field substructure is described in physical domain by FEM. The dynamics of the waveguide will also be represented as an equivalent mechanical impedance matrix.

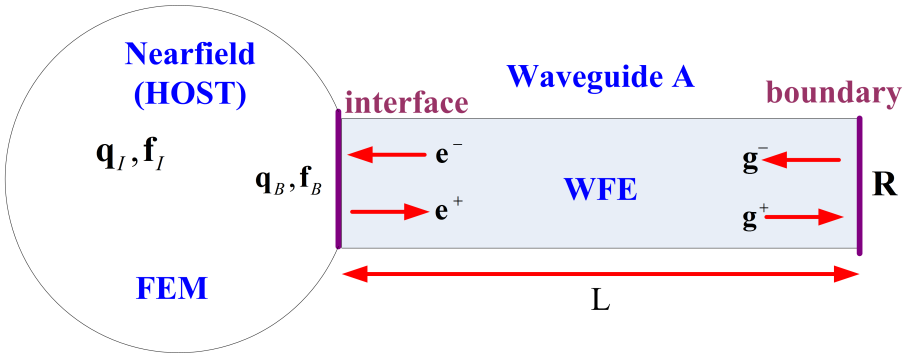

Figure 3.7: Illustration of connection between near-field domain and a waveguide.

Firstly, at the interface the displacement and force can be expanded into wave amplitudes, writes

$$\begin{pmatrix} \mathbf{q}_\mathrm{B} \\ \mathbf{f}_\mathrm{B} \end{pmatrix} = \begin{bmatrix} \Phi_\mathrm{q}^+ & \Phi_\mathrm{q}^- \\ \Phi_\mathrm{f}^+ & \Phi_\mathrm{f}^- \end{bmatrix} \begin{pmatrix} \mathbf{e}^+ \\ \mathbf{e}^- \end{pmatrix} \tag{3.32}$$

while at the other end the reflection matrix $\mathbf{R}$ leads to

$$\mathbf{g}^- = \mathbf{R}\mathbf{g}^+ \tag{3.33}$$

Additionally, the transfer relation in wave domain constrains the wave amplitude between different cross-sections as:

$$\begin{pmatrix} \mathbf{e}^+ \\ \mathbf{e}^- \end{pmatrix} = \begin{bmatrix} {}^+\Lambda_\mathrm{a}^{L_\mathrm{a}/\Delta_\mathrm{a}} & \\ & {}^-\Lambda_\mathrm{a}^{L_\mathrm{a}/\Delta_\mathrm{a}} \end{bmatrix} \begin{pmatrix} \mathbf{g}^+ \\ \mathbf{g}^- \end{pmatrix} \tag{3.34}$$

where L_a is the overall length, Δ_a is the length of a unit cell and ${}^+\Lambda_\mathrm{a}$ and ${}^-\Lambda_\mathrm{a}$ are the diagonal matrices consisting of positive and negative eigenvalues for waveguide A respectively.

Introducing equations (3.33) and (3.34) into (3.32), and eliminating all wave amplitudes, leads to

$$\mathbf{f}_\mathrm{B} = \mathbf{H}_\mathrm{eq}\mathbf{q}_\mathrm{B} \tag{3.35}$$

where

$$\mathbf{H}_\mathrm{eq} = \left[\Phi_\mathrm{f}^+ + \Phi_\mathrm{f}^-\mathbf{R}_a\right]\left[\Phi_\mathrm{q}^+ + \Phi_\mathrm{q}^-\mathbf{R}_a\right]^{-1} \tag{3.36}$$

and

$$\mathbf{R}_a = {}^-\Lambda_\mathrm{a}^{-L_\mathrm{a}/\Delta_\mathrm{a}} \cdot \mathbf{R} \cdot {}^+\Lambda_\mathrm{a}^{L_\mathrm{a}/\Delta_\mathrm{a}} \tag{3.37}$$

Matrix $\mathbf{H}_{\text{eq}}$ is the searched equivalent mechanical impedance. If reduced wave bases are used for the waveguides, Equation (3.36) can be re-written as

$$\mathbf{H}_{\text{eq}} = \left[\Phi_{\text{f}}^{+}\Theta_{\text{q}}^{+} + \Phi_{\text{f}}^{-}\mathbf{R}_a\Theta_{\text{q}}^{+}\right]\left[\Phi_{\text{q}}^{+}\Theta_{\text{q}}^{+} + \Phi_{\text{q}}^{-}\mathbf{R}_a\Theta_{\text{q}}^{+}\right]^{-1} \tag{3.38}$$

3.3.3 Solving and post-processing

Once the dynamics of the waveguides are condensed into equivalent impedance matrices, they can be assembled into the near-field equations. Now we have the dynamic equations obtained of the built-up structures, expressed only by near-field DOFs

$$\begin{bmatrix}\mathbf{H}_{\text{II}} & \mathbf{H}_{\text{IB}} \\ \mathbf{H}_{\text{BI}} & \mathbf{H}_{\text{BB}} + \mathbf{H}_{\text{eq}}\end{bmatrix}\begin{pmatrix}\mathbf{q}_{\text{I}} \\ \mathbf{q}_{\text{B}}\end{pmatrix} = \begin{pmatrix}\mathbf{f}_{\text{I}} \\ \mathbf{0}\end{pmatrix} \tag{3.39}$$

where subscripts **I** and **B** respectively indicate the internal DOFs of the near-field part and the DOFs connected to the waveguides.

The response of the complete structure is calculated in different scales, by the following steps:

1. **Near-field scale**. The near-field response $\mathbf{q}_{\text{I}}$ and $\mathbf{q}_{\text{B}}$ are obtained by solving Equation (3.39), and internal forces at the interface $\mathbf{f}_{\text{B}}$ are calculated by equation (3.35).

2. **Waveguide scale**. For the nearest waveguide, wave amplitudes $\mathbf{d}^{+}$ and $\mathbf{d}^{-}$ at the interface with the near-field are determined by solving Equations (3.32), where the orthogonality relations can be employed to avoid ill-conditioning. For the subsequent waveguides, wave amplitudes $\mathbf{e}^{+}$ and $\mathbf{e}^{-}$ at the interface are calculated by introducing the wave amplitudes of the previous waveguide into equation (3.17). The wave amplitudes and the corresponding physical response inside a substructure are determined in the WFEM framework as mention in chapter 2. The energy flow through the nth cross-section of a substructure reads

$$P_n = \frac{1}{2}\text{Re}\left(-j\omega\mathbf{f}_n \cdot \bar{\mathbf{q}}_n\right) \tag{3.40}$$

3. **Cell scale**. The response of the internal DOFs of a unit cell can be recovered once the boundary DOFs are known. The specific equations are related to the unit cell model. If the unit cell is modeled by full FEM, then $\mathbf{q}_{\text{I}}$ is recovered by

$$\begin{pmatrix}\mathbf{q}_{\text{I}} \\ \mathbf{q}_{\text{E}}\end{pmatrix} = \begin{bmatrix}\tilde{\mathbf{D}}_{\text{II}} & \tilde{\mathbf{D}}_{\text{IE}} \\ \tilde{\mathbf{D}}_{\text{EI}} & \tilde{\mathbf{D}}_{\text{EE}}\end{bmatrix}^{-1}\begin{bmatrix}\tilde{\mathbf{D}}_{\text{IL}} & \tilde{\mathbf{D}}_{\text{IR}} \\ \tilde{\mathbf{D}}_{\text{EL}} & \tilde{\mathbf{D}}_{\text{ER}}\end{bmatrix}\begin{pmatrix}\mathbf{q}_{\text{L}} \\ \mathbf{q}_{\text{R}}\end{pmatrix} \tag{3.41}$$

   If the reduced model proposed in this chapter is used, the internal modal DOFs are recovered by

$$\begin{pmatrix}\mathbf{y} \\ \mathbf{q}_{\text{E}}\end{pmatrix} = \begin{bmatrix}\tilde{\mathbf{D}}_{\text{yy}} & \tilde{\mathbf{D}}_{\text{yE}} \\ \tilde{\mathbf{D}}_{\text{Ey}} & \tilde{\mathbf{D}}_{\text{EE}}\end{bmatrix}^{-1}\begin{bmatrix}\tilde{\mathbf{D}}_{\text{yL}} & \tilde{\mathbf{D}}_{\text{yR}} \\ \tilde{\mathbf{D}}_{\text{EL}} & \tilde{\mathbf{D}}_{\text{ER}}\end{bmatrix}\begin{pmatrix}\mathbf{q}_{\text{L}} \\ \mathbf{q}_{\text{R}}\end{pmatrix} \tag{3.42}$$

   and introducing $\mathbf{y}$, $\mathbf{q}_{\text{L}}$, $\mathbf{q}_{\text{R}}$ and $\mathbf{q}_{\text{E}}$ int Equation (3.13), $\mathbf{q}_{\text{I}}$ can be obtained.

The proposed methodology is intrinsically a multi-scale approach. To investigate the dynamics around excitation (input mobility, input power and energy storage in the near-field etc.), the response in the near-field scale might be sufficient. While for evaluating certain waveguide by energy flow and transmission loss etc., the response of the waveguide scale is sufficient. To present the detailed response of the unit cells, the cell scale can be used.

3.4 Validations

3.4.1 Energy flow in an infinite uniform beam

Let us consider an infinite uniform beam undergoes the excitation at the origin. The structure is modeled by Euler-Bernoulli beam elements. Indeed this uniform structure can be analyzed by WFEM alone as a single waveguide. To validate the proposed method it is divided into the near-field part from $x = -1\,\mathrm{m}$ to $x = 1\,\mathrm{m}$ and 4 waveguides (2 finite, 2 infinite) with identical geometric and material parameters as shown in figure 3.8. The cross-section of the structure is a rectangle with height of $5 \times 10^{-2}\,\mathrm{m}$ and width of $5 \times 10^{-2}\,\mathrm{m}$. The considered material is steel with light Rayleigh damping, and the Young's modulus $E = (1 + 10^{-4} j\omega) \times 2.11 \times 10^{11}\,\mathrm{Pa}$ and density $7.8 \times 10^{3}\,\mathrm{kg/m^3}$. Concerning the waveguide modeling, unit cell length of 0.01 m is considered. It should be noted that for uniform waveguide it is enough to consider one element as a unit cell, here 10 elements are used just to validate the condensation and the post-processing of the methodology.

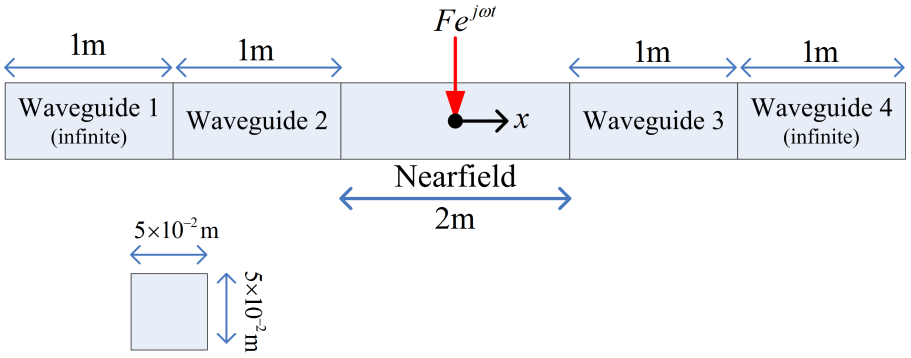

Figure 3.8: Calculation layout of infinite uniform beam.

Following the proposed procedure, the wave bases of each waveguide are calculated by WFEM with DSM of a unit cell given by FEM package. The dispersion curves of the positive going waves are shown in figure 3.9 in comparison with the analytical solutions. The analytical solution could be found by introducing $u(x,t) = e^{j(\omega t - kx)}$ into the Euler-Bernoulli equation

$$\rho A \frac{\partial^2 u(x,t)}{\partial t^2} + EI \frac{\partial^4 u(x,t)}{\partial x^4} = 0$$

and introducing $v(x,t) = e^{j(\omega t - kx)}$ into the longitudinal equation

$$\rho A \frac{\partial^2 v(x,t)}{\partial t^2} - EA \frac{\partial^2 v(x,t)}{\partial x^2} = 0$$

Then they yield 6 wavenumbers for each frequency, in which 3 of them are associated with positive-going waves, write

$$k_{\mathrm{l}} = \omega\sqrt{\rho/E}$$
$$k_{\mathrm{fp}} = \sqrt{\omega}\left(\frac{\rho A}{EI}\right)^{1/4}$$
$$k_{\mathrm{fe}} = -j\sqrt{\omega}\left(\frac{\rho A}{EI}\right)^{1/4}$$

where k_{l} denotes the longitudinal wave, k_{fp} the propagating flexural wave and k_{fe} the evanescent flexural wave. Note that with damping all the waves have complex wavenumbers.

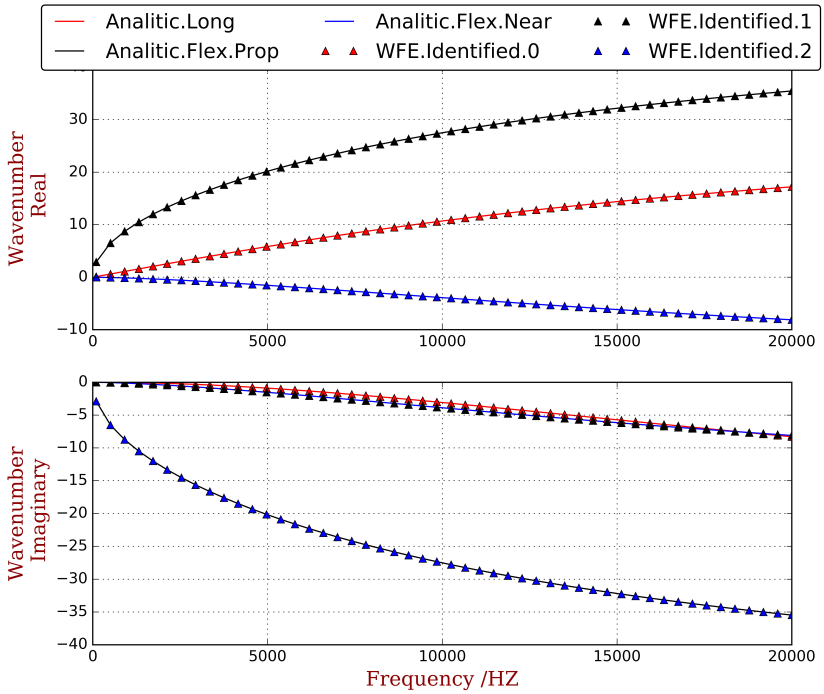

Figure 3.9: The dispersion curves of the waveguides.

Solving eigenvalue problem (3.9) in different frequencies, the initial results are discrete points in the wavenumber-frequency diagram. In order to present the evolution of a same wave at different frequencies, one needs to search through these points and to link the points with similar waveshapes. Here the Modal Assurance Criterion (MAC) is used to identify the points with similar waveshapes among frequencies. MAC gives the similarity of two shapes ϕ_1 and ϕ_2 as

$$\mathrm{MAC} = \frac{(\phi_1^{\mathrm{H}} \cdot \phi_2)^2}{(\phi_1^{\mathrm{H}} \cdot \phi_1)(\phi_2^{\mathrm{H}} \cdot \phi_2)} \tag{3.43}$$

The MAC is a real value which varies from 0 to 1. In practice we define a threshold $\delta \in [0, 1]$ so that if MAC $> \delta$, two waveshapes are considered as a same wave. Empirical

values for δ in the case of periodic structures are between 0.4 to 0.8. On the other hand for isotropic structures, correlation can achieve with values as high as 0.99. In practice a high δ value should firstly be attempted. If no correlated waves are found, a lower δ value is used until all selected eigenvalues are correlated to a set of wave type. In this work $\delta = 0.7$ is used. Note that this identification is just an interpretation of the eigenvalue solutions among different frequencies and does not affect the forced response calculation. This simple approach leads to good results in most of the applications, except when modal veering and crossing occur.

Figure 3.10 compares the forced response results with the analytical solution (see the work of [82] for detail). The results of analytical solution is drawn by solid line while the results of the proposed method are presented by different marker referring to different scales. The contribution of evanescent waves can be seen in the near-field. The propagating waves dominate the rest of the response so that the phase changes linearly in space. The energy flow is obtained accordingly, and the results are compared in Figure 3.11, where a negative value indicates the energy flow in negative x direction. Because of damping, the overall energy flow P_a has a downward trend in space. As explained by [82], for flexural waves the energy flows under two forms, one associates with u_{y} DOF, denoted by P_u and another with θ DOF denoted by P_m. For mechanical field excited by a transverse force, at the excitation point all the power is associated with P_u, with the increase of distance some proportion of this power is transfered to P_m and at last half of the incident power is transfered. All these comparisons have shown very good agreement indicating that the proposed method can well capture the dynamics of this infinite problem.

3.4.2 Forced response of a finite piezoelectric structure

In the second validation, let us increase the complexity of the structure. A finite solid-element meshed structure is considered, shown in figure 3.12. It is constructed by bonding 10 groups of co-located piezoelectric patches onto a uniform host structure excited at the center. Five groups of piezoelectric patches are periodically distributed at the right side of the excitation while 5 other groups are located on the other side. The structure is clamped on the right end and free at the left. The considered host material is steel without damping, with a Young's modulus of $E = 2.11 \times 10^{11}$ Pa and a density of $7.8 \times 10^3\,\mathrm{kg/m^3}$. The used piezoelectric material is PZT4 with parameters listed in Appendix A. While applying the proposed method, this structure are divided into five parts: one near-field part, two piezoelectric waveguides and two uniform far-field waveguides, as shown in figure 3.12. The meshes for a unit cell of the piezoelectric waveguides and far-field waveguides are shown in figure 3.13a and 3.13b respectively where x is the propagating direction.

The dispersion curves of far-field waveguides in a frequency range of $[0, 80]$ kHz are presented in Figure 3.14. All the typical positive-going waves are observed. Four propagating waves are recognized (wave index 0, 1, 4 and 5) and their shapes are shown in figure 3.15. It can be seen that wave 0 represents the flexural wave in z direction (figure 3.15a), wave 1 represents the flexural wave in y direction (figure 3.15b), wave 4 represents the torsional wave (figure 3.15c), and wave 5 represents the longitudinal wave (figure 3.15d). Also two typical evanescent waves are observed, labeled wave 2 and wave 3, representing the evanescent flexural waves in z and y direction respectively.

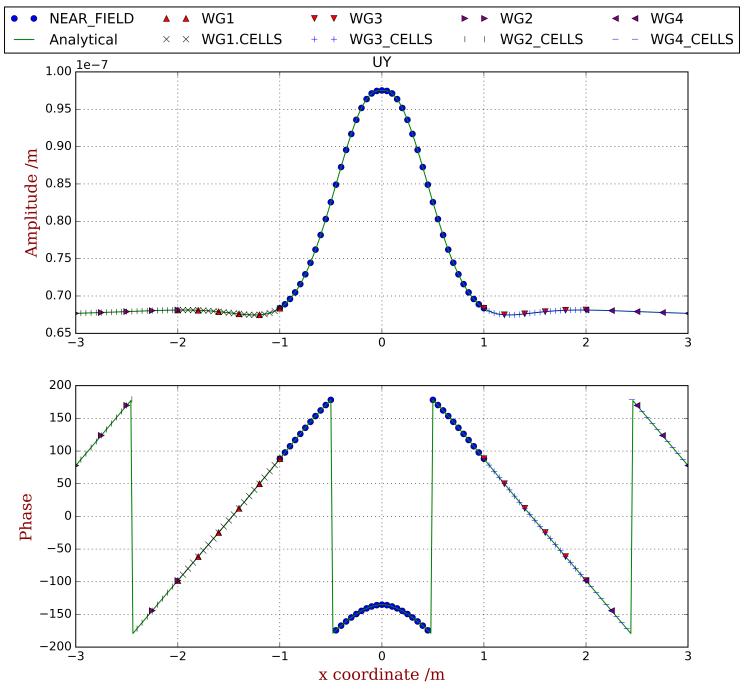

Figure 3.10: Comparison of the displacement response between the analytical solution and the proposed method

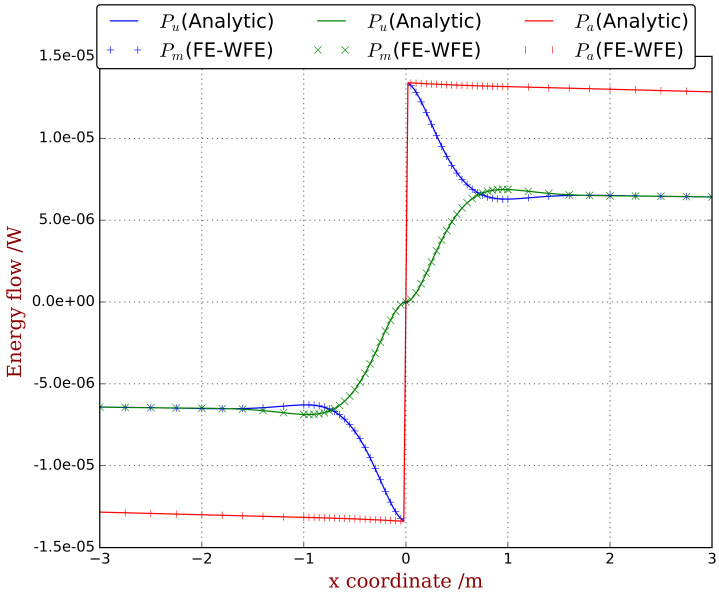

Figure 3.11: Comparisons of the energy flow between the analytical solution and the proposed method

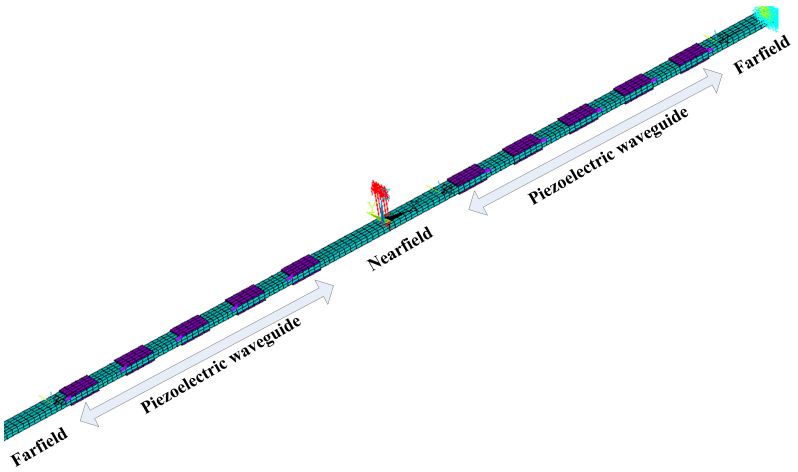

Figure 3.12: The calculation layout of the finite piezoelectric structure

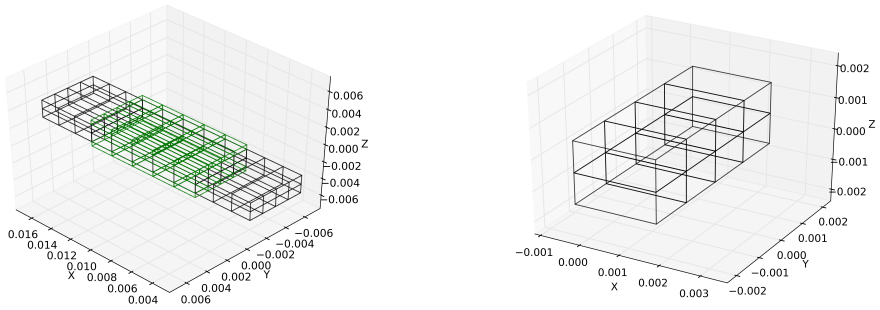

(a) Piezoelectric unit cell (b) Far-field unit cell

Figure 3.13: Unit cells of the piezoelectric and the far-field waveguides

To establish the wave bases of the piezoelectric waveguides, the proposed modal reduction approach is employed. All the internal mechanical DOFs are regarded as $\mathbf{q}_c$, they have been condensed by only considering 10 modal DOFs. All the electric DOFs are regarded as $\mathbf{q}_n$ so that they are kept into the reduced dynamic stiffness matrix. Figure 3.16 compares the stiffness matrix of a unit cell before and after modal reduction. It can be seen in Figure 3.16a that, before the reduction, the matrix is sparse and large (722×722). While after the reduction it tends to be dense and with a much smaller size (102×102). In the condensation process, 90 boundary DOFs are retained, which means only a 12×12 matrix of the internal DOFs needs to be inverted after the reduction, otherwise the inverse of a 632×632 matrix of internal DOFs should be computed.

The dispersion curves of the piezoelectric waveguides are shown in figure 3.17, with all the kept positive going waves included. The results are firstly validated by comparison with those obtained without the modal reduction. Furthermore, as it was indicated by [96] that the bounding frequencies of the band gaps can be calculated by two modal analysis on one unit cell with the corresponding left and right DOFs under the constrain $\mathbf{q}_L = \mathbf{q}_R$ and $\mathbf{q}_L = -\mathbf{q}_R$ respectively. So a classical modal analysis performed to offer the

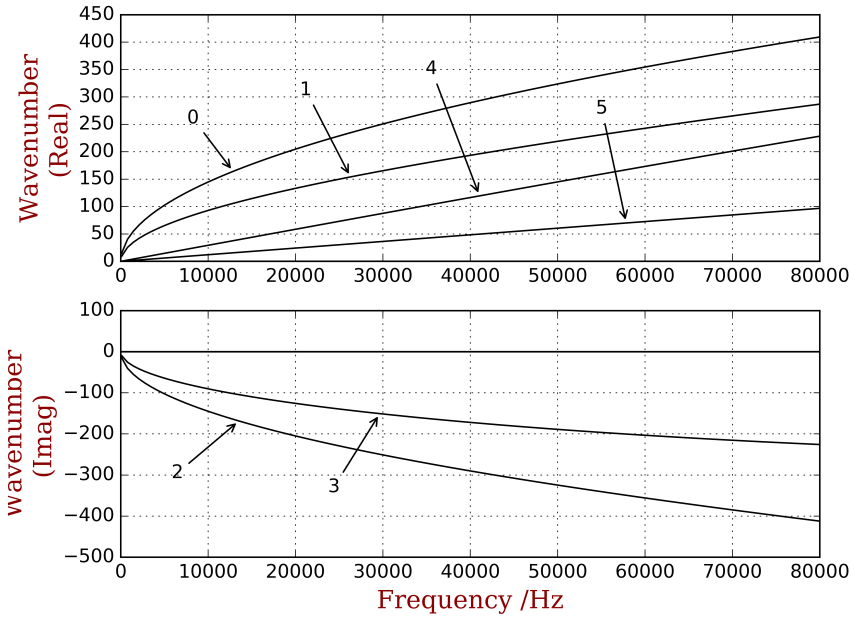

Figure 3.14: The dispersion curves of the far-field waveguides

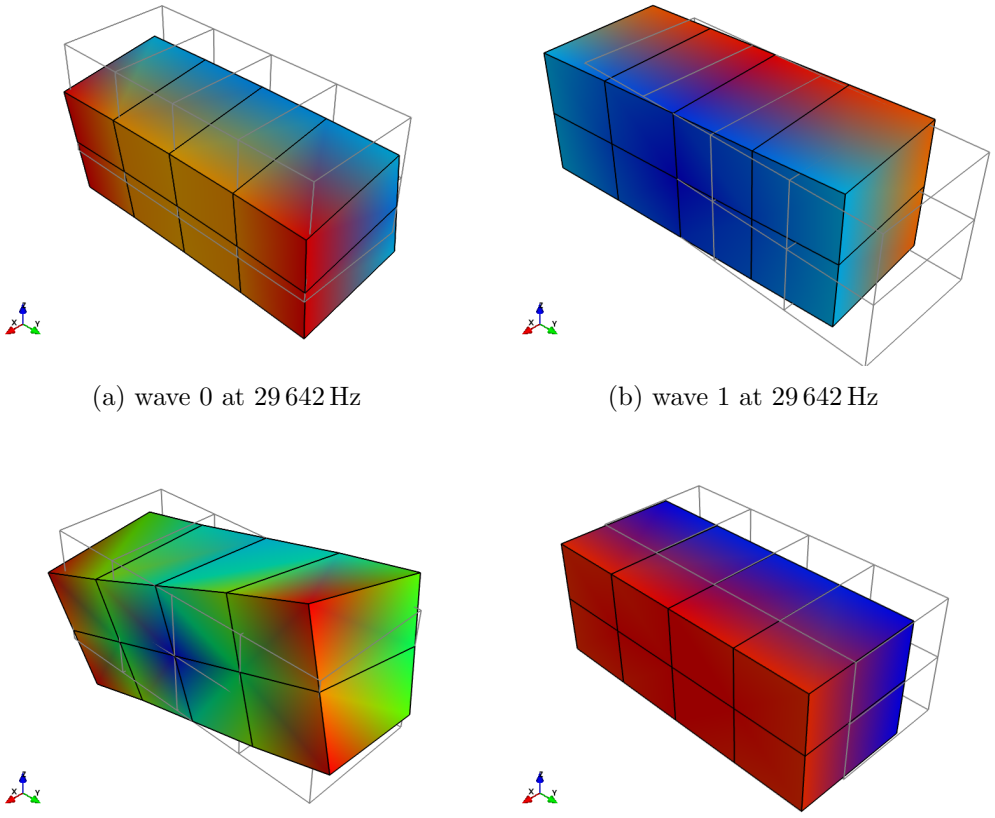

(a) wave 0 at 29 642 Hz

(b) wave 1 at 29 642 Hz

(c) wave 4 at 63 214 Hz

(d) wave 5 at 29 642 Hz

Figure 3.15: Some waveshapes of the far-field waveguides. wave 0, 1, 4, 5 are z-flexural, y-flexural, torsional and longitudinal waves respectively.

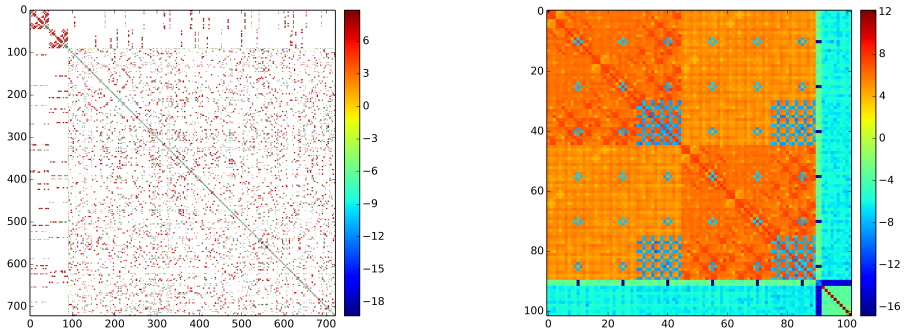

(a) Before modal reduction (b) After modal reduction

Figure 3.16: Illustration of stiffness matrix of a unit cell in the form of $log_{10}(|\cdot|)$

frequency locations of the band gaps. Both comparison are summarized in figure 3.18, good agreement can also be observed.

In Figure 3.17, overall 6 waves are observed, in which 4 waves (wave index 0, 1, 4 and 5) are propagating and 2 waves (wave index 2 and 3) are evanescent. Their shapes are shown in figure 3.19, which indicates that wave 0 and 2 are propagating and evanescent flexural waves in z direction respectively (Figure 3.19a and 3.19c), wave 1 and 3 are the propagating and evanescent flexural waves in y direction (Figure 3.19b and 3.19d), wave 4 is the torsional wave (Figure 3.19e) and wave 5 is the longitudinal wave (Figure 3.19f).

With the reduced wave bases of the piezoelectric and far-field waveguides, the proposed methodology is used to analyze the structural forced response. The validation data come from the full FE model of the whole assembled structure, as shown in figure 3.12. In the calculation, a resistance $R = 1 \times 10^5\,\Omega$ is shunted to each piezoelectric patch. The FRF of the u_z DOF of one of the nodes which receives excitation is compared in figure 3.20 in a wide frequency range, from 10 Hz up to 14 000 Hz. The response detail at 400 Hz are also compared in figure 3.21 between full FE model and the proposed hybrid model. The results are firstly presented on the near-field scale. Then the response of the waveguide scale and unit cell scale are post-processed. Good agreement can be seen in both figures. It should be noted that two reduction have been made on different stages. To obtain the wave basis, a structural-modal reduction was conducted in order to accelerate the calculation. Additionally, in forced response analysis, a reduced wave basis was employed to avoid ill-conditioning. In this validation case, 10 of the overall 632 structural modes are retained in the first reduction. Concerning reduced wave basis, only 6 of the overall 45 waves in the piezoelectric waveguides and 42 waves of the overall 45 waves in far-field waveguides are kept. The agreement with the full model results indicates that these reductions are accurate and the proposed method is applicable to solid-element modeling case.

For more complex electric circuits, the FEM-WFEM method with the reduced model can also provide good results. Figure 3.22 compares the results from different methods, when an identical resistor-inductor circuit is shunted to each piezoelectric patch. The calculated frequency is 3120 Hz, the resistance is 10 Ω and the inductance is 2.945 H.

The advantages in terms of computational time obtained from the proposed method

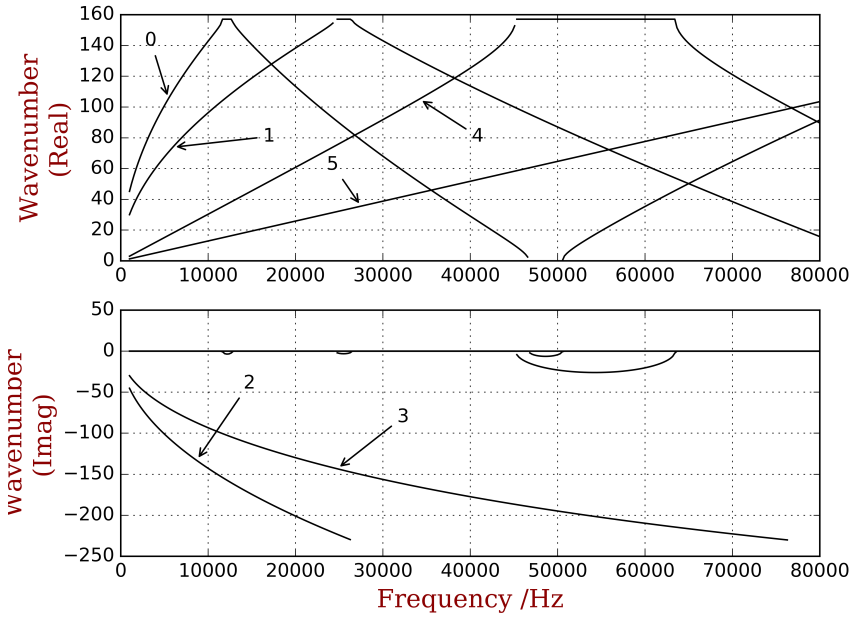

Figure 3.17: The dispersion curves of the piezoelectric waveguide

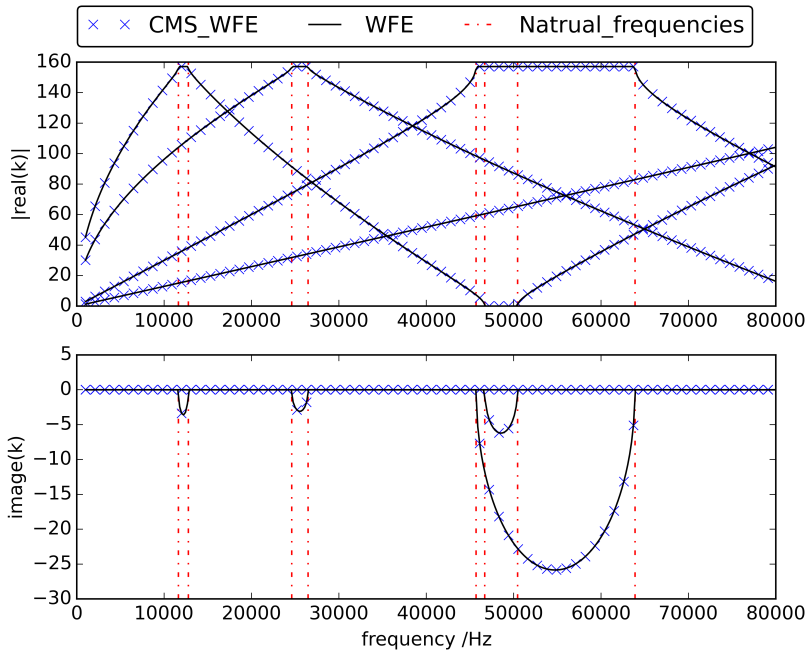

Figure 3.18: Validation of the obtained dispersion curves

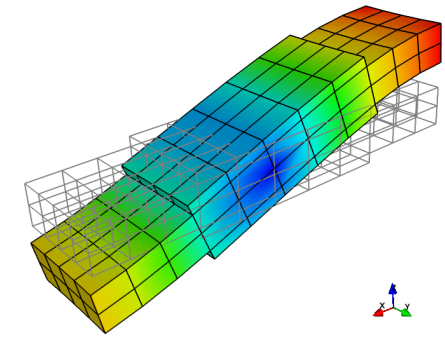

(a) wave 0 at 7191 Hz

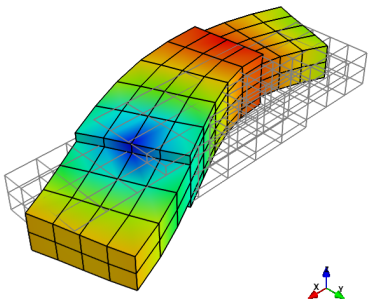

(b) wave 1 at 5457 Hz

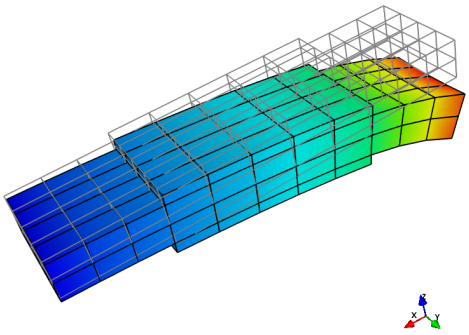

(c) wave 2 at 9667 Hz

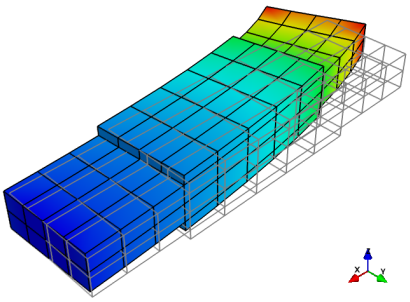

(d) wave 3 at 19 326 Hz

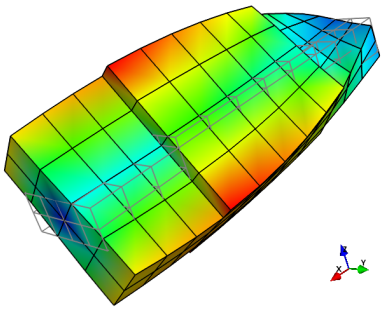

(e) wave 4 at 29 231 Hz

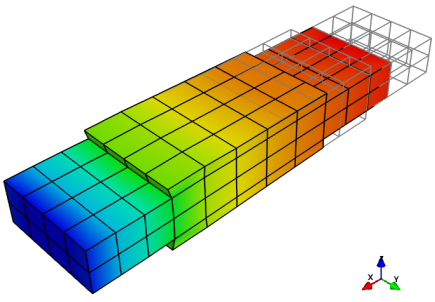

(f) wave 5 at 49 538 Hz

Figure 3.19: Some waveshapes of the piezoelectric waveguides. Wave 0, 1, 2, 3, 4, 5 are z-flexural propagation, y-flexural propagation, z-flexural evanescent, y-flexural evanescent, torsional and longitudinal waves respectively.

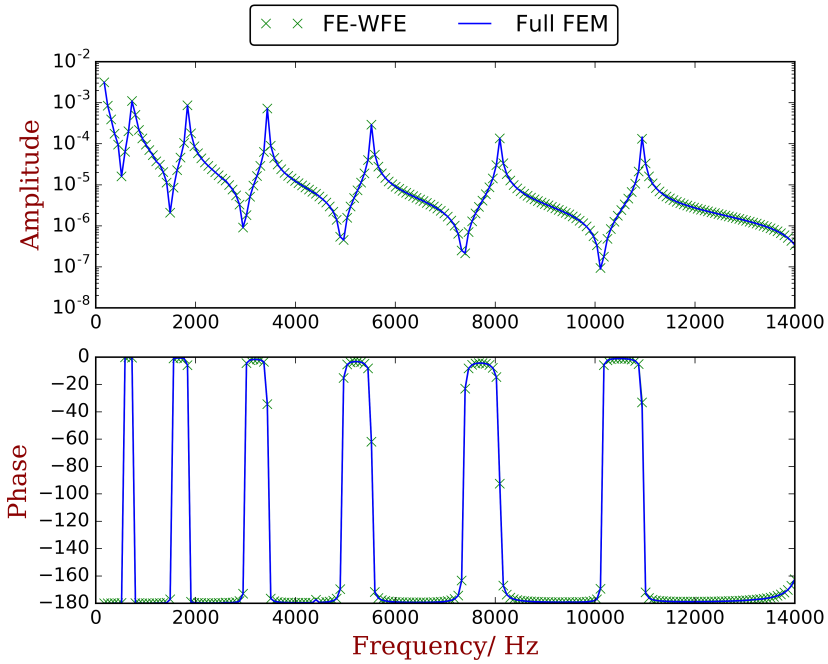

Figure 3.20: The FRF of the structure: u_Z DOF of a node receives excitation

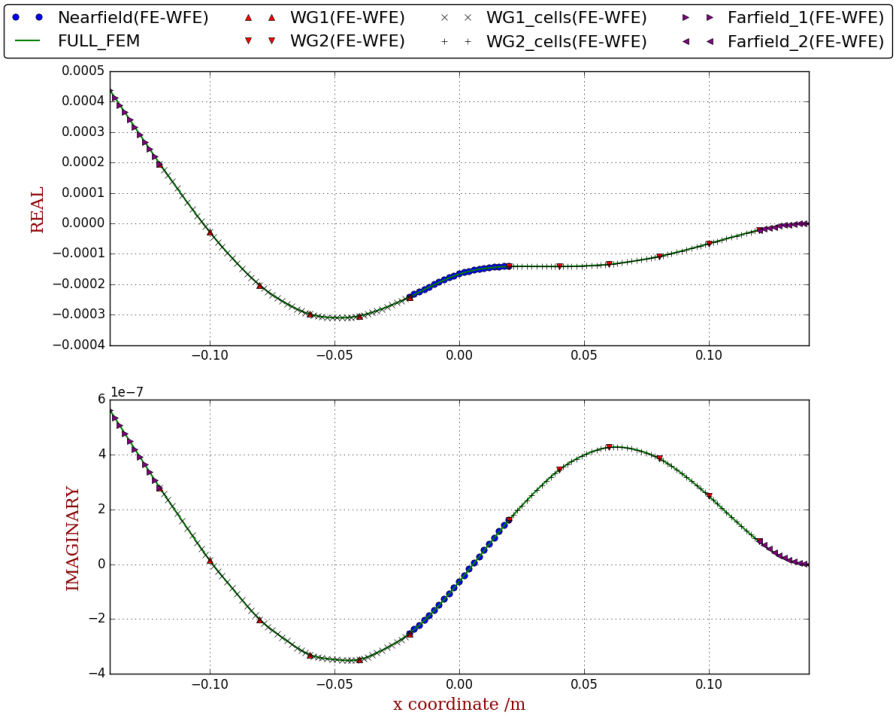

Figure 3.21: Response detail at 400 Hz: displacement of u_z DOF of all the middle line nodes

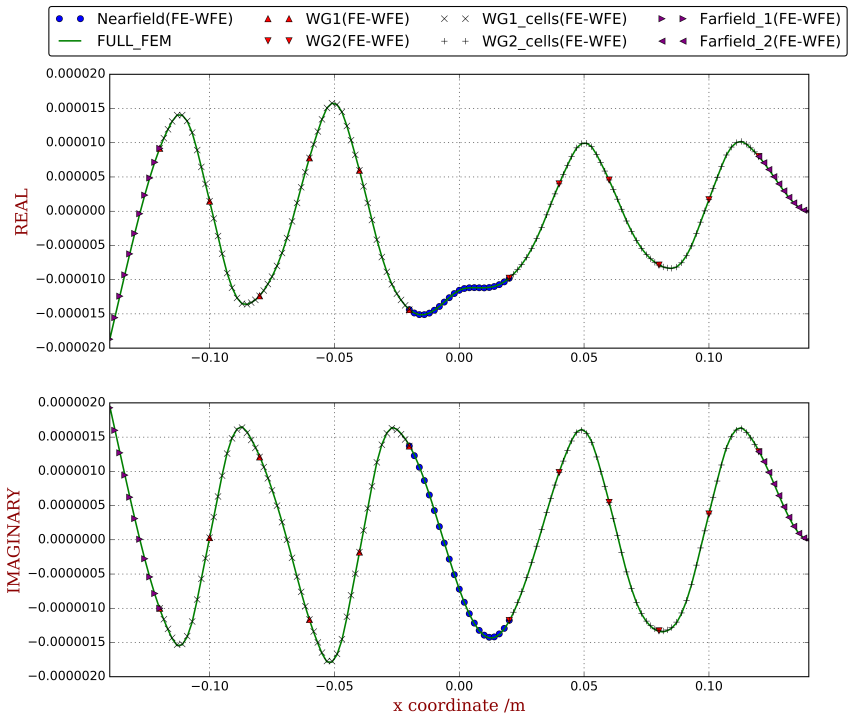

Figure 3.22: Response detail at 3120 Hz when an identical R-L circuit is shunted to each piezoelectric patches: displacement of u_z DOF of all the middle line nodes

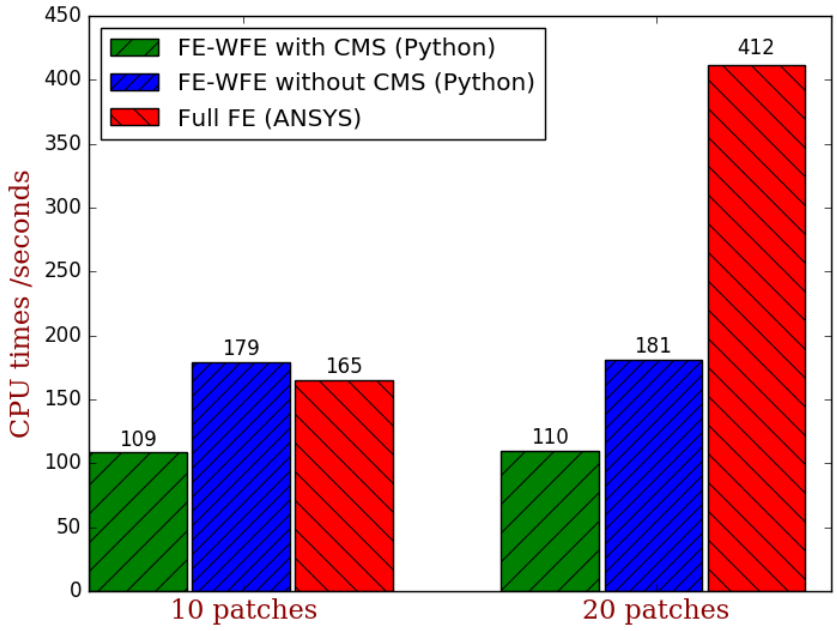

Figure 3.23: The consumed CPU time of different methods

are presented in Figure 3.23, showing a comparison of a computational time for the FRF of the structure discussed in this section. The FEM-WFEM hybrid models (implemented in Python) with or without modal condensation technique are compared with the full FE model (ANSYS 13.0). Performance differences can also be affected by the used computer languages or commercial FE platforms. From figure 3.23, it can be seen that: 1) More computational time is saved by using FEM-WFEM models with the increase of unit cell (patch) number; 2) With the increase of the number of patches (unit cells), the computational times of the FEM-WFEM models remain nearly the same, while the time consumed by the full FE model is highly increased (by 150 percent when the number of patches is doubled); 3) In both cases, employing modal condensation on the unit cells induces around 33 percent of time saving to the FEM-WFEM model. Note that the comparison are made by results obtained through different framework of computer program based on quite different programing languages. Generally, a commercial software can have a well optimized framework. Despite all that, a remarkable acceleration is achieved, indicating the advantages of the proposed numerical tools.

3.4.3 Energy flow from excitation to infinite farfield through finite piezoelectric substructures

Let us consider an open built-up structure with piezoelectric coupling. Indeed we can simply change the free-clamped boundary condition of the structure considered in the previous section (Figure 3.12) to the infinite-infinite condition. This can be done by setting a zero boundary reflection matrix. However, the model shown in Figure 3.12 is based on 3D solid mesh. It is difficult to find another analytical or numerical tool to validate the results if we set the boundary conditions to be infinite. For this reason, we still use a beam-based model, the aim is to validate the proposed numerical tool and give some preliminary discussions.

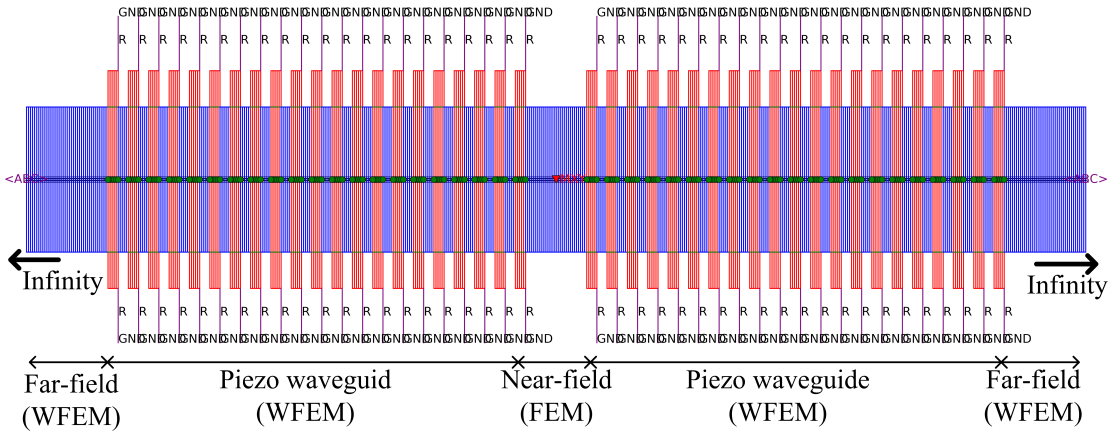

Figure 3.24: FE mesh of the considered built-up structure, it is built by a uniform beam with 21 groups of collocated piezoelectric patches respectively on the left and right parts of the excitation (at $x = 0$).

The considered built-up structure is shown in Figure 3.24. It is built by a uniform beam with 21 groups of collocated piezoelectric patches respectively on the left and right parts of

the origin. The excitation is also located at $x = 0$, in the form of bending moment with amplitude 1 N m. The host beam material is steel with Young's modulus 2.11×10^{11} Pa and density 7.8×10^3 kgm^{-3}. All mechanical damping is neglected. The host beam has width x=5×10^{-3} m and height 1×10^{-3} m. The piezoelectric material is PZT4 shown in Appendix A. Each PZT patch has a same shape, with height 5×10^{-4} m, width 5×10^{-3} m, and length x=0.1 m. The distance between two PZT patches is x=0.1 m. The PZT patches which locate closest to the origin are at $x = \pm 0.3$ m.

The FEM tool presented in Appendix B is used to model such a structure. But all the elements shown in Figure 3.24 has to be included. The ABC presented in Appendix C can be used to simulate the far-field dynamics. In combine they provides another way of solving the force response problem. The results will be used as a reference. For the proposed FEM-WFEM hybrid method, the built-up structure is divided into 5 parts as shown in the Figure 3.24. The FE mesh of the PZT waveguide is shown in Figure 3.25.

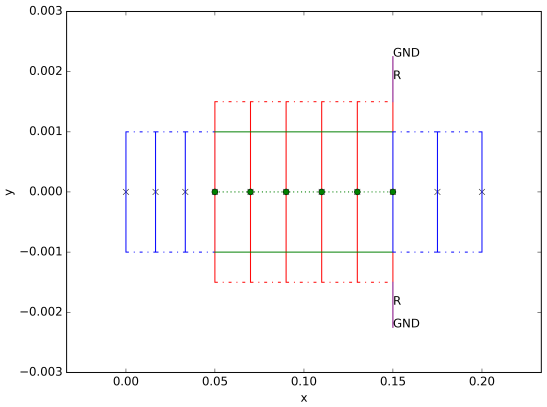

Figure 3.25: FE mesh of the unit cell of the PZT waveguide.

The calculations are made in the following situation using two methods (FEM with ABC, and FEM-WFEM):

1. Undamped waveguide working at a propagating frequency. The frequency is set to 100 Hz and all the PZT patches are set to SC status. Results are shown in Figures 3.26 and 3.27.

2. Damped waveguide working at a propagating frequency. The frequency is set to 100 Hz and each PZT patche is shunted to a resistor with $1 \times 10^5\,\Omega$. Results are shown in Figures 3.28 and 3.29.

3. Undamped waveguide working at a band-gap frequency. The frequency is set to 123 Hz and all the PZT patches are set to SC status. Results are shown in Figures 3.30 and 3.31.

4. Damped waveguide working at a band-gap frequency. The frequency is set to 123 Hz and each PZT patche is shunted to a resistor with $1 \times 10^5\,\Omega$. Results are shown in Figures 3.32 and 3.33.

In all the situations, good agreements can be seen between the full FEM and FEM-WFEM hybrid models. The wave propagating features in periodic substructure is different

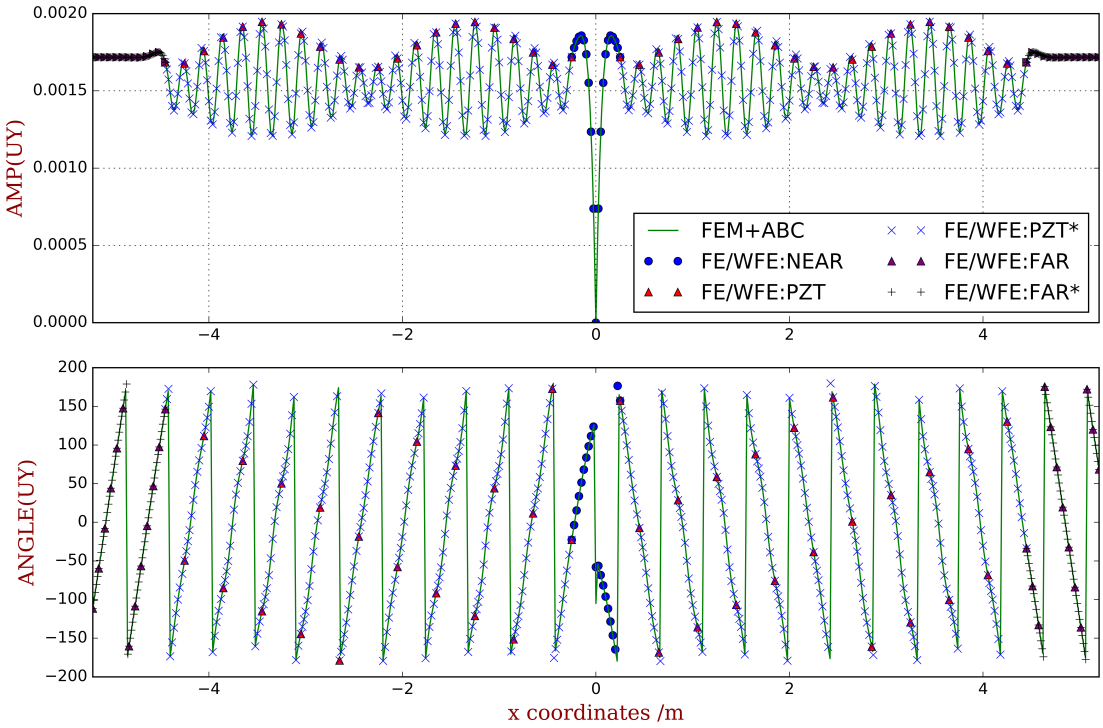

Figure 3.26: Harmonic deformation of the built-up structure at a propagating frequency of the flexural wave (100 Hz). All the PZT patches are set to SC status.

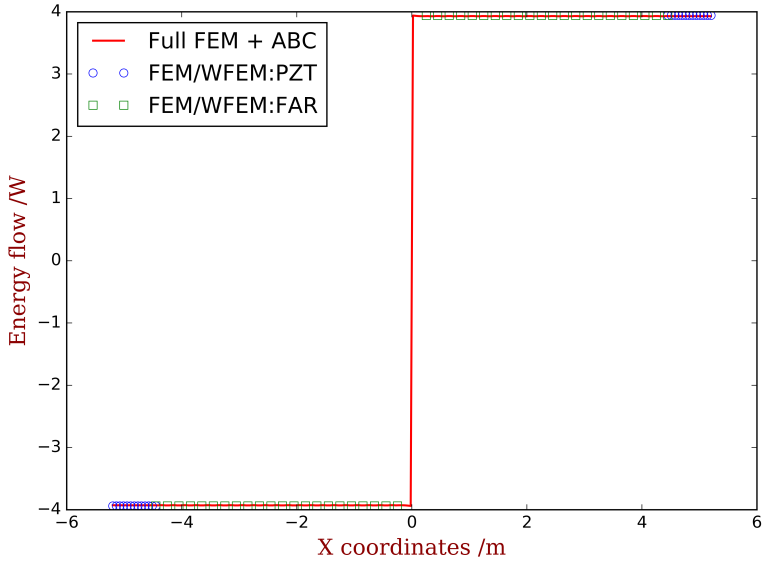

Figure 3.27: Energy flow of the built-up structure at a propagating frequency of the flexural wave (100 Hz). All the PZT patches are set to SC status.

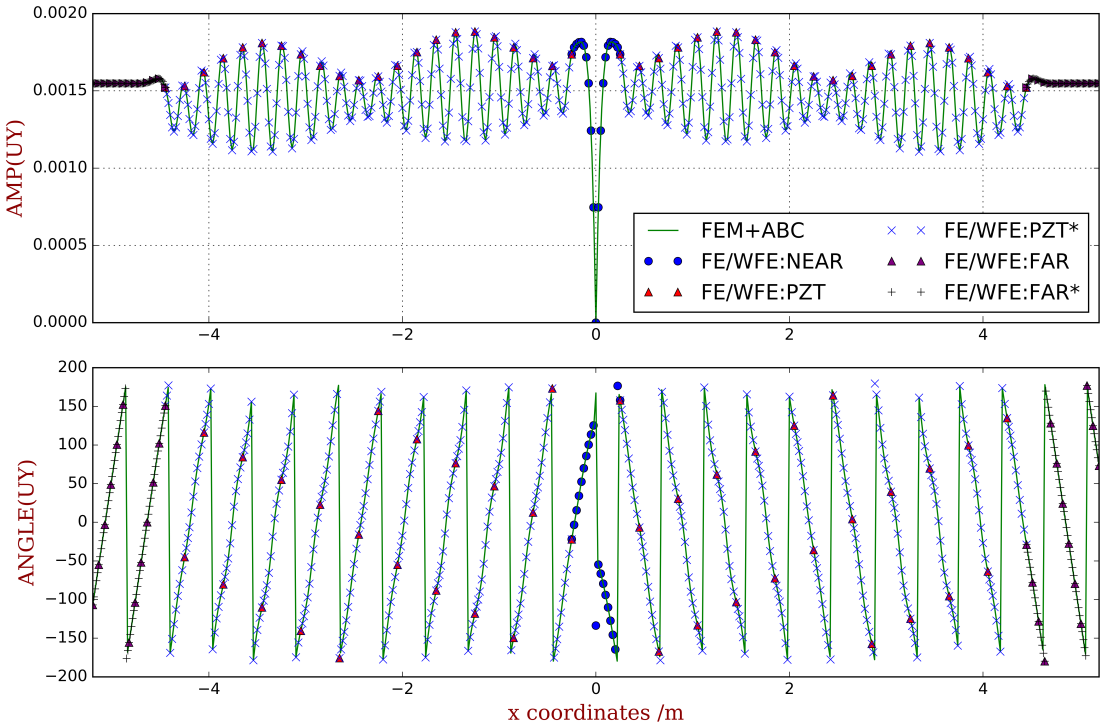

Figure 3.28: Harmonic deformation of the built-up structure at a propagating frequency of the flexural wave (100 Hz). Each PZT patch is shunted with a Resistor with $1 \times 10^5\,\Omega$.

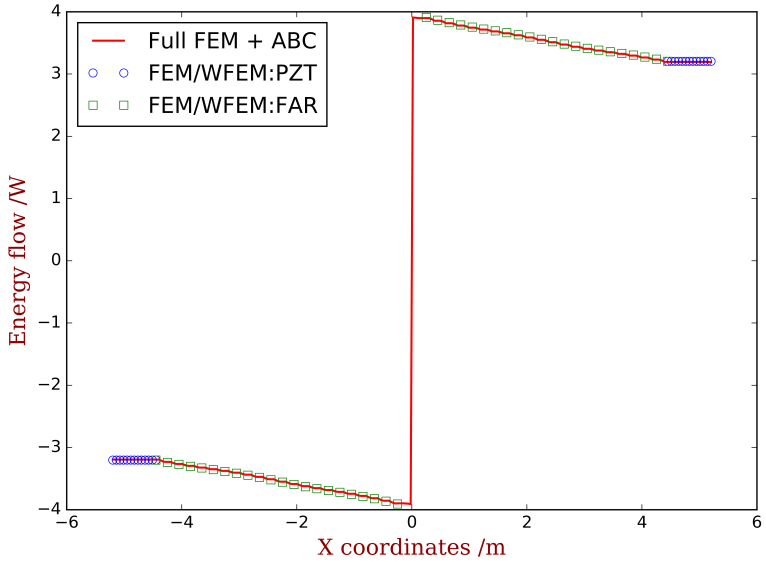

Figure 3.29: Energy flow of the built-up structure at a propagating frequency of the flexural wave (100 Hz). Each PZT patch is shunted with a Resistor with $1 \times 10^5\,\Omega$.

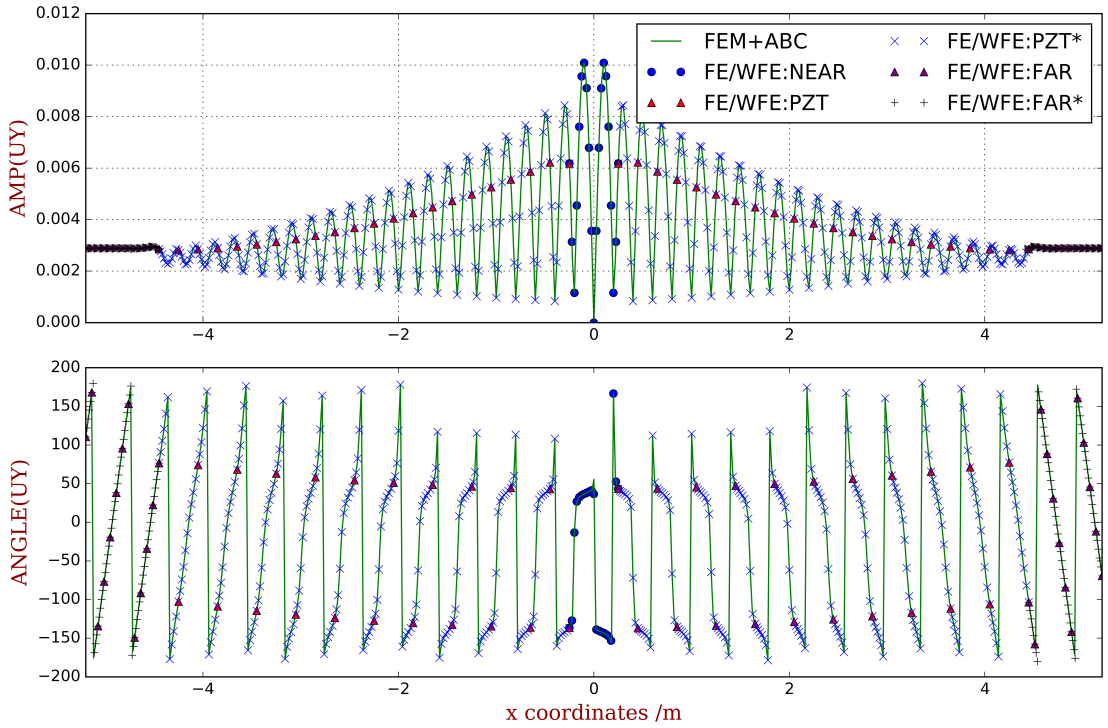

Figure 3.30: Harmonic deformation of the built-up structure at a band-gap frequency of the flexural wave (123 Hz). All the PZT patches are set to SC status.

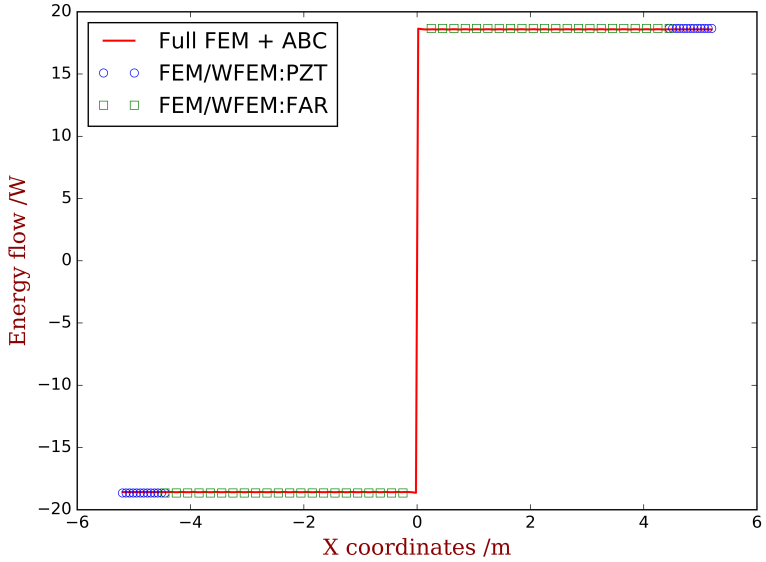

Figure 3.31: Energy flow of the built-up structure at a band-gap frequency of the flexural wave (123 Hz). All the PZT patches are set to SC status.

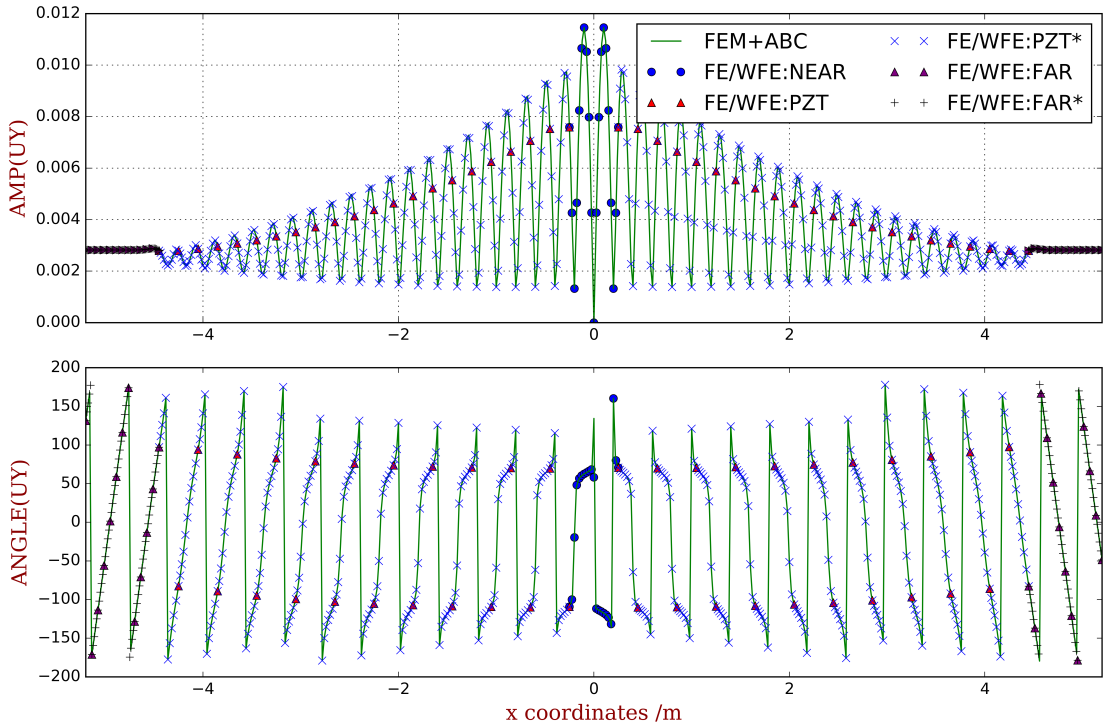

Figure 3.32: Harmonic deformation of the built-up structure at a band-gap frequency of the flexural wave (123 Hz). Each PZT patch is shunted with a Resistor with $1 \times 10^5\,\Omega$.

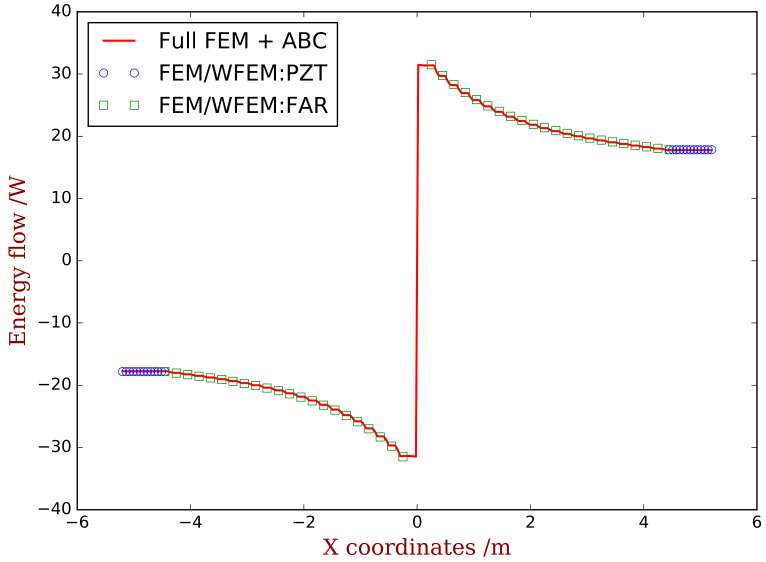

Figure 3.33: Energy flow of the built-up structure at a band-gap frequency of the flexural wave (123 Hz). Each PZT patch is shunted with a Resistor with $1 \times 10^5\,\Omega$.

from the uniform case (Figure 3.10). Two scales of deformation can be seen in Figure 3.26, representing the dynamics of the waveguide and of the unit cell. When damping exists, the energy low is decaying in space (Figure 3.29) and the waves become oscillating decaying (Figure 3.29). When the waveguide works in a band-gap frequency, the deformation becomes decaying in space (Figure 3.30) but a constant energy flow can be observed (Figure 3.31). This actually acknowledges the fact that evanescent waves can also carry energy as indicated by Ref. [194].

It is interesting to see that this energy flow is even larger than the case where the waveguide works in a propagating frequency 3.26. This means that a band gap in the periodic substructure does not directly link to a low-vibration and low-energy-flow frequency range of the built-up structure. However, only by analyze the wave characteristics of the waveguide in isolation one could not observe this phenomenon.

3.5 Conclusions

A general multi-scale numerical tool for computing the forced response and energy flow is proposed in this chapter. The method can be applied for complex structures with both periodic and non-periodic parts. The major numerical strategy is to model the non-periodic part by FEM and the waveguides by WFEM, and then to adapt the models of the substructures. Owing to the use of WFEM, when the number of unit cells is increasing, the CPU time would not be significantly increased.

A reduced model for WFEM is proposed for the cases when there are piezoelectric material and shunts in the unit cells. It modifies the work of Zhou et al. [88] by excluding the electric DOFs from the reduction process. The proposed reduction process is independent with the electric impedance so it has advantages when designing a piezoelectric system where repetitive calculations are required. An enhanced eigenvalue scheme is proposed to mitigate the ill-conditioning. The reduced model allows us to capture the dynamics of unit cell by few unit cell modes. The use of this reduced model can further accelerate the analysis of the FEM-WFEM approach. To do that the use of left eigenvectors are necessary. The FEM-WFEM framework does not constrain the use of any reduced models for WFEM, so the methods presented in chapter 2 can also be applied.

The hybrid FEM-WFEM approach was validated by variety of situations, where models based on analytical solutions, beam-level and solid level finite elements are used as references. The correlation of results attest that the proposed method is accurate for both wave-dominated infinite structures and mode-dominated finite structures. Especially, the use of resistor and resistor-inductor shunting circuits are also validated.

Some preliminary results concerning the energy flow through piezoelectric waveguide to the infinite far-field is presented. We show that *a band gap in the periodic substructure does not directly link to a low-vibration and low-energy-flow frequency range of the built-up structure*. This is due to the fact that a finite substructure working in band gap can not reflecting all the injected energy flow. In such situations indeed the displacement is decaying in space but the energy flow remain constant (not zero). The only way to 'attenuate' the energy is the damping mechanism. These results underline the necessity of designing waveguides by integrating it into the host structure rather than designing in isolation.

Chapter 4

Wave electromechanical coupling factor for the guided waves in periodic piezoelectric structures

Abstract: This chapter addresses the evaluation of electromechanical coupling for the guided waves in piezoelectric composites. The Wave Electromechanical Coupling Factor (WEMCF) is defined by two different ways, leading to a frequency formula and an energy formula. During the passage of one wave, we show that the fraction of electric energy over the mechanical one is linked to the variance between the open-circuit and short-circuit propagating frequencies with the same wavenumber. If an appropriate indicator is chosen for the electric energy, the WEMCF is consistent with the Modal Electromechanical Coupling Factor (MEMCF) when a wave shape is also a modal shape of the structure. This could happen at the border frequencies of a band gap. By using the Wave and Finite Element Method (WFEM), WEMCF can be calculated via post-processing. Using the model reduction scheme proposed in Chapter 3, the calculation can be further simplified and accelerated. The analytical findings are validated by numerical results. An application is given based on a built-up structure with periodic piezoelectric substructures, showing the strong correlation between WEMCF and the best energy transmission loss of the resistive PZT waveguide.

Contents

4.1 Introduction

The electromechanical coupling factor (EMCF) has important influences in many applications of piezoelectric structures, such as vibration control, actuating and sensing. In terms of structural modes, the Modal Electromechanical Coupling Factor (MEMCF) can either be estimated by the open-circuit (OC) and short-circuit (SC) natural frequencies [6] or by an energy-based formula [64]. A detailed review can be found in section 1.3.

However, in terms of waves, few criteria are available. Chen et al. [65] calculated EMCF by $k = (V_{\text{oc}} - V_{\text{sc}})/V_{\text{sc}}$ for Rayleigh-type surface acoustic waves in a semi-infinite with alternating piezoelectric and non-piezoelectric super-lattices, where V_{oc} and V_{sc} are the group velocity in open-circuit and short-circuit situation respectively. Fan et al. [66] used the Green's function method to calculate the EMCF for a Lamb wave in a multi-layered plate. To the author's knowledge, no research effort has been devoted to evaluate the EMCF for the guided waves in 1D and 2D periodic structures.

In this chapter, the EMCF for guided waves will be addressed, termed Wave Electromechanical Coupling Factor (WEMCF). We will first present some preliminary discussions to show the main concerns when defining the WEMCF: the first one is the consistency with the MEMCF; and the second one is the estimation of WEMCF for general piezoelectric waveguides. To address the first challenge an energy formula is proposed and analytically demonstrated. To address the second concern, Wave and Finite Element Method (WFEM) is employed to calculate the WEMCF as a post-process of the free wave analysis. A numerical example is shown, validating the analytical findings. It is also shown that the use of the reduced unit cell model can rapidly and accurately capture the WEMCF. After that the control of energy flow for a built-up structure is considered as an application. Two configurations of the PZT waveguide with different WEMCF are optimized respectively in order attenuate the energy flow. We show that the best performance of the resistive waveguide is strongly correlated to the WEMCF.

4.2 Preliminary discussions

According to the literature [123], when all the piezoelectric patches of a periodic structure are set to the SC or OC statuses. Different dispersion curves will be observed, as illustrated in Figure 4.1. This implies that we can use the relative difference of the propagating frequencies of OC and SC statues to define the WEMCF as what have been done concerning MEMCF [2, 6, 64].

Note that the deformation of the unit cell at the border frequencies of a band gap, namely A B and C in Figure 4.1, are also the modal shapes of the unit cell under certain boundaries conditions [96]. This fact indicates that the coupling strength of these waves (A, B and C) can also be given by MEMCF, writes

$$\mathcal{K}_{\text{W}}^2 = \frac{\omega_{\text{OC}}^2 - \omega_{\text{SC}}^2}{\omega_{\text{SC}}^2} \tag{4.1}$$

where ω_{OC} and ω_{SC} are open and short circuit natural frequencies. Extending Equation (4.1) at other frequencies leads to an definition of WEMCF. The main advantage of this definition is that it allows WEMCF to be consistence with MEMCF at the border frequencies of a band gap. It is reasonable for a same deformation of the unit cell to

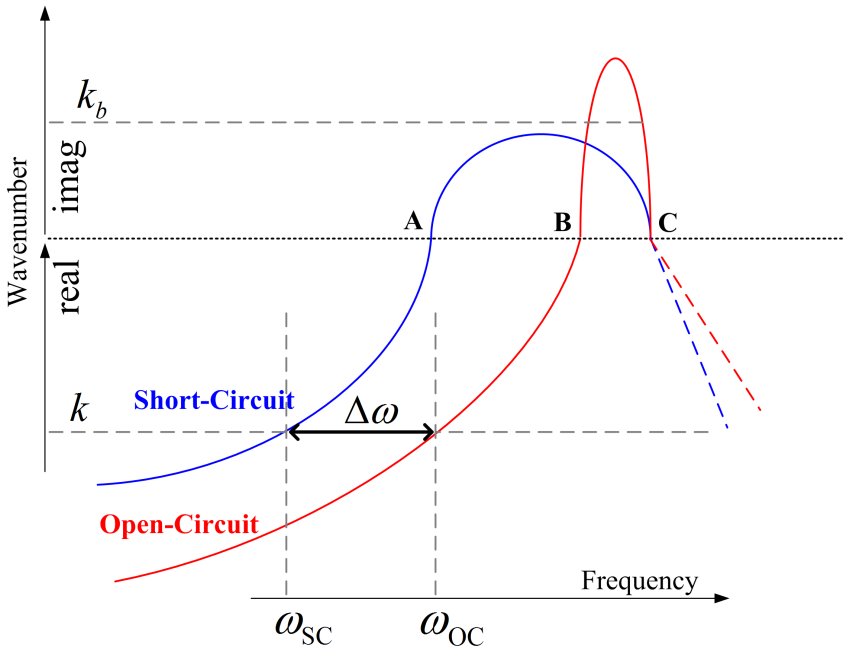

Figure 4.1: Illustration of dispersion curves for OC and SC status of a piezoelectric waveguide.

be given a same number of its electromechanical feature, no matter the deformation is understood as a wave or a mode.

Definition of WEMCF by Equation (4.1) may be reasonable and intuitive. But there are two main challenges. The first one is that Equation (4.1) works only for propagating waves, because band gaps may have different depth in OC and SC statuses, shown in Figure 4.1. Consequently it is difficult to link the evanescent waves between OC and SC. The second challenge is related to computational issues. For complex waveguide whose dispersion relations has wave veering and intersection (see the example in Chapter 6), it will be difficult to recognize same type of propagating waves from the dispersion relations at OC and SC statues.

Alternatively, inspired by the dual formula for MEMCF, we may also WEMCF by the fraction of certain energy fractions at one electrode status:

$$\mathcal{K}_1^2 = \frac{W_\mathrm{e}}{V} \tag{4.2}$$

where W_e is the electric energy and V is the mechanical energy. This alternative definition works for both evanescent waves and propagating waves. It only requires the dispersion curves at one situation so no efforts are needed to link the waves between OC and SC.

Wave shapes have to be known to quantitatively calculate W_e and V. Wave and Finite Element Method (WFEM) can be employed to analyze the wave shapes. More importantly the energies can be calculated by the reduced model with a smaller number of DOFs. This way the computing of WEMCF can be accelerated.

In the following sections we will present two different ways for the calculation of the energy terms in Equation (4.2). Since the consistency with MEMCF is strongly desired, that means the one gives more accurate approximation of Equation (4.1) is of

more interest. During the following discussions, some conclusions of the inverse formula of WFEM are required in the analytical derivation. For the sake of clarity we will first briefly review the inverse formula of WFEM before the introduction of two implementations of WFEM. Note that the inverse formula is just used to demonstrate some properties of the WEMCF, when it comes to calculations the direct formula presented in the previous chapters are used.

4.3 WFEM with inverse formula

As discussed in previous chapters, in absence of any external loads and neglecting damping, the dynamic equations of a unit cell in the periodic piezoelectric structure write

$$\mathbf{M}\begin{pmatrix}\ddot{\mathbf{q}}_{\mathrm{L}}\\ \ddot{\mathbf{q}}_{\mathrm{R}}\\ \ddot{\mathbf{q}}_{\mathrm{I}}\\ \ddot{\mathbf{q}}_{\mathrm{E}}\end{pmatrix}+\mathbf{K}\begin{pmatrix}\mathbf{q}_{\mathrm{L}}\\ \mathbf{q}_{\mathrm{R}}\\ \mathbf{q}_{\mathrm{I}}\\ \mathbf{q}_{\mathrm{E}}\end{pmatrix}=\begin{pmatrix}\mathbf{f}_{\mathrm{L}}\\ \mathbf{f}_{\mathrm{R}}\\ \mathbf{0}\\ \mathbf{0}\end{pmatrix} \tag{4.3}$$

Subscripts L, R, I and E respectively refer to the left-side, right-side and internal mechanical DOFs and the electric voltage DOFs, illustrated in Figure 4.2. Specifically, the mass matrix has the form of

$$\mathbf{M}=\begin{bmatrix}\mathbf{M}_{\mathrm{LL}} & \mathbf{M}_{\mathrm{LR}} & \mathbf{M}_{\mathrm{LI}} & \mathbf{0}\\ \mathbf{M}_{\mathrm{LR}}^{\mathrm{T}} & \mathbf{M}_{\mathrm{RR}} & \mathbf{M}_{\mathrm{RI}} & \mathbf{0}\\ \mathbf{M}_{\mathrm{LI}}^{\mathrm{T}} & \mathbf{M}_{\mathrm{RI}}^{\mathrm{T}} & \mathbf{M}_{\mathrm{II}} & \mathbf{0}\\ \mathbf{0} & \mathbf{0} & \mathbf{0} & \mathbf{0}\end{bmatrix} \tag{4.4}$$

and the generalized stiffness matrix $\mathbf{K}$ writes

$$\mathbf{K}=\begin{bmatrix}\mathbf{G} & -\mathbf{P}\\ \mathbf{P}^{\mathrm{T}} & \mathbf{C}_{\mathrm{p}}+\mathbf{Y}\end{bmatrix} \tag{4.5}$$

where $\mathbf{G}$ refers to the mechanical stiffness, $\mathbf{P}$ the piezoelectric matrices, $\mathbf{C}_{\mathrm{p}}$ the intrinsic capacitance matrix and $\mathbf{Y}$ external electric impedance.

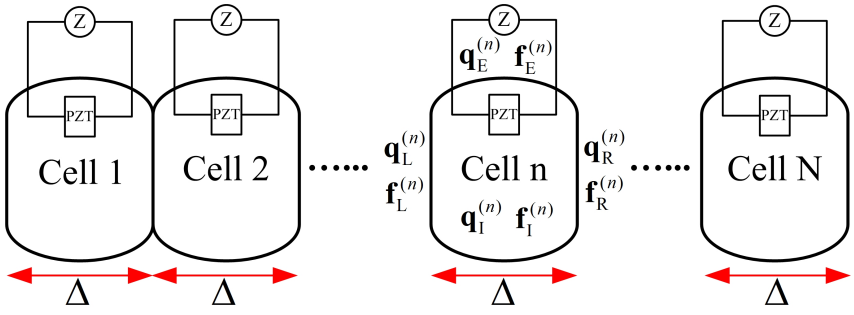

Figure 4.2: Illustration of the periodic piezoelectric structure.

According to the Bloch theory, the wave of the form $e^{j\omega t-kx}$ that travels in the periodic structure should satisfy the condition

$$\mathbf{q}_{\mathrm{R}}=\lambda\mathbf{q}_{\mathrm{L}} \tag{4.6}$$

where $\lambda = e^{-jk\Delta}$; k is the wavenumber and Δ is the length of the unit cell. Additionally, the equilibrium between the adjacent cells implies

$$\mathbf{f}_{\mathrm{R}} = -\lambda \mathbf{f}_{\mathrm{L}} \tag{4.7}$$

Equation (4.6) and (4.7) can be rewritten into matrix forms, as

$$\mathbf{q} = \begin{pmatrix} \mathbf{q}_{\mathrm{L}} \\ \mathbf{q}_{\mathrm{R}} \\ \mathbf{q}_{\mathrm{I}} \\ \mathbf{q}_{\mathrm{E}} \end{pmatrix} = \begin{bmatrix} \mathbf{I} & \mathbf{0} & \mathbf{0} \\ \lambda\mathbf{I} & \mathbf{0} & \mathbf{0} \\ \mathbf{0} & \mathbf{I} & \mathbf{0} \\ \mathbf{0} & \mathbf{0} & \mathbf{I} \end{bmatrix} \begin{pmatrix} \mathbf{q}_{\mathrm{L}} \\ \mathbf{q}_{\mathrm{I}} \\ \mathbf{q}_{\mathrm{E}} \end{pmatrix} = \mathbf{T}_{\mathrm{b}} \hat{\mathbf{q}} \tag{4.8}$$

and

$$\begin{bmatrix} \mathbf{I} & \lambda^{-1}\mathbf{I} & \mathbf{0} & \mathbf{0} \\ \mathbf{0} & \mathbf{0} & \mathbf{I} & \mathbf{0} \\ \mathbf{0} & \mathbf{0} & \mathbf{0} & \mathbf{I} \end{bmatrix} \begin{pmatrix} \mathbf{f}_{\mathrm{L}} \\ \mathbf{f}_{\mathrm{R}} \\ \mathbf{f}_{\mathrm{I}} \\ \mathbf{f}_{\mathrm{E}} \end{pmatrix} = \mathbf{T}_{\mathrm{e}} \mathbf{f} = \begin{pmatrix} \mathbf{0} \\ \mathbf{0} \\ \mathbf{0} \end{pmatrix} \tag{4.9}$$

Introducing these two transformations to Equation (4.3), by per-multiplying $\mathbf{T}_{\mathrm{e}}$ and multiplying $\mathbf{T}_{\mathrm{b}}$ at both sides of the equation, we have

$$-\omega^2 \hat{\mathbf{M}} \hat{\mathbf{q}} + \hat{\mathbf{K}} \hat{\mathbf{q}} = \mathbf{0} \tag{4.10}$$

where

$$\hat{\mathbf{M}} = \mathbf{T}_{\mathrm{e}} \mathbf{M} \mathbf{T}_{\mathrm{b}} \tag{4.11}$$

$$\hat{\mathbf{K}} = \mathbf{T}_{\mathrm{e}} \mathbf{K} \mathbf{T}_{\mathrm{b}} \tag{4.12}$$

With a given wavenumber k, eigenvalue problem (4.10) yields a group of solutions in pair $(\omega, \hat{\mathbf{q}})$. The overall number of solutions for one wavenumber equals to the number of DOFs in one unit cell. Each of them represents a wave with shape $\mathbf{q} = \mathbf{T}_{\mathrm{e}} \hat{\mathbf{q}}$ that propagate at frequency ω and wavenumber k. For a 1D periodic structure, the wavenumber k can complex numbers but the imaginary parts are of limited values (according to band gaps or damping). This means that not for any given $k \in \mathbb{C}$ there is a solution of Equation (4.10). Generally we only search for solutions when $k \in \mathbb{R}$ and according the periodicity $k \in [-\pi, \pi]$, this only gives the dispersion curves of the propagating waves. For these reasons in this thesis we always use the direct formula (giving ω, searching for wavenumber and wave shapes) to analyze the full dispersion curves. Here we introduce the inverse formula just to provide some equations required in the following sections, such as Equation (4.10), (4.11) and (4.12).

4.4 Wave electromechanical coupling factor (WEMCF)

4.4.1 Two implementations

Suppose the OC dispersion curves have already been found by WFEM. For a wave with shape $\phi_{\mathrm{OC}} = \begin{pmatrix} \phi_{\mathrm{L}}^{\mathrm{T}} & \phi_{\mathrm{R}}^{\mathrm{T}} & \phi_{\mathrm{I}}^{\mathrm{T}} & \phi_{\mathrm{E}}^{\mathrm{T}} \end{pmatrix}^{\mathrm{T}}$, wavenumber k and frequency ω_{OC}. Two implementations of Equation (4.2) for WEMCF are propose, as

$$\mathcal{K}_{1f}^2 = \frac{W_{\mathrm{free}}}{V} \tag{4.13}$$

and

$$\mathcal{K}_{1b}^2 = \frac{W_{\text{block}}}{V} \tag{4.14}$$

where

$$V = (\phi_{\text{OC}}^*)^{\text{H}} \mathbf{G} \phi_{\text{OC}}^* \tag{4.15}$$

is the mechanical potential energy, and

$$W_{\text{free}} = \phi_{\text{E}}^{\text{H}} \left(\mathbf{C}_{\text{p}} + \mathbf{P}^{\text{T}} \mathbf{G}^{-1} \mathbf{P} \right) \phi_{\text{E}} \tag{4.16}$$

is the electric potential energy stored in the free intrinsic capacitance which is the capacitance when imposing $\mathbf{f}_{\text{L}} = \mathbf{f}_{\text{R}} = \mathbf{f}_{\text{I}} = \mathbf{0}$. Moreover,

$$W_{\text{block}} = \phi_{\text{E}}^{\text{H}} \mathbf{C}_{\text{p}} \phi_{\text{E}} \tag{4.17}$$

is the electric potential energy stored in the block capacitance which is $\mathbf{C}_{\text{p}}$, and

$$\phi_{\text{OC}}^* = \begin{pmatrix} \phi_{\text{L}}^{\text{T}} & \phi_{\text{R}}^{\text{T}} & \phi_{\text{I}}^{\text{T}} & \mathbf{0} \end{pmatrix}^{\text{T}} \tag{4.18}$$

for the simplification of equations. Both $\mathcal{K}_{1f}^2$ and $\mathcal{K}_{1b}^2$ are the approximations of $\mathcal{K}_{\text{W}}^2$ based on different assumptions. The demonstrations are given as follows.

4.4.2 Demonstrations

If the wave is a propagating one, wavenumber k is a real number therefore λ is a complex value with amplitude 1. Consequently $\mathbf{T}_{\text{b}}$ in Equation (4.8) is the conjugate transpose of $\mathbf{T}_{\text{e}}$ in Equation (4.9), namely

$$\mathbf{T}_{\text{b}} = \mathbf{T}_{\text{e}}^{\text{H}} \tag{4.19}$$

Introducing the open-circuit eigenvector $\hat{\mathbf{q}} = \hat{\phi}_{\text{OC}} = \begin{pmatrix} \phi_{\text{L}}^{\text{T}} & \phi_{\text{I}}^{\text{T}} & \phi_{\text{E}}^{\text{T}} \end{pmatrix}^{\text{T}}$ into Equation (4.10) and multiplying both sides of the equation by $\hat{\phi}_{\text{OC}}^{\text{H}}$, it gives

$$\omega_{OC}^2 = \frac{\hat{\phi}_{\text{OC}}^{\text{H}} \hat{\mathbf{K}} \hat{\phi}_{\text{OC}}}{\hat{\phi}_{\text{OC}}^{\text{H}} \hat{\mathbf{M}} \hat{\phi}_{\text{OC}}} \tag{4.20}$$

and according to Equations (4.19), (4.11) and (4.12), we know

$$\hat{\phi}_{\text{OC}}^{\text{H}} \hat{\mathbf{K}} \hat{\phi}_{\text{OC}} = \phi_{\text{OC}}^{\text{H}} \mathbf{K} \phi_{\text{OC}}$$
$$\hat{\phi}_{\text{OC}}^{\text{H}} \hat{\mathbf{M}} \hat{\phi}_{\text{OC}} = \phi_{\text{OC}}^{\text{H}} \mathbf{M} \phi_{\text{OC}}$$

leading to

$$\omega_{OC}^2 = \frac{\hat{\phi}_{\text{OC}}^{\text{H}} \hat{\mathbf{K}} \hat{\phi}_{\text{OC}}}{\hat{\phi}_{\text{OC}}^{\text{H}} \hat{\mathbf{M}} \hat{\phi}_{\text{OC}}} = \frac{\phi_{\text{OC}}^{\text{H}} \mathbf{K} \phi_{\text{OC}}}{\phi_{\text{OC}}^{\text{H}} \mathbf{M} \phi_{\text{OC}}} \tag{4.21}$$

This means that once the waveshape is known, we will also know the associated wavenumber. Equation (4.21) shows such a relation in OC status, latter we will also do this in SC status. But we will not use the "real" SC waveshape to calculate SC propagating frequency but use the information in OC status to have a good guess of the SC waveshape and use it to estimate the SC propagating frequency.

4.4.2.1 Case 1

For short-circuit situation, if we assume that mechanical deformation under a same wavenumber k remains the same, namely

$$\phi_{\mathrm{SC},1} = \begin{pmatrix} \phi_{\mathrm{L}}^{\mathrm{T}} & \phi_{\mathrm{R}}^{\mathrm{T}} & \phi_{\mathrm{I}}^{\mathrm{T}} & \mathbf{0} \end{pmatrix}^{\mathrm{T}} \tag{4.22}$$

Introducing $\hat{\phi}_{\mathrm{SC},1} = \begin{pmatrix} \phi_{\mathrm{L}}^{\mathrm{T}} & \phi_{\mathrm{I}}^{\mathrm{T}} & \mathbf{0} \end{pmatrix}^{\mathrm{T}}$ into Equation (4.10) and multiplying both sides of the equation by $\hat{\phi}_{\mathrm{SC},1}^{\mathrm{H}}$, it gives

$$\omega_{SC,1}^2 = \frac{\hat{\phi}_{\mathrm{SC},1}^{\mathrm{H}} \hat{\mathbf{K}} \hat{\phi}_{\mathrm{SC},1}}{\hat{\phi}_{\mathrm{SC},1}^{\mathrm{H}} \hat{\mathbf{M}} \hat{\phi}_{\mathrm{SC},1}} = \frac{\phi_{\mathrm{SC},1}^{\mathrm{H}} \mathbf{K} \phi_{\mathrm{SC},1}}{\phi_{\mathrm{SC},1}^{\mathrm{H}} \mathbf{M} \phi_{\mathrm{SC},1}} \tag{4.23}$$

where $\omega_{SC,1}$ is an approximated frequency for the SC case. Note that $\mathbf{M}$ matrix has zero terms in the lines correspond to the electric DOFs, shown in Equation (4.4), it makes

$$\phi_{\mathrm{OC}}^{\mathrm{H}} \mathbf{M} \phi_{\mathrm{OC}} = \phi_{\mathrm{SC},1}^{\mathrm{H}} \mathbf{M} \phi_{\mathrm{SC},1} \tag{4.24}$$

According to Equation (4.22) and (4.5), there is

$$\phi_{\mathrm{OC}}^{\mathrm{H}} \mathbf{K} \phi_{\mathrm{OC}} = \phi_{\mathrm{SC},1}^{\mathrm{H}} \mathbf{K} \phi_{\mathrm{SC},1} + \phi_{\mathrm{E}}^{\mathrm{H}} \mathbf{C}_{\mathrm{p}} \phi_{\mathrm{E}} \tag{4.25}$$

Introducing Equations (4.21) and (4.23) into (4.1) and using (4.24) and (4.25), we obtain

$$\frac{\omega_{\mathrm{OC}}^2 - \omega_{\mathrm{SC},1}^2}{\omega_{\mathrm{SC},1}^2} = \frac{\phi_{\mathrm{E}}^{\mathrm{H}} \mathbf{C}_{\mathrm{p}} \phi_{\mathrm{E}}}{(\phi_{\mathrm{OC}}^*)^{\mathrm{H}} \mathbf{G} \phi_{\mathrm{OC}}^*} \tag{4.26}$$

The right-hand-side of Equation (4.26) is exactly the same as Equation (4.14). The left side of Equation (4.26) is an approximation of Equation (4.1). In this regard, we show that

$$\mathcal{K}_{\mathrm{W}}^2 \approx \mathcal{K}_{1b}^2 \tag{4.27}$$

which means that $\mathcal{K}_{1b}^2$ is an approximation of $\mathcal{K}_{\mathrm{W}}^2$ with the assumption (4.22).

4.4.2.2 Case 2

The core of the demonstration in the previous section is to guess the SC wave shape based on the OC wave shape, and it was assumed that the mechanical deformation under a same wavenumber k remains the same in the SC and OC situations. More accurately, we can remove the static contribution of the OC voltage from the mechanical field so as to approximate the SC waveshape $\phi_{\mathrm{SC},2}$. Specifically,

$$\phi_{\mathrm{SC},2} = \phi_{\mathrm{OC}} - \begin{pmatrix} \mathbf{G}^{-1}\mathbf{P}\phi_{\mathrm{E}} \\ \phi_{\mathrm{E}} \end{pmatrix} \tag{4.28}$$

$$= \phi_{\mathrm{SC},1} - \begin{pmatrix} \mathbf{G}^{-1}\mathbf{P}\phi_{\mathrm{E}} \\ \mathbf{0} \end{pmatrix} \tag{4.29}$$

Similarly, the following statement hold

$$\omega_{SC,2}^2 = \frac{\hat{\phi}_{\mathrm{SC},2}^{\mathrm{H}} \hat{\mathbf{K}} \hat{\phi}_{\mathrm{SC},2}}{\hat{\phi}_{\mathrm{SC},2}^{\mathrm{H}} \hat{\mathbf{M}} \hat{\phi}_{\mathrm{SC},2}} = \frac{\phi_{\mathrm{SC},2}^{\mathrm{H}} \mathbf{K} \phi_{\mathrm{SC},2}}{\phi_{\mathrm{SC},2}^{\mathrm{H}} \mathbf{M} \phi_{\mathrm{SC},2}} \tag{4.30}$$

and with the fact that

$$\phi_{\mathrm{OC}}^{\mathrm{H}}\mathbf{K}\phi_{\mathrm{OC}} = \phi_{\mathrm{SC},2}^{\mathrm{H}}\mathbf{K}\phi_{\mathrm{SC},2} + \phi_{\mathrm{E}}^{\mathrm{H}}\left(\mathbf{C}_{\mathrm{p}} + \mathbf{P}^{\mathrm{T}}\mathbf{G}^{-1}\mathbf{P}\right)\phi_{\mathrm{E}} \tag{4.31}$$

we can give another implementation of $\mathcal{K}_1^2$, as

$$\frac{\omega_{\mathrm{OC}}^2 - \omega_{\mathrm{SC},2}^2}{\omega_{\mathrm{SC},2}^2} = \frac{\phi_{\mathrm{E}}^{\mathrm{H}}\left(\mathbf{C}_{\mathrm{p}} + \mathbf{P}^{\mathrm{T}}\mathbf{G}^{-1}\mathbf{P}\right)\phi_{\mathrm{E}}}{(\phi_{\mathrm{OC}}^{*})^{\mathrm{H}}\mathbf{G}\phi_{\mathrm{OC}}^{*}} \tag{4.32}$$

Comparing this Equation with Equation (4.1) and (4.13), leads to

$$\mathcal{K}_{\mathrm{W}}^2 \approx \mathcal{K}_{1f}^2 \tag{4.33}$$

which means that $\mathcal{K}_{1f}^2$ is also an approximation of $\mathcal{K}_{\mathrm{W}}^2$ with the assumption (4.29).

4.5 Validations

By now we proposed three different ways to calculate WEMCF: one frequency formula (4.1) and two energy formulas (4.13) and (4.14). Considering the implementation of WFEM (full or reduced unit cell models), there are more paths for WEMCF, as shown in Figure 4.4. For the calculation of $\mathcal{K}_{\mathrm{W}}^2$, there are two ways to calculate the required SC and OC frequencies. For the $\mathcal{K}_{1\mathrm{f}}^2$ and $\mathcal{K}_{1\mathrm{b}}^2$ that are based on energy terms, the shapes of the whole unit cell are required. To do that three paths are possible: the full shapes obtained by full WFEM which is the slowest, the full shapes obtained by reduced WFEM which and the reduced shapes obtained by reduced WFEM. In combine there are 8 different ways for WFEM: 3 for $\mathcal{K}_{1\mathrm{f}}^2$, 3 for $\mathcal{K}_{1\mathrm{b}}^2$ and another 2 for $\mathcal{K}_{\mathrm{W}}^2$.

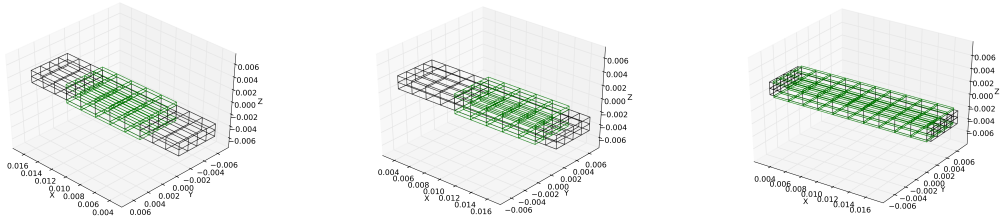

(a) (b) (c)

Figure 4.3: Unit cells of the piezoelectric waveguides considered in this chapter: (a) unit cell A which has been used in Chapter 3; (b) unit cell B which is a non-symmetric way of choosing the unit cell for the infinite periodic structure with unit cell A; (c) unit cell C which has longer PZT patches.

As mentioned, the consistency of WEMCF with MEMCF is strongly desired, and to avoid additional numerical errors, the $\mathcal{K}_{\mathrm{W}}^2$ calculated by full WFEM is regarded as reference. The piezoelectric waveguide with unit cell A shown in Figure 4.3a is used and the z-axis transverse wave is targeted. A complete numerical investigation of such 8 different paths are conducted, and the highlighted results are presented in Figure 4.5. The main observation is that all 3 paths for $\mathcal{K}_{1\mathrm{b}}^2$ have significant errors, even though the

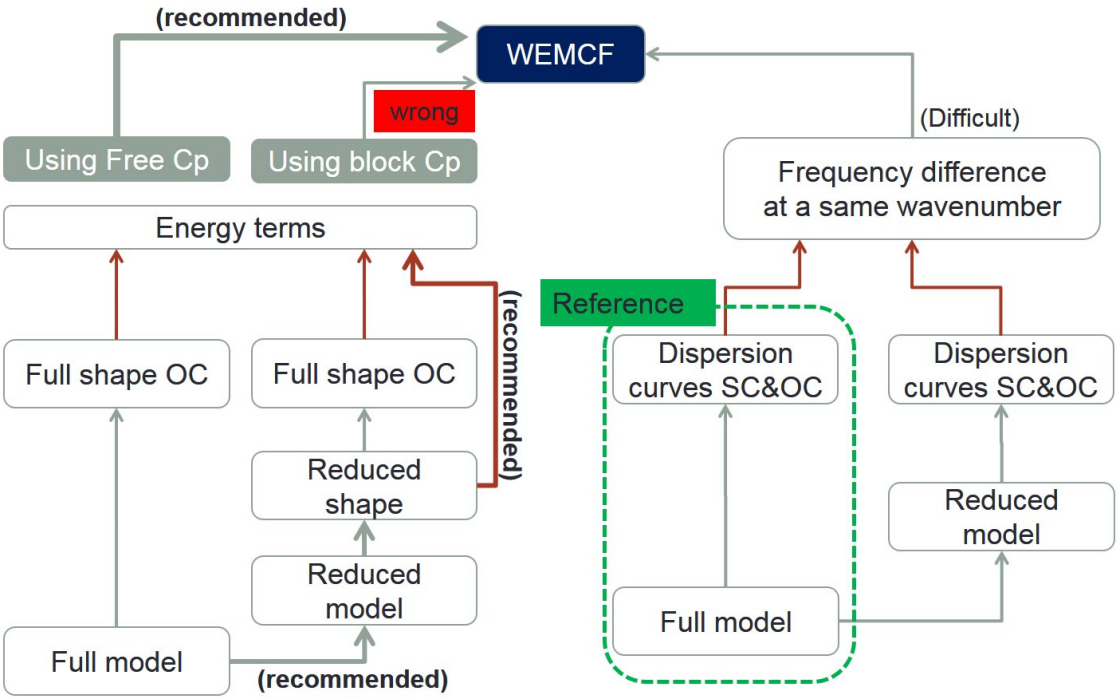

Figure 4.4: Illustration of different paths for the calculation of WEMCF in the framework of WFEM.

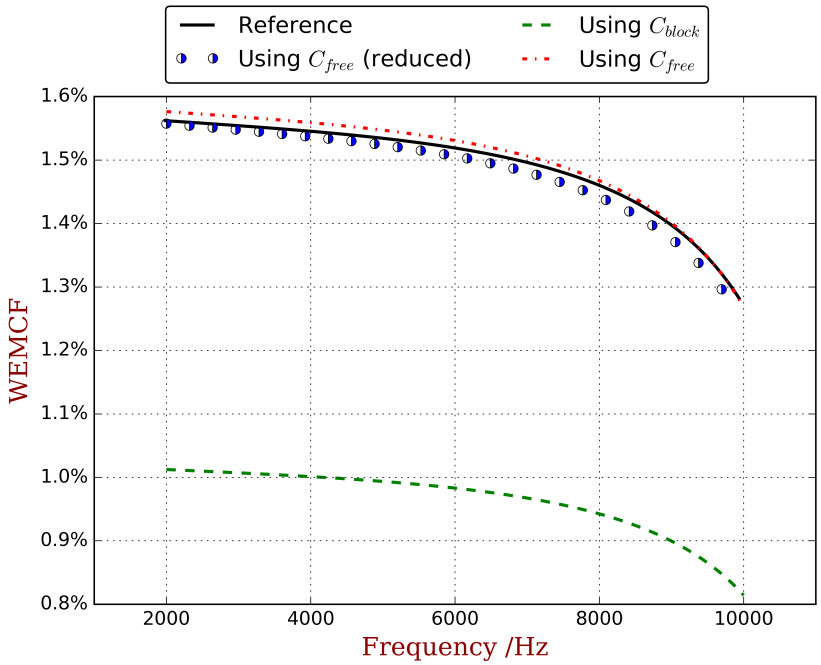

Figure 4.5: Comparison of WEMCF calculated by using: full WFEM with $\mathcal{K}_{\mathrm{W}}$ (reference), full WFEM with $\mathcal{K}_{1\mathrm{b}}$, full WFEM with $\mathcal{K}_{1\mathrm{f}}$ and reduced waveshape with $\mathcal{K}_{1\mathrm{f}}$ (recommended).

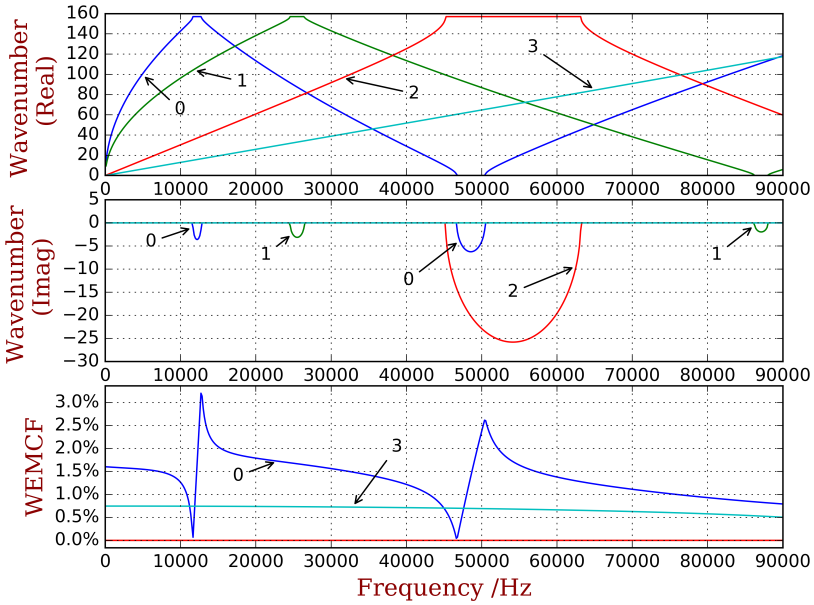

Figure 4.6: Dispersion curves and WEMCF for the piezoelectric waveguide with unit cell A: only wave 0 (z transverse) and 3 (longitudinal) has significant values.

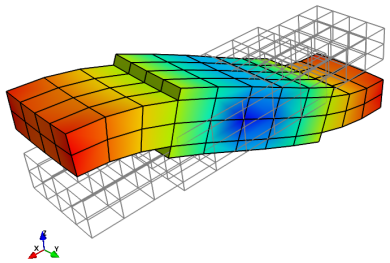

(a) 11 634 Hz: low WEMCF

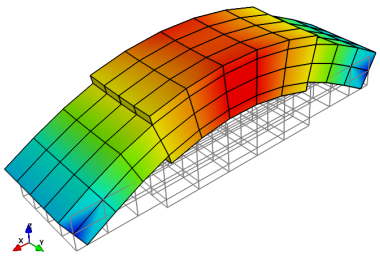

(b) 12 556 Hz: large WEMCF

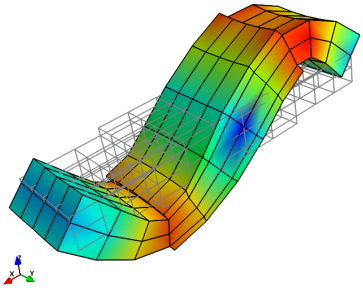

(c) 46 475 Hz: low WEMCF

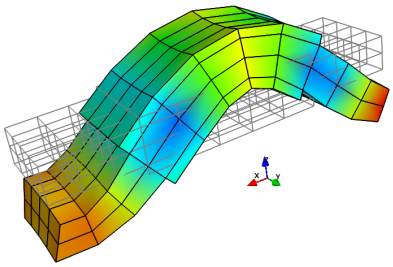

(d) 50 077 Hz: large WEMCF

Figure 4.7: Waveshape of wave 0 of unit cell A at the border frequencies of the band gaps.

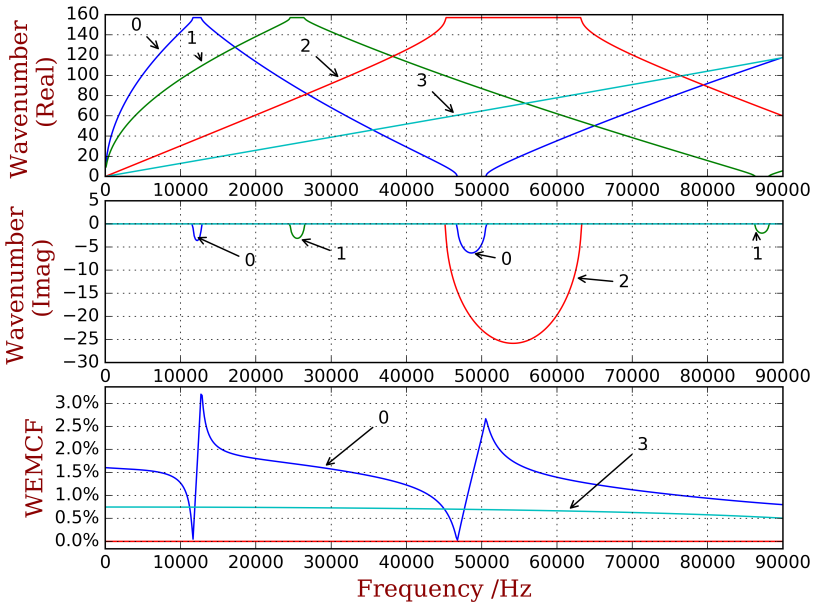

Figure 4.8: Dispersion curves and WEMCF for the piezoelectric waveguide with unit cell B; the results are the same as that with unit cell A.

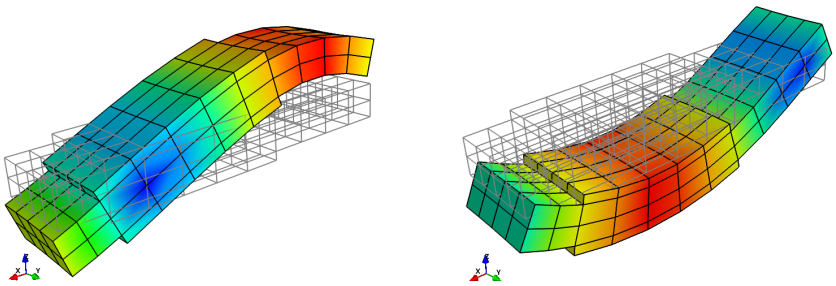

(a) 11 634 Hz: low WEMCF (b) 12 556 Hz: large WEMCF

Figure 4.9: Waveshape of wave 0 of unit cell B at the border frequencies of the band gaps.

overall tendencies are the same as the reference. The other 5 paths all return acceptable results with relative error less than 3%. This may due to the fact that assumption (4.29) is more precise than (4.22).

A complete result of WEMCF for the piezoelectric periodic structure with unit cell A is shown in Figure 4.6. It is shown that the z-axis transverse wave (wave 0) has the most significant electromechanical coupling. Weaker WEMCF is observed for the longitudinal wave. No coupling effects are reported for the torsional and y-axis waves. These conclusions can be acknowledged by the geometric configuration of the unit cell and engineering common sense. It is interesting to see that the largest and lowest values happens at the border frequencies of the band gaps. The waveshapes of these waves are presented in Figure 4.7. The symmetric wave shapes generates different kind of charges on

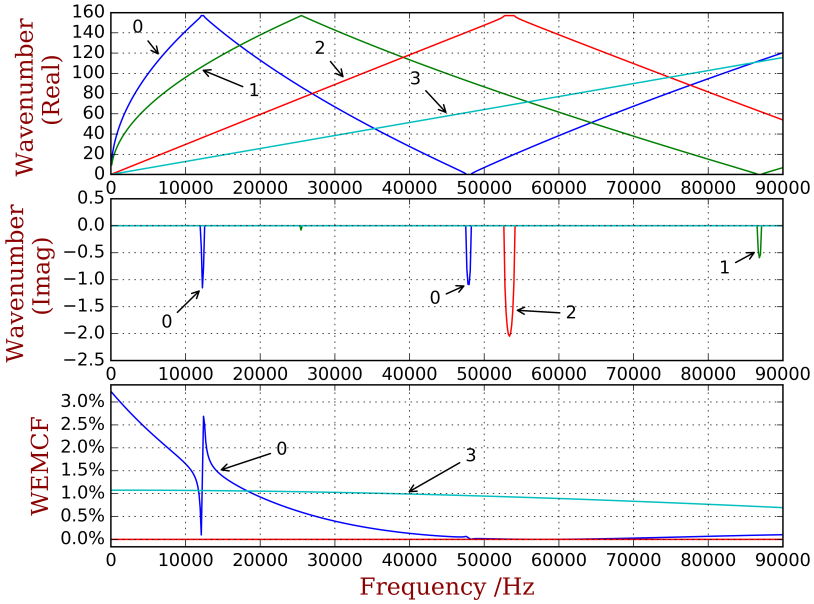

Figure 4.10: Dispersion curves and WEMCF for the piezoelectric waveguide with unit cell C.

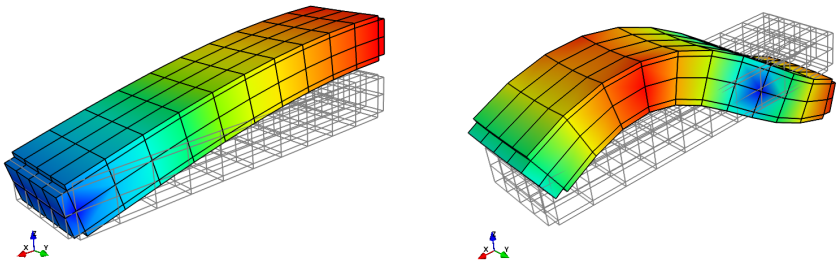

(a) (b)

Figure 4.11: Waveshape of wave 0 of unit cell C: (a) at the first propagating zone; (b) at the second propagating zone.

the electrode, canceling each other, leading to a very low WEMCF. On the contrary, anti-symmetric shapes always generate same kind of charges hence maximize the WEMCF.

As discussed, among all the valid paths, the ones using $\mathcal{K}^2_{\mathrm{W}}$ are difficult to be programmed for general cases. There remains 3 valid paths for $\mathcal{K}^2_{\mathrm{1f}}$: (1) using full shapes obtained from full WFEM; (2) using full shapes obtained from reduced WFEM; (3) using reduced shapes. The CPU time for obtaining the full dispersion characteristics with WFEM of unit cell A are compared in Figure 4.12. It shown that the post-processing for WEMCF for the full WFEM is a heavy task, and the CPU time is nearly 3 times of the free-wave analysis. While the reduced unit cell model is used, the computing time for WEMCF is reduced even still based on full wave shapes. The CPU time has the same

magnitude as the free-wave analysis. This is due to the fact that the reduced model can accelerate the mapping from the cross-section DOFs to the internal DOFs by avoiding the matrix inverse. Only minor additional time is required when reduced shapes are used to compute the energy terms for WEMCF, it reduces the post-processing by 99% in comparison to the full WFEM.

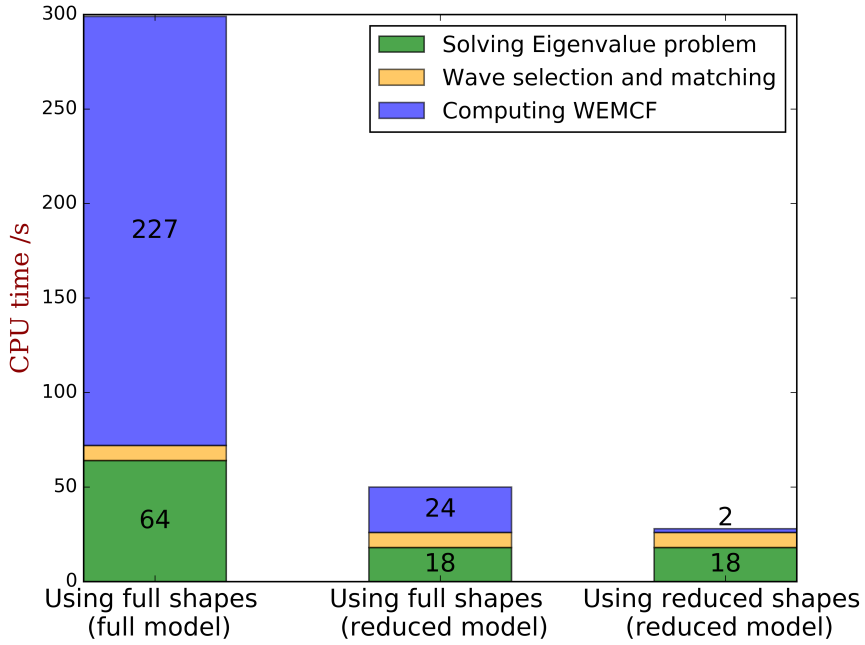

Figure 4.12: CPU time for the full dispersion characteristics with WFEM of unit cell A by the energy formula $\mathcal{K}_{1f}^2$ where the energies are calculated by: (1) using full shapes obtained from full WFEM; (2) using full shapes obtained from reduced WFEM; (3) using reduced shapes.

The infinite periodic structure with unit cell A can also be represented by an unsymmetrical unit cell B, shown in Figure 4.3b. As discussed in the literature [84], the dispersion curves should be the same as unit cell A. This conclusion is acknowledged in Figure 4.8. We also show that the WEMCF results remain the same as well. The minimal and maximal WEMCF still happen at the border frequencies of band gaps. While using the unsymmetrical unit cell, the wave shape of a unit cell no longer has symmetricity as shown in Figure 4.9, but the deformation on the PZT patches are still symmetric or anti-symmetric, leading to zero or maximum WEMCF.

Finally, we analyze the WEMCF of PZT waveguide with unit cell C, shown in Figure 4.3c. The unit cell has the same length as unit cell A and B but with longer PZT patches. The results are shown in Figure 4.10, where we observe a better WEMCF in lower frequencies than higher ones. This can be explained by checking the wave shapes shown in Figure 4.11. It can be seen that in higher frequencies the charges generated by the deformation will start to cancel each other. The comparison between unit cell A and C also acknowledges the engineering common sense that long PZT path works poorly in high frequencies.

4.6 Application: the design of resistive PZT waveguides

Let us consider a built-up structure constructed by bonding $2N$ groups of co-located piezoelectric patches onto a uniform host structure. N groups of piezoelectric patches are periodically distributed at the right side of the excitation while N other groups are located on the other side. The structure is infinite both to the left and right side. The considered host material is steel without damping, with a Young's modulus of $E = 2.11 \times 10^{11}$ Pa and a density of 7.8×10^3 kg/m^3. The used piezoelectric material is PZT4. The FEM/WFEM hybrid method described in Chapter 3 can be used to analyze the energy flow and forced response. To do that, this structure is divided into five parts: one nearfield part, two piezoelectric waveguides and two uniform far-field waveguides, as shown in Figure 4.13.

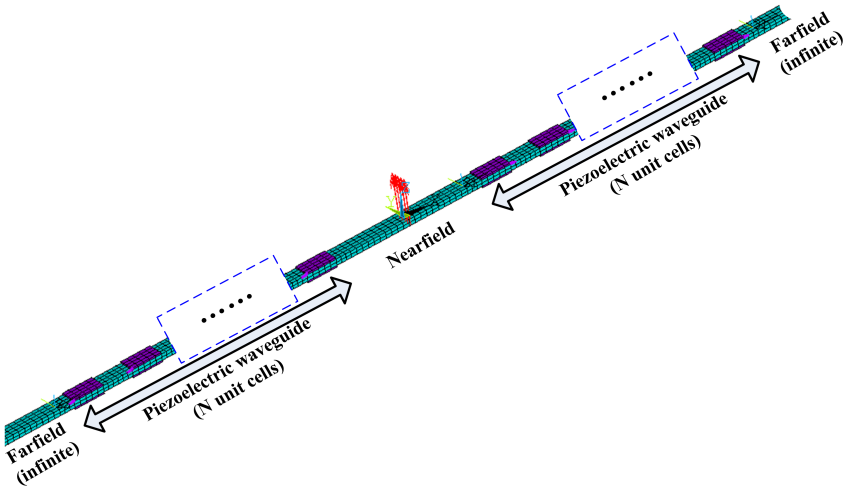

Figure 4.13: The considered built-up structure and the dividing of substructures : nearfield part, piezo-waveguides and far-field parts.

Here we fix $N = 21$ and by shunting resistors to the PZT patches, the energy flow can be attenuated. The aims are: (1) to find a criterion to represent the performance of the PZT waveguide; (2) to show the relation between the performance criterion and the WEMCF.

4.6.1 Energy transmission loss

Here we use unit cell A to construct the waveguide. Two cases of excitation applied on the nearfield are considered, where the only difference is the location of forces:

- Excitation case 1: the external forces are applied in u_z DOF of all the nodes that are located in the origin cross-section of the nearfield ($x = 0$) with an amplitude of 1 N.
- Excitation case 2: the external forces are applied in u_z DOF of all the nodes that are located in the cross-section where $x = 4 \times 10^{-3}$ m, also with an amplitude of 1 N.

The input and output power are obtained for different excitations, shown in Figure 4.14a and 4.14b respectively. Specifically, the input power is evaluated by the input forces

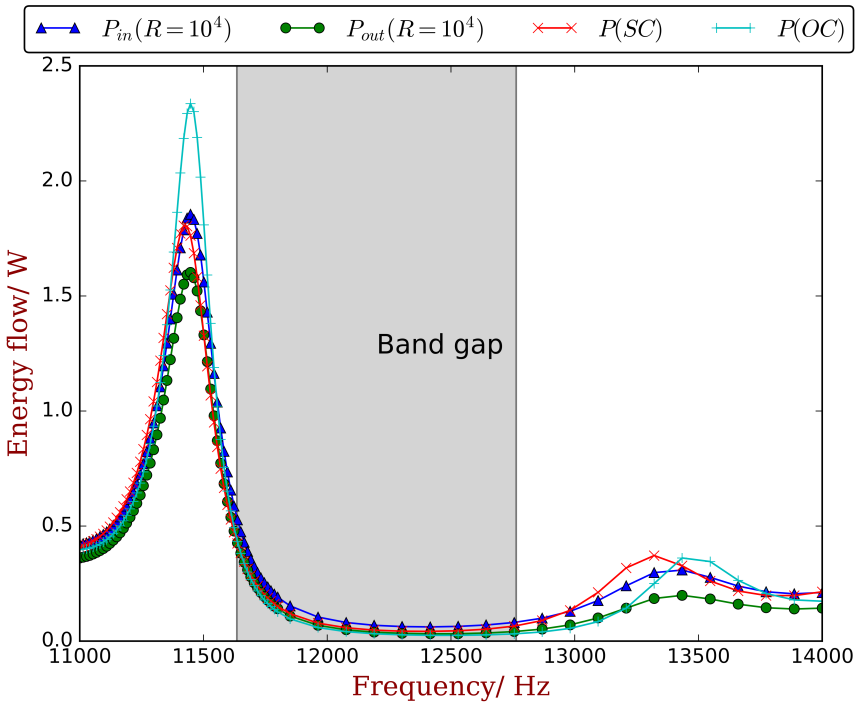

(a)

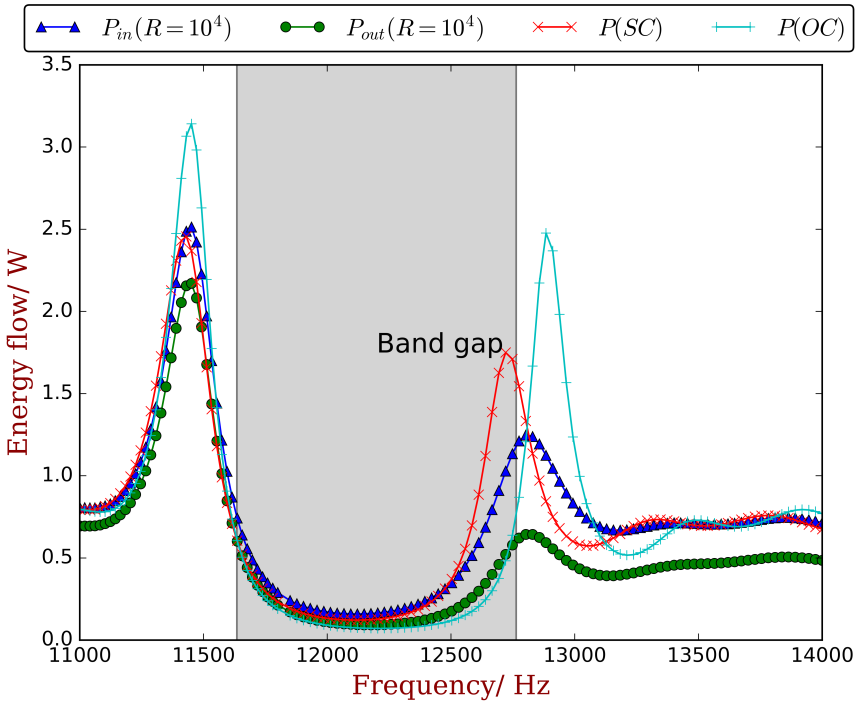

(b)

Figure 4.14: Input and outflow power caused by: (a) excitation case 1; (b) excitation case 2.

and the velocity response of the applied nodes. The output power is evaluated at the ends of the left and right piezoelectric waveguide.

For each excitation, a resistive shunt of $R = 1 \times 10^4\,\Omega$ is considered. As references, the Open-Circuit (OC), namely $R = \infty$ and the Short-Circuit (SC), namely $R = 0$ situations are also calculated. In OC and SC situations, the output power equals the input, hence in Figures 4.14a and 4.14b the input and output power are represented by same lines. Figures 4.14a and 4.14b show the influence of the electric impedance on the whole assembled system. Damping effect induced by the resistance are illustrated by the difference of the output and input power. It can be seen that an additional strong peak appears in the case 2 excitation, even in the SC situation. Interestingly, this peak is located very closely or inside the band gap. The existence of this peak in the band gap again acknowledges that a band gap may not always result in a 'low energy transmission' or 'low structural response' phenomenon.

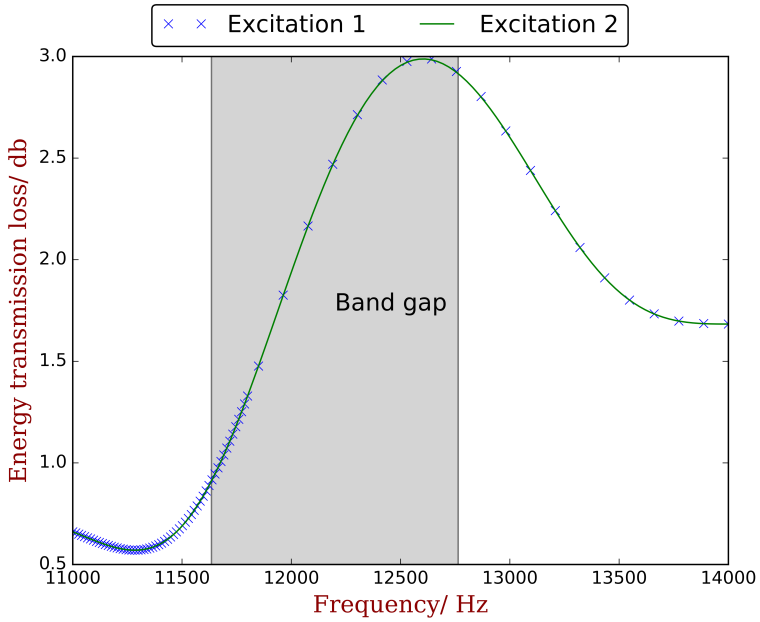

Figure 4.15: Comparison of transmission loss for excitation case 1 and case 2

Additionally, a power Transmission Loss (TL) indicator is defined as

$$\mathrm{TL} = 10 log_{10}\left(\frac{P_{\mathrm{in}}}{P_{\mathrm{out}}}\right) \tag{4.34}$$

and evaluated in both excitation cases. The results concerning power transmission loss are compared in Figure 4.15. It can be seen that the TL in the two excitations are identical. This happens because a same type of wave is excited (flexural wave along z axis), and the dissipative ability induced by the electric shunts into a wave is independent with the excitation. The peak of TL appears inside the band gap. Combining the results of energy flow, we can remark that there is no direct link between a strong dissipative ability (high TL) and a lower net energy flow. It is due to the fact that the input power is strongly affected by the nearfield natural.

By these calculation, we show that the TL is independent with the nearfield natures and we will use it to represent the energy attenuation features of a resistive PZT waveguide.

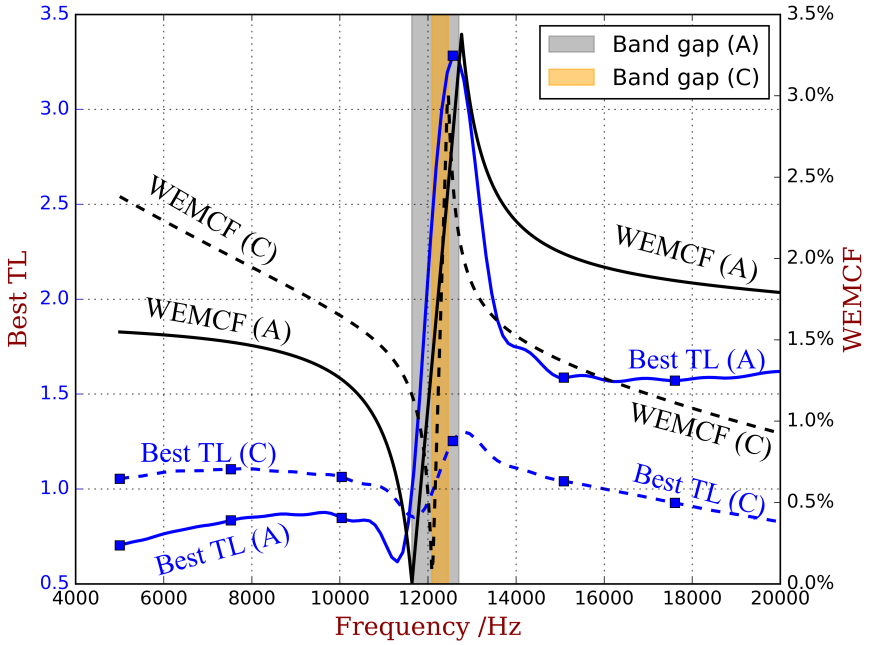

Figure 4.16: The best TL and WEMCF with respect to the frequency for PZT waveguide with unit cell A and unit cell C.

4.6.2 Optimization for the best TL

Here we still let $N = 21$ and conduct the parametric studies of TL with respect to the frequency and resistance. PZT waveguides with unit cell A and C are considered respectively, and the results are shown in Figure 4.17. It can be seen that the best TL and the associated resistance vary with frequency. Results also indicate some correlation between the best TL and the WEMCF: unit cell A has a better WEMCF in the second propagating zone; and the best TL is larger in the second propagating zone than in the first one, shown in Figure 4.17a; unit cell C has better WEMCF in the first propagating zone than the second, and a lower best TL can be observed in higher frequencies.

To illustrate this correlation more clearly, we plot the best TL with respect to the frequency when using unit cells A and C in Figure 4.16, in association with the WEMCF of wave 0 of unit cell A and C. In the first propagating zone, we can see that unit cell A has stronger WEMCF than C, and the best TL when using A is better than C. In the second propagating zone, we can see that unit cell A has weaker WEMCF than C, and the best TL when using A is weaker than C.

This correlation between WEMCF and best TL allows to compare configurations of unit cell without performing the forced response and energy analysis of the built-up structure. It means the design for the geometric and electric parameters can be done separately: first we determine the geometric parameters so as to achieve the best

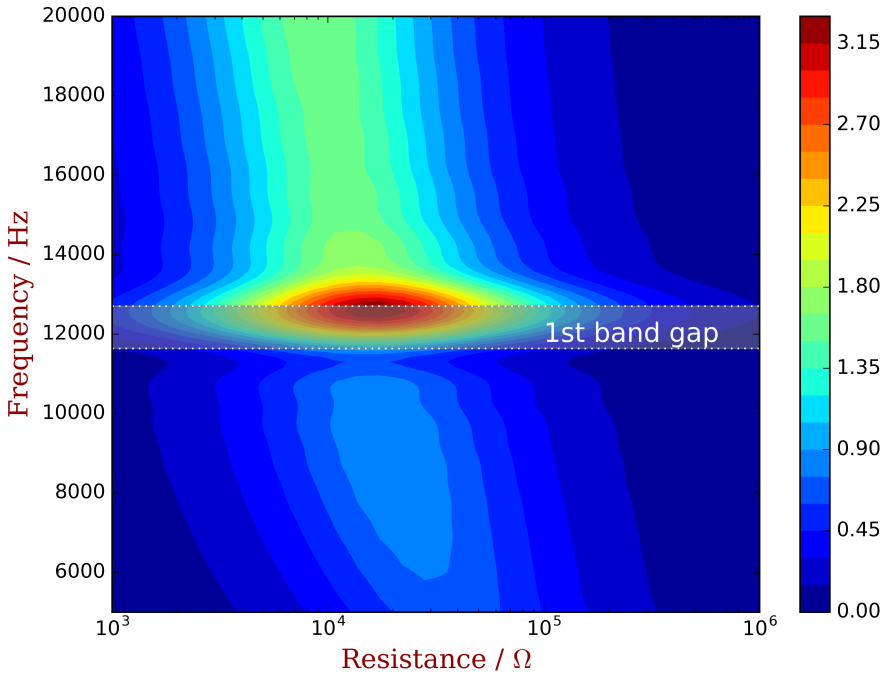

(a)

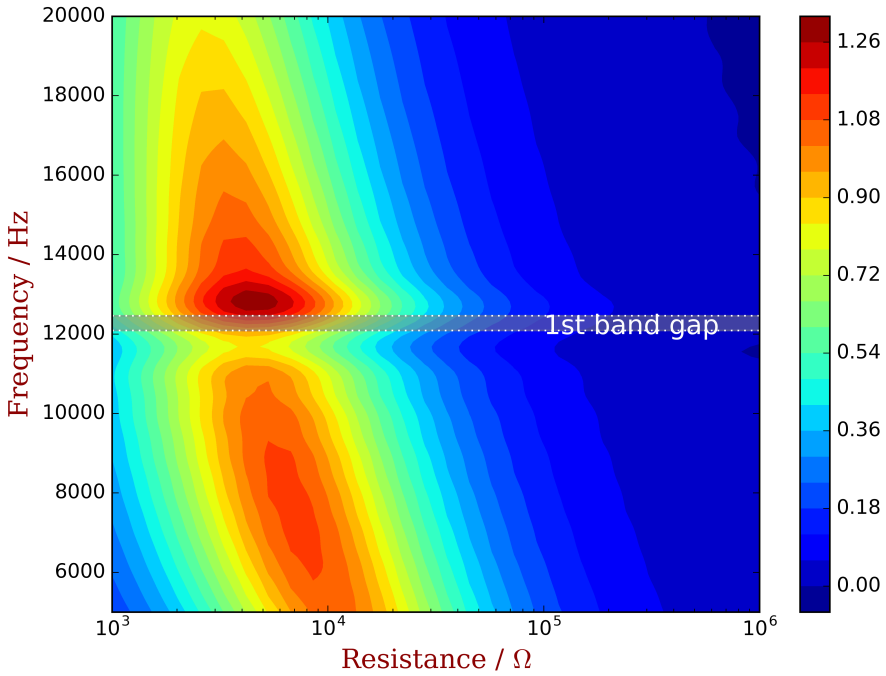

(b)

Figure 4.17: Parametric study of power transmission loss with respect to frequency and resistance, when the piezoelectric waveguides use: (a) unit cell A; (b) unit cell C.

WEMCF, only by free-wave analysis and post-processing; then we only consider the unit cell with optimized geometrics to determine the electric parameters so as to achieve the best power attenuation.

4.7 Conclusions

In this chapter we propose the concept of Wave Electromechanical Coupling Factor (WEMCF). We show that to maintain the consistency with the classical Modal Electromechanical Coupling Factor, the WEMCF should also be defined by the frequency difference of the OC and SC statues. However, this definition has difficulties in calculation for general piezoelectric waveguide for the need of computing dispersion curves twice and matching waves between SC and OC statuses. An effective energy formula for WEMCF is proposed, namely

$$\mathcal{K}_{1f}^2 = \frac{W_{\text{free}}}{V}$$

where V is the mechanical energy during the passage of the wave and W_{free} is the electric energy stored in the free intrinsic capacitance. We show that this energy formula is equivalent to the frequency formula. But with the energy formula we only need to analyze the dispersion curves once and do not need to match waves from different electrode statuses.

This indicator can be calculated as a post-processing of the WFEM. The post-processing can be time-consuming if the full WFEM is used. We recommend the use of reduced wave shapes for a fast calculation of WEMCF; it reduces the CPU time for computing WEMCF of the example structure to less than 1%.

An application is given, concerning the energy flow attenuation in a built-up structure by resistive PZT shunts. We show that the power transmission loss (TL) can be a good indicator to represent the power attenuation feature of the waveguide because it is independent with the nearfield excitation. Parametric study shows that the WEMCF is strongly correlated to the best TL. This provides more insights to understand the waveguide performance and it also allows the design for the geometric and electric parameters to be done separately.

Chapter 5

A wave-based design of semi-active piezoelectric composites for broadband vibration control

Abstract: This chapter deals with the design of periodic piezoelectric structures for broadband vibration control. By shunting identical negative capacitances to the periodically distributed piezoelectric patches, a wide and continuous band gap is created so as to cover the frequency range of interest. This way the modal density of the structure is reduced and the modal shapes are localized at the boundaries. A large proportion of the energy can then be removed or dissipated by a small number of dampers or energy harvesters integrated within the negative capacitance circuits. A design process is proposed to achieve the wide band gap. The overall amount of piezoelectric materials is constrained in order to keep mass of structures low. The Wave Electromechanical Coupling Factor (WEMCF) is used as the criterion to optimize the geometric configuration. This allows to reach the largest width of the band gap by using a stable value of negative capacitance. The control of multiple high-order modes of a cantilever beam is considered as an example. The vibration reduction performance of the designed piezoelectric structures is presented and the influences of band gap resonance, resistor and the boundary condition are discussed. The proposed approach is fully based on wave characteristics and it does not rely on any modal information. It is therefore promising for applications at mid- and high frequencies where the access to exact modal information is difficult.

Contents

5.1 Introduction

Structural vibration is among key topics in aeronautic, automotive and naval industries. It is closely related to the reliability and comfort of the vehicles. In many situations, the vibration level needs to be reduced in a wide frequency range which contains plenty of structural modes. Additionally, the vibration reduction techniques are often required to be lightweight, especially in the aeronautic and automobile industries.

Since the 1970s, piezoelectric strategies for vibration control are drawing increasing attention. The non centrosymmetric crystalline structure in piezoelectric materials endows them with the ability to transform mechanical energy into electrical one and vice versa [6]. By shunting an electric circuit one can modify the overall mechanical properties without significantly increasing the structural weight. As it was shown by Hagood et al. [18], a piezoelectric patch shunted by resistor-inductor circuit can be understood as a lightweight tuned-mass damper for the structure, hence it can be used to control a single vibration mode.

To achieve a broadband vibration control, one idea is to design a circuit with multiple tuning frequencies, where each of them can be set to one resonance frequency of the host structure. For example an applicable circuit can be made of several L-R-C branches in parallel [143], or band-pass filters in parallel [145]. However certain modes may not interact with the electric field. This happens when the shape of the electrode filters out the corresponding modal strain [2]. Consequently, even with the aforementioned circuits, the response contribution of the filtered modes inside the target frequency band will not be reduced. To ensure good coupling between the electric field and multiple structural modes, distributed piezoelectric strategies can be employed. One can use several patches and locate them in such a way that no mode is filtered at the considered frequencies [147]. Alternatively, as proposed by Li et al. [59], a large piezoelectric patch with discretized electrodes can also be used to optimize the generalized coupling factors for several modes.

The aforementioned broadband approaches can be classified as 'mode-based' methods because the modal frequencies and shapes must be known prior to the design. The success of these strategies is strongly dependent on the accuracy of the modal information of the host structure. Unfortunately the exact modal frequencies and shapes of a structure are difficult to know in mid- and high frequencies, because the boundaries are no longer ideal [82] and the system is highly sensitive to parameter uncertainties. Synchronized Switching Damping (SSD) based approaches [165, 166, 169, 170] do not rely on any tuned electric techniques, and therefore overcome this problem. However in a multi-mode vibration context the definition of the switching point still remains a challenge for the design of a SSD system [178, 202].

Alternatively, the 'wave-based' methods have drawn considerable research attention these years with the development of the periodic structures or 'phononic materials' [81]. In the wave perception, structural deformation is regarded as the superposition of the wave motions, while natural modes are understood as standing waves induced by the reflection of waves on the boundaries [76–78]. The underlying idea of the wave-based methods for vibration reduction is to modify the wave properties in the targeted frequency band so as to dissipate or to localize the injected energy [157, 203]. Since the waves are independent of the boundary conditions, the vibration reduction features induced by waves is not sensitive to boundary conditions.

One concept that is widely used among the wave-based methods is the 'band gap' which appears in periodic structures. Bad gaps are frequency ranges in which propagating waves become evanescent [75]. They can either be caused by the inhomogeneity of the mechanical impedance in one unit cell of periodic structures (Bragg band gaps), or caused by tuned resonators (local resonance (LR) band gaps). Langley [195] showed that the waves in the band gaps hardly contribute to the overall modal density of a finite periodic structure. In other words, the structure would have fewer (often zero) natural modes in the band gaps, therefore probably a lower response. This brings naturally to the idea of integrating periodic waveguides into the host structure and intentionally design the frequency locations of band gaps so that they cover the target frequencies [197, 198]. However, it is important to remind that resonance peaks can still appear within a band gap in the Frequency Response Function (FRF) of a finite periodic structure. This phenomenon has been observed both numerically and experimentally [204, 205]. Mead [96] showed that the appearance of these modes are related to boundary conditions and that there are at most two modes inside one band gap. Few work can be found in the literature to clearly explain the mechanism and to provide means to mitigate the negative influences of the band gap resonances.

To create band gaps artificially, periodically distributed piezoelectric patches with inductance circuits have already been considered in the literature [123, 201]. the work of Chen er al. [123] on 2D structures shows that band gaps caused by piezoelectric strategies feature strong directivity. Xiao et al. [92] show that tuning a LR band gap near a Bragg band gap can induce a widened hybrid band gap. Concerning the design of the electric impedances, several simple criteria have been proposed [72, 157, 203] to optimize the periodically shunted electric impedances. Results show that the optimized resistance of the external circuit has to be negative to cancel the material damping in order to reflect all the injecting waves. This actually indicates that the localization of vibration does not require any damping. These work have shown the feasibility of controlling the dynamics of the structure by designing certain electric circuits. However, to the authors' knowledge, less attention has been paid on geometric design of the piezoelectric substructures or composites.

In this chapter, a methodology is proposed for the design of periodic piezoelectric structure with negative capacitances. The aim is to achieve a band gap which is wide enough to cover the target frequency range. The overall mass of the piezoelectric materials is strictly constrained, while the stability of the semi-active circuit has to be considered. The parameters are determined totally by wave properties. To do this, Wave and Finite Element Method (WFEM, see chapter 3 for detail) is employed to analyze the wave characteristics. The Wave Electromechanical Coupling Factor (WEMCF, see chapter 4 for detail) is used to optimize the geometric parameters of the piezoelectric system.

A cantilever beam is chosen as an example, and a frequency range which contains multiple higher order modes is treated. The consequences induced by the band gap, especially the mechanisms for band gap resonances are clarified. Using the vibration localization features of the band gap resonances, an efficient way of mitigate them is proposed and validated. Finally the vibration reduction performance is examined under different boundary conditions.

5.2 Example: cantilever beam

To illustrate the design process, a cantilever beam with rectangular cross section is considered as an example. The material is steel with Young's modulus 2.1×10^{11} Pa and mass density $\rho_{\mathrm{b}} = 7.8 \times 10^{3}\,\mathrm{kg/m^3}$. The length of the beam is $L_{\mathrm{b}} = 1\,\mathrm{m}$, the height is $H_{\mathrm{b}} = 2 \times 10^{-2}\,\mathrm{m}$ and the width is $5 \times 10^{-2}\,\mathrm{m}$. Rayleigh damping is introduced into the material by setting the mass term coefficient $\alpha = 1$ and stiffness term coefficient $\beta = 1 \times 10^{-7}$. This gives light damping of all the modes under 5000 Hz (around 0.05%). An external point force with amplitude 1 N is applied at the free end ($x = 0\mathrm{m}$).

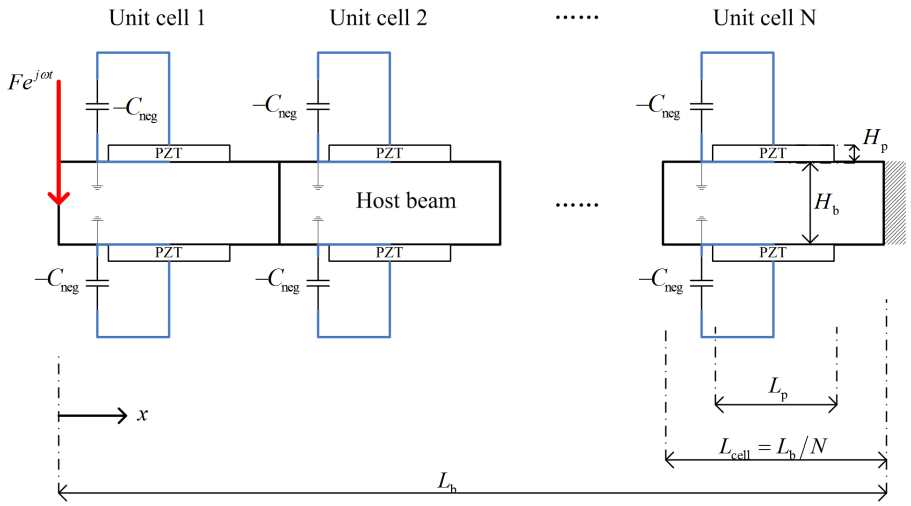

Figure 5.1: Illustration of the periodic piezoelectric beam.

The structure is modeled by beam elements in the following FEM and WFEM simulations. Traditional Euler-Bernoulli beam element is used to model the parts without piezoelectric materials. A 1D Finite Element scheme is used to capture the piezoelectric composite parts. The detailed information and validation of the finite element scheme is presented in Appendix BThe piezoelectric material is PZT4 and the detailed material constants can be found in Appendix A.

Frequency range [900Hz, 2000Hz] which covers the 5th, 6th and 7th resonances is targeted. The objective is to reduce the forced response of the beam in this frequency range. Collocated piezoelectric patches are periodically distributed on the beam as shown in Figure 5.1. An identical negative-capacitance is shunted to each patch, then the external electric admittance between the charge and the voltage becomes

$$Y = \frac{Q}{V} = -C_{\mathrm{neg}} \tag{5.1}$$

where C_{neg} is the absolute value of negative capacitance. For such a vibration control system, design parameters are the number of the piezoelectric patches N, height of a patch H_{p}, length of a patch L_{p} and the negative capacitance C_{neg}.

Also some constrains need to be considered. The first one is the overall mass of the piezoelectric patches. We define the mass ratio, describing how much weight is added by

piezoelectric material to the host structure, as

$$r_{\mathrm{m}} = \frac{2N\rho_{\mathrm{p}}L_{\mathrm{p}}H_{\mathrm{p}}}{\rho_{\mathrm{b}}L_{\mathrm{b}}H_{\mathrm{b}}} \tag{5.2}$$

where the factor 2 comes from the use of collocated patches. During the design r_{m} is required to be as small as possible. Secondly, since negative capacitance circuits are used, C_{neg} should be selected from the stable zone so that it would not make the structure unstable.

The process for determining the parameters to reduce the vibration response at the frequencies of interest under these restrictions is presented in the following sections.

5.3 Design process and results

In the design process, the geometric parameters and the electric parameters are determined consecutively. Through the geometric design, the best WEMCF is found in the targeted frequency range. This ensures that the mechanical characteristics can be efficiently modified by the electric parameters. Then the next step is the design of the negative capacitance so as to have a band gap covering the targeted frequency range. Compromise has to be made between the mass of the piezoelectric material and the safe margin of the circuit. The general flow chart of the design process is shown in Figure 5.2, and it will be explained with the example structure in detail.

5.3.1 Geometric design

The objective of the geometric design is to establish best WEMCF over all the targeted frequency band. Since the geometric parameters of the host beam are known as constants, the geometric parameters for the piezoelectric patches (L_{p} and H_{p}) can be represented by non-dimensional ratios:

$$r_{\mathrm{L}} = \frac{L_{\mathrm{p}}}{L_{\mathrm{cell}}} = N\frac{L_{\mathrm{p}}}{L_{\mathrm{b}}} \tag{5.3}$$

$$r_{\mathrm{H}} = \frac{2H_{\mathrm{p}}}{H_{\mathrm{b}}} \tag{5.4}$$

where r_{L} is the length ratio between piezoelectric patches to the host beam, and r_{H} is the height ratio. Substituting Equation (5.3) and (5.4) to (5.2), it gives

$$r_{\mathrm{m}} = r_{\mathrm{L}}r_{\mathrm{H}}\frac{\rho_{\mathrm{p}}}{\rho_{\mathrm{b}}} \tag{5.5}$$

In the first place, the number of patches N should be given. It strongly changes the periodicity of the system hence significantly affects the initial wave properties. The dispersion curves and the associated WEMCF are calculated when N varies from 2 to 7. Some of them are shown in Figure 5.3, where $r_{\mathrm{H}} = 1$ and $r_{\mathrm{L}} = 0.5$. In these calculation, the PZT patches are open-circuit.

It is shown that the choice of the number of patches gives quite different initial dispersion curves to the design. One (e.g. $N = 4$) or several (e.g. $N = 2$) band gaps appear around the targeted frequency range. They are caused only by the periodicity of the

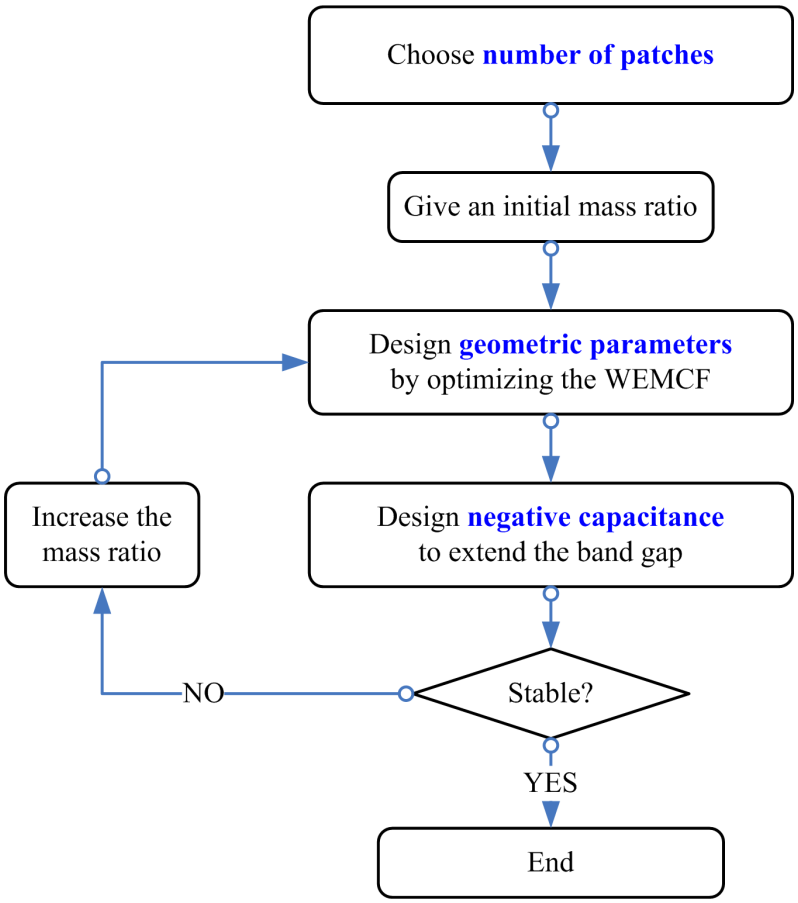

Figure 5.2: Flow chart of the design process.

mechanical properties of the piezoelectric patches. Since the open-circuit patches does not dramatically change the dynamic contrast in the unit cells, these initial band gaps are narrow. That is why we need to extend them by the electric circuits through electromechanical coupling mechanisms. The WEMCF of the waves vary drastically around the band gaps. Local maximum and minimum points of WEMCF locate at the bounding frequencies of the band gaps. This is due to the fact that at these frequencies anti-symmetric and symmetric standing waves arise into the cell [96]. An anti-symmetric wave generates an equal amount of positive and negative charges on the electrode, inducing zero overall charge. On the contrary, a symmetric wave shape always generates only one type of charge on the electrode which leads to a maximum overall change. Very small coupling factors can also happen inside a propagating zone, as shown by the line associated with $N = 2$ around 1.5×10^3 Hz.

A very small WEMCF value means that it is difficult or even impossible to adjust the mechanical properties by modifying the electric characteristics. Therefore one should shift the waves with low WEMCF outside the targeted range. For a given N, parameter studies are conducted with respect to r_{L} and r_{H}. Note that the values of the r_{L} and r_{H} should also satisfy Equation (5.5). With a given mass ratio r_{m}, r_{L} and r_{H} can only be selected along a line $f\left(r_{\mathrm{H}}, r_{\mathrm{L}}\right) = r_{\mathrm{m}}$ where $f()$ can be found in Equation (5.5).

For the calculation of each set of geometric parameters, the frequency-dependent re-

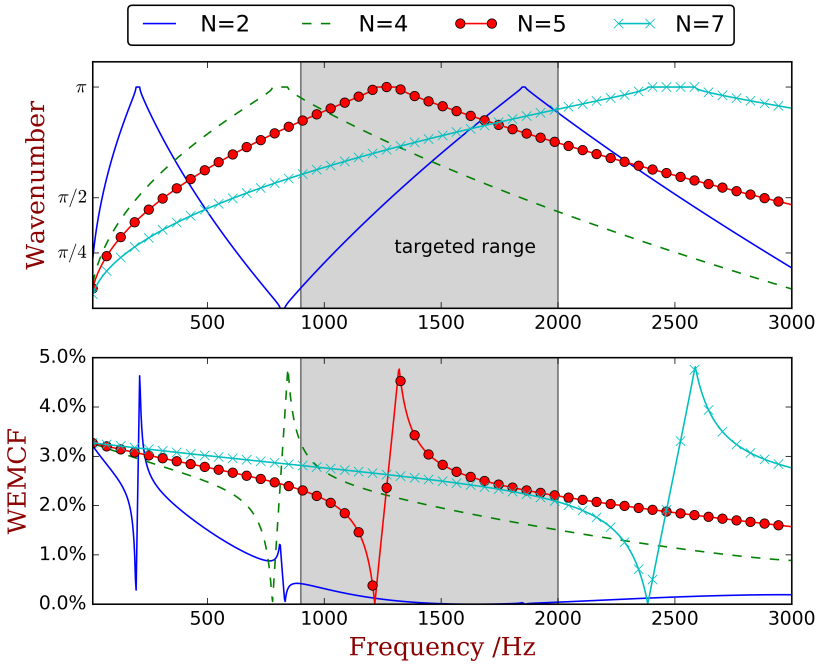

Figure 5.3: Dispersion relation and WEMCF of the structure with different number of patches (N), when $r_{\mathrm{H}} = 0.5$ and $r_{\mathrm{L}} = 0.75$

sults of $\mathcal{K}^2$ are summarized into two criteria defined on the targeted frequency zone; they are: 1) the average WEMCF, denoted by $\mathcal{K}^2_{\mathrm{aver}}$ and 2) the minimum WEMCF, denoted by $\mathcal{K}^2_{\mathrm{min}}$. Then the objective is to search r_{L} and r_{H} along a given mass ratio to: achieve largest $\mathcal{K}^2_{\mathrm{aver}}$ and simultaneously satisfy $\mathcal{K}^2_{\mathrm{min}} > \delta_{\mathrm{cr}}$. The threshold δ_{cr} is used to exclude the cases where waves with very low WEMCF be inside the targeted frequency range. In this chapter $\delta_{\mathrm{cr}} = 0.005$ is used.

Here we show the results of $N = 4$ in detail. Figure 5.4 shows the parameter studies of $\mathcal{K}^2_{\mathrm{aver}}$ and $\mathcal{K}^2_{\mathrm{min}}$ with r_{L} and r_{H}. The statement $\mathcal{K}^2_{\mathrm{min}} > \delta_{\mathrm{cr}}$ stands for most $(r_{\mathrm{L}}, r_{\mathrm{H}})$ values as it is shown in Figure 5.4b. However it is shown in Figure 5.4a that $\mathcal{K}^2_{\mathrm{aver}}$ peaks around $(r_{\mathrm{L}} = 0.8, r_{\mathrm{H}} = 2)$. The corresponding added mass ratio r_{m} reaches approximately 1.6, which is not a light-weight solution. A compromise has to be found. Instead of having the global best point for $\mathcal{K}^2$ the choice of parameters will be made to have the best $\mathcal{K}^2$ under the restriction of the mass of piezoelectric materials. Lines along which the mass ratio remain constant are plotted as well on Figure 5.4.

With the constrains $r_{\mathrm{m}} = 0.1$, $r_{\mathrm{m}} = 0.3$ and $r_{\mathrm{m}} = 0.5$ respectively, the results of $\mathcal{K}^2_{\mathrm{aver}}$ and $\mathcal{K}^2_{\mathrm{min}}$ are shown in Figure 5.5. Best solutions are found for each r_{m} and listed in Table 5.1. They are also labeled by A, B and C respectively in Figure 5.4 and 5.5. According to the results, the overall coupling condition becomes weaker when the mass ratio decreases. Differences will be made when designing the electric impedance, and as it will be shown later, there might not exist a stable design of the negative capacitance if the coupling is too weak. In that case it is recommended to increase the added mass and re-run the design, as shown in Figure 5.2. Alternatively one can propose several designs with different added mass as what we did for the $N = 4$ case.

Following the same procedure, the results when N is assigned to other values are

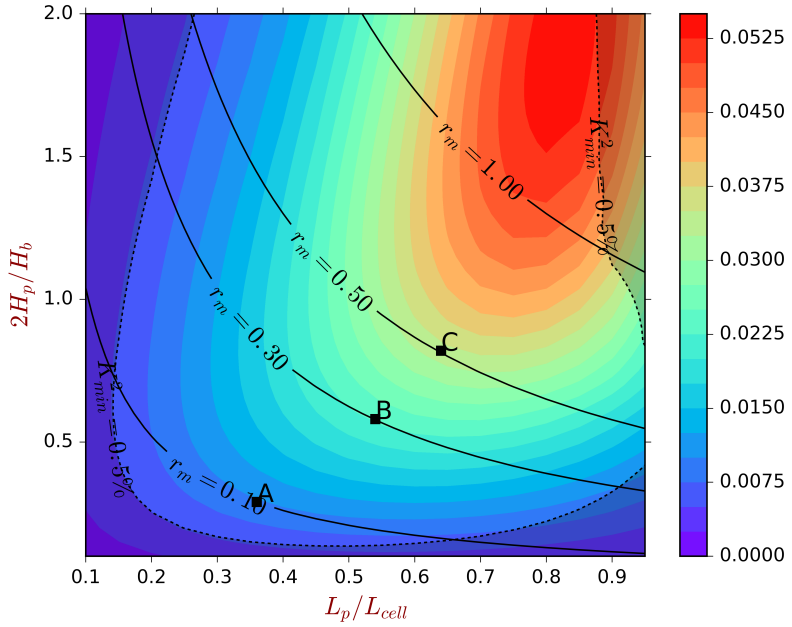

(a) Average coupling factor

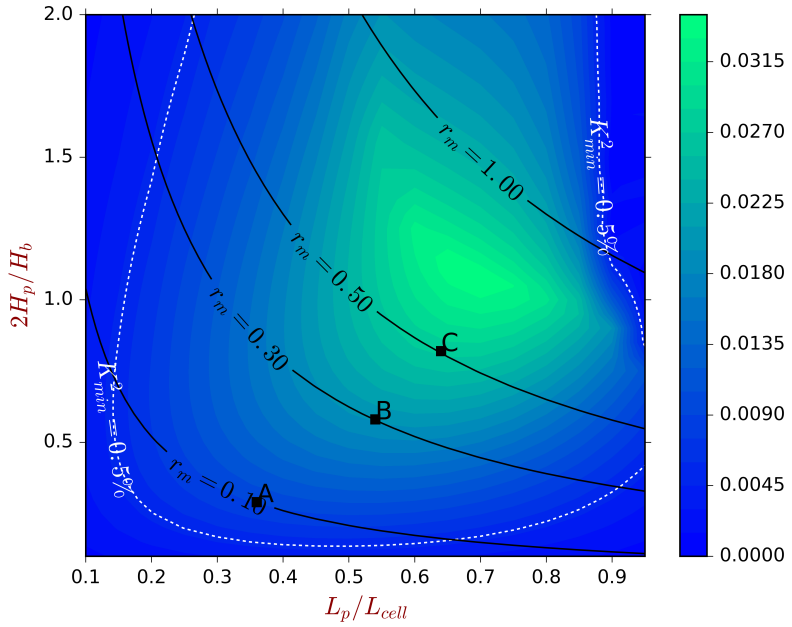

(b) Minimum coupling factor

Figure 5.4: Average and minimum WEMCF from 900 Hz to 2000 Hz with respect to the patch height and length when $N = 4$. Label A, B and C respectively refer to the optimized points along different given mass ratios. A for $r_{\mathrm{m}} = 0.1$, B for $r_{\mathrm{m}} = 0.3$ and C for $r_{\mathrm{m}} = 0.5$.

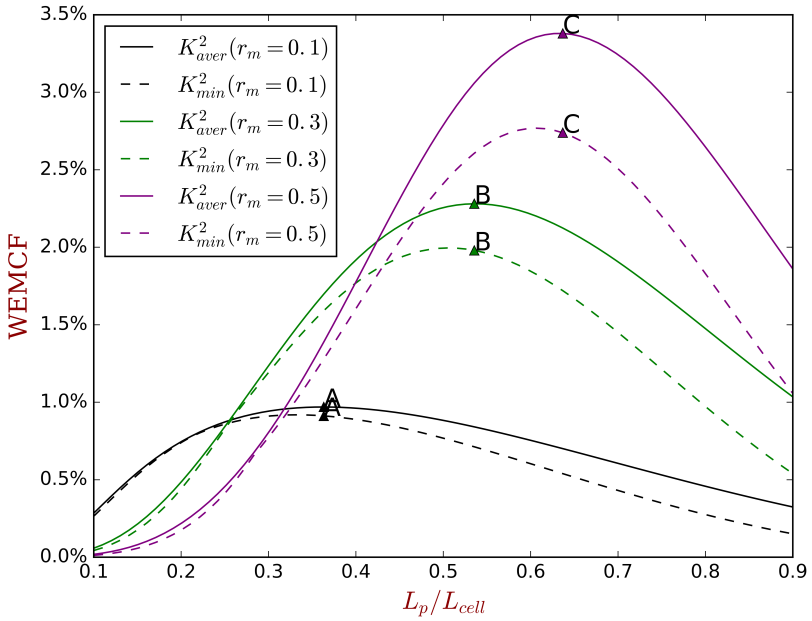

Figure 5.5: Average and minimum WEMCF with respect to the patch length when the mass ratio is constrained. Label A, B and C are respectively the optimized points along different given mass ratios. A for $r_{\mathrm{m}} = 0.1$, B for $r_{\mathrm{m}} = 0.3$ and C for $r_{\mathrm{m}} = 0.5$.

Table 5.1: Proposed geometric designs of $N = 4$ case

mass ratio r_{m}	length ratio r_{L}	height ratio r_{H}	$\mathcal{K}^2_{\mathrm{aver}}$	$\mathcal{K}^2_{\mathrm{min}}$	label
0.1	0.36	0.29	0.97%	0.91%	A
0.3	0.54	0.58	2.28%	1.98%	B
0.5	0.64	0.82	3.38%	2.74%	C

summarized in Table 5.2. Unlike the $N = 4$ case where configurations can be found at very low mass ratio, in some cases, for example when $N = 3$ and $N = 6$, the mass ratio has to be relatively higher, otherwise the WEMCF are very small at certain frequencies. The average coupling factor for $N = 3$ and $N = 6$ cases can be found in Figure 5.6. The domain satisfying $\mathcal{K}^2_{\mathrm{min}} > \delta_{\mathrm{cr}}$ is highlighted and it barely intersects the line of $r_{\mathrm{m}} = 0.6$ when $N = 3$ and the line $r_{\mathrm{m}} = 0.8$ when $N = 6$. These configuration might not be regarded as 'light weight' designs but since they have higher coupling factors we keep them as references and carry on with them in the following-up design process.

Moreover, it is not always possible to find a configuration satisfying all the constrains for a given number of patches, as it is shown in Table 5.2 for the $N = 5$ case. From Figure 5.7, it can be seen that no matter the length and the height of the piezoelectric patches, the minimum coupling factor remains very small. Nevertheless, we still search for a configuration along the line where mass ratio $r_{\mathrm{m}} = 0.3$ and the 'optimal' point is labeled by H* (despite not satisfying the criterion $\mathcal{K}^2_{\mathrm{min}} > \delta_{\mathrm{cr}}$). Configure H* provides similar level of average coupling factor as others but it has frequencies at which the electromechanical

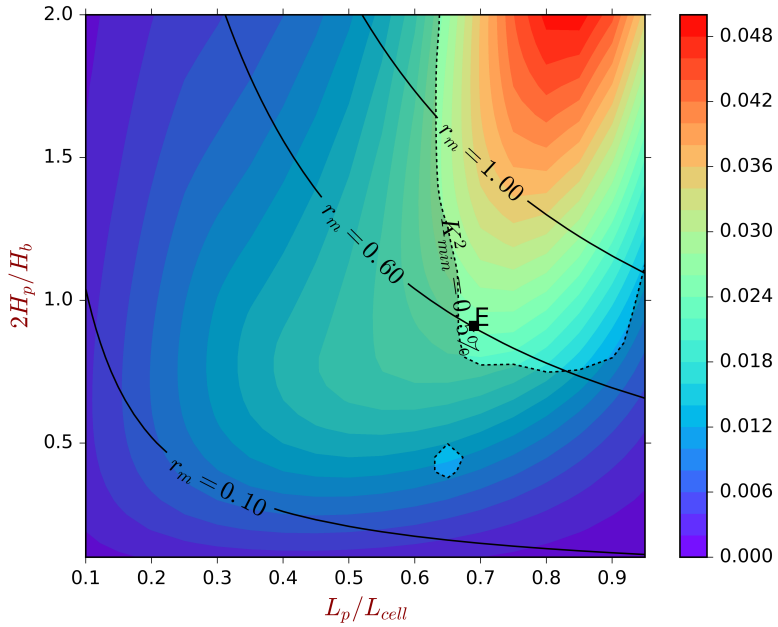

(a) $N = 3$

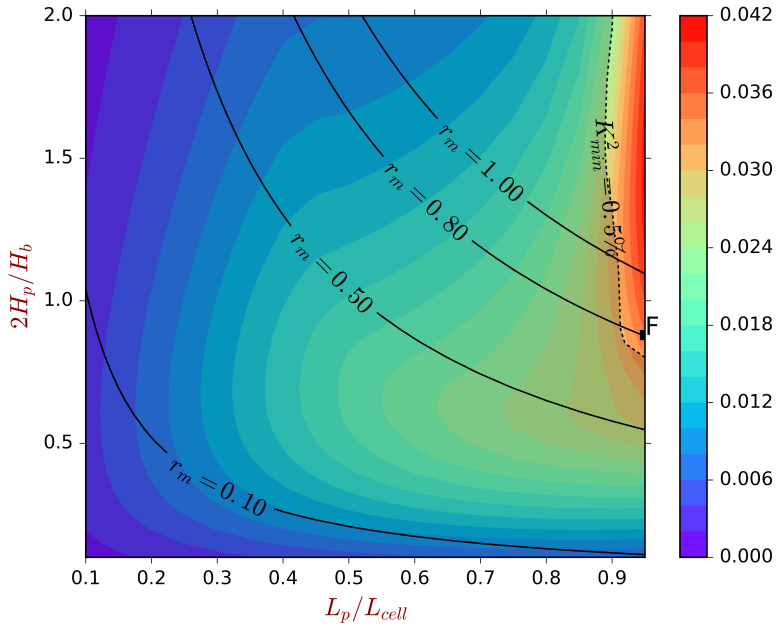

(b) $N = 6$

Figure 5.6: Average coupling factor from 900 Hz to 2000 Hz with respect to the patch height and length when $N = 3$ and $N = 6$. Label E and F refer to the optimized points along the given mass ratios.

Table 5.2: Proposed geometric configurations of other N values

N	mass ratio r_{m}	length ratio r_{L}	height ratio r_{H}	$\mathcal{K}^2_{\mathrm{aver}}$	$\mathcal{K}^2_{\mathrm{min}}$	label
2	0.55	0.49	1.16	2.55%	1.50%	D
3	0.60	0.70	0.89	2.44%	0.89%	E
5	0.30	0.58	0.53	2.31%	2.65×10^{-5}	H*
6	0.80	0.95	0.37	3.57%	1.35%	F
7	0.30	0.84	0.37	2.29%	1.91%	G

coupling is rather weak. This configuration is kept as a negative reference and it will also be carried into the next design process.

5.3.2 Negative capacitance design

After the geometric design, several configurations are proposed where parameters N, L_{p} and H_{p} are given. For each configuration, we will check whether it is possible to have a band gap to cover the targeted frequency range by designing negative capacitances. The stability of the semi-active piezoelectric system can be analyzed by a structural modal analysis of one unit cell [203]. Namely, the eigenvalue problem

$$\left(\begin{bmatrix} \mathbf{K}_{\mathrm{II}} & -\mathbf{H}_{\mathrm{IE}} \\ \mathbf{H}_{\mathrm{IE}}^{\mathrm{T}} & \mathbf{C}_{\mathrm{p}} - \mathbf{C}_{\mathrm{neg}} \end{bmatrix} - \omega_{\mathrm{n}}^2 \begin{bmatrix} \mathbf{M}_{\mathrm{II}} & \mathbf{0} \\ \mathbf{0} & \mathbf{0} \end{bmatrix} \right) \begin{pmatrix} \mathbf{q}_{\mathrm{I}} \\ \mathbf{q}_{\mathrm{E}} \end{pmatrix} = \begin{pmatrix} \mathbf{0} \\ \mathbf{0} \end{pmatrix} \tag{5.6}$$

will be analyzed with different C_{neg} values. Equation (5.6) is obtained by Equations (3.3) and (5.1) with the consideration of the fix-fix boundary condition ($\mathbf{q}_{\mathrm{L}} = \mathbf{q}_{\mathrm{R}} = \mathbf{0}$). Other boundary conditions, such as free-free and free-fix can also be used, and they yield very close results (in our case the data remains the same until the fifth effective number), as shown in Figure 5.8. This is due to the fact that at the border of the unstable zone, the negative capacitance dramatically changes the overall stiffness of the structure. Different boundary conditions change the original effective stiffness but the extent is negligible in comparison with the change caused by the negative capacitance. The unstable zone of C_{neg} is the region in which the negative eigenvalues appear. Figure 5.9 shows the first eigenvalue obtained by Equation (5.6) for each configuration. In Figures 5.8 and 5.9, both positive and negative values are presented by the logarithmic scale and the unstable zone is highlighted by a gray color. The detailed values are recorded in Table 5.3. It is important to note that the stability issues considered here are from a theoretical point of view. In practice, to implement a negative capacitance shunt there are more details to be considered [158].

Knowing the stability zone, the design of negative capacitance can be conducted by repetitively calculating the dispersion curves with different values of C_{neg}. The results of some configurations are presented in where the attenuation constant (imaginary part of the wavenumber) of the positive-going flexural wave under different C_{neg} and frequencies are shown. The objective of this step is to find a C_{neg} value outside the unstable zone, and with this value the periodic structure has a band gap covering the whole targeted frequency. The unstable zone for negative capacitance is represented by a light gray

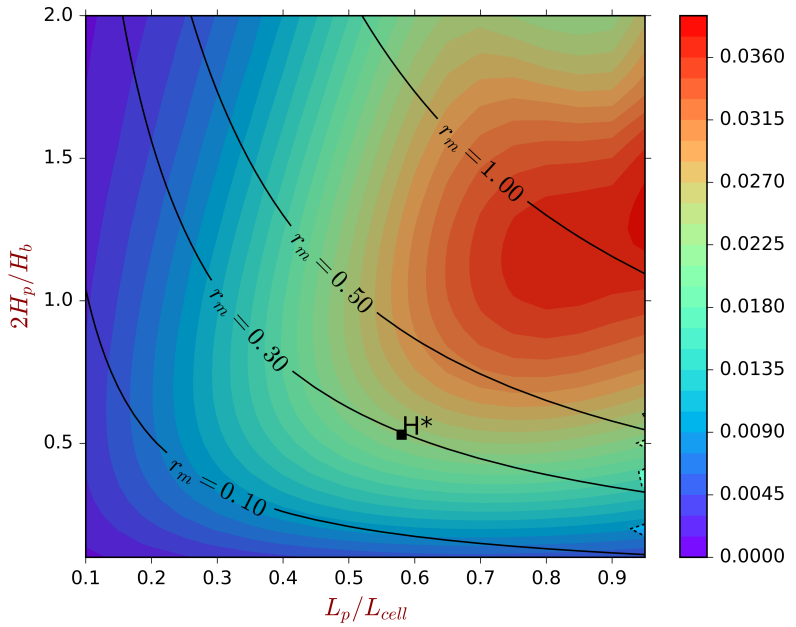

(a) Average coupling factor

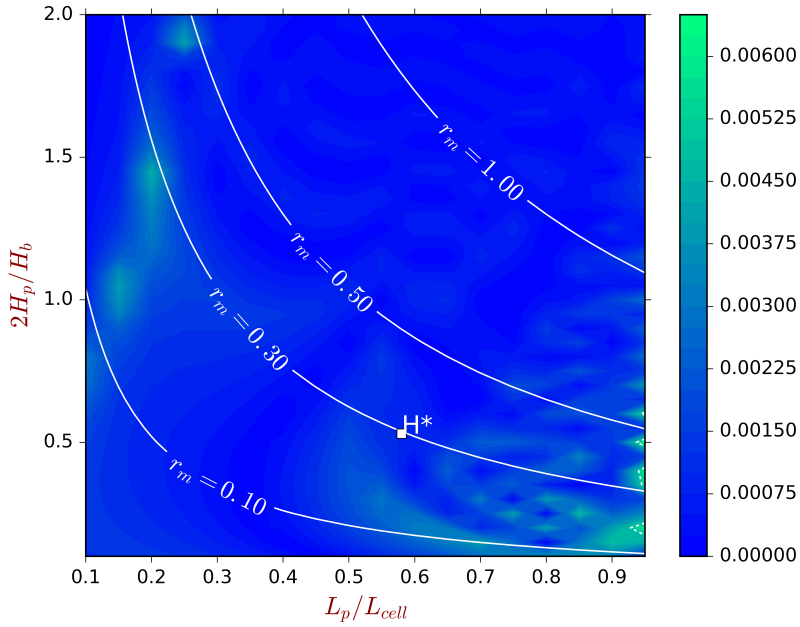

(b) Minimum coupling factor

Figure 5.7: Average and minimum coupling factors from 900 Hz to 2000 Hz with respect to the patch height and length when $N = 5$. Label H* refer to the negative reference.

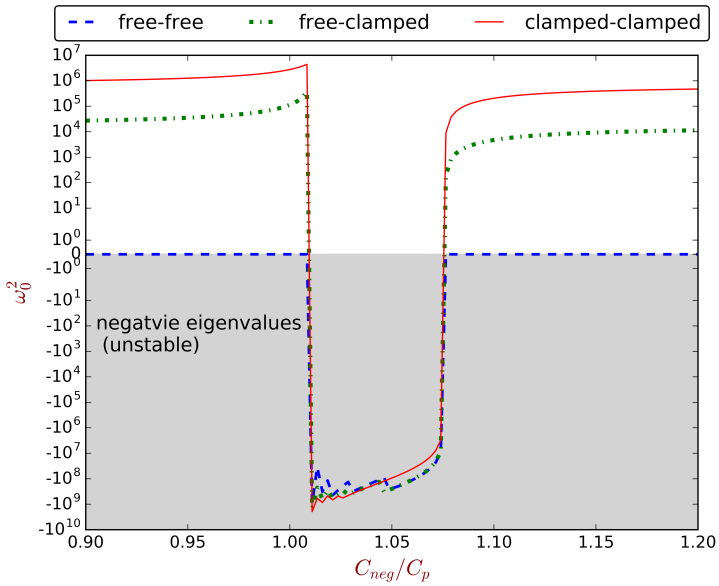

Figure 5.8: First eigenvalues with respect to negative capacitance under different boundary conditions.

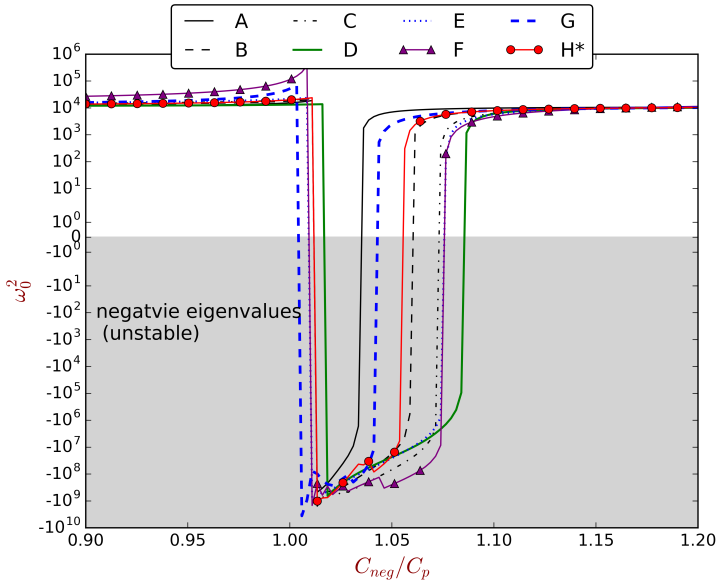

Figure 5.9: First eigenvalues with respect to negative capacitance for each geometric configuration.

box. The final choice of the negative capacitance for each configuration, if existed, is highlighted by a yellow line.

The comparison between configuration A (Figure 5.10) and B (Figure 5.11) highlights the influence caused by the choice of the average coupling factor. As was recorded in Table 5.2, both A and B have the same number of patches but A is obtained upon a lower mass ratio and it has lower average coupling factors. Figure 5.10 shows that all the desired C_{neg} values for configuration A are in the unstable zone. However, for configuration B it

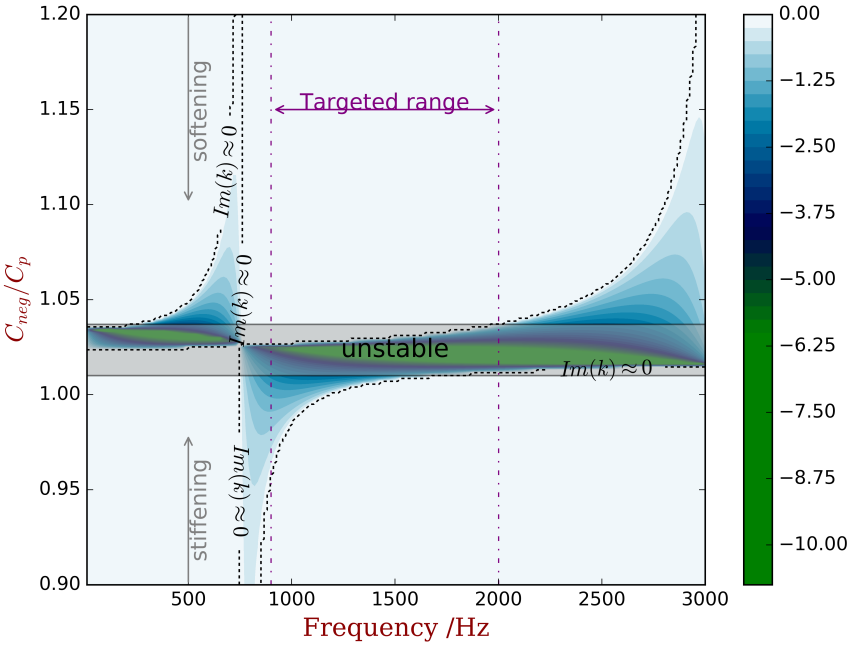

Figure 5.10: Configuration A: attenuation constant with respect to the negative capacitance and frequency. The final choice does not exist.

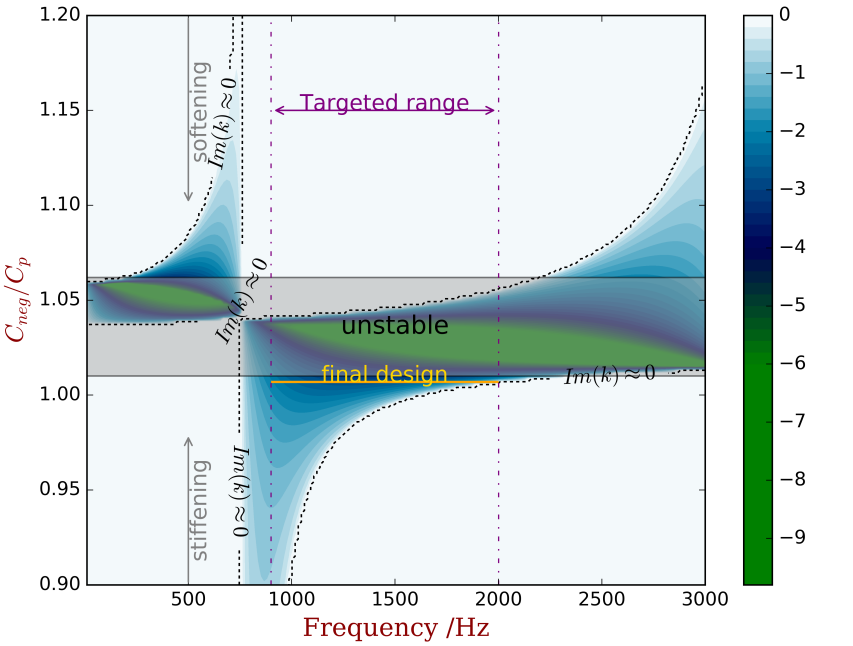

Figure 5.11: Configuration B: attenuation constant with respect to the negative capacitance and frequency. The final choice of the negative capacitance is highlighted by a yellow line.

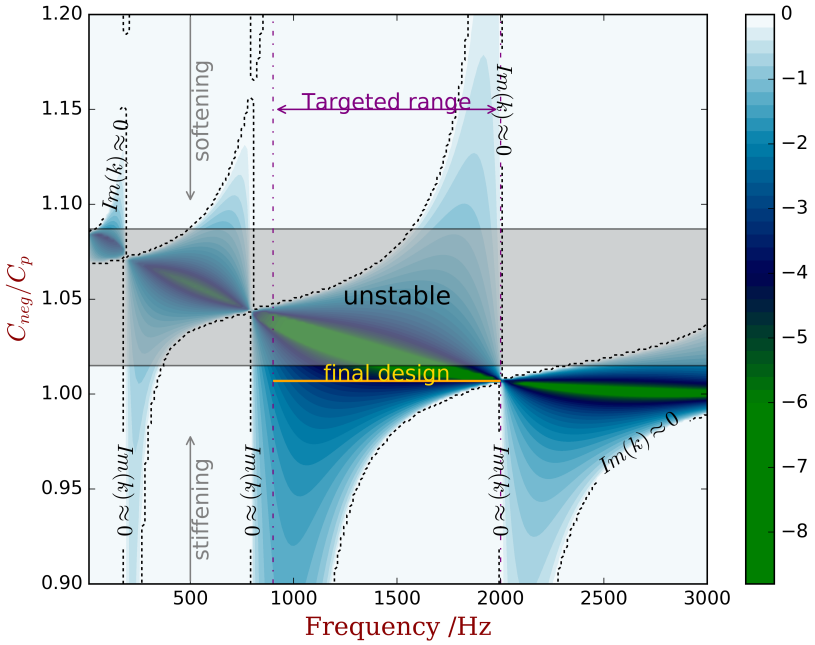

Figure 5.12: Configuration D: attenuation constant with respect to the negative capacitance and frequency. The final choice of the negative capacitance is highlighted by a yellow line.

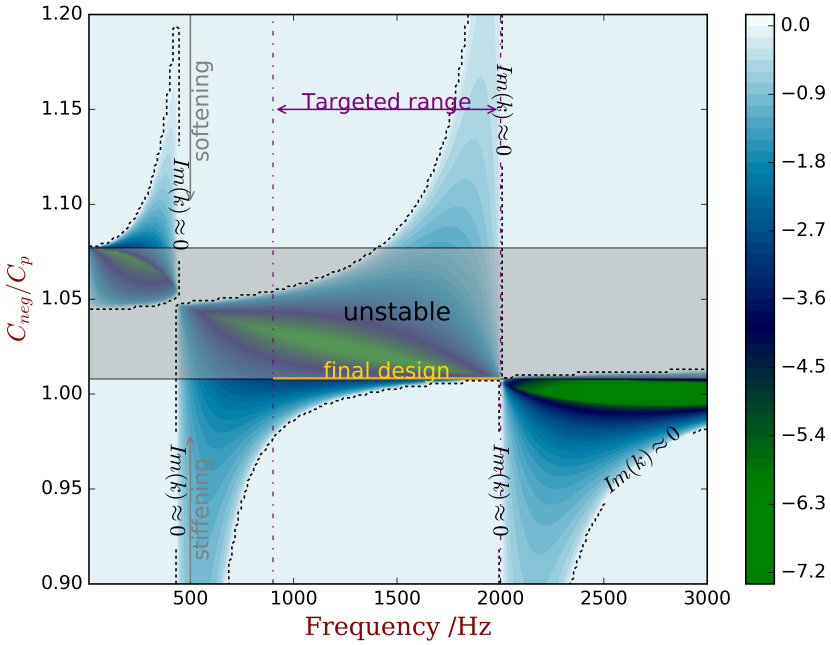

Figure 5.13: Configuration E: attenuation constant with respect to the negative capacitance and frequency. The final choice of the negative capacitance is highlighted by a yellow line.

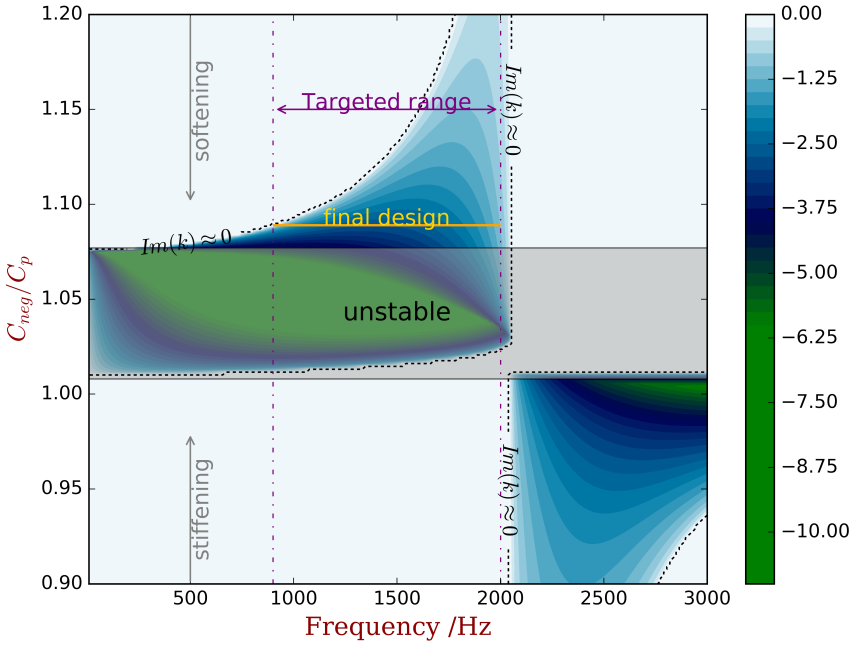

Figure 5.14: Configuration F: attenuation constant with respect to the negative capacitance and frequency. The final choice of the negative capacitance is highlighted by a yellow line.

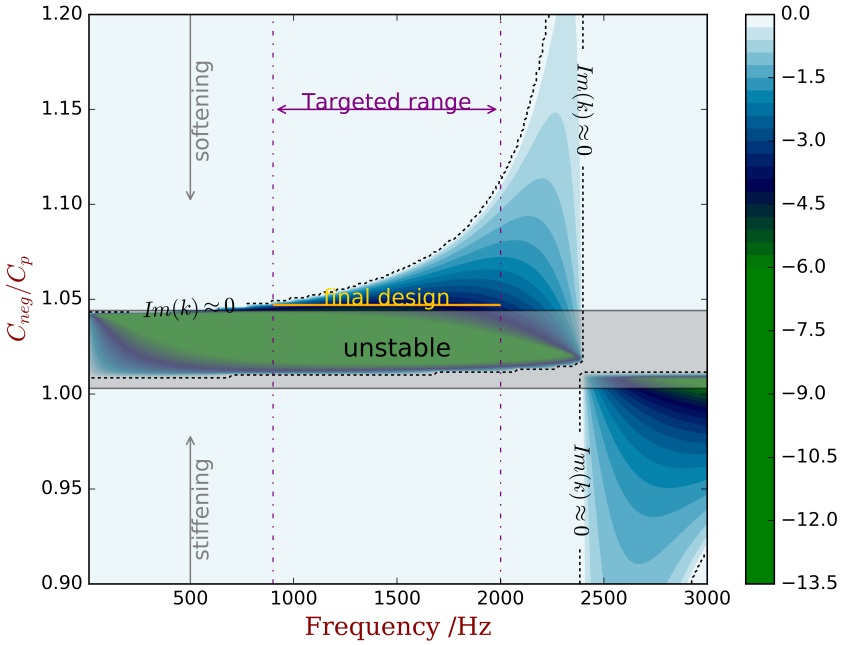

Figure 5.15: Configuration G: attenuation constant with respect to the negative capacitance and frequency. The final choice of the negative capacitance is highlighted by a yellow line.

Table 5.3: Summaries of the impedance design

label	N	unstable zone for $C_{\text{neg}}/C_{\text{ps}}$	designed $C_{\text{neg}}/C_{\text{ps}}$	property
A	4	$(1.010, 1.037)$	N/A	
B	4	$(1.010, 1.062)$	1.007	stiffening
C	4	$(1.010, 1.074)$	0.999	stiffening
D	2	$(1.015, 1.087)$	1.006	stiffening
E	3	$(1.008, 1.077)$	1.008	stiffening
F	6	$(1.008, 1.077)$	1.089	*softening*
G	7	$(1.003, 1.044)$	1.047	*softening*
H*	5	$(1.010, 1.057)$	N/A	

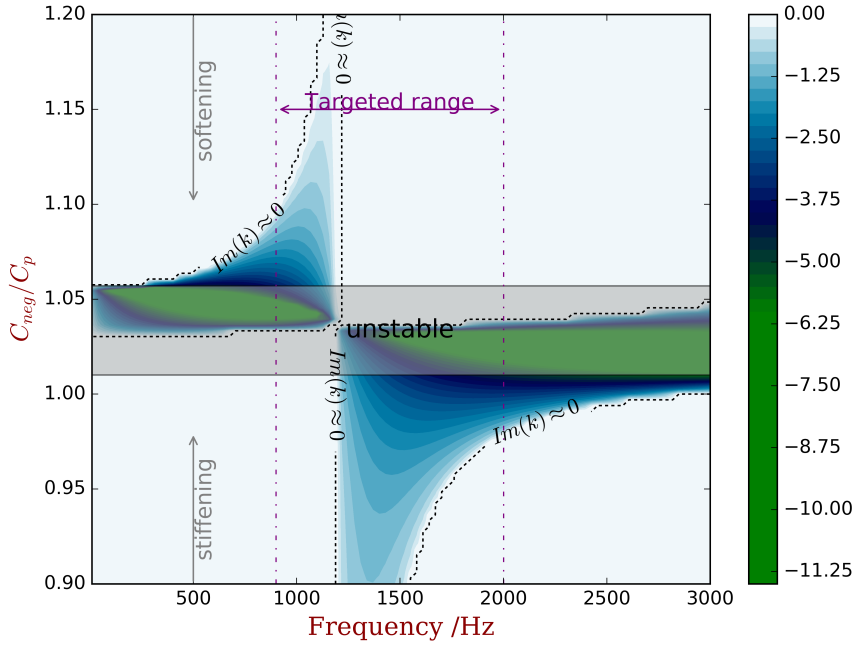

Figure 5.16: Configuration H*: attenuation constant of with respect to the negative capacitance and frequency. The final choice does not exist.

is possible to find a stable C_{neg} to create a broad band gap. It is also worth to note that the used band gap can be the first one (Figure 5.14), the second one (Figure 5.11) or the third one (Figure 5.12), depending on how many piezoelectric patches are used.

As was explained before, the Bragg band gaps are induced by the contrast of the dynamic stiffness in the unit cell. It can be seen that both softening and stiffening features of the negative capacitance can create broad band gaps, and the details are also listed in Table 5.3.

It is impossible to find a C_{neg} value for configuration H*, but the reason is different from A (overall coupling is too weak). For H*, there are always frequencies with very low WEMCF. Consequently, inside the targeted frequency range it is impossible to have a continuous band gap, as shown in Figure 5.16. This result indicates the reason why we

need to satisfy the condition $\mathcal{K}^2_{\text{min}} > \delta_{\text{cr}}$ during the geometric design.

It is worth to note that the designed negative capacitances listed in Table 5.3 are very close to the unstable zone. In practice a safety margin is needed, otherwise any perturbation in the electrical parameters has the potential to destabilize the circuit. Except configuration E, each design proposed in this chapter has some safety margin. To extend the safety margin one can use more piezoelectric materials (see configuration A, B and C) or use different number of patches (see configuration D and G). Generally, the system will become heavier if larger margin is required. A compromise has to be found between the width of the safety margin and the system weight. That is the reason why we did not directly minimize the mass ratio at a given number of patches but set different values of it and make comparisons. Moreover, in this chapter we use the PZT4 material as an example. In practice it is suggested to use other piezoelectric materials that have lower density. Once the material is given and the requirements of the safety margin is known, the method proposed in this chapter can be directly applied to optimize the mass ratio as well.

In summary, the choice of N gives different initial band gap parameters (locations and width). In some cases, solutions can be found at very low mass ratio ($N = 4, 7$), while in other cases solutions only exist when higher mass ratio is considered ($N = 2, 3, 6$). Specially in some cases ($N = 5$), no solution can be found. The mass ratio constrains the parameter space of the geometric parameters hence further affects the optimal WEMCF. WEMCF further links to the safe margin of negative capacitance. So at a lower mass ratio it might not possible to find a stable negative capacitance design (configuration A). Note that at a same mass ratio there can also be multiple designs (30%, for B and G) or no design (10%), depending on the number of patches. To achieve a design, the flow chart shown in Figure 5.2 is not unique, alternatively one can also select a mass ratio value and optimize across all N values and same conclusions will be found.

5.4 Performance and discussions

5.4.1 Band gap resonance

After the aforementioned design process, several piezoelectric structures are found, and the parameters are listed in Tables 5.2 and 5.3. Each of the structure has a continuous band gap covering the targeted frequency range (from 900 Hz to 2000 Hz). In this section the vibration reduction performance of these structures is presented and explained when a harmonic point force is applied at the free tip (see Figure 5.1).

In the band gap, the modal density is reduced. This feature is highlighted by Figure 5.17 where the response of design B is presented in comparison with the original one. Results of the rotational DOF are shown. The displacement DOF can also be used and they lead to same conclusions. We don't show these results due to space limitations. Another reason is that rotational DOF might be of more interest and importance at higher frequencies as indicated by [82]. No resonance appears in the targeted frequency range therefore the averaged response is significantly reduced. The C_{neg} applied lies in the stiffening area so that the static response (0 Hz) is reduced accordingly. The targeted frequency range is covered by the first band gap as shown in Figure 5.11, hence [0 Hz, 900 Hz] is a propagating zone. It can deduced from Mead's work [96] that there

are either N-1 or N resonance peaks in a propagating zone, depending on the boundary conditions, where N is the number of unit cells. There are 4 unit cells in design B and in Figure 5.17 four resonance peaks are found, which matches well with the expectation.

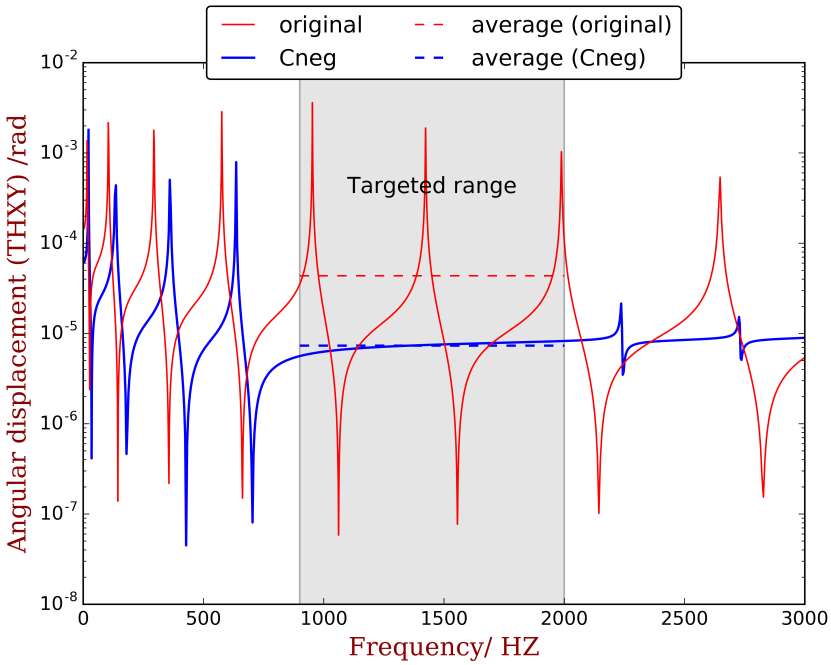

Figure 5.17: FRF of the rotation DOF at the excitation point ($x = 0\,\mathrm{m}$) of design B in comparison with the response of the original uniform structure.

However, a band gap does not guarantee to eliminate all the modes inside it, but ensures that all modes in it have localized shapes. The existence of band gap resonances can be deduced from Mead's work [95, 96] concerning the relationship between the natural frequencies of finite periodic structures and the bounding frequencies of the band gaps. It was proved that only under certain boundary conditions some natural frequencies will locate on the edges of the band gaps. Otherwise natural frequencies can locate either inside or outside the band gaps. For mono-coupled systems, the boundary conditions leading to zero band gap resonance can be predicted. For example a periodically simply supported beam, the corresponding boundary condition is to have the structure clamped at both ends. For multi-coupled periodic structures, e.g. the beam considered here, these special boundary conditions become complicated. Some DOFs have to be fixed and others are free according to the symmetry and for different kind of waves they may be different. More importantly, these boundary conditions exist only when the unit cells are symmetric. This implies that it might be difficult to avoid the band gap resonances, especially for complex periodic structures.

It is worth to note that a band gap resonance does not conflict with the wave-shielding mechanism of the evanescent waves. Indeed, a single evanescent wave does not transmit energy. Only based on this, it is hard to explain the existence of a pure natural mode in which the whole structure can reach an infinite kinetic energy except the nodes of the modal shape. Bobrovnitskii [194, 206] and Kurze [207] explained that if there are two evanescent waves (which is the case for a finite structure) with opposite directions

and they form a 'mixed evanescent field' which enables an energy flow. This energy flow allows the injected power to be transmitted all over the structure. If the energy can accumulate under certain situation (phase closure), a resonance will raise. Further more, a band gap resonance can also be understood by the phase-closure principle [78] which explains how waves can form a resonance. Namely once a propagating wave achieves a closed-phase or zero-decay as it completes the circle around the whole system, it will create a standing wave which corresponds to a structural mode. When an evanescent wave is traced in the periodic structure the wave amplitude is decreasing, but the boundaries can produces a reflected evanescent wave with larger amplitude than the incident one (reflection coefficient larger than 1.0) [95], compensating the amplitude drop during the travel. So it is still possible for an evanescent wave to achieve the phase closure conditions on its own so as to form a mode. We can deduce that the modal shapes of the band gap resonances are localized around the boundaries.

The band gap resonances can be seen from Figure 5.19 and 5.20 where the response of design G are presented. 2 peaks of the FRF raise inside the band gap. Modal analysis confirms that the two peaks correspond to two modes at 1035 Hz and 1890 Hz respectively. The shapes of these two modes are shown in Figure 5.18, in comparison with a mode outside the band gap (at 4758 Hz). As expected, large proportion of the vibration is concentrated around the boundaries because they are formed by evanescent waves. On the contrary, the mode at 4758 Hz is formed by propagation waves so it has uniformly distributed nodes and anti-nodes. Due to the energy localization, the frequency averaged response of the excitation point is increased as shown in Figure 5.19. On the other hand, the response away from the excitation is reduced shown in Figure 5.20.

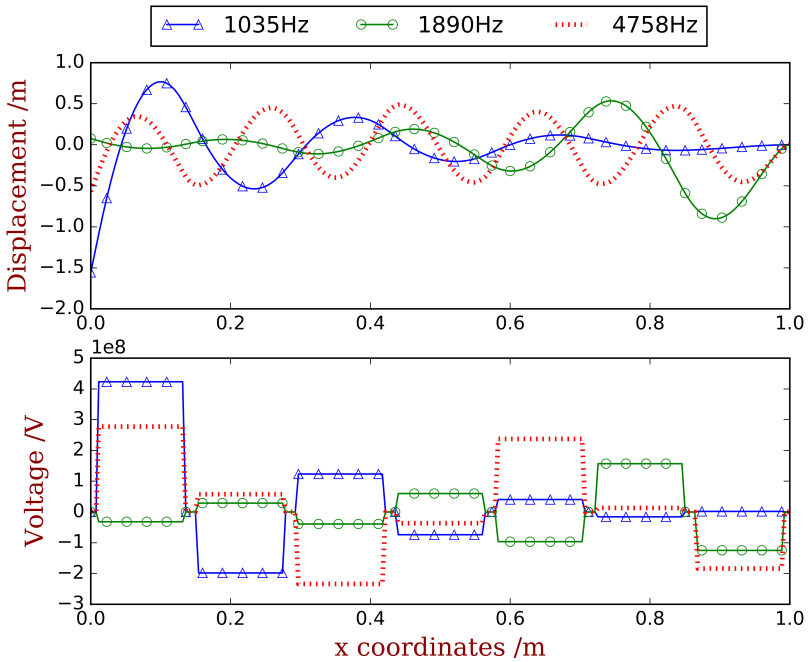

Figure 5.18: Modal shapes of band gap resonances in design G (at 1035 Hz and 1890 Hz) in comparison with a common mode (at 4758 Hz)

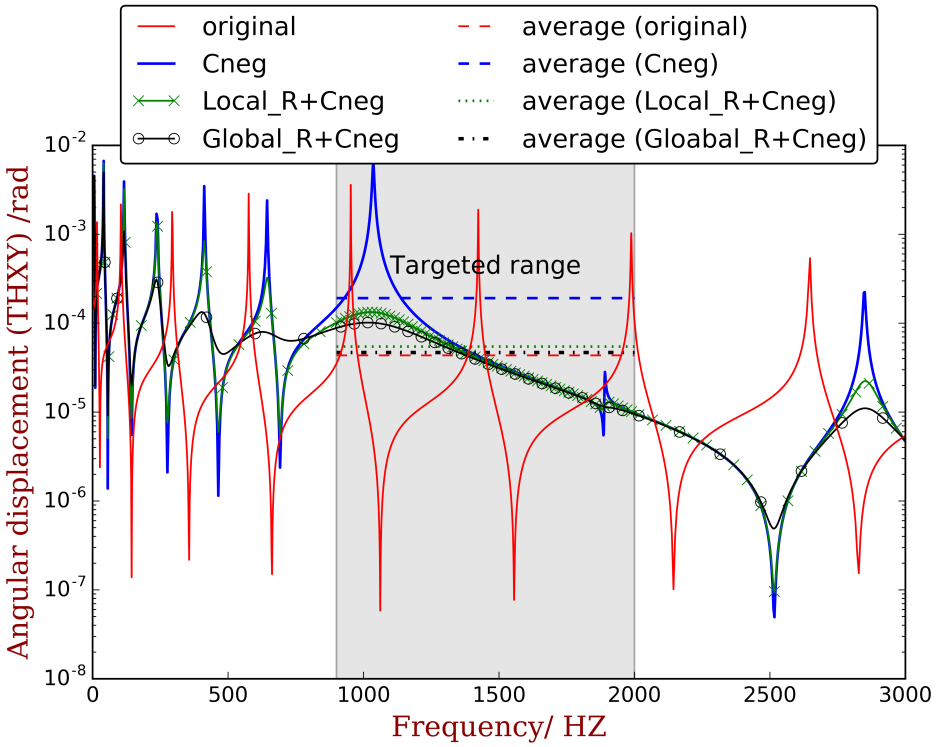

Figure 5.19: FRF of the rotation DOF at the excitation point ($x = 0.0\,\mathrm{m}$) of design G.

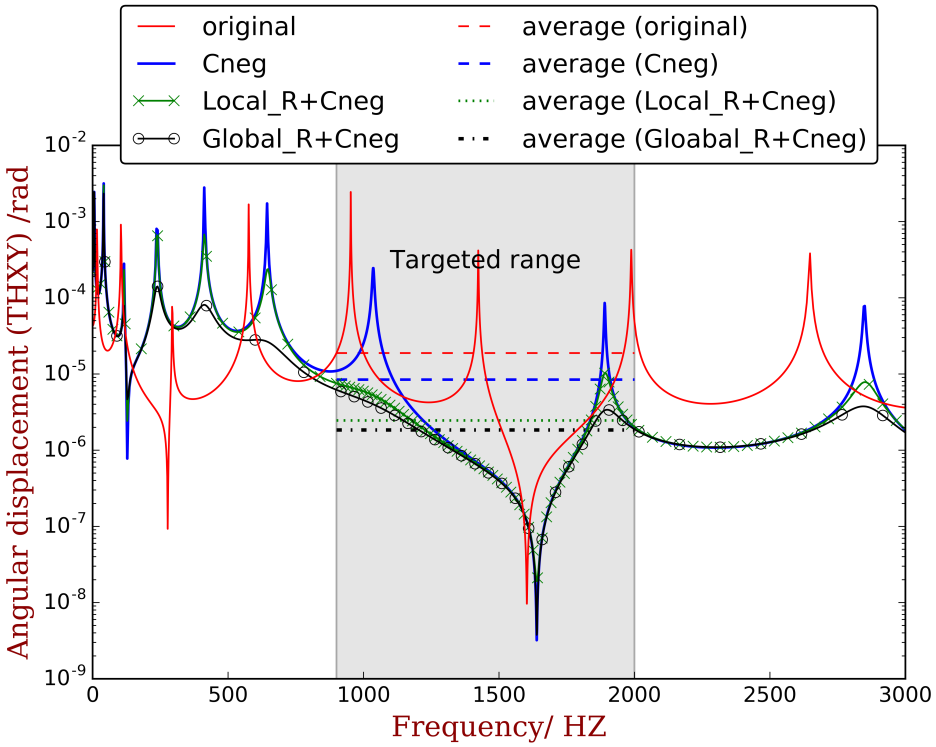

Figure 5.20: FRF of the rotation DOF away from the excitation point ($x = 0.7\,\mathrm{m}$) of design G

5.4.2 Resistor/harvester

Interestingly, the vibration of some parts of the structure (away from the source) has already been reduced due to energy concentration. In this case only the impedance contrast of the unit cell is changed and no additional damping mechanisms (resistor or energy harvester) are introduced. In addition to this, the electric energy is also localized to the same area, as shown in Figure 5.18, which allows to efficiently remove the energy and therefore to reduce the vibration of the whole structure.

To illustrate this, resistors are considered in design G as a representation of any electric circuits that possess damping or energy harvesting ability. They are connected to the negative capacitance in series so that the electric impedance becomes:

$$Y = \frac{Q}{V} = \frac{1}{-1/C_{\text{neg}} + j\omega R} \tag{5.7}$$

where R is the resistance. Two different cases of distributing the resistances are considered. In the first case an identical resistor with 20 Ω is connected to each negative capacitance, and in total 7 resistors are used, called global resistance hereafter in this chapter. In the second case only 2 resistors with 20 Ω are used, being connected to the energy localized zones, namely the first and the last patches, called local resistance.

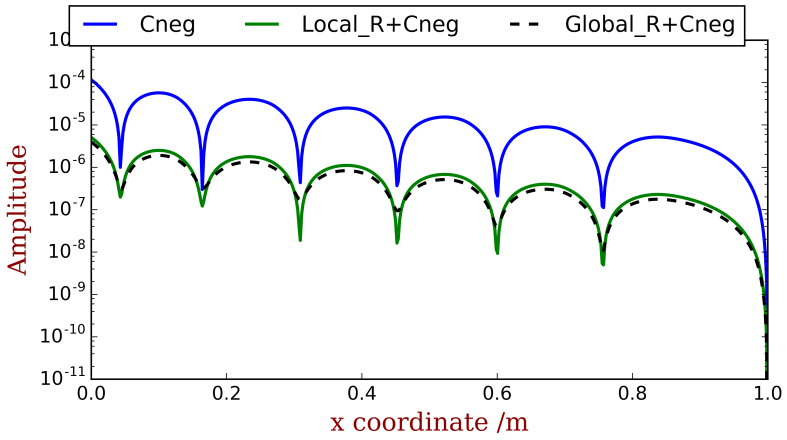

Figure 5.21: Deformation of configuration G at 1030 Hz with and without resistance.

The FRF at the excitation point ($x = 0$ m) of the two cases are calculated and compared in Figure 5.19. It can be seen that the vibration peaks caused by the band gap resonances are reduced by the damping mechanism induced by the resistors. Figure 5.20 presents the FRF at $x = 0.7$ m. The frequency averaged response is further suppressed because of the additional damping. More importantly, inside the band gap, the global resistance and local one have nearly the same performance, while in the propagating zone the global resistance performs much better. This can be explained by the features of the modal shapes of a band gap resonances as discussed before. The results indicate that the local resistance is as an efficient way of removing the energy of a band gap resonance, because the number of dampers/harvesters is much smaller than the global way.

Figure 5.21 compares deformation of the forced response peak at 1030 Hz among zero resistance, global resistance and local resistance. It can be seen that with resistance,

no matter global or local, the deformation is still localized. A band gap resonance is essentially a solution of the eigenvalue problem which yields all the normal resonances. So the common sense that the damping would not significantly change the modal shape still works for a band gap resonance. Once again the results show only minor differences between the local and the global distribution of the resistances.

As listed in Table 5.3, the negative capacitance used here is very close to its unstable zone, so the electromechanical coupling is very strong when the negative capacitances are connected. In this situation, the resistance can be chosen from a wide range of values. It exists an optimal point depending on the frequency but on-optimal values can already induce significant damping. For design G, resistances from $10\,\Omega$ to $1 \times 10^4\,\Omega$ are all applicable (results are not presented). This gives a large tolerance if the resistance is replaced by an energy harvesting circuit in the future.

5.4.3 Boundary conditions

During the design, no modal information of the structure is required. This implies that the designed structures may have some features insensitive to boundary condition. With the cantilever boundary condition, design B does not have band gap resonances as shown in Figure 5.17. To examine the influence of boundary condition, a massless spring is introduced to design B at the free tip ($x = 0.0\,\mathrm{m}$). Figure 5.22 shows the evolution of the FRF at $x = 0.75\,\mathrm{m}$ with respect to the supporting stiffness. One band gap resonance can be seen at some supporting stiffness. Nevertheless, the modal density in the targeted range is lower than the other frequency ranges with same bandwidth. Figure 5.23 summarizes the frequency averaged response at $x = 0.0\,\mathrm{m}$ and $x = 0.75\,\mathrm{m}$. A locally distributed resistance is also considered and compared, namely one resistor of $50\,\Omega$ (the value is roughly chosen for the same reason as noted at the end of the last subsection) is connected to the patch nearest to the excitation and another resistance to the patch closest to the clamped end.

It can be seen that the band gap enlarges the response difference between the near-field ($x = 0\,\mathrm{m}$) and far-field ($x = 0.75\,\mathrm{m}$). Band gap resonances arise in a continuous range of the supporting stiffness. In the absence of the band gap resonance, both near-field and far-field response can be reduced in comparison with the original one. When band gap resonances appear, the near-field response could be larger than the original response. On the other hand, the far-field response can always be reduced no matter whether there are band gap resonances or not. When damping mechanism is introduced only at the boundaries, the negative influences of band gap resonances are effectively mitigated. The far-field response is further reduced while the near-field response can be controlled to a lower level in comparison to the original structure. This is due to the fact that a large proportion of the vibrational energy is suppressed or removed. Although the exact value concerning the vibration reduction degree varies, the response is dramatically reduced over the given frequency band with all the given boundary conditions. In this regard, the vibration reduction ability of the designed structures is boundary condition insensitive.

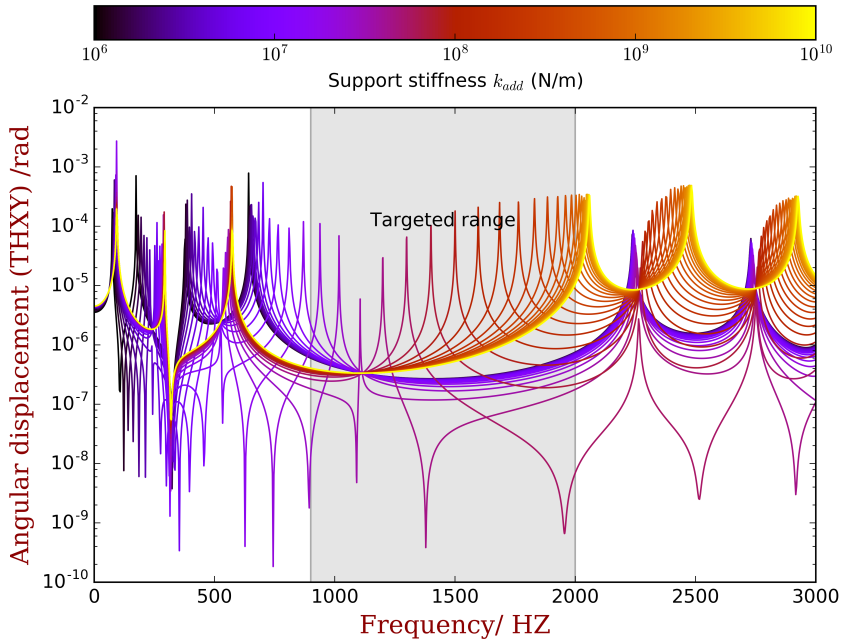

Figure 5.22: FRF of the rotation DOF away from the excitation point ($x = 0.75\,\mathrm{m}$) of design B with respect to the supporting stiffness

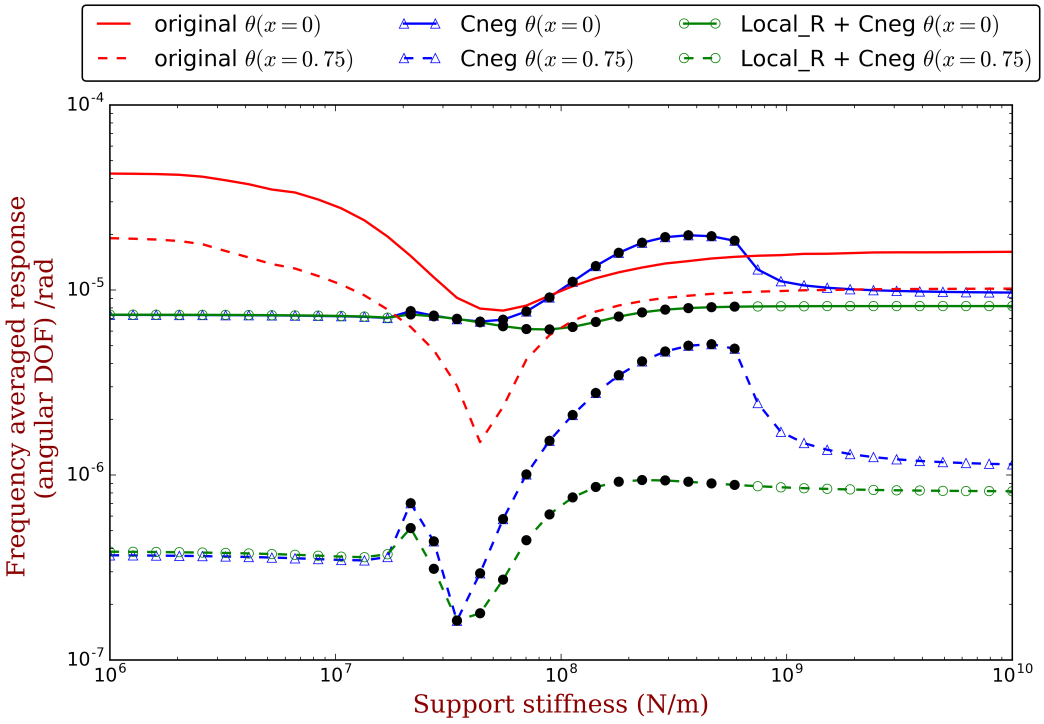

Figure 5.23: Frequency averaged response at $x = 0.0\,\mathrm{m}$ and $x = 0.75\,\mathrm{m}$ of design B with respect to the supporting stiffness.

5.5 Conclusions

The Wave Electromechanical Coupling Factor (WEMCF) can be used to design the geometric parameters of a piezoelectric system. It is defined by the ratio of the electric energy over the mechanical energy during the passage of a wave. WEMCF can be easily calculated as a post-process of the existing wave dispersion numerical tools. We show that WEMCF is closely related to the success of obtaining a continuous band gap by negative capacitance. If the frequency averaged WEMCF is too weak, the desired C_{neg} value might be in the unstable zone. Additionally, one should also avoid to have very low minimum WEMCF, otherwise a propagating zone will always be in the frequency range of interest.

A design process is proposed in which the geometric and electric parameters are determined consecutively in an iterative process. Both the average and minimum values of WEMCF are used as criteria. These criteria are optimized when the overall mass of the piezoelectric materials is constrained. Through the proposed design process, several light-weight and stable semi-active piezoelectric systems are found, that all have a broad band gap covering the interested frequency range. Results indicate that the amount of piezoelectric materials should not be lower than a certain level otherwise the WEMCF could not be good enough to extend the band gap with stable negative capacitances. For the examples given in this chapter, the smallest weight of the PZT4 material used in the final designs is around 30% of the host structure.

The designed piezoelectric structures have lower modal density than the original structure because of the band gap. Under some boundary conditions the modal density can even be zero. Consequently the vibration is dramatically reduced. However it is not always the case, band gap resonance can arise depending on the boundary condition. We show that this phenomenon is not abnormal or confusing and it can be understood in several ways. The modal shape of a band gap resonance is rather localized around the boundaries, so the response in these areas will be increased. However, the part away from the boundaries still have lower response, no matter whether there are band gap resonances or not. These features are achieved only by enlarging the dynamic contrast of the unit cell rather than increasing damping.

According to the vibration localization features of the band gap resonances, we show that the vibrational energy can be removed by introducing only one resistor or harvester to the PZT patch at each boundary. Inside the band gap, the vibration reduction performance is almost identical with the case in which all the patches are connected to the same resistor. This might lead us to an efficient way to harvest the energy and to combine energy harvesting with the vibration reduction.

The systems are designed without knowing any modal information of the host structure. Moreover, the vibration reduction performance is also boundary condition insensitive as it is examined by changing the supporting stiffness. Therefore this method is promising at mid- and high frequencies where exact modal information is difficult to access.

Chapter 6

Wave propagation and forced response of a thin-wall structure with periodic piezoelectric shunts

Abstract: Thin-wall structures are of great interest in many areas of mechanical engineering such as the automotive industry. Such components play a leading role in the energy transfer paths from the engine sources to panels, creating sound radiation and unwanted vibration leading to fatigue, and associated structural borne sound phenomenon. Mastering the dynamical behavior of thin-wall structures can provide an efficient and physically satisfactory means to passively optimize the car chassis. In this chapter we apply the proposed numerical tools to a thin-wall structure coupled with periodic piezoelectric patches and electric circuits. The aim is to (1) illustrate the industrial application of the numerical methods; and (2) re-examine the conclusions obtained by simpler structures. Both free wave characteristics and forced response are analyzed, where resistive and resonance circuits are considered. The WFEM with reduced unit cell model is then validated by the WFEM with full unit cell model and the full FEM model. It is shown that if the control factors for the reduction technique are properly chosen, it can improve the accuracy while accelerating the calculation as expected. Resulting from the complexity of the thin-wall structure, we show that some enhancements are not optional but imperative. Additionally, the two equivalent ways for WEMCF are confirmed by the both lower-order and high-order waves of the thin-wall structure.

Contents

6.1 Outlines of the numerical tools

6.1.1 WFEM with reduced unit cell model

The main steps concerning the analysis of free waves and forced response by the WFEM with reduced unit cell model are summarized in Figure 6.1. Free wave analysis starts from solving the eigenvalue problem

$$\left(\begin{bmatrix} \mathbf{0} & \sigma\mathbf{I} \\ -\mathbf{D}_{\mathrm{RL}} & -\mathbf{D}_{\mathrm{RR}} \end{bmatrix} - \lambda \begin{bmatrix} \sigma\mathbf{I} & \mathbf{0} \\ \mathbf{D}_{\mathrm{LL}} & \mathbf{D}_{\mathrm{LR}} \end{bmatrix} \right) \begin{pmatrix} \mathbf{q}_{\mathrm{L}} \\ \mathbf{q}_{\mathrm{R}} \end{pmatrix} = \mathbf{0} \tag{6.1}$$

at different frequencies, where $\sigma = \|\mathbf{D}_{\mathrm{RR}}\|_{\mathbf{2}}/\mathbf{N^2}$ and more context can be found in Chapter 3. If $\sigma = 1$, then Equation 6.1 is the original eigenvalue scheme that is widely considered in the literature. The initial results are discrete points in the wavenumber-frequency diagram. Commonly the propagating waves and waves in the band gaps are of greater interest. In order to present the evolution of these waves at different frequencies, one needs to filter the strong evanescent waves by checking the propagating constant. The next step is searching through frequency points and linking the points with similar waveshapes. To do that the Modal Assurance Criterion (MAC) is used to similarity of waveshapes among frequencies. After wave matching, the data is presented by several curves, each showing the relationship between the frequency and wavenumber, termed dispersion curve.

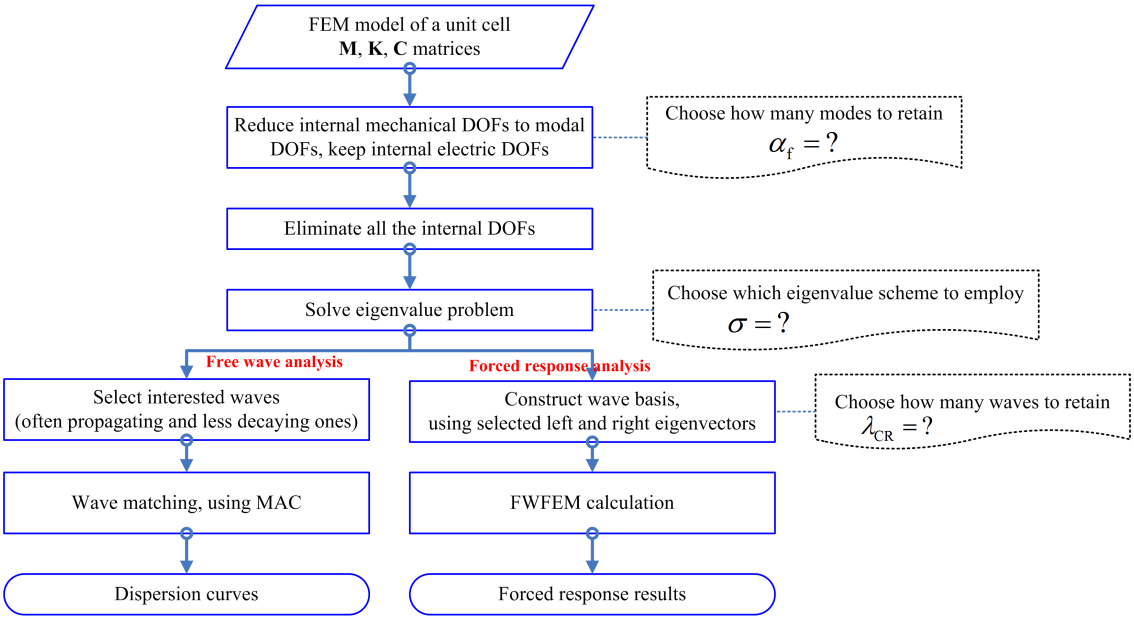

Figure 6.1: Flow chart of the enhanced wave and finite element method

In the forced response analysis, a wider rang of waves are selected from the eigenvalue problems, forming the reduced wave basis. This is due to the fact that some evanescent waves must be taken into account to provide sufficient shape functions for the cross-section deformation. Wave-matching among frequencies is not necessary. But the left eigenvectors are needed. Efforts have to be paid on distinguishing the positive-going and negative-going waves.

Three factors control the accuracy of the reduced wave basis: (1) factor α_{f} for choosing the retained modes of the unit cell and (2) factor σ used in the eigenvalue scheme to balance the magnitude of matrix elements and (3) factor λ_{CR} that truncates the full wave basis to form the reduced one. As it was reported in the literature [182], the strongly evanescent waves yielded by the original eigenvalue scheme are of significant errors. Therefore when all the waves were included in the forced response calculation, unacceptable error was observed. If these waves hardly contribute to the overall response, we can neglect them so as to avoid the numerical errors. However no clear rules for the choosing of λ_{CR} can be found in the literature. In the work of Waki [182], $\lambda_{\mathrm{CR}} = e$ is used; in the previous work of the thesis, $\lambda_{\mathrm{CR}} = 10$ is used for a simple solid waveguide (in Chapter 3); $\lambda_{\mathrm{CR}} = 10^9$ is used for a non-symmetric waveguide (in Chapter 2).

By applying the enhanced WFEM to the thin-wall structure, we re-examine the influences of the three factors: the number of the retained modes, eigenvalue scheme and the number of the kept waves.

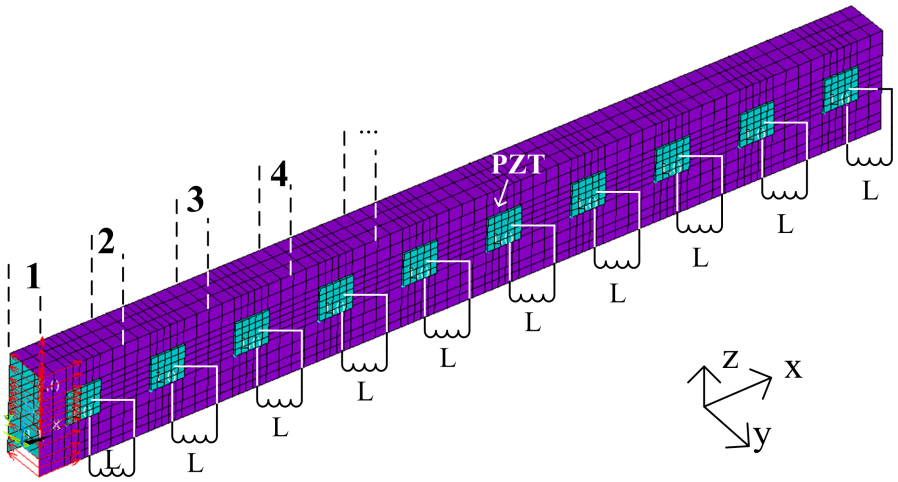

Figure 6.2: FE model for the finite thin-wall structure.

6.1.2 WEMCF

WEMCF measures the coupling strength between the mechanical and electric field for waves, and it is defined (in Chapter 4) by the fraction of the electric energy W_{free} over the elastic energy V during the passage of the wave, namely

$$\mathcal{K}_{1f}^2 = \frac{W_{\mathrm{free}}}{V} \tag{6.2}$$

WEMCF has been used as a criterion for the design of the piezoelectric beam as shown in Chapter 5. Additionally, one important feature of WEMCF is that it can also be calculated by the frequency difference of the OC and SC status, namely

$$\mathcal{K}_{\mathrm{W}}^2 = \frac{\omega_{\mathrm{OC}}^2 - \omega_{\mathrm{SC}}^2}{\omega_{\mathrm{SC}}^2} \tag{6.3}$$

It is demonstrated that $\mathcal{K}_{1f}^2 \approx \mathcal{K}_{\mathrm{W}}^2$ in Chapter 4. This actually indicates that the proposed WEMCF is consistent with the MEMCF at the border frequencies of the band gaps.

By analyzing the WEMCF of some typical waves in the thin-wall structure, we re-examine statement of $\mathcal{K}_1^2 = \mathcal{K}_2^2$. Moreover, WEMCF is used as a energy criterion, to validate the accuracy of the WFEM with reduce unit cell model.

6.2 The considered thin-wall structure

Figure 6.2 shows the thin-wall structure. Piezoelectric patches are periodically bonded on to it and for each unit cell there are two PZT patches. The geometric parameters of one unit cell are shown in Figure 6.3 by international units and so as the FE mesh. For one unit cell, the overall number of DOFs is 1896, with 336 on the left and right side, 1558 on the internal mechanical part and 2 on the electric part. The host material is steel with Young's modulus 2.11×10^{11} Pa and density 7.8×10^3 kg/m^3, and the piezoelectric patches are made of PZT4 (see Appendix A).

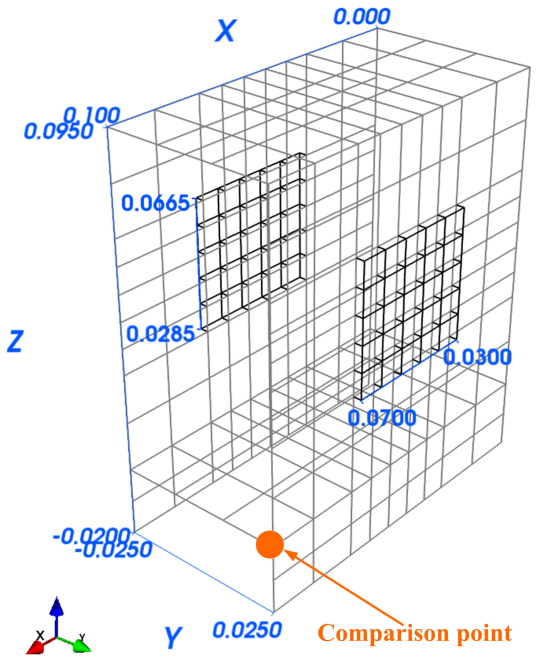

Figure 6.3: FE model for one unit cell of the thin-wall structure.

6.3 Free wave characteristics

6.3.1 With open-circuit shunts

Here we set the electric impedance to the open-circuit status, namely $\mathbf{Y} = \mathbf{0}$. The dispersion curves are calculated from 0 Hz to 2000 Hz by the full FE model of the unit cell at first. The positive-going waves with $\lambda < 10$ are shown in Figure 6.4a. The first two subplots show the real and imaginary parts of the wavenumbers respectively. The third subplot presents the WEMCF of the waves.

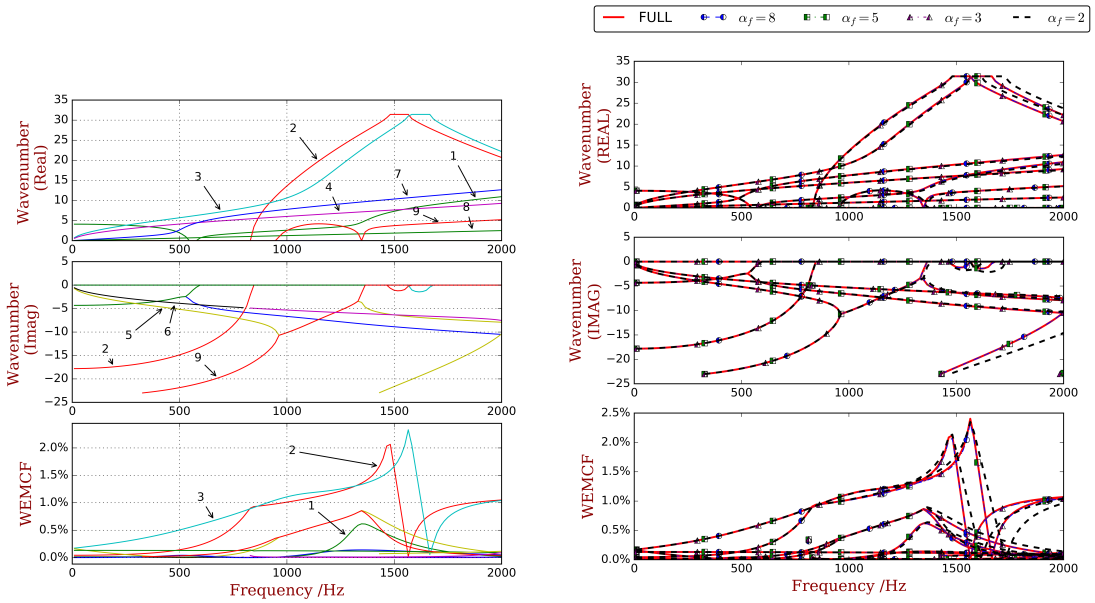

(a) (b)

Figure 6.4: Dispersion curves and WEMCF of the positive-going waves with $\lambda < 10$ when piezoelectric patches are open-circuit: (a) Results obtained by full unit cell model; (b) Comparison of reduced model with different α_f.

In Figure 6.4a, several waves are recognized and labeled with different numbers. Waves 3, 4, 7, 8 are always propagating since 0 Hz, the waveshapes indicate that they are respectively Y-axis flexural, Z-axis flexural, torsional and longitudinal waves, as shown in Figure 6.5. With the increase of the frequency, some evanescent waves, for example no. 1, 2 and 9, are shifting to propagating waves. The cut-on frequency of wave 2 is around 800 Hz and it represents the pumping wave, as shown in Figure 6.5b. Two Bragg band gaps are observed around 1500 Hz, created on wave 2 and 3 respectively. At the bounding frequencies of the band gaps, WEMCF reaches the local maximum and minimum values. This can be understood by checking the corresponding waveshapes. At 1264 Hz the waveshapes of wave 2 is shown in Figure 6.5a, and the shape is symmetric along the X-axis. Consequently it generates different kinds of charge on the electrode and the overall change and electric energy is zero.

Figure 6.4b compares the results obtained by full model and the proposed reduced model when α_f equals to 2, 3, 5 and 8. For each case 120 frequency points are calculated; the CPU time and the size of reduced model are listed in Table 6.1. For the reduced model with $\alpha_\mathrm{f} \geqslant 3$, good agreements are observed both on wavenumber and WEMCF. For the $\alpha_\mathrm{f} = 2$ case, the reduced model gives inaccurate results after the first band gaps. Only 2 modes are retained when $\alpha_\mathrm{f} = 2$, that explains the inaccuracy at higher frequencies. The difference at CPU time among the reduced models are minor, and the using of these reduced models save around 50 percent of the CPU time. In this regard, it is better to set a relatively larger value of α_f so as to ensure the accuracy while accelerating the calculating.

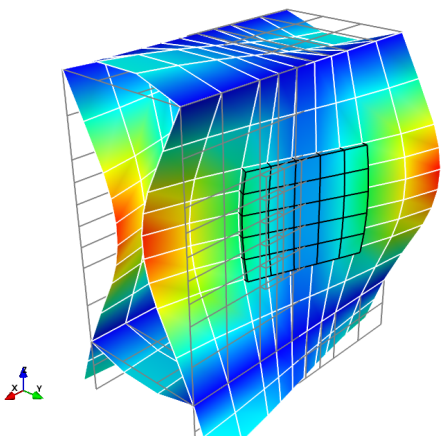

(a) wave 2 at 1264 Hz

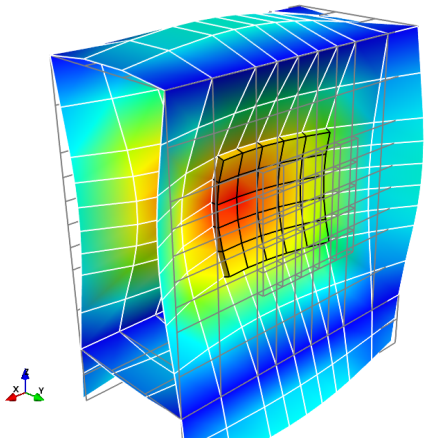

(b) wave 2 at 1464 Hz

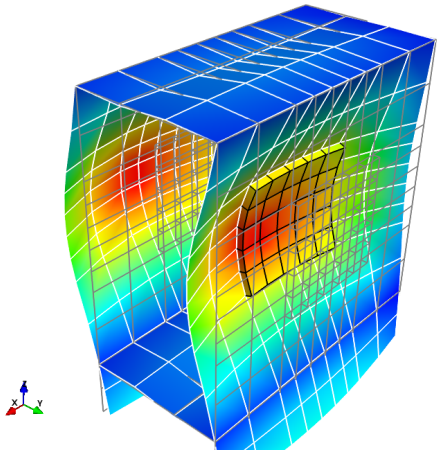

(c) wave 3 at 1381 Hz

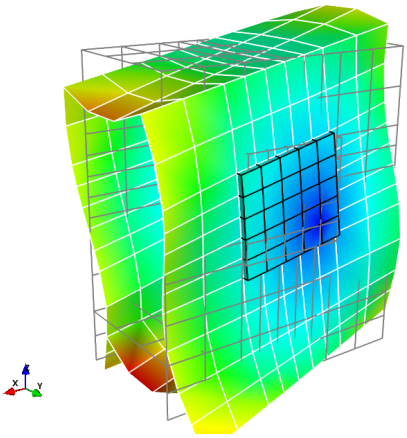

(d) wave 4 at 1867 Hz

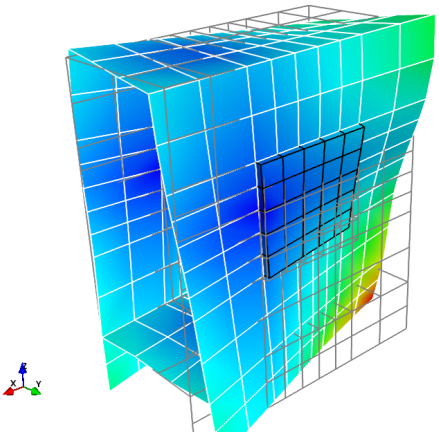

(e) wave 7 at 1682 Hz

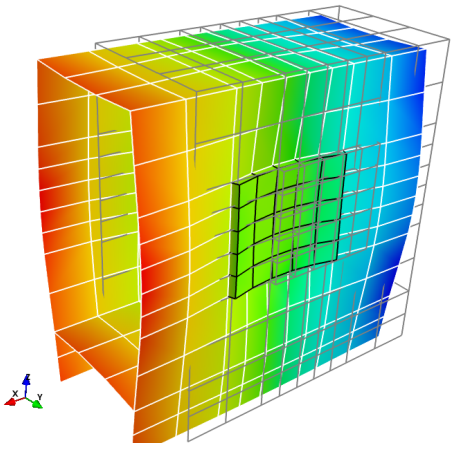

(f) wave 8 at 1732 Hz

Figure 6.5: Some propagating waveshapes of the thin-wall structure when piezoelectric patches are open-circuit. The waves tranvel along the X-axis. Waves 2, 3, 4, 7, 8 are respectively pumping, Y-axis flexural, Z-axis flexural, torsional and longitudinal waves.

Table 6.1: Computation cost among different models for free wave analysis

Model	Internal mechanical DOFs	CPU Time /s
Full	1558	82.3
$\alpha_{\mathrm{f}} = 2$	2	40.7
$\alpha_{\mathrm{f}} = 3$	9	41.3
$\alpha_{\mathrm{f}} = 5$	15	42.0
$\alpha_{\mathrm{f}} = 8$	30	43.2

6.3.2 Validation of two equivalent ways for WEMCF

The results of WEMCF shown in Figure 6.4a and 6.4b are calculated by Equation 6.2 using the energy fraction. This is also the recommended way to calculate WEMCF. Alternatively, WEMCF can also be calculated from Equation 6.3, even though it is much more complex than the previouse way. To do that another calculation with short-circuit is conducted and 3 waves are selected for comparison, including both low-order and high-order waves. The comparison of the results are shown in Figure 6.6. The results acknowledge the statement that $\mathcal{K}_{1f}^2 \approx \mathcal{K}_{\mathrm{W}}^2$. This illustrate the use of WEMCF for complex waveguides.

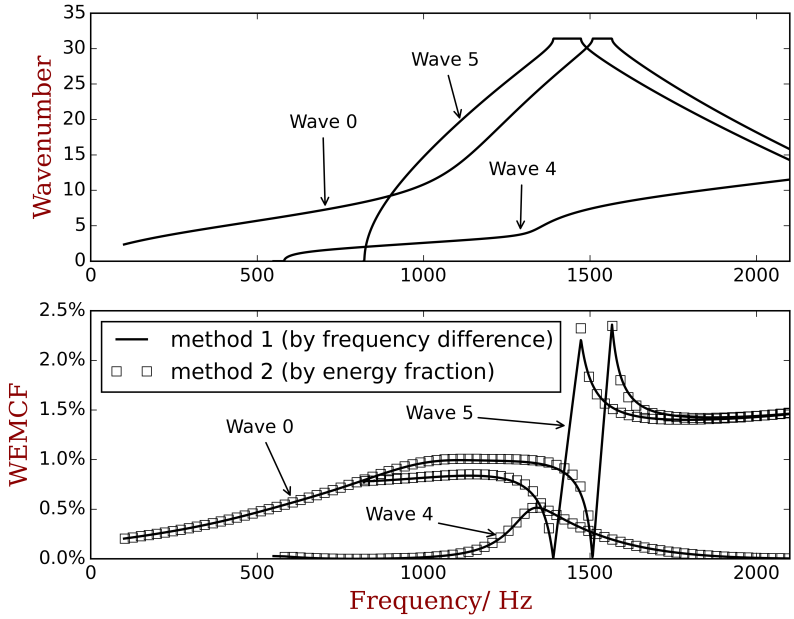

Figure 6.6: The comparison of WEMCF calculated from different means, for wave 0, 4 and 5.

6.3.3 With inductor shunts

Here we connect an identical inductor $L = 2.69\,\mathrm{H}$ to the each PZT patch in the unit cell, so as to tune with the intrinsic capacitance at 1300 Hz. The dispersion curves analyzed by

full unit cell model are presented in Figure 6.7. Two additional band gaps can be found from 1260 Hz to 1300 Hz. These band gaps are caused by the tuning effects of the shunted inductor and the intrinsic capacitance hence they are termed the 'local resonance (LR) band gap' in the literature [81]. The depth of the LR band gaps are much greater than the Bragg band gaps, therefore the waveshapes decay dramatically in space. This feature can be seen from the waveshapes of the pumping wave and flexural wave at 1297 Hz, as shown in Figure 6.8.

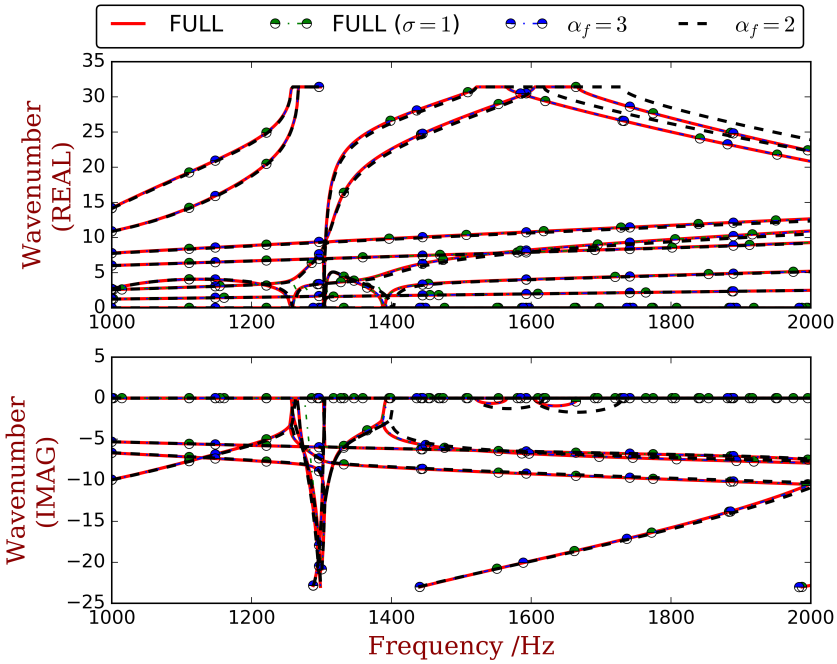

Figure 6.7: Dispersion curves of the positive-going waves with $\lambda < 10$ when piezoelectric patches are shunted with identical inductors, obtained by full WFEM with eigenvalue scheme (6.1), full WFEM with original eigenvalue scheme and reduced WFEM with $\alpha_\mathrm{f} = 3$ and $\alpha_\mathrm{f} = 2$.

The reduced model with $\alpha_\mathrm{f} = 2$ are $\alpha_\mathrm{f} = 3$ are also employed on the same problem and the results are compared in Figure 6.7. The remarks are similar with the open-circuit case. The reduced model with $\alpha_\mathrm{f} = 2$ starts to lose accuracy at higher frequencies around 1400 Hz because the modes are inappropriately truncated. In addition, the original eigenvalue scheme ($\sigma = 1$) is applied to the full unit cell model. The results are also compared in Figure 6.7 and labeled as 'FULL($\sigma = 1$)'. Good agreements can bu found in comparison with the other results obtained by using original scheme (6.1).

In the free wave analysis, we presented the positive-going waves with $|\lambda| < 10$, namely the less-decaying ones and compared them in terms of the dispersion relation and WEMCF. To have accurate predictions, the magnitude balance adjustment factor σ is optional. The reduced model is applicable to accelerate the computation when α_f is greater than 3.

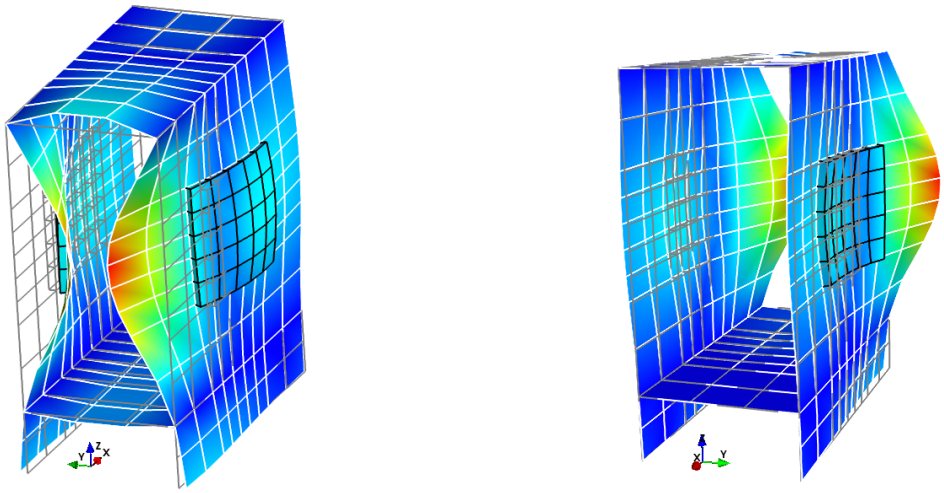

(a) Pumping wave (b) Y-axis flexural wave

Figure 6.8: Waveshapes inside the LR band gap (at 1297 Hz).

6.4 Forced response (inductor shunts)

As it is shown in Figure 6.2, the periodic structure is shunted with identical inductors at each PZT patches, the inductance is the same as that used in the previous section ($L = 2.69\,\mathrm{H}$). The cross-sections are numbered by their x positions. We applied unit forces on UX, UY, and UZ DOFs only at one edge of the first cross-section, in order to excite more waves. Free boundary conditions are considered at rest DOFs of the left and right boundaries. The full FEM model of the whole structure is used as the reference. The analyzed frequency range is from 1000 Hz to 2000 Hz, with 900 points for the WFEM and 180 points for the full FEM. In this section, the UY displacement of the corner node at each cross-section labeled in Figure 6.3 is post-processed and compared with different methods.

Firstly, we discuss the accuracy of the eigenvalue schemes. Figure 6.9 compares the results obtained by using original eigenvalue scheme (labeled 'FWFE($\sigma = 1$)') and the modified eigenvalue scheme (6.1) (labeled 'FWFE'). Full FE model of the unit cell and full wave basis are used in both calculations. Figure 6.9a represents the Frequency Response Function (FRF) at the excitation cross-section, and it can be seen that results obtained by original eigenvalue scheme has significant errors at a lot frequencies, especially around 1200 Hz, 1500 Hz and 1800 Hz. While checking the FRF at cross-section 3, shown in Figure 6.9b, the results obtained by original eigenvalue scheme matches very well with the reference at the whole frequency range. This clearly shows that the errors observed in Figure 6.9a are induced by the strong evanescent waves that are included in the full wave basis. The results also indicate that original eigenvalue scheme could not predict the strong evanescent waves with a acceptable accuracy. On the contrary, the results obtained by eigenvalue scheme (6.1) have good agreements with the reference at both cross-sections. This implies that the proposed eigenvalue scheme can properly predict the strong evanescent waves.

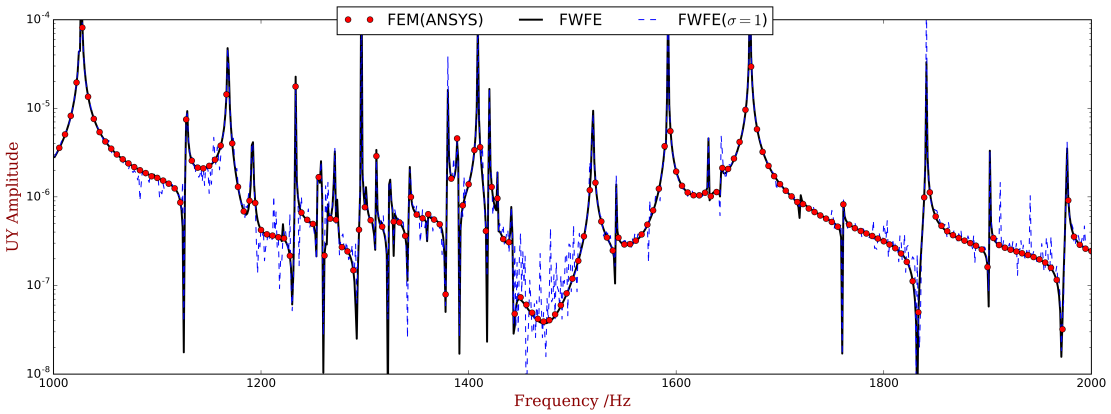

(a) On the first cross-section

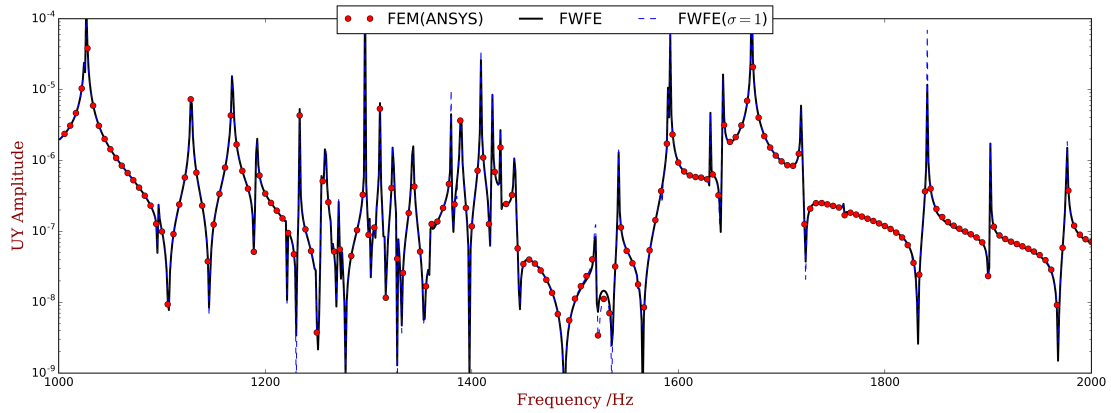

(b) On the third cross-section

Figure 6.9: Comparison of FRF obtained by different eigencvalue schemes. Here the WFEM uses full unit cell model and full wave basis.

Secondly we compare the influence of the reduced wave basis. Factors $\lambda_{\mathrm{CR}} = 10^3$, $\lambda_{\mathrm{CR}} = 10^7$, $\lambda_{\mathrm{CR}} = 10^8$, $\lambda_{\mathrm{CR}} = 10^9$ are respectively considered. The numbers of kept waves are compared in Figure 6.10. The results are summarized in Figure 6.11. It was reported in the literature [24, 182] on relatively simple cased that a very small λ_{CR} is sufficient. In the considered case, unacceptable error is observed when $\lambda_{\mathrm{CR}} = 10^3$ is used, which is larger than what was used in the aforementioned literature. Even when $\lambda_{\mathrm{CR}} = 10^7$ is considered by which 85 percent of the waves are retained, at some frequencies (eg. from 1400 Hz to 1600 Hz) it will still induce some errors. According to the results, $\lambda_{\mathrm{CR}} = 10^8$ is recommended, by which less than 10 waves are neglected.

In Figure 6.11, the proposed eigenvalue scheme is used for all the cases. However, when using the original eigenvalue scheme, frequently it failed to distinguish same number of positive-going and negative-going waves when large λ_{CR} is given because of the errors. The following-up process of the forced response is consequently not applicable. In our calculation, only when $\lambda_{\mathrm{CR}} = 10^3$ the forced response with original eigenvalue scheme works. According to the aforementioned results, it is insufficient to have a good agreements with the reference. Moreover, incorrectly neglecting evanescent waves might break

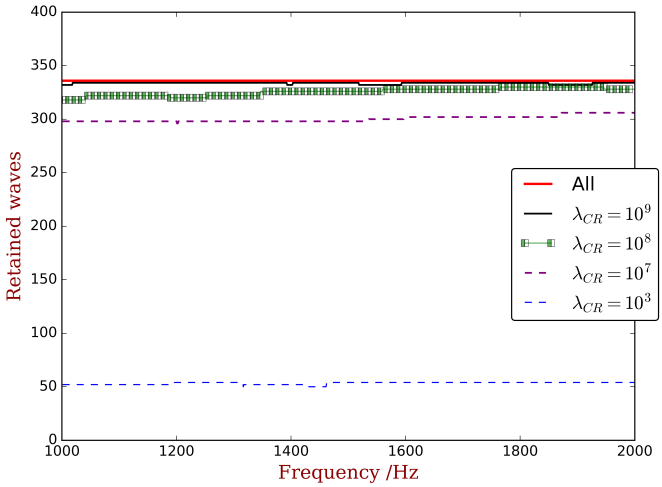

Figure 6.10: The comparison concerning the number of retained waves

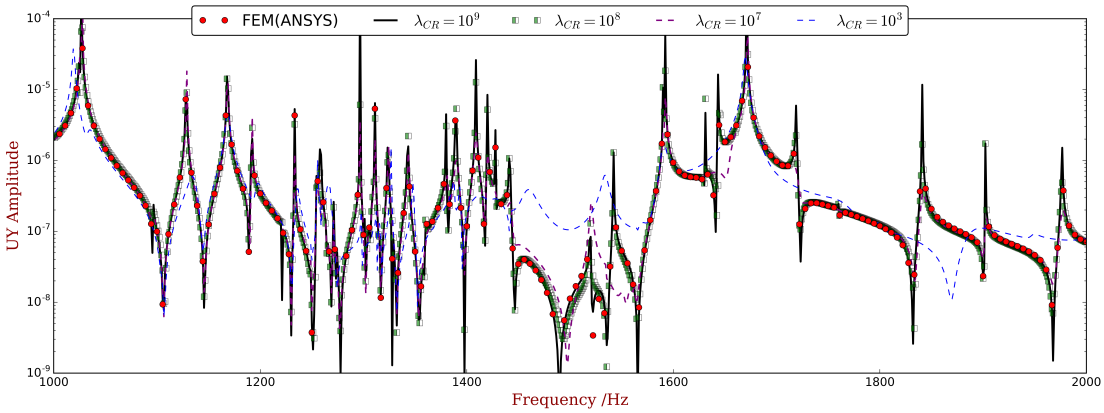

Figure 6.11: Comparison of FRF obtained by keeping different waves. Here the WFEM uses full unit cell model.

the conservation of energy and power. This explains the 'damping' behavior observed of the $\lambda_{\mathrm{CR}} = 10^3$ curve in Figure 6.11.

Thirdly we verify the reduced model of the unit cell. Factor α_{f} was set to 9, 8, 6 and 4 respectively and the results are compared in Figure 6.12. When $\alpha_{\mathrm{f}} = 6$ is used, the FRF at some frequencies (eg. from 1500 Hz to 1700 Hz) still have errors. According to the results, $\alpha_{\mathrm{f}} = 8$ is recommended, by which 40 modes are retained from the overall 1558 ones. This threshold is more strict that was made for the free wave analysis concerning less-decaying waves. Nevertheless, the error induced by the reduced model is not as serious as it in the wave reduction if the control factor is not correctly chosen.

The computational costs of methods with different choices of factors are compared in Table 6.2. It is shown that the using of wave basis has already dramatically reduced the calculation time, and by employing the reduced model the computing can be further accelerated. The transfer matrix in the wave domain is diagonal, so the truncation of the wave basis does not induce an additional acceleration.

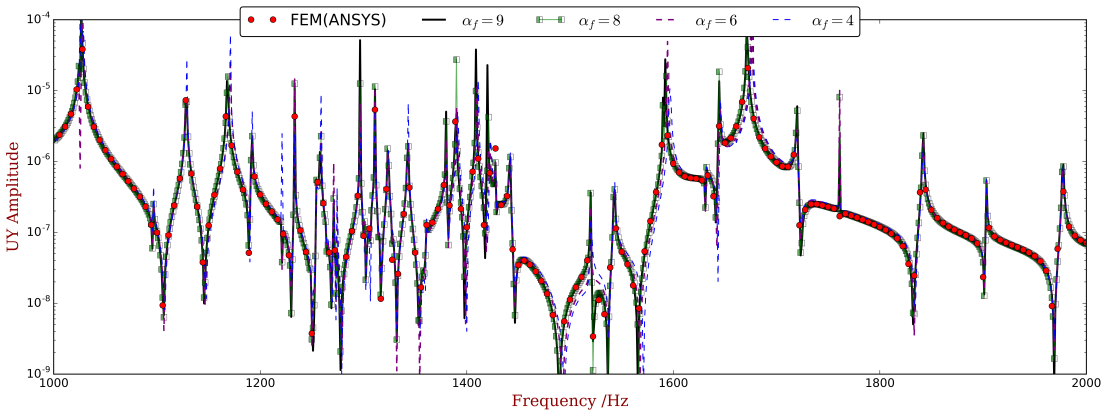

Figure 6.12: Comparison of FRF obtained by keeping different modes. The WFEM methods used here are with reduced wave basis, and $\lambda = 10^9$.

Table 6.2: Computation cost of different models for forced response

method	factors	retained waves	frequency points	CPU time /s
FEM (ANSYS)	N/A	N/A	180	4274
WFEM (Python)	$\lambda_{\mathrm{CR}} = +\infty$, $\alpha_{\mathrm{f}} = +\infty$	336	900	630
WFEM (Python)	$\lambda_{\mathrm{CR}} = 10^8$, $\alpha_{\mathrm{f}} = 8$	320 ± 5	900	347
WFEM (Python)	$\lambda_{\mathrm{CR}} = 10^3$, $\alpha_{\mathrm{f}} = 8$	51 ± 2	900	340

6.5 Conclusions

In this chapter, the analysis of a electromechanical thin-wall structure is conducted by the proposed numerical tools in the thesis. We show that the wave characteristics, electromechanical coupling features and the forced response of the considered thin-wall structure can be accurately obtained with a reasonable calculation time.

The complex dynamics of thin-wall structure provides are used to re-examine some obtained conclusions in the previous chapters. The first one is the use of the WFEM with reduced unit cell model and a new eigenvalue scheme. we show that for free wave analysis, where the less-decaying waves are of more interest, the new eigenvalue scheme is optional. But for the forced response analysis it is imperative. We also show that by keeping few modes ($\alpha_{\mathrm{f}} = 8$) of the unit cell, a effective unit cell model can be constructed and it provides good results for the R-L resonance shunts. Moreover, by using such reduced model, the analysis of free wave is reduced by 50% and forced response by 90 %. Finally, we show that when excitation is complex and many waves are excited, more evanescent waves are required for a good prediction for the forced response, here $\lambda_{\mathrm{CR}} = 10^8$ is used, retaining nearly all the waves. Note that the use of a reduced wave basis is more for an purpose of accuracy not for acceleration. The second re-examined conclusion is the two equivalent ways for the calculation of WEMCF. The equivalence is validated at both low-order waves with simpler shapes and high-order waves with more complex shapes. This means we can still use the energy fraction to predict the WEMCF, leading to a convenient way for the electromechanical analysis of complex piezoelectric waveguides.

Conclusions

Piezoelectric shunt circuits provide new electric design variables for the mechanical property, which leads to an artificial modification of the guided wave characteristics. The conducted work concerns the modeling, understanding, evaluation and design of the guided waves in piezoelectric composites (periodic structures), leading to useful applications. The main contributions of the conducted work are summarized below:

- **The extensions of Wave and Finite Element method**, including four aspects:

  1. Several new reduced models based on free-interface CMS in combine with an enhanced eigenvalue scheme have been proposed for the free-wave analysis. The reduced models are applicable for any waveguides with proportional damping. According to the numerical investigation on an asymmetric thin-wall structure, we recommend the used of MacNeal's reduction method in terms of efficiency, which reduces the CPU time of free-wave analysis by 97%. The exact substructure method is suggested in terms of the minimum model size, retaining only 16 of the overall 4416 DOFs.
  2. A new reduced model for the piezoelectric periodic structures has been proposed for the free-wave analysis. It is also applicable for waveguides with local dampers. The proposed reduction process is independent with the electric impedance so it has advantages when designing a piezoelectric system where repetitive calculations are required. The application on a thin-wall piezoelectric structure shows that the CPU time of free wave is reduced by 50% and forced response by 90%.
  3. A new multi-scale numerical tool for computing the forced response and energy flow is proposed. The method can be applied for built-up structures consist of both periodic and non-periodic parts with finite/infinite extent. The major idea is to model the non-periodic part by FEM and the periodic parts by WFEM, and then to adapt the models of the substructures. Owing to the use of WFEM, when the number of unit cells in periodic substructures is increasing, the CPU time would not be significantly increased and remains low. Numerical study on a finite built-up structure in forced response analysis shows a CPU time reduction by 75% in comparison with the full FEM when there are 20 PZT patches.
  4. Detailed numerical investigations concerning the use of reduced wave basis in forced response analysis have been conducted on several different structures. We show that some strong evanescent waves have to be kept even though there are some inaccuracies in the wavenumbers, and the results still have good agreements to the full finite element model. Directly truncating those strong evanescent waves induces significant errors. This is due to the fact that sufficient wave shapes has to be kept in the wave basis so as to approximately satisfy the constrains on the boundaries. Also we confirm the necessity of using the left eigenvectors to replace to inverse of the right eigenvector matrix.

- **The proposal of Wave Electromechanical Coupling Factor (WEMCF)**, including:

    1. The definitions of WEMCF. The concept of WEMCF is proposed to quantitatively evaluate the coupling strength between the electric and mechanical fields during the passage of a wave. We show that the WEMCF can be calculated either by an energy formula or by frequency formula. The equivalence of these two formulas makes WEMCF consistent with the Modal Electromechanical Coupling Factor.
    2. The calculation of WEMCF. The WEMCF can be post-processed from the free-wave characteristics obtained from WFEM through the energy formula. This way the WEMCF can be calculated by computing dispersion curves only once and does not need wave matching between OC and SC statuses. However, the post-processing of WEMCF can be a time-consuming task for full WFEM. The reduced model can be used to accelerate the calculation while maintain the accuracy. For the example structure, it reduces the CPU time to less than 1%. The consistency with the frequency and energy formulas and the use of reduced model for WEMCF are validated by a solid PZT waveguide and also by a thin-wall PZT waveguide with both low-order and high-order waves.
    3. The applications of WEMCF. The WEMCF is directly linked to the performance of the waveguide. It is strongly correlated to the best energy transmission loss of the resistive PZT waveguide in a built-up structure. It is also linked to the extreme width of the band gap that can be extended by a stable Negative capacitance. Hence the design for the geometric and electric parameters can be done separately, and WEMCF can be used as an optimization objective during the geometric design.

- **The clarification of several concepts**, including:

    1. A band gap does not guarantee to eliminate all the modes inside it (even though sometime the modal density can be zero), but ensures that all modes in it have localized shapes.
    2. A band gap in the periodic substructure does not directly link to a low-vibration and low-energy-flow frequency range of the built-up structure. It is due to the fact that a mix evanescent field can carry energy.
    3. Both band gaps and damping can induce a non-zero imaginary part of wavenumber, which means the attenuation of displacement when the wave is traveling towards a far-field. However, the non-zero imaginary part of wavenumber does not necessarily indicate the attenuation of energy flow. Damping mechanism can 'attenuate' energy; but a undamped finite periodic substructure can not 'attenuate' energy at band gap frequencies.

- **The development of design process for multi-mode vibration control based on band-gap mechanisms**. Negative capacitance is used with a stability consideration to enlarge the band gap. The geometric and electric parameters are determined consecutively in an iterative process when the overall mass of the

piezoelectric materials is constrained. The design process is purely based on wave characteristics and it does not need any modal information of the host structure. We shown that the vibration reduction performance is also boundary condition insensitive. Therefore this method is promising at mid- and high frequencies where exact modal information is difficult to access. The amount of piezoelectric materials should not be lower than a certain level, otherwise the desired band gap can not be achieved with stable negative capacitances.

- **Suppression of band-gap resonances**. According to the vibration localization feature of the band gap resonances, we show that the vibrational energy can be effectively removed by introducing few resistor to the negative capacitance circuits near boundaries. Inside the band gap, the vibration reduction performance is almost identical with the case in which all the patches are connected to the same resistor.

Perspectives

A straightforward direction for the future work is to extend or examine the numerical strategies, coupling indicators and design processed into 2D structures. For instance we can still build a 2D unit cell model by the free modes plus residual effects and impose 2D periodic conditions, so as to analyze the free waves in a 2D waveguide. Since using wave basis to calculate the forced response of a finite 2D has some difficulties to handle the boundary conditions. The wave basis may be used to locate the band gaps rather than being used in forced response. In principle, WEMCF is also applicable in 2D cases, so we can still use it to design the geometrics. Similar ideas can be used to design a light-weight structure with a wide band gap covering the working range of the 2D structure. It remains unknown concerning the details and performances. Other suggested ideas for future studies are:

- Applications of other CMS techniques to model the unit cell for WFEM. By now the considered reduced models are based on some assumptions on the structural damping. To extend the fast analyzing ability for the heavily damped structure with non-proportional damping, some methods mentioned in Ref. [208] maybe applicable.

- The predictions of band gap resonances. We observed that the band gap resonances emerge when boundary stiffness is in a continuous range. It seems that there are some general rules to determine the existence of these resonances, especially from the wave perceptions. To do that the phase-closure principle [78] may be a promising tool.

- Geometric optimization for the WEMCF of multiple waves. In our work we managed to reduce the vibration caused by one wave type in a wide frequency range. It is necessary to consider multiple waves if the structure and excitation is complex. To do that significant WEMCF should be achieved for multiple waves by geometric design. It may leads to a multi-input & multi-objective optimization problem.

- Generating energy by band-gap resonances. Instead of dissipating the localized energy, it is promising to harvest energy from the structure. The localization allows the use of few harvesters to remove large proportion of mechanical energy. To do that we also need to know under which boundary conditions there will be band gap resonances, which is an open question.

- Considering the influences of the 'mistuning' among unit cells of a periodic structure. In our work perfect periodic structures are considered. Even though some studies have pointed out the performance of the periodic structure would not significantly change if there are insignificant perturbation on the parameters, it is still interesting to know the perturbation on which parameter will more likely worsen the performance, which corresponds to a sensitive analysis.

- Experimental validations. The features of band gap resonances need to be experimentally validated so as to confirm our understandings. Also the vibration reduction

systems proposed in Chapter 5 require experimental validations. The main challenge is that the NCs are very close to the instable zone. We may first experimentally measure the stability of the NCs and then use the proposed design method to give geometric and electric parameters. Note that the periodic structures use in experiments are actually near-periodic structures, so the success of the validations also indicate the robustness of the system.

Publications during the thesis

International Journals

- **Y. Fan**, M. Collet, M. Ichchou, L. Li, O. Bareille, and Z. Dimitrijevic, Wave electromechanical coupling factor for the guided waves in periodic piezoelectric structures, *Smart Materials and Structures*, under review.
- **Y. Fan**, C. W. Zhou, J. P. Laine, M. Ichchou, and L. Li, Model reduction schemes for the wave and finite element method using free modes of the unit cell, *Journal of Sound and Vibration*, under review.
- **Y. Fan**, M. Collet, M. Ichchou, L. Li, O. Bareille, and Z. Dimitrijevic, Enhanced wave and finite element method for wave propagation and forced response prediction in periodic piezoelectric structures, *Chinese Journal of Aeronautics*, in press, 2016.
- **Y. Fan**, M. Collet, M. Ichchou, L. Li, O. Bareille, and Z. Dimitrijevic, A wave-based design of semi-active piezoelectric composites for broadband vibration control, *Smart Materials and Structures*, 25(5): 055032 (15pp), 2016.
- **Y. Fan**, M. Collet, M. Ichchou, L. Li, O. Bareille, and Z. Dimitrijevic, Energy flow prediction in built-up structures through a hybrid finite element/wave and finite element approach, *Mechanical System and Signal Processing*, 66–67: 137–58, 2016.
- L. Li, P. Deng, and **Y. Fan**, Dynamic characteristics of a cyclic-periodic structure with a piezoelectric network, *Chinese Journal of Aeronautics*, 28(5): 1426–37, 2015.

International Conferences

- **Y. Fan**, M. Collet, M. Ichchou, L. Li, O. Bareille, and Z. Dimitrijevic, Optimization of periodically distributed piezoelectric patches for the control of the energy flow in thin-wall structures, *ISMA2016 conference on Noise and Vibration Engineering*, September 19-21, 2016, Leuven, Belgium.
- **Y. Fan**, M. Collet, M. Ichchou, L. Li, O. Bareille, and Z. Dimitrijevic, On definition and evaluation of the wave electromechanical coupling factor, *CSNDD2016: 3rd International Conference on Structural Nonlinear Dynamics and Diagnosis*, May 23-25, 2016, Marrakech, Morocco.
- M. Collet, **Y. Fan**, and M. Ichchou, Periodically distributed piezoelectric patches optimization for waves attenuation and vibrations damping, *The Journal Acoustic Society of America*, 138(3): 1920–1920, 2015. (ASA 170th meeting, 2-6 November 2015)
- **Y. Fan**, M. Collet, M. Ichchou, L. Li, O. Bareille, and Z. Dimitrijevic, Energy flow optimization in built-up structures with periodically distributed piezoelectric composite, *SMASIS2015: ASME Conference On Smart Materials, Adaptive Structures and Intelligent Systems*, September 21-23, 2015, Denver, Colorado, USA.

- **Y. Fan**, M. Collet, M. Ichchou, L. Li, O. Bareille, and Z. Dimitrijevic, Energy flow prediction in piezoelectric composite structures through a hybrid finite element/wave and finite element approach, *DYNCOMP2015: International Conference On Dynamics of Composite Structures*, June 2-4, 2015, Arles, France.

- **Y. Fan**, M. Collet, M. Ichchou, L. Li, O. Bareille, and Z. Dimitrijevic, Electromechanical coupling of periodical piezoelectric composite in wave domain. *8th Beihang-Centrale Workshop*, May 21-22, 2015, Marseille, France.

- **Y. Fan**, M. Collet, M. Ichchou, L. Li, O. Bareille, and Z. Dimitrijevic, Design of periodic piezoelectric shunting system for control of injected power in 1d waveguide. *VISHNO2014: Vibrations, Shocks and Noise*, Jun 16-19, 2014, Aix En Provence, France.

- **Y. Fan**, L. Li, and M. Ichchou, Longitudinal wave propagation behavior in a uniform infinite rod with conservative PZT shunts and PZT networks. *6th Beihang-Centrale Workshop*, December 11-12, 2012, Lille, France.

National/ Regional Conferences

- **Y. Fan**, M. Collet, M. Ichchou, L. Li, O. Bareille, and Z. Dimitrijevic, A wave-based design of semi-active piezoelectric composites for broadband vibration control, *JJCAB2015: Journées des Jeunes Chercheurs en vibrations, Acoustique et Bruit*, November 5-6, 2015, Besançon, France.

- **Y. Fan**, M. Collet, M. Ichchou, L. Li, O. Bareille, and Z. Dimitrijevic, Control of energy flow in structures using periodic piezoelectric shunts, *CeLyA summer school of Mid and high frequency modelling in structural acoustics*, July 1-3, 2015, Lyon, France.

- **Y. Fan**, M. Collet, M. Ichchou, L. Li, O. Bareille, and Z. Dimitrijevic, Control of injected power in waveguide using periodic piezoelectric shunts, *JJCAB2014: Journées des Jeunes Chercheurs en vibrations, Acoustique et Bruit*, November 6-7, 2014, Lyon, France.

Appendix A

Material properties of the piezoelectric material (PZT4)

Mass density: $\rho = 7500\text{kg/m}^3$
Material stiffness matrix evaluated at constant electric field:

$$[c^E] = 10^{10} \times \begin{bmatrix} 13.2 & 7.1 & 7.3 & & & \\ 7.1 & 13.9 & 7.3 & & & \\ 7.3 & 7.3 & 11.5 & & & \\ & & & 3.06 & & \\ & & & & 3.06 & \\ & & & & & 3.06 \end{bmatrix} \text{Pa}$$

Permittivity matrix evaluated at constant strain:

$$[\varepsilon^S] = \begin{bmatrix} 805\varepsilon_0 & & \\ & 805\varepsilon_0 & \\ & & 805\varepsilon_0 \end{bmatrix}$$

where $\varepsilon_0 = 8.85 \times 10^{-12}\text{C}/(\text{V} \cdot \text{m})$
Piezoelectric stress coupling matrix:

$$[e] = \begin{bmatrix} & & 4.1 \\ & & 4.1 \\ & & -14.1 \\ & -10.5 & \\ -10.5 & & \\ & & \end{bmatrix} \text{N}/(\text{V} \cdot \text{m})$$

Appendix B

Finite element for triple-layered piezoelectric beams

B.1 One dimensional constitutive relation

The proposed finite element is used to describe the triple-layered piezoelectric composite beam shown in Figure B.1. With electric field established along the poling direction (axis 3, along the thickness of element, see Table B.1), the full constitutive equations of piezoelectric materials writes

$$\{T\} = [c^E]\{S\} - [e]\{E\} \tag{B.1}$$

$$\{D\} = [e]^{\mathrm{T}}\{S\} + [\varepsilon^{\mathrm{S}}]\{E\} \tag{B.2}$$

where $\{T\}$ is the stress vector with 6 components, $\{S\}$ the strain vector with 6 components, $\{E\}$ the electric field vector with 3 components, $\{D\}$ the charge intensity vector with 3 components. The matrices, $[c^e]$, $[e]$, $[\varepsilon^S]$ are stiffness matrix evaluated at constant electric field, piezoelectric matrix, permittivity matrix evaluated at constant strain, respectively. The terms used here are consistent with [6]

subscript	element coordinate	description
1	x	length
2	z	width
3	y	poling direction, thickness
4	zy (23)	
5	yx (31)	
6	xz (12)	

Table B.1: Axis and subscript notation.

According to the Euler-Bernoulli assumption, the beam bended in axis 3 induces dominated strain and stress in axis 1, while the stress along axis 2 and all the shear strains are neglected. For stress along axis 3, there are two situations: 1) the size along axis 3 is **large** enough in comparison with axis 1 and 2 so that strain along axis 3 will be neglected (plane strain), and 2) the size along axis 3 is **small** enough in comparison with axis 1 and 2 so that stress along axis 3 will be neglected (plane stress). In our case we consider the plane stress situation, then the terms T_2, T_3, S_4, S_5, S_6, E_1, and E_2 in Equations (B.1) and (B.2) have already been known as zero. By eliminating these terms, an 1D constitutive equation for the piezoelectric beam could be obtained

$$T_1 = \acute{c}_{11}S_1 - \acute{e}_{13}E_3 \tag{B.3}$$

$$D_3 = \acute{e}_{13}S_1 + \acute{\varepsilon}_{33}E_3 \tag{B.4}$$

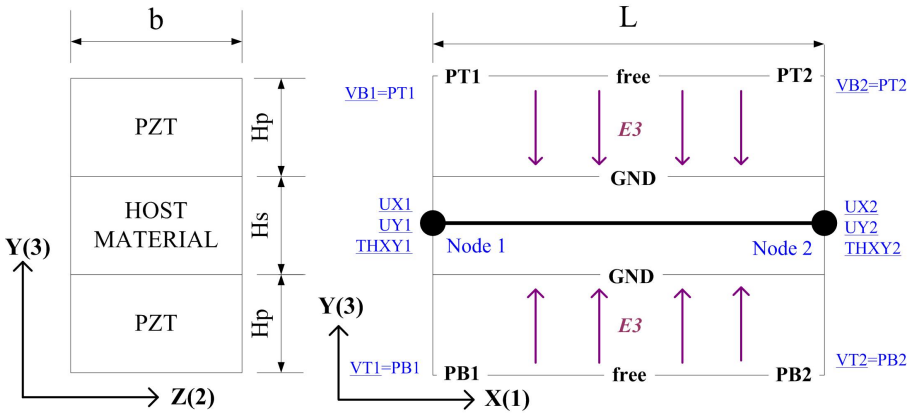

Figure B.1: Geometric parameters and DOFs of Piezoelectric beam element.

The values of these equivalent parameters are quite different from the corresponding terms in Equations (B.1) and (B.2) (i.e. c_{11}, e_{13}, ε_{33}). For example, the 1D constitutive relation of the PZT4 material presented in Appendix A is

$$\begin{Bmatrix} T_1 \\ D_3 \end{Bmatrix} = \begin{bmatrix} 7.86e10 & 9.3 \\ -9.3 & 1080\varepsilon_0 \end{bmatrix} \begin{Bmatrix} S_1 \\ E_3 \end{Bmatrix}$$

We can find

$$(\acute{c}_{11} - c_{11})/c_{11} = -40.5\%$$
$$(\acute{e}_{13} - e_{13})/e_{13} = 126.7\%$$
$$(\acute{\varepsilon}_{33} - \varepsilon_{33})/\varepsilon_{33} = 63.7\%$$

showing significant differences induced by the plane stress assumptions. As it will be shown latter in the validation cases, this treatment is necessary and correct.

B.2 Dynamic equations

The geometric parameters of the element are shown in Figure B.1 and listed in Table B.2. Concerning the electric field, we regard the side that contacts to the host layer as GND (i.e. has constant zero potential), and the another side as electrode-free. This enables the element to handle the distributed electrodes in the future. The element has two nodes, each of them has 5 DOFs, listed in Table B.3. The corresponding nodal loads are: forces (F_x,F_y), moment (M) and electric charges (Q_t, Q_b).

notation	description
b	width of the element
L	length of the element
h_p	height of the piezoelectric layer
h_s	height of the host layer

Table B.2: Geometric parameters of the piezoelectric element.

The polling direction of the top layer will be determined by the input data of the constitutive equations. Namely it depends on the sign of term $\acute{e}_{13}$, as a negative value

indicates that the poling direction is along positive y-axis. For the bottom layer, the polling is defined by parameter κ by means of $\acute{e}_{13,\mathrm{b}} = \kappa \acute{e}_{13}$ so that $\kappa = 1$ for the same direction as the top layer, $\kappa = -1$ for the opposite direction.

nodal DOF	description	corresponding load
U_x	displacement along x-axis	F_x
U_y	displacement along y-axis	F_y
θ	rotation from x-axis to y-axis	M
V_t	potential of the top free side	Q_t
V_b	potential of the bottom free side	Q_b

Table B.3: DOFs of the piezoelectric element.

To derive the dynamic equations of the element, first we define three space domains to identify two piezoelectric layers and the host layer:

$$\begin{aligned}
\Omega_\mathrm{s} &= \{(x,y,z) | y \in [-h_\mathrm{s}/2, h_\mathrm{s}/2], x \in [0,L], z \in [0,b]\} \\
\Omega_\mathrm{t} &= \{(x,y,z) | y \in [h_\mathrm{s}/2, h_\mathrm{p}+h_\mathrm{s}/2], x \in [0,L], z \in [0,b]\} \\
\Omega_\mathrm{b} &= \{(x,y,z) | y \in [-h_\mathrm{p}-h_\mathrm{s}/2, -h_\mathrm{s}/2], x \in [0,L], z \in [0,b]\}
\end{aligned}$$

Then the constitutive relations of the triple layered beam could be written in three cases:

$$\begin{cases}
T_1 = c_\mathrm{s} S_1 & (x,y,z) \in \Omega_\mathrm{s} \\
\begin{Bmatrix} T_1 \\ D_3 \end{Bmatrix} = \begin{bmatrix} \acute{c}_{11} & -\acute{e}_{13} \\ \acute{e}_{13} & \acute{\varepsilon}_{33} \end{bmatrix} \begin{Bmatrix} S_1 \\ E_3 \end{Bmatrix} & (x,y,z) \in \Omega_\mathrm{t} \\
\begin{Bmatrix} T_1 \\ D_3 \end{Bmatrix} = \begin{bmatrix} \acute{c}_{11} & -\kappa\acute{e}_{13} \\ \kappa\acute{e}_{13} & \acute{\varepsilon}_{33} \end{bmatrix} \begin{Bmatrix} S_1 \\ E_3 \end{Bmatrix} & (x,y,z) \in \Omega_\mathrm{b}
\end{cases} \tag{B.5}$$

Additionally, it is better to write the nodal variables in vector form, as:

$$\begin{aligned}
\{U_\mathrm{N}\} &= \begin{bmatrix} U_{\mathrm{x},1} & U_{\mathrm{x},2} & U_{\mathrm{y},1} & \theta_1 & U_{\mathrm{y},2} & \theta_2 \end{bmatrix} \\
\{V_\mathrm{N}\} &= \begin{bmatrix} V_{\mathrm{t},1} & V_{\mathrm{t},2} & V_{\mathrm{b},1} & V_{\mathrm{b},2} \end{bmatrix} \\
\{F_\mathrm{N}\} &= \begin{bmatrix} F_{\mathrm{x},1} & F_{\mathrm{x},2} & F_{\mathrm{y},1} & M_1 & F_{\mathrm{y},2} & M_2 \end{bmatrix} \\
\{Q_\mathrm{N}\} &= \begin{bmatrix} Q_{\mathrm{t},1} & Q_{\mathrm{t},2} & Q_{\mathrm{b},1} & Q_{\mathrm{b},2} \end{bmatrix}
\end{aligned}$$

Then we interpolate the continuous mechanical field into an weighted summary of the nodal displacements:

$$\begin{Bmatrix} u_\mathrm{x}(x) \\ u_\mathrm{y}(x) \end{Bmatrix} = [N_\mathrm{m}]\{U_\mathrm{N}\} = \begin{bmatrix} N_1 & N_2 & 0 & 0 & 0 & 0 \\ 0 & 0 & N_3 & N_4 & N_5 & N_6 \end{bmatrix} \{U_\mathrm{N}\} \tag{B.6}$$

Similarly, for the electric potential:

$$P(x,y,z) = \begin{cases}
[N_\mathrm{t}]\{V_\mathrm{N}\} = \begin{bmatrix} N_7 & N_8 & 0 & 0 \end{bmatrix} \{V_\mathrm{N}\} & (x,y,z) \in \Omega_\mathrm{t} \\
[N_\mathrm{b}]\{V_\mathrm{N}\} = \begin{bmatrix} 0 & 0 & N_9 & N_{10} \end{bmatrix} \{V_\mathrm{N}\} & (x,y,z) \in \Omega_\mathrm{b} \\
0 & (x,y,z) \in \Omega_\mathrm{s}
\end{cases} \tag{B.7}$$

According to the Euler-Bernoulli theory, the strain caused by the deformation is

$$S_1(x,y) = \frac{\mathrm{d}u_\mathrm{x}}{\mathrm{d}x} - y\frac{\mathrm{d}^2u_\mathrm{y}}{\mathrm{d}x^2} \tag{B.8}$$

Introducing Equation (B.6) into (B.8), we express the strain filed by means of nodal displacements

$$S_1(x,y) = [B_\mathrm{m}]\{U_\mathrm{N}\} = \begin{bmatrix} B_1 & B_2 & B_3 & B_3 & B_4 & B_5 & B_6 \end{bmatrix}\{U_\mathrm{N}\} \tag{B.9}$$

For the electric parts, the electric filed could be deduced from the potential by

$$E_3(x,y,z) = -\frac{\partial P(x,y,z)}{\partial y} \tag{B.10}$$

Introducing equation (B.7) into equation (B.10), we express the electric filed by means of nodal voltages as well

$$E_3(x,y,z) = \begin{cases} [B_\mathrm{t}]\{V_\mathrm{N}\} = \begin{bmatrix} B_7 & B_8 & 0 & 0 \end{bmatrix}\{V_\mathrm{N}\} & (x,y,z) \in \Omega_\mathrm{t} \\ [B_\mathrm{b}]\{V_\mathrm{N}\} = \begin{bmatrix} 0 & 0 & -B_7 & -B_8 \end{bmatrix}\{V_\mathrm{N}\} & (x,y,z) \in \Omega_\mathrm{b} \\ 0 & (x,y,z) \in \Omega_\mathrm{s} \end{cases} \tag{B.11}$$

The shape functions N_1 to N_{10} and B_1 to B_8 are

$$N_1 = 1 - \xi \tag{B.12}$$

$$N_2 = \xi \tag{B.13}$$

$$N_3 = 1 - 3\xi^2 + 2\xi^3 \tag{B.14}$$

$$N_4 = L\left(\xi - 2\xi^2 + \xi^3\right) \tag{B.15}$$

$$N_5 = 3\xi^2 - 2\xi^3 \tag{B.16}$$

$$N_6 = L\left(-\xi^2 + \xi^3\right) \tag{B.17}$$

$$N_7 = \left(-\frac{h_\mathrm{s}/2 - y}{h_\mathrm{p}}\right)(1 - \xi) \tag{B.18}$$

$$N_8 = \left(-\frac{h_\mathrm{s}/2 - y}{h_\mathrm{p}}\right)\xi \tag{B.19}$$

$$N_9 = \left(-\frac{h_\mathrm{s}/2 + y}{h_\mathrm{p}}\right)(1 - \xi) \tag{B.20}$$

$$N_{10} = \left(-\frac{h_\mathrm{s}/2 + y}{h_\mathrm{p}}\right)\xi \tag{B.21}$$

$$B_1 = -\frac{1}{L} \tag{B.22}$$

$$B_2 = \frac{1}{L} \tag{B.23}$$

$$B_3 = -\frac{y}{L^2}(-6 + 12\xi) \tag{B.24}$$

$$B_4 = -\frac{y}{L}(-4+6\xi) \tag{B.25}$$

$$B_5 = -\frac{y}{L^2}(6-12\xi) \tag{B.26}$$

$$B_6 = -\frac{y}{L}(-2+6\xi) \tag{B.27}$$

$$B_7 = -\frac{1-\xi}{h_\mathrm{p}} \tag{B.28}$$

$$B_8 = -\frac{\xi}{h_\mathrm{p}} \tag{B.29}$$

where $\xi = x/L$. Note that in N_8 to N_{10} a linear through-thickness voltage variation is assumed, which is not the only choice as reviewed by [49].

After expressing the continuous element field by nodal variables, the generalized Lagrange equation for electromechanical systems [2] is employed; it writes

$$\frac{\mathrm{d}}{\mathrm{d}t}\left(\frac{\partial \mathcal{L}}{\partial \dot{U}_{\mathrm{N},i}}\right) - \frac{\partial \mathcal{L}}{\partial U_{\mathrm{N},i}} = \frac{\partial}{\partial(\delta U_{\mathrm{N},i})}\delta\mathcal{W}_\mathrm{nc} \tag{B.30}$$

$$-\frac{\partial \mathcal{L}}{\partial V_{\mathrm{N},i}} = \frac{\partial}{\partial(\delta V_{\mathrm{N},i})}\delta\mathcal{W}_\mathrm{nc} \tag{B.31}$$

where $\mathbf{L}$ is the Lagrange indicator, given by

$$\mathcal{L} = \mathcal{T}^* + \mathcal{W}_\mathrm{e}^* - \mathcal{V} \tag{B.32}$$

and $\mathcal{T}^*$ the kinetic co-energy, $\mathcal{W}_\mathrm{e}^*$ the electric co-energy, $\mathcal{V}$ the mechanical potential energy, and $\delta\mathcal{W}_\mathrm{nc}$ the virtual work of the external loads.

Kinetic energy

The kinetic energy of the element writes

$$\mathcal{T}^* = \int_\Omega \frac{1}{2}\rho(y)\dot{u}_\mathrm{x}^2(x)\mathrm{d}\Omega + \int_\Omega \frac{1}{2}\rho(y)\dot{u}_\mathrm{y}^2(x)\mathrm{d}\Omega \tag{B.33}$$

Introducing Equation (B.6) into Equation (B.33), the kinetic energy could be represented in terms of nodal displacement

$$\mathcal{T}^* = \frac{1}{2}\{\dot{U}_\mathrm{N}\}^\mathrm{T}[M_e]\{\dot{U}_\mathrm{N}\} \tag{B.34}$$

where

$$[M_e] = \int_{\Omega_\mathrm{s}} \rho_\mathrm{s}[N_\mathrm{m}]^\mathrm{T}[N_\mathrm{m}]\mathrm{d}\Omega + \int_{\Omega_\mathrm{t}\cap\Omega_\mathrm{b}} \rho_\mathrm{p}[N_\mathrm{m}]^\mathrm{T}[N_\mathrm{m}]\mathrm{d}\Omega \tag{B.35}$$

After integration, it becomes

$$[M_e] = \begin{vmatrix} m\begin{vmatrix}1/3 & 1/6\\ 1/6 & 1/3\end{vmatrix} & & [0]_{2\times 4} & \\ & & & \\ [0]_{4\times 2} & & \frac{m}{420}\begin{vmatrix}156 & 22L & 54 & -13L\\ 22L & 4L^2 & 13L & -3L^2\\ 54 & 13L & 156 & -22L\\ -13L & -3L^2 & -22L & 4L^2\end{vmatrix} \end{vmatrix} \tag{B.36}$$

where $m = (\rho_\mathrm{s}h_\mathrm{s} + 2\rho_\mathrm{p}h_\mathrm{p})bL$, representing the overall mass of the element.

Mechanical potential energy

The mechanical potential energy of the element writes

$$\mathcal{V} = \frac{1}{2}\int_{\Omega_\mathrm{s}} c_\mathrm{s} S_1^2 \mathrm{d}\Omega + \frac{1}{2}\int_{\Omega_\mathrm{b}\cap\Omega_\mathrm{t}} \acute{c}_{11} S_1^2 \mathrm{d}\Omega - \frac{1}{2}\int_{\Omega_\mathrm{t}} \acute{e}_{13} S_1 E_3 \mathrm{d}\Omega - \frac{1}{2}\int_{\Omega_\mathrm{b}} \kappa \acute{e}_{13} S_1 E_3 \mathrm{d}\Omega \quad \text{(B.37)}$$

in which Equation (B.5) is used to simplify the integration domain. Introducing Equations (B.9) and (B.11) into (B.37), the mechanical potential energy could be represented in terms of nodal variables

$$\mathcal{V} = \frac{1}{2}\{U_\mathrm{N}\}^\mathrm{T}[K_e]\{U_\mathrm{N}\} - \frac{1}{2}\{U_\mathrm{N}\}^\mathrm{T}[H_e]\{V_\mathrm{N}\} \quad \text{(B.38)}$$

where

$$[K_e] = \int_{\Omega_\mathrm{s}} c_\mathrm{s}[B_\mathrm{m}]^\mathrm{T}[B_\mathrm{m}]\mathrm{d}\Omega + \int_{\Omega_\mathrm{t}\cap\Omega_\mathrm{b}} \acute{c}_{11}[B_\mathrm{m}]^\mathrm{T}[B_\mathrm{m}]\mathrm{d}\Omega \quad \text{(B.39)}$$

$$[H_e] = \int_{\Omega_\mathrm{t}} \acute{e}_{13}[B_\mathrm{m}]^\mathrm{T}[B_\mathrm{t}]\mathrm{d}\Omega + \int_{\Omega_\mathrm{b}} \kappa \acute{e}_{13}[B_\mathrm{m}]^\mathrm{T}[B_\mathrm{b}]\mathrm{d}\Omega \quad \text{(B.40)}$$

After integration, they become:

$$[K_e] = \begin{vmatrix} k_\mathrm{x}\begin{vmatrix} 1 & -1 \\ 1 & -1 \end{vmatrix} & & [0]_{2\times 4} & & \\ & & & & \\ [0]_{4\times 2} & & k_\mathrm{y}\begin{vmatrix} 12 & 6L & -12 & 6L \\ 6L & 4L^2 & -6L & 2L^2 \\ -12 & -6L^2 & 12 & -6L \\ 6L & 2L^2 & -6L & 4L \end{vmatrix} \end{vmatrix} \quad \text{(B.41)}$$

and

$$[H_e] = \begin{vmatrix} h_\mathrm{x}\begin{vmatrix} 1 & 1 \\ -1 & -1 \end{vmatrix} & \kappa h_\mathrm{x}\begin{vmatrix} -1 & -1 \\ 1 & 1 \end{vmatrix} \\ h_\mathrm{y}\begin{vmatrix} -1 & 1 \\ -L & 0 \\ 1 & -1 \\ 0 & L \end{vmatrix} & \kappa h_\mathrm{y}\begin{vmatrix} -1 & 1 \\ -L & 0 \\ 1 & -1 \\ 0 & L \end{vmatrix} \end{vmatrix} \quad \text{(B.42)}$$

where

$$k_\mathrm{x} = \frac{c_\mathrm{s} h_\mathrm{s} b}{L} + \frac{2\acute{c}_{11} h_\mathrm{p} b}{L}$$

$$k_\mathrm{y} = \frac{c_\mathrm{s} I_\mathrm{s} b}{L} + \frac{2\acute{c}_{11} I_\mathrm{p} b}{L}, I_\mathrm{s} = \frac{h_\mathrm{s}^3 b}{12}, I_\mathrm{p} = \frac{h_\mathrm{p}^3 b}{12} + h_\mathrm{p} b\left(\frac{h_\mathrm{p}+h_\mathrm{s}}{2}\right)^2$$

$$h_\mathrm{x} = \frac{\acute{e}_{13} b}{2}$$

$$h_\mathrm{y} = \frac{\acute{e}_{13}\gamma_\mathrm{p}}{L h_\mathrm{p}}, \gamma_\mathrm{p} = b h_\mathrm{p}\frac{h_\mathrm{p}+h_\mathrm{s}}{2}$$

Electric co-energy

The electric co-energy writes

$$\mathcal{W}_\mathrm{e} = \frac{1}{2}\int_{\Omega_\mathrm{b}\cap\Omega_\mathrm{t}} \acute{\varepsilon}_{33} E_3^2 \mathrm{d}\Omega + \frac{1}{2}\int_{\Omega_\mathrm{t}} \acute{e}_{13} S_1 E_3 \mathrm{d}\Omega + \frac{1}{2}\int_{\Omega_\mathrm{b}} \kappa \acute{e}_{13} S_1 E_3 \mathrm{d}\Omega \quad \text{(B.43)}$$

Introducing Equations (B.9) and (B.11) into (B.43), the electric co-energy could be represented in terms of nodal variables

$$\mathcal{W}_e^* = \frac{1}{2}\{V_\mathrm{N}\}^\mathrm{T}[H_e]^\mathrm{T}\{U_\mathrm{N}\} + \frac{1}{2}\{V_\mathrm{N}\}^\mathrm{T}[C_e]\{V_\mathrm{N}\} \tag{B.44}$$

where $[H_\mathrm{e}]$ is shown in Equation (B.42), and

$$[C_e] = \int_{\Omega_\mathrm{t}} \acute{\varepsilon}_{13}[B_\mathrm{t}]^\mathrm{T}[B_\mathrm{t}]\mathrm{d}\Omega + \int_{\Omega_\mathrm{b}} \acute{\varepsilon}_{13}[B_\mathrm{b}]^\mathrm{T}[B_\mathrm{b}]\mathrm{d}\Omega \tag{B.45}$$

After integration, it becomes

$$[C_e] = C_\mathrm{pzt}\begin{vmatrix} 1/3 & 1/6 & & \\ 1/6 & 1/3 & [0]_{2\times2} & \\ & & 1/3 & 1/6 \\ [0]_{2\times2} & & 1/6 & 1/3 \end{vmatrix} \tag{B.46}$$

where $C_\mathrm{pzt} = \acute{\varepsilon}_{33}bL/h_\mathrm{p}$ is the intrinsic capacitance of one piezoelectric layer.

Element matrices

Now the kinetic co-energy (B.34), mechanical potential energy (B.38) and electric co-energy (B.44) all have been expressed by means of nodal variables. Introducing them into the Lagrange indicator (B.32) makes

$$\mathcal{L} = \frac{1}{2}\{\dot{U}_\mathrm{N}\}^\mathrm{T}[M_e]\{\dot{U}_\mathrm{N}\} + \{V_\mathrm{N}\}^\mathrm{T}[H_e]^\mathrm{T}\{U_\mathrm{N}\} + \frac{1}{2}\{V_\mathrm{N}\}^\mathrm{T}[C_e]\{V_\mathrm{N}\} - \frac{1}{2}\{U_\mathrm{N}\}^\mathrm{T}[K_e]\{U_\mathrm{N}\} \tag{B.47}$$

Introducing Equation (B.47) into (B.31), and with term $\delta\mathcal{W}_\mathrm{nc}$ given by

$$\delta\mathcal{W}_\mathrm{nc} = \{\delta U_\mathrm{N}\}^\mathrm{T}\cdot\{F_\mathrm{N}\} - \{\delta V_\mathrm{N}\}^\mathrm{T}\cdot\{Q_\mathrm{N}\} \tag{B.48}$$

eventually we obtain the dynamics of the element in terms of nodal variables

$$[M_\mathrm{e}]\{\ddot{U}_\mathrm{N}\} + [K_\mathrm{e}]\{U_\mathrm{N}\} - [H_\mathrm{e}]\{V_\mathrm{N}\} = \{F_\mathrm{N}\} \tag{B.49}$$

$$[H_\mathrm{e}]^\mathrm{T}\{U_\mathrm{N}\} + [C_\mathrm{e}]\{V_\mathrm{N}\} = \{Q_\mathrm{N}\} \tag{B.50}$$

where $[M_\mathrm{e}]$ is the element mass matrix, $[K_\mathrm{e}]$ the element stiffness matrix, $[H_\mathrm{e}]$ the element piezoelectric matrix, and $[C_\mathrm{e}]$ the element capacitance matrix.

B.3 Electric circuits and electrodes

The shunted electric circuits could be resistors (R_t, R_b), capacitors (C_t, C_b), inductors (L_t, L_b) or their combinations. This part is modeled by another element with only one node and 4 DOFs. The governing equation writes

$$[M_\mathrm{c}]\{\ddot{E}_\mathrm{N}\} + [D_\mathrm{c}]\{\dot{E}_\mathrm{N}\} + [K_\mathrm{c}]\{E_\mathrm{N}\} = \{0\} \tag{B.51}$$

where

$$\{E_{\mathrm{N}}\} = \{\ V_{\mathrm{t},1} \quad Q_{\mathrm{t},1} \quad V_{\mathrm{b},1} \quad Q_{\mathrm{b},1}\ \}^{\mathrm{T}} \tag{B.52}$$

is the element nodal variable vector, and the element matrices are

$$[M_{\mathrm{c}}] = \begin{vmatrix} 0 & 0 & & \\ 0 & L_{\mathrm{t}} & [0]_{2\times 2} & \\ & & 0 & 0 \\ [0]_{2\times 2} & & 0 & L_{\mathrm{b}} \end{vmatrix} \tag{B.53}$$

$$[D_{\mathrm{c}}] = \begin{vmatrix} 0 & 0 & & \\ 0 & R_{\mathrm{t}} & [0]_{2\times 2} & \\ & & 0 & 0 \\ [0]_{2\times 2} & & 0 & R_{\mathrm{b}} \end{vmatrix} \tag{B.54}$$

$$[K_{\mathrm{c}}] = \begin{vmatrix} 0 & -1 & & \\ -1 & C_{\mathrm{t}}^{-1} & [0]_{2\times 2} & \\ & & 0 & -1 \\ [0]_{2\times 2} & & -1 & C_{\mathrm{b}}^{-1} \end{vmatrix} \tag{B.55}$$

Matrices $[K_{\mathrm{c}}]$, $[D_{\mathrm{c}}]$ and $[M_{\mathrm{c}}]$ are then assembled into the overall stiffness matrix, damping matrix and mass matrix respectively according to the connection of the elements.

Electrodes, for instant very thin Copper layers, are often covered on the piezoelectric material in practice. Since the proposed piezoelectric element is electrode free, extra efforts must taken to simulate the electrodes. A electrode forces every point on it has identical potential, this effect could be regard as a group of constraining equations among those electric DOFs. Generally, there are two approaches of introducing additional constraining equations into FEM, one is Lagrange Multiplier Method [209] and another is Penalty Method [210]. Since the Multiplier Method will induce zero diagonal components in stiffness matrix and also increase the dimension of problem, here the Penalty Method is used. The basic idea is to add a new term into the unconstrained mechanical potential energy to obtain the constrained mechanical potential energy; it writes

$$\mathcal{V}_{\mathrm{c}} = \mathcal{V} + \{\tau\}^{\mathrm{T}}[\alpha]\{\tau\} \tag{B.56}$$

where $[\alpha]$ is a diagonal matrix for the penalty factors, and

$$\{\tau\} = [A]\{U\} - \{B\} \tag{B.57}$$

To this end, the constraining equations

$$[A]\{U\} - \{B\} = \{0\} \tag{B.58}$$

are taken into account of the Lagrange indicator by an approximate way, where $\{U\}$ is overall variable vector including displacement and voltage DOFs. Replacing the unconstrained mechanical potential energy by the constrained one as shown in Equation (B.56) in Lagrange Equation (B.31), the constrained dynamics equations becomes

$$[M]\{\ddot{U}\} + ([K] + [A]^{\mathrm{T}}[\alpha][A])\{U\} = \{F\} + [A]^{\mathrm{T}}[\alpha][B] \tag{B.59}$$

where the electric constrains have been taken into account.

B.4 Validations

Overall 24 test cases were conducted in order to validate the FEM code we have developed (referred to as 'P1DFEM'). All of these text cases have shown very good agreements with the reference. The selected cases presented here are related to the validation of: 1) the accuracy of the piezoelectric beam element, and 2) the implementation of the general finite element procedure.

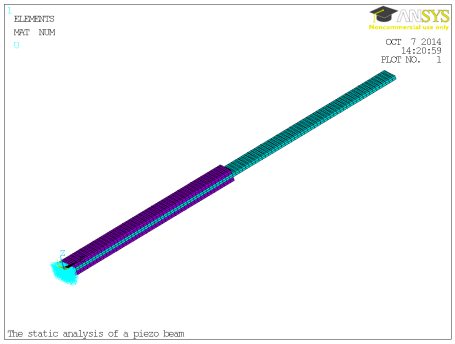

(a) in ANSYS

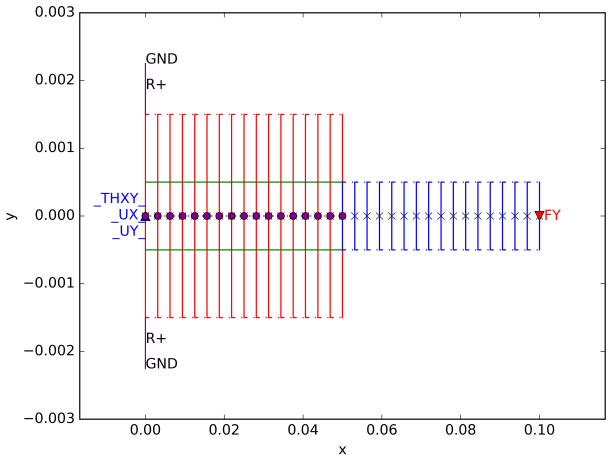

(b) in P1DFEM

Figure B.2: FEM meshes of the cantilevered beam.

A same cantilevered structure was modeled by ANSYS and P1DFEM respectively. It is 0.1 m long with rectangular cross-section (width 5×10^{-3} m and height 1×10^{-3} m). Two Piezoelectric patches are co-located at the first half, with width 5×10^{-3} m and height 1×10^{-3} m. In ANSYS, solid elements (SOLID45 and SOLID95) are used as shown in Figure B.2a where the purple part is the piezoelectric layer. In P1DFEM, conventional Euler-Bernoulli beam elements are used to model the host structure and the proposed elements are used to model the piezoelectric parts. Figure B.2b shows the meshes in P1DFEM, where the red part is the piezoelectric elements. The host material is steel, with Young's modulus 2.1×10^{11} Pa and mass density 7.8×10^3 kg/m^3. The piezoelectric material is PZT4, presented in Appendix A.

Firstly, the natural frequencies of the structure with open circuit were calculated and

compared, shown in Figure B.3. The ANSYS results are selected so that only longitudinal and flexural modes are taken into the comparison. It is shown that relative error ANSYS and P1DFEM is less than 4% regarding the first 10 modes.

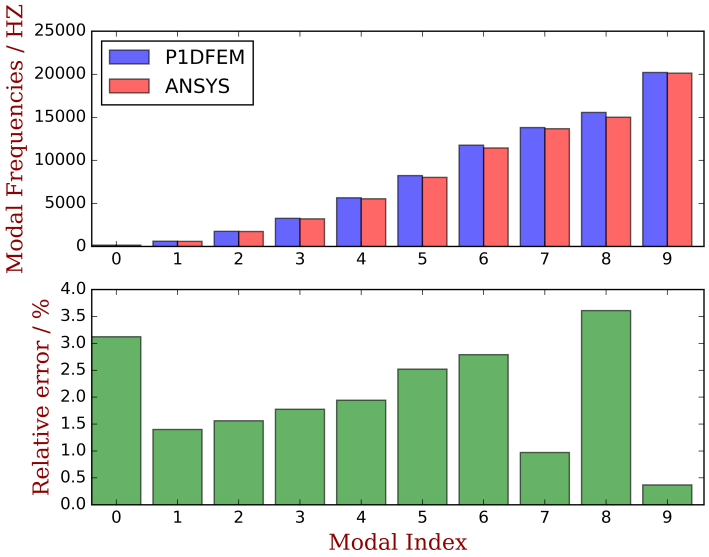

Figure B.3: First 10 natural frequencies.

Secondly, the static response of the structure was computed, giving one of the electrode a 1V voltage set another to short-circuit. The aim is to test the accuracy of electromechanical coupling from the electric field to mechanical field. Figure B.4 compares the results in DOF U_x and U_y. Both longitudinal and transverse motions are excited, reveal the face that DOFs U_x and U_y are coupled only through the electric field.

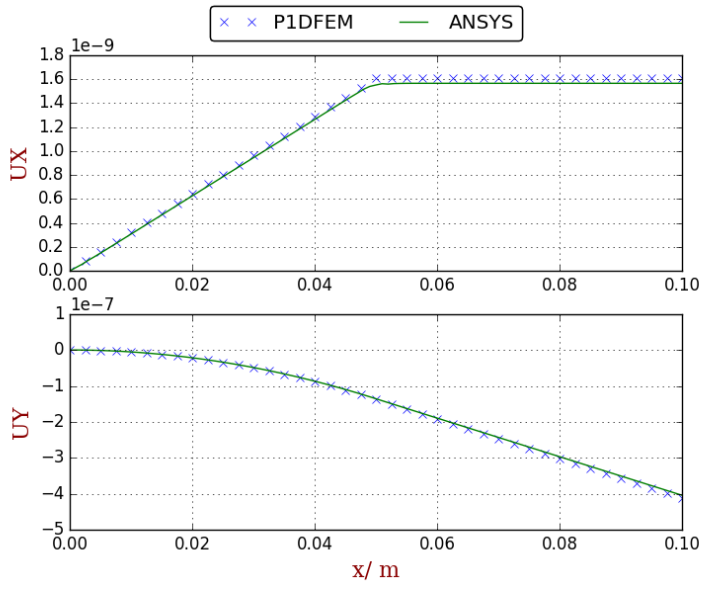

Figure B.4: Static response to the electric excitation.

Thirdly, the static response to a transverse force at the free tip was computed. The aim is to test the accuracy of electromechanical coupling from the mechanical field to electric field. The response are compared in Figure B.5. Note that the ANSYS results of THXY (θ) in Figure B.5a were not directly exported from ANSYS but obtained by performing numerical differential on the exported UY results.

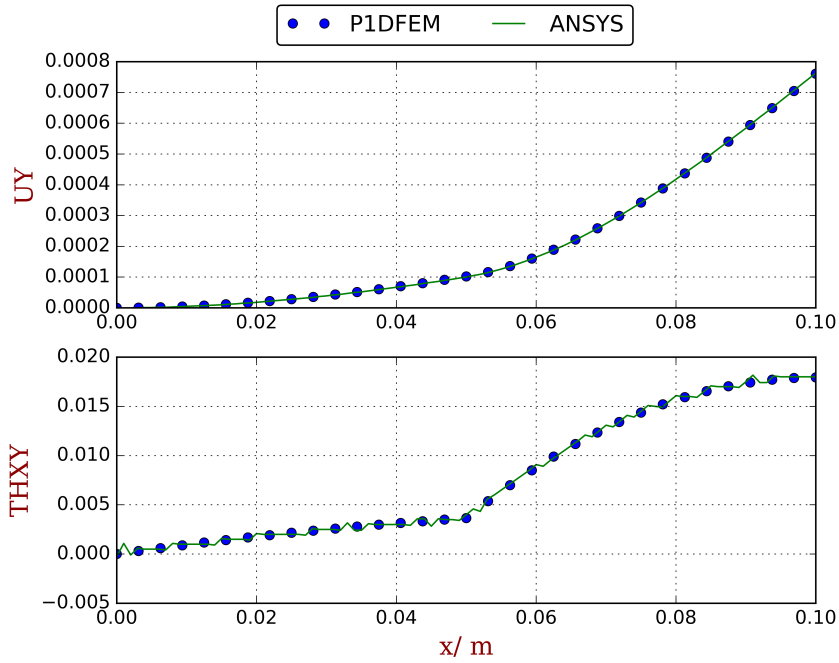

(a) U_y and θ

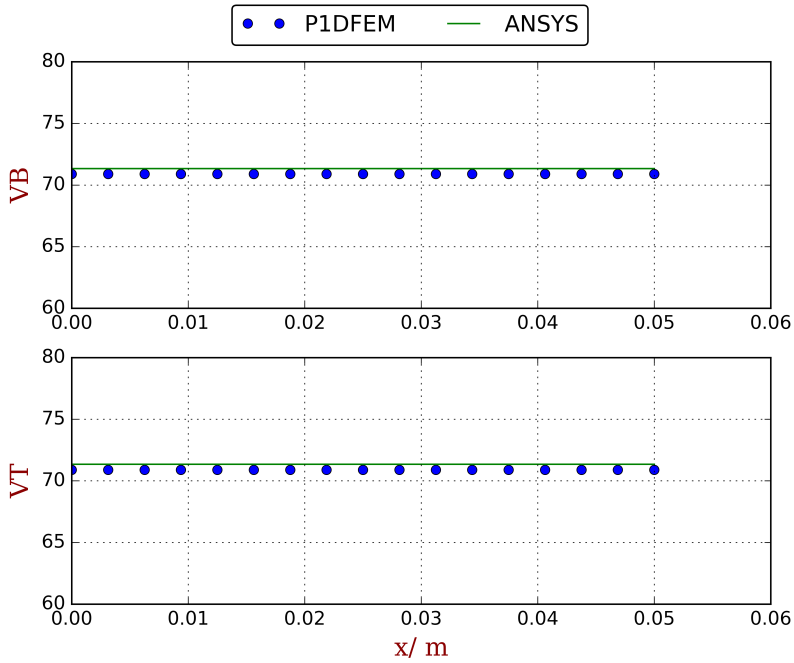

(b) V_t and V_b

Figure B.5: Static response to the mechanical excitation.

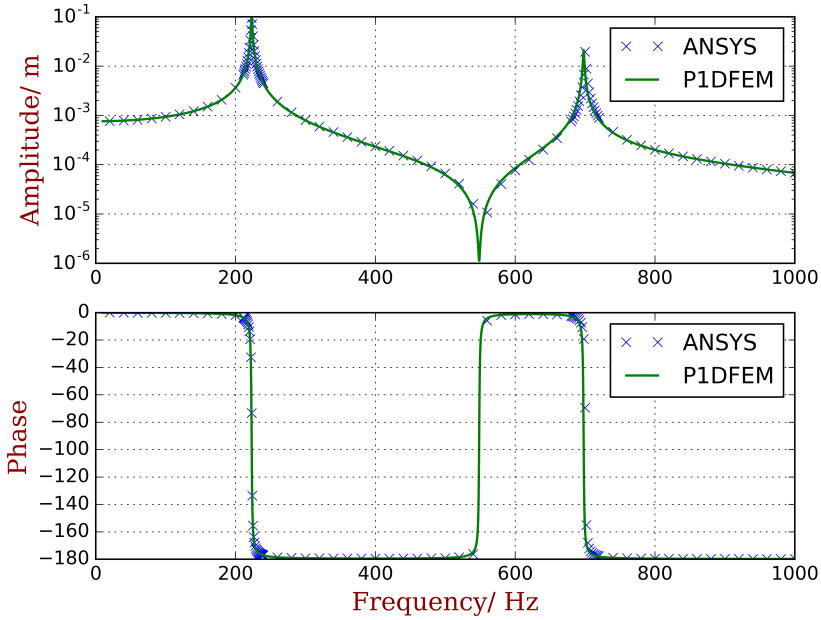

(a) U_y

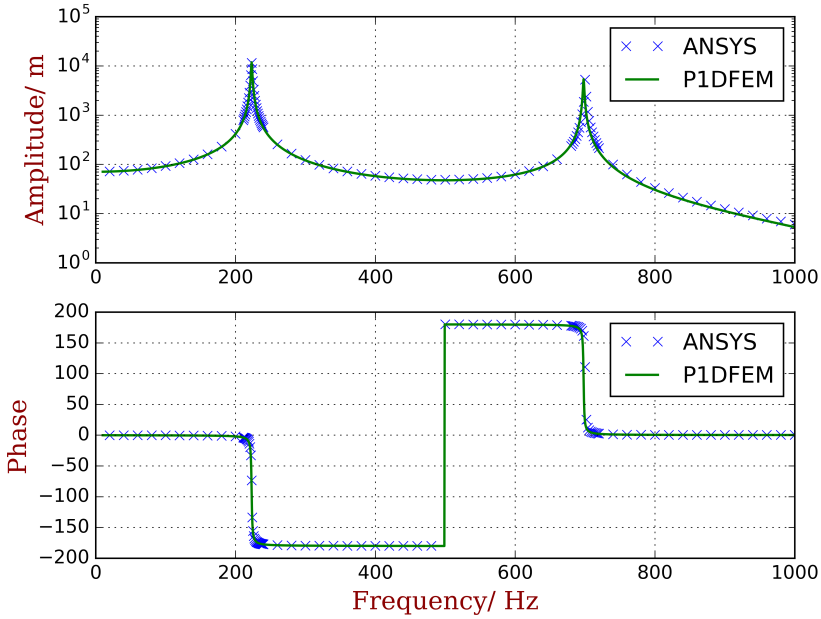

(b) V_t

Figure B.6: Dynamic response to the mechanical excitation.

Fourthly, harmonic response to the applied force at the free end were computed from 0 Hz to 1000 Hz. The piezoelectric patches are open-circuit. The aim is to test the implementation of the finite element procedure and the dynamic coupling of the mechanical and electric fields. The Frequency Response Function (FRF) are compared regarding the transverse displacement at the free top (Figure B.6a) and the potential of the upper

piezoelectric path (Figure B.6b).

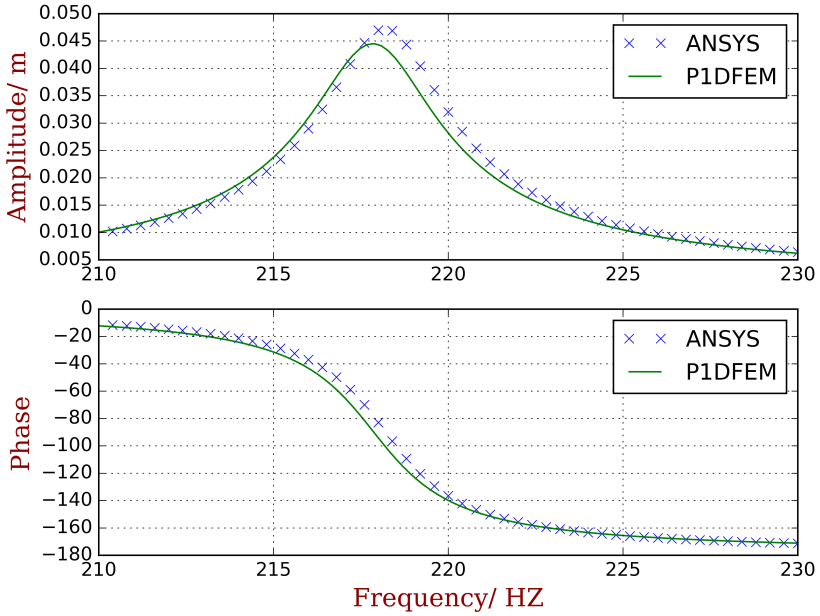

Figure B.7: FRF when resistive shunts with $R_t = R_b = 1 \times 10^5\,\Omega$ are used.

Eventually, the FRF around the first resonance (from 210 Hz to 230 Hz) was compared when resistive shunts with $R_t = R_b = 1 \times 10^5\,\Omega$ are considered. The aim is to test the accuracy of concerning the dynamic behavior of piezoelectric shunts. All these comparisons have shown good agreements between results obtained from P1DFEM and ANSYS. The correlation indicates that the assumptions (Euler-Bernoulli, 1D constitutive relation, linear through-thickness voltage variation) are suitable and they are correctly implemented.

Appendix C

Artificial boundary conditions (ABC) for rods and beams

ABC for infinite rod

The longitudinal motion u of an uniform infinite rod is governed by

$$EA\frac{\partial^2 u(x,t)}{\partial t^2} - A\rho\frac{\partial^2 u(x,t)}{\partial x^2} = P_u(x,t) \tag{C.1}$$

where A is the cross-section area, ρ the mass density and E the Young's modulus. In terms of the harmonic (steady-state) motion at angular frequency ω, the displacement u at $x_\mathrm{b} > 0$ writes

$$u(x_\mathrm{b},t) = Ue^{j(\omega t - kx_\mathrm{b})} \tag{C.2}$$

where $k_u = \omega\sqrt{\rho/E}$ is the longitudinal wavenumber for the positive-going wave. Equation (C.2) holds when there are no external loads at the far-field, namely $P_u(x > x_\mathrm{b}, t) = 0$. Then the internal force applied to the far-field at $x_\mathrm{b} > 0$ becomes

$$f(x_\mathrm{b},t) = EA\frac{\partial u}{\partial x}(x_\mathrm{b},t) = jEAk_u u(x_\mathrm{b},t) \tag{C.3}$$

So that we obtain the dynamic stiffness of the far field

$$H_u = \frac{f(x_\mathrm{b},t)}{u(x_\mathrm{b},t)} = jEAk_u = j\omega A\sqrt{E\rho} \tag{C.4}$$

Equation (C.4) indicates that the far-field is equivalently a viscous damper, with damping coefficient $C_\mathrm{e} = A\sqrt{E\rho}$. This allows us to implement the ABC by bounding a damper element at the boundaries of the near-field.

ABC for infinite beam

The governing equation of an infinite uniform Euler-Bernoulli beam writes

$$\rho A\frac{\partial^2 v(x,t)}{\partial t^2} + EI\frac{\partial^4 v(x,t)}{\partial x^4} = P(x,t) \tag{C.5}$$

where I is the second moment of area of the cross-section. In terms of the harmonic (steady-state) motion at angular frequency ω, transverse displacement v at $x_\mathrm{b} > 0$ writes

$$v(x_\mathrm{b},t) = \left(Ae^{jk_v x_\mathrm{b}} + \sum_i^m B_i e^{-k_v(x_\mathrm{b}-x_\mathrm{i})}\right)e^{-j\omega t} \tag{C.6}$$

where $k_v = \sqrt[4]{\omega^2(\rho A)/(EI)}$. Equation (C.6) holds when there are no external loads at the far-field, namely $P_v(x > x_\mathrm{b}, t) = 0$. Terms A and B_i are determined by the m excitations. We can neglect the exponentially decaying terms caused by the evanescent waves and only keep periodic terms corresponding to the propagating waves; it gives

$$v(x_\mathrm{b}, t) \approx A e^{jk_v x_\mathrm{b}} e^{-j\omega t} \tag{C.7}$$

The rotation θ, internal bending moment M_i and transverse force F_i can then be deduced

$$\begin{cases} \theta(x_\mathrm{b}, t) = \dfrac{\partial v}{\partial x}(x_\mathrm{b}, t) = jk_v v(x_\mathrm{b}, t) & \text{(C.8)} \\ M_\mathrm{i}(x_\mathrm{b}, t) = -EI\dfrac{\partial^2 v}{\partial x^2}(x_\mathrm{b}, t) = EIk_v^2 v(x_\mathrm{b}, t) & \text{(C.9)} \\ F_\mathrm{i}(x_\mathrm{b}, t) = -EI\dfrac{\partial^3 v}{\partial x^3}(x_\mathrm{b}, t) = -jEIk_v^3 v(x_\mathrm{b}, t) & \text{(C.10)} \end{cases}$$

From Equations (C.7), (C.8), (C.9) and (C.10), the equivalent dynamic stiffness can be found

$$\begin{cases} H_v = \dfrac{F_\mathrm{i}(x_\mathrm{b}, t)}{v(x_\mathrm{b}, t)} = -jEIk_v^3 & \text{(C.11)} \\ H_\theta = \dfrac{M_\mathrm{i}(x_\mathrm{b}, t)}{\theta(x_\mathrm{b}, t)} = -jEIk_v & \text{(C.12)} \end{cases}$$

It could be seen that H_v and H_θ have transcendental relations with frequency ω. The ABC of longitudinal wave (C.4) can be simply regarded as a damper, so it is applicable in both time-domain and frequency domain solvers. In flexural wave case the ABC we found could only be used in frequency domain solvers directly. Because they do not correspond to a simple combination of mass, stiffness or damper.

The ABC for Euler-Bernoulli beams can also be implemented by bounding two springs between v and θ DOFs to the ground respectively at the ends of the near-field. However, the stiffness coefficients are frequency dependent according to Equations (C.11) and (C.12).

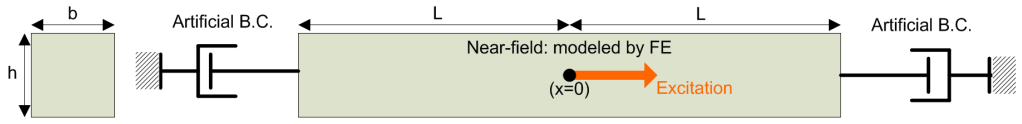

Figure C.1: Illustration of the FE model with ABC for the uniform beam.

Validations

A uniform infinite beam under excitation at the origin is considered as an example to validate the ABC and the implementation of these ABC in P1DFEM. The analytical solutions presented by [82] are used as reference. The beam and the model is illustrated in Figure C.1, where up to $L = 1\,\mathrm{m}$ at the left and right sides are modeled by FEM,

and the rest part are modeled by ABC. The beam has rectangular cross-section $b = h = 5 \times 10^{-2}$ m, Young's modulus 2.1×10^{11} Pa and mass density 7.8×10^{3} kg/m^3.

The origin mobility to the transverse force was calculated from 10 Hz to 1000 Hz, and the results are compared in Figure C.2. No resonance appears at the curves because the structure do not have any reflection mechanisms that induce standing waves.

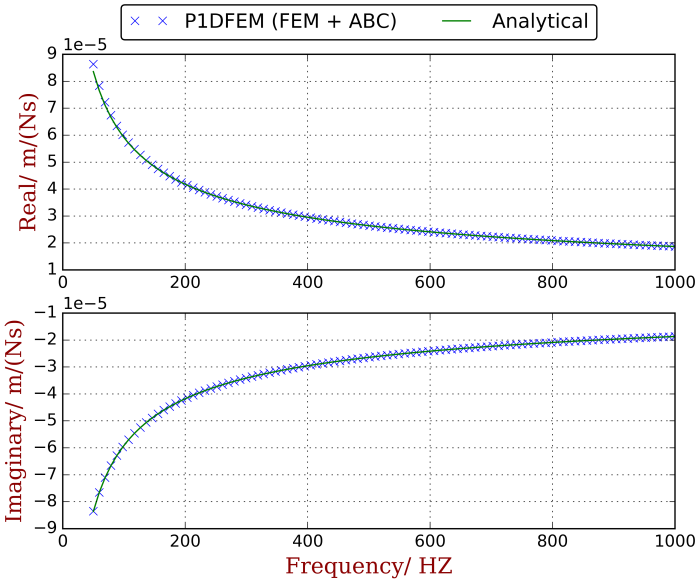

Figure C.2: Origin mobility to transverse force

Next, we fix the frequency at 400 Hz and validate the spatial distribution of the solutions. Applying a longitudinal excitation, the deformation and internal forces can be calculated, shown in C.3a, and the energy flow are then compared, shown in C.3b. Applying a bending moment, the flexural waves can be excited and the transverse deformation and internal forces are shown in Figure C.4a. The contribution of the evanescent waves can be clearly seen. Energy flow is shown in Figure C.4b where the power associated with v and θ DOFs are plotted separately and labeled as P_{u} and P_{m}.

All these comparisons have shown a very good agreement indicating the ABC for rods and beams are correctly implemented.

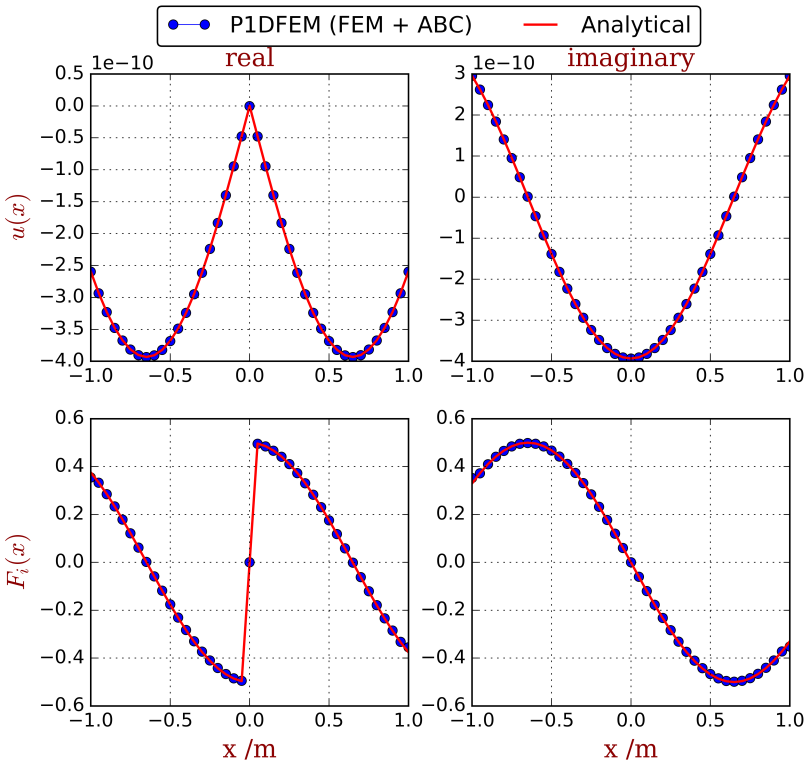

(a)

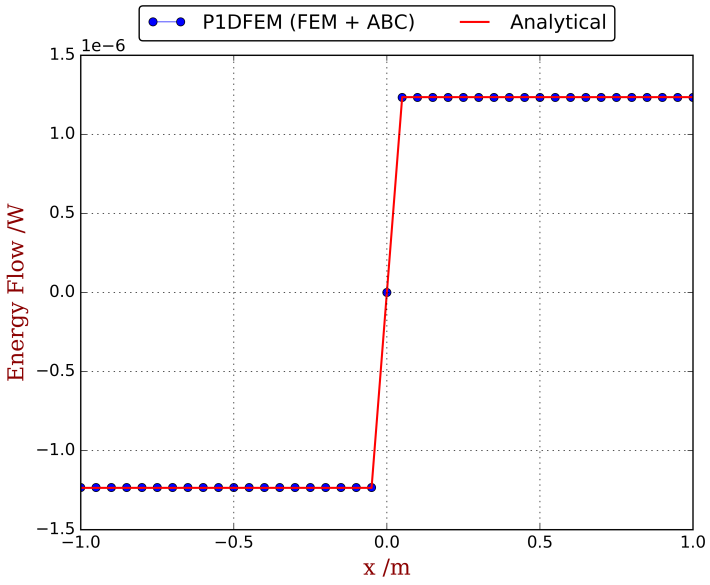

(b)

Figure C.3: Spatial distribution of the response induced by longitudinal force: (a) displacement and internal forces; (b) Energy flow.

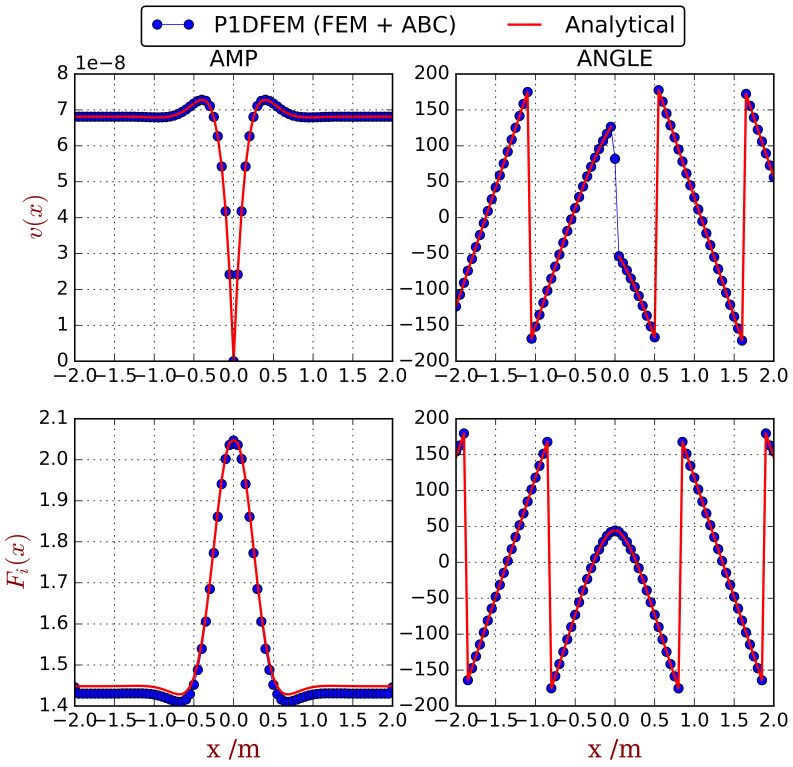

(a)

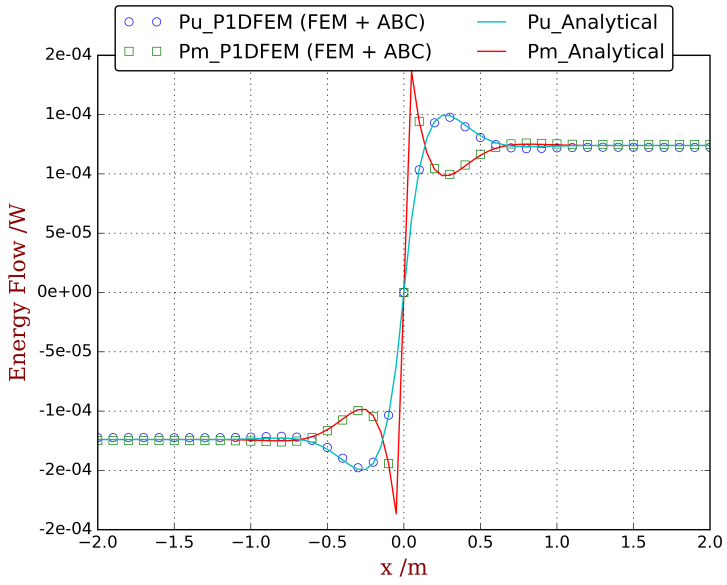

(b)

Figure C.4: Spatial distribution of the response induced by bending moment: (a) displacement and internal forces; (b) Energy flow

Appendix D

The relationship of the left eigenvectors obtained from Equation (3.9) and from Equation (2.8)

Given that the row vector $\begin{pmatrix} \mathbf{x}_q^T & \mathbf{x}_f^T \end{pmatrix}$ is a left eigenvector obtained from Equation (3.9) and the associated eigenvalue is λ; by the definition of the left eigenvalue problem, they satisfy

$$\begin{pmatrix} \mathbf{x}_q^T & \mathbf{x}_f^T \end{pmatrix} \left(\begin{bmatrix} \mathbf{0} & \sigma\mathbf{I} \\ -\mathbf{D}_{RL} & -\mathbf{D}_{RR} \end{bmatrix} - \lambda \begin{bmatrix} \sigma\mathbf{I} & \mathbf{0} \\ \mathbf{D}_{LL} & \mathbf{D}_{LR} \end{bmatrix} \right) = \mathbf{0} \tag{D.1}$$

and it leads to

$$\begin{pmatrix} \sigma\mathbf{x}_q^T & \mathbf{x}_f^T \end{pmatrix} (\mathbf{A}_R - \lambda\mathbf{A}_L) = \mathbf{0} \tag{D.2}$$

where

$$\mathbf{A}_L = \begin{bmatrix} \mathbf{I} & \mathbf{0} \\ \mathbf{D}_{LL} & \mathbf{D}_{LR} \end{bmatrix} \tag{D.3}$$

and

$$\mathbf{A}_R = \begin{bmatrix} \mathbf{0} & \mathbf{I} \\ -\mathbf{D}_{RL} & -\mathbf{D}_{RR} \end{bmatrix} \tag{D.4}$$

Right multiplying the inverse the matrix $\mathbf{A}_L$, Equation (D.2) becomes

$$\begin{pmatrix} \sigma\mathbf{x}_q^T & \mathbf{x}_f^T \end{pmatrix} \left(\hat{\mathbf{T}} - \lambda\mathbf{I} \right) = \mathbf{0} \tag{D.5}$$

where

$$\hat{\mathbf{T}} = \mathbf{A}_R\mathbf{A}_L^{-1} \tag{D.6}$$

At the other hand, from Equation (3.7) we know that

$$\begin{pmatrix} \mathbf{q}_L \\ \mathbf{f}_L \end{pmatrix} = \mathbf{A}_L \begin{pmatrix} \mathbf{q}_L \\ \mathbf{q}_R \end{pmatrix} \tag{D.7}$$

and

$$\begin{pmatrix} \mathbf{q}_R \\ -\mathbf{f}_R \end{pmatrix} = \mathbf{A}_R \begin{pmatrix} \mathbf{a}_L \\ \mathbf{q}_R \end{pmatrix} \tag{D.8}$$

Equations (D.7) and (D.8) imply that

$$\begin{pmatrix} \mathbf{q}_R \\ \mathbf{f}_R \end{pmatrix} = \mathbf{A}_R\mathbf{A}_L^{-1} \begin{pmatrix} \mathbf{q}_L \\ -\mathbf{f}_L \end{pmatrix} = \hat{\mathbf{T}} \begin{pmatrix} \mathbf{q}_L \\ -\mathbf{f}_L \end{pmatrix} \tag{D.9}$$

Equation (D.5) indicates that $\begin{pmatrix} \sigma \mathbf{x}_{\mathrm{q}}^{\mathrm{T}} & \mathbf{x}_{\mathrm{f}}^{\mathrm{T}} \end{pmatrix}$ is also a left eigenvector of matrix $\hat{\mathbf{T}}$ and the associated eigenvalue is λ. Equation (D.9) reveals that $\hat{\mathbf{T}}$ is actually the transfer matrix of the unit cell. In conclusion, we have proved that, if $\begin{pmatrix} \mathbf{x}_{\mathrm{q}}^{\mathrm{T}} & \mathbf{x}_{\mathrm{f}}^{\mathrm{T}} \end{pmatrix}$ is an left eigenvector of Equation (3.9), then $\begin{pmatrix} \sigma \mathbf{x}_{\mathrm{q}}^{\mathrm{T}} & \mathbf{x}_{\mathrm{f}}^{\mathrm{T}} \end{pmatrix}$ is the left eigenvector of the transfer matrix with the same eigenvalue.

Appendix E

The relationship of the left eigenvectors obtained from Equation (2.72) and from Equation (2.8)

Given that the row vector $\begin{pmatrix} \mathbf{x}_{\mathrm{q}}^{\mathrm{T}} & \mathbf{x}_{\mathrm{f}}^{\mathrm{T}} \end{pmatrix}$ is a left eigenvector obtained from Equation (2.72) and the associated eigenvalue is λ; by the definition of the left eigenvalue problem, they satisfy

$$\begin{pmatrix} \mathbf{x}_{\mathrm{q}}^{\mathrm{T}} & \mathbf{x}_{\mathrm{f}}^{\mathrm{T}} \end{pmatrix} \left(\begin{bmatrix} \mathbf{H}_{\mathrm{RL}} & \mathbf{H}_{\mathrm{RR}} \\ \mathbf{0} & \bar{\sigma}\mathbf{I} \end{bmatrix} - \lambda \begin{bmatrix} \mathbf{H}_{\mathrm{LL}} & \mathbf{H}_{\mathrm{LR}} \\ -\bar{\sigma}\mathbf{I} & \mathbf{0} \end{bmatrix} \right) = \mathbf{0} \tag{E.1}$$

and it leads to

$$\begin{pmatrix} \mathbf{x}_{\mathrm{q}}^{\mathrm{T}} & \bar{\sigma}\mathbf{x}_{\mathrm{f}}^{\mathrm{T}} \end{pmatrix} (\mathbf{A}_{\mathrm{R}} - \lambda \mathbf{A}_{\mathrm{L}}) = \mathbf{0} \tag{E.2}$$

where

$$\mathbf{A}_{\mathrm{L}} = \begin{bmatrix} \mathbf{H}_{\mathrm{LL}} & \mathbf{H}_{\mathrm{LR}} \\ -\mathbf{I} & \mathbf{0} \end{bmatrix} \tag{E.3}$$

and

$$\mathbf{A}_{\mathrm{R}} = \begin{bmatrix} \mathbf{H}_{\mathrm{RL}} & \mathbf{H}_{\mathrm{RR}} \\ \mathbf{0} & \mathbf{I} \end{bmatrix} \tag{E.4}$$

Right multiply the inverse the matrix $\mathbf{A}_{\mathrm{L}}$, Equation (E.2) becomes

$$\begin{pmatrix} \mathbf{x}_{\mathrm{q}}^{\mathrm{T}} & \bar{\sigma}\mathbf{x}_{\mathrm{f}}^{\mathrm{T}} \end{pmatrix} \left(\hat{\mathbf{T}} - \lambda \mathbf{I} \right) = \mathbf{0} \tag{E.5}$$

where

$$\hat{\mathbf{T}} = \mathbf{A}_{\mathrm{R}} \mathbf{A}_{\mathrm{L}}^{-1} \tag{E.6}$$

At the other hand, from Equation (2.71) we know that

$$\begin{pmatrix} \mathbf{q}_{\mathrm{L}} \\ -\mathbf{f}_{\mathrm{L}} \end{pmatrix} = \mathbf{A}_{\mathrm{L}} \begin{pmatrix} \mathbf{f}_{\mathrm{L}} \\ \mathbf{f}_{\mathrm{R}} \end{pmatrix} \tag{E.7}$$

and

$$\begin{pmatrix} \mathbf{q}_{\mathrm{R}} \\ \mathbf{f}_{\mathrm{R}} \end{pmatrix} = \mathbf{A}_{\mathrm{R}} \begin{pmatrix} \mathbf{f}_{\mathrm{L}} \\ \mathbf{f}_{\mathrm{R}} \end{pmatrix} \tag{E.8}$$

Equations (E.7) and (E.8) imply that

$$\begin{pmatrix} \mathbf{q}_{\mathrm{R}} \\ \mathbf{f}_{\mathrm{R}} \end{pmatrix} = \mathbf{A}_{\mathrm{R}} \mathbf{A}_{\mathrm{L}}^{-1} \begin{pmatrix} \mathbf{q}_{\mathrm{L}} \\ -\mathbf{f}_{\mathrm{L}} \end{pmatrix} = \hat{\mathbf{T}} \begin{pmatrix} \mathbf{q}_{\mathrm{L}} \\ -\mathbf{f}_{\mathrm{L}} \end{pmatrix} \tag{E.9}$$

Equation (E.5) indicates that $\begin{pmatrix} \mathbf{x}_{\mathrm{q}}^{\mathrm{T}} & \bar{\sigma}\mathbf{x}_{\mathrm{f}}^{\mathrm{T}} \end{pmatrix}$ is also a left eigenvector of matrix $\hat{\mathbf{T}}$ and the associated eigenvalue is λ. Equation (E.9) reveals that $\hat{\mathbf{T}}$ is actually the transfer matrix of the unit cell. In conclusion, we have proved that, if $\begin{pmatrix} \mathbf{x}_{\mathrm{q}}^{\mathrm{T}} & \mathbf{x}_{\mathrm{f}}^{\mathrm{T}} \end{pmatrix}$ is an left eigenvector of Equation (2.72), then $\begin{pmatrix} \mathbf{x}_{\mathrm{q}}^{\mathrm{T}} & \bar{\sigma}\mathbf{x}_{\mathrm{f}}^{\mathrm{T}} \end{pmatrix}$ is the left eigenvector of the transfer matrix with the same eigenvalue.

Appendix F

Supplementary results for Chapter 5

Here we show the dispersion curves of each final design proposed in chapter 5. In the figures, 'P+' refers to the positive-going propagating waves and 'E+' the positive-going evanescent waves. The specific negative capacitance values are listed in Table 5.3. Additionally, the geometric parameters listed in Table 5.1 and 5.2 are illustrated by plotting the full FE mesh. Note that configuration A can doe lead to a stable design, so only the FE mesh is shown.

Configuration A

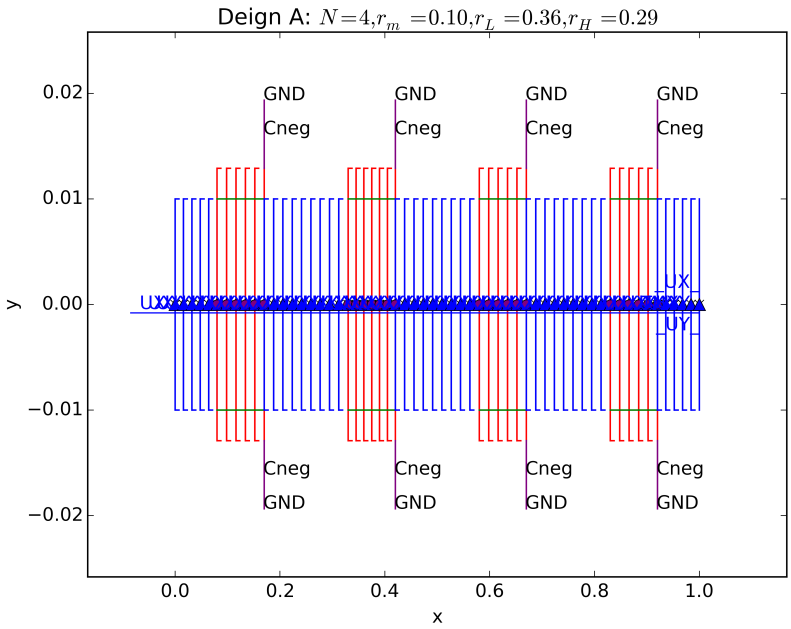

Figure F.1: Finite element mesh of the cantilever beam with configuration A.

Configuration B

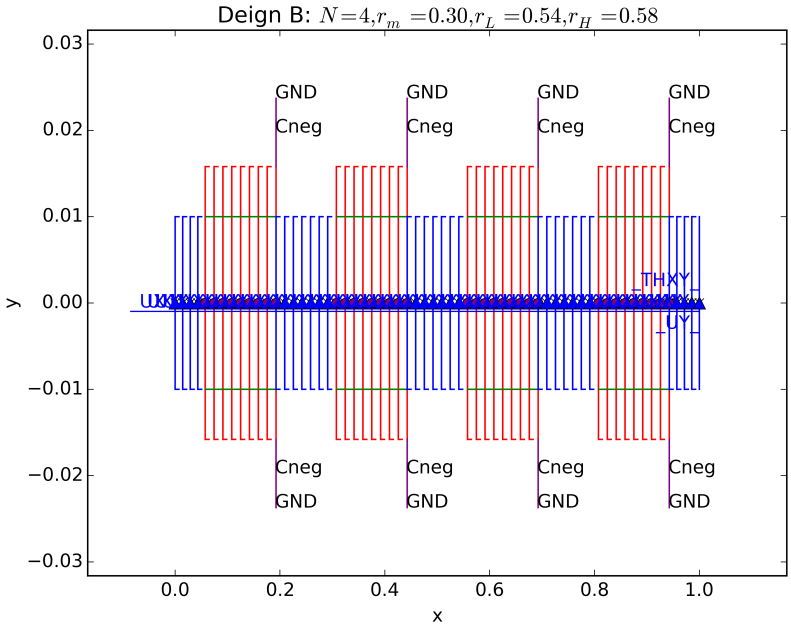

Figure F.2: Finite element mesh of the cantilever beam with configuration B.

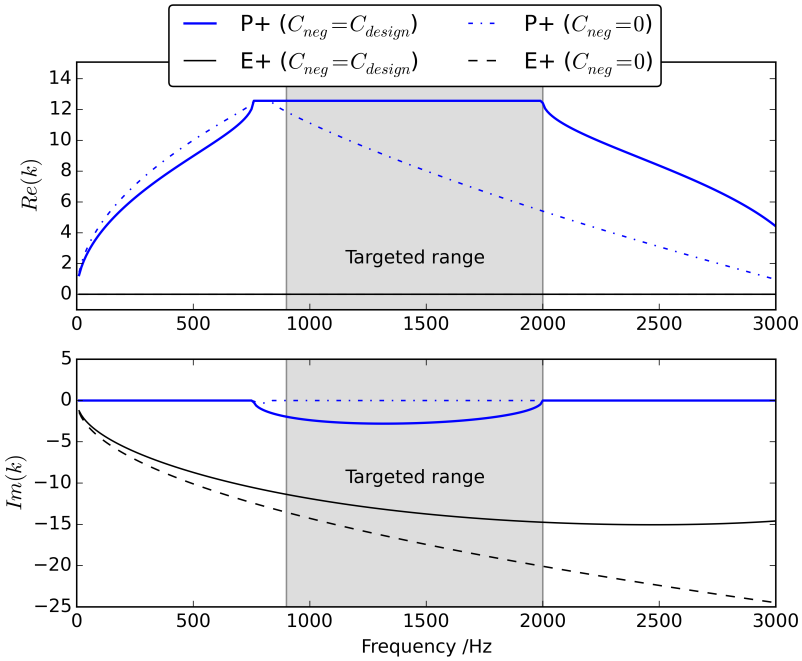

Figure F.3: Dispersion curves of the possitive-going waves when the designed negative capacitance is shunted to configuration B, in comparison to the open-circuit results.

Configuration C

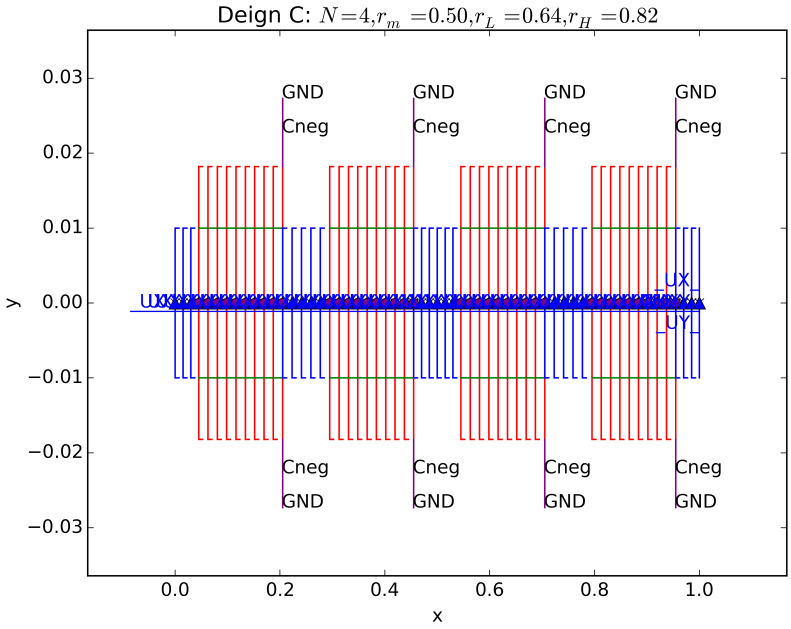

Figure F.4: Finite element mesh of the cantilever beam with configuration C.

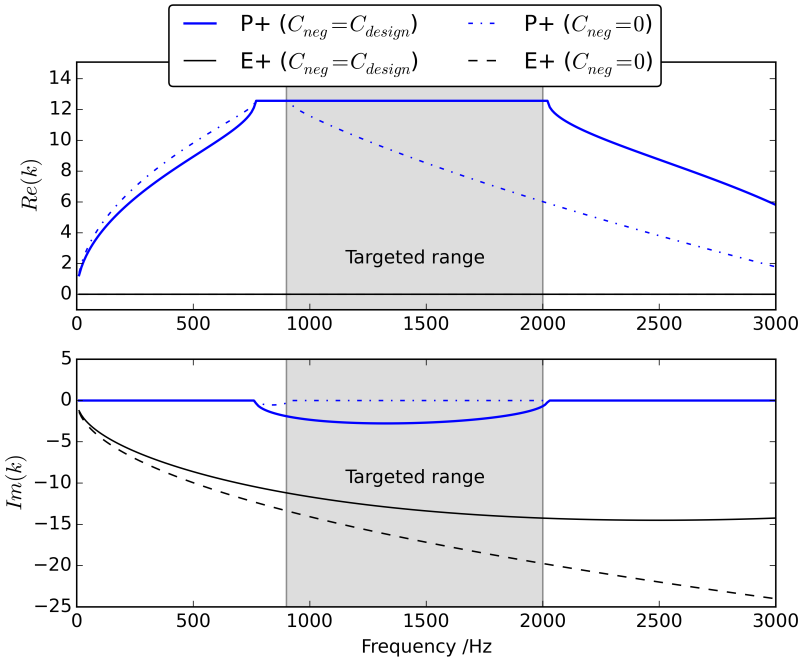

Figure F.5: Dispersion curves of the possitive-going waves when the designed negative capacitance is shunted to configuration C, in comparison to the open-circuit results.

Configuration D

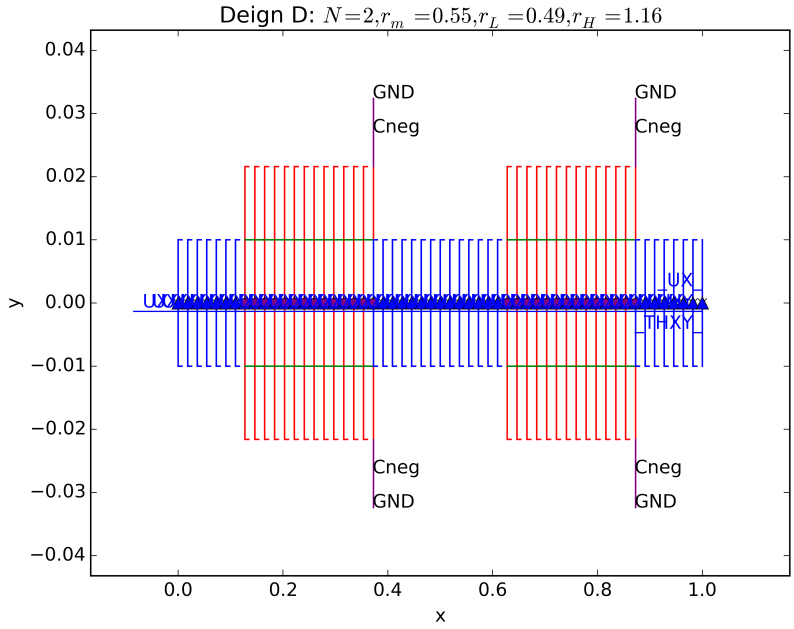

Figure F.6: Finite element mesh of the cantilever beam with configuration D.

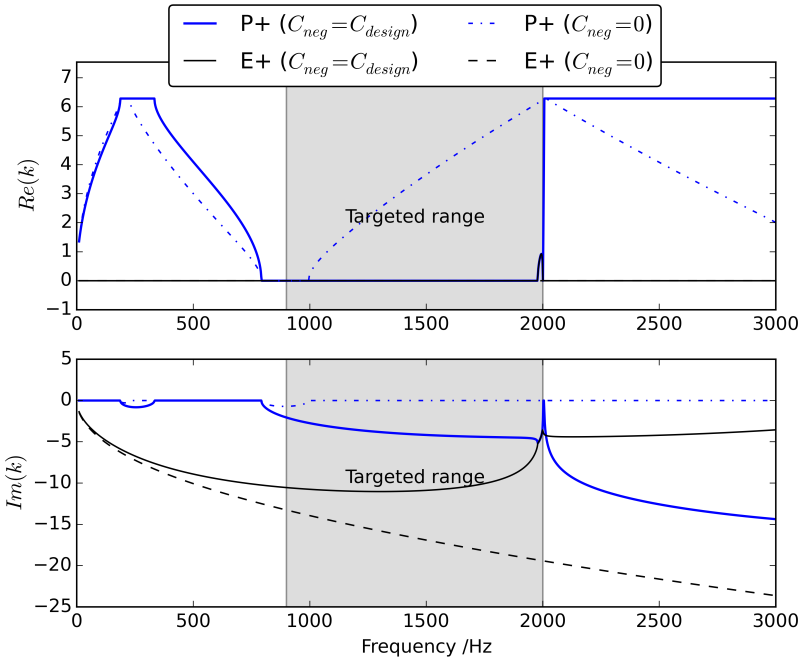

Figure F.7: Dispersion curves of the possitive-going waves when the designed negative capacitance is shunted to configuration D, in comparison to the open-circuit results.

Configuration E

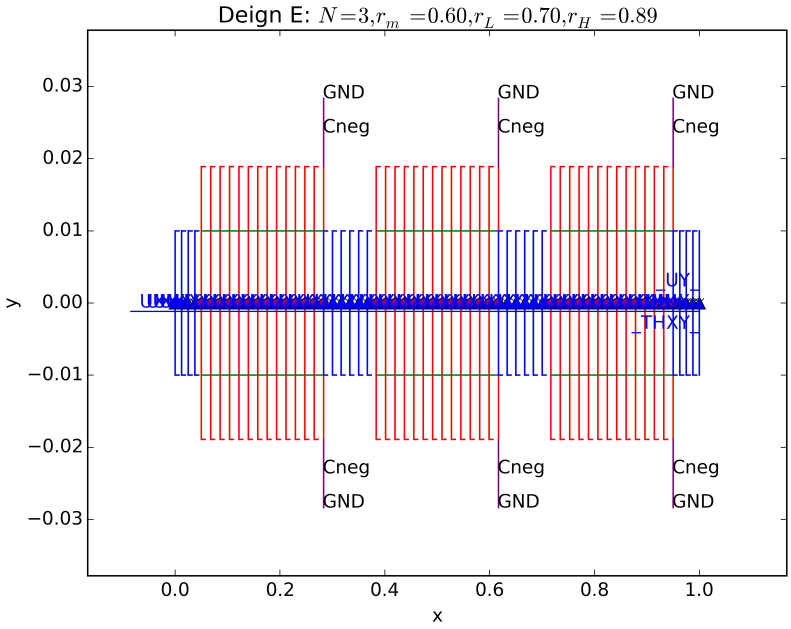

Figure F.8: Finite element mesh of the cantilever beam with configuration E.

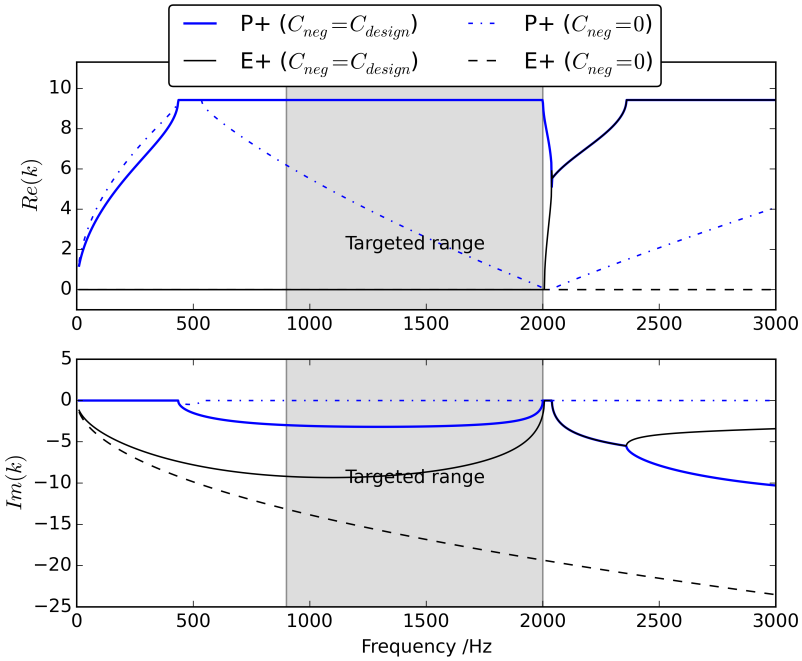

Figure F.9: Dispersion curves of the possitive-going waves when the designed negative capacitance is shunted to configuration E, in comparison to the open-circuit results.

Configuration F

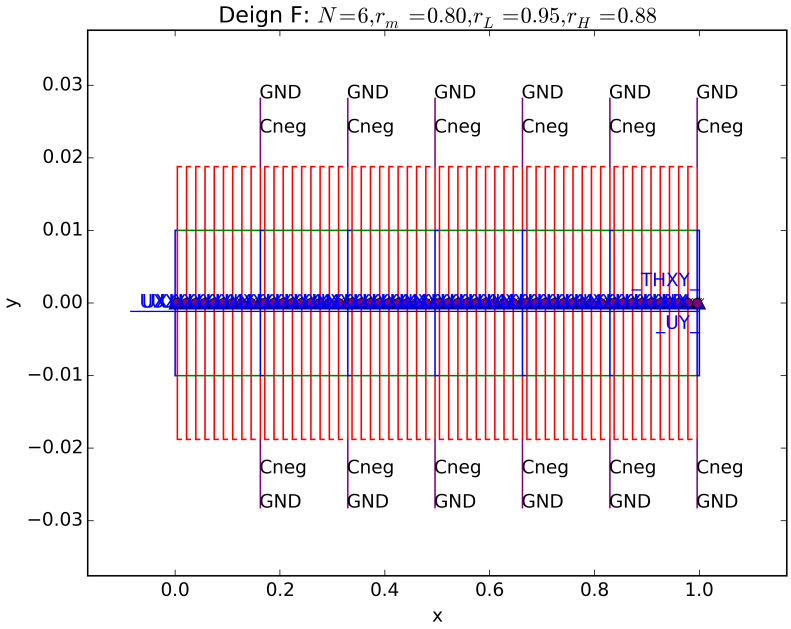

Figure F.10: Finite element mesh of the cantilever beam with configuration F.

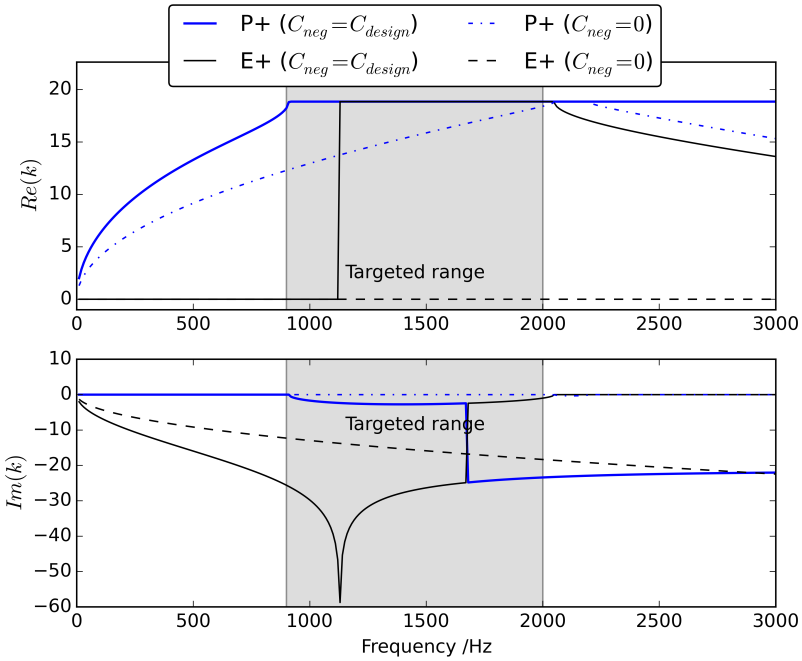

Figure F.11: Dispersion curves of the possitive-going waves when the designed negative capacitance is shunted to configuration F, in comparison to the open-circuit results.

Configuration G

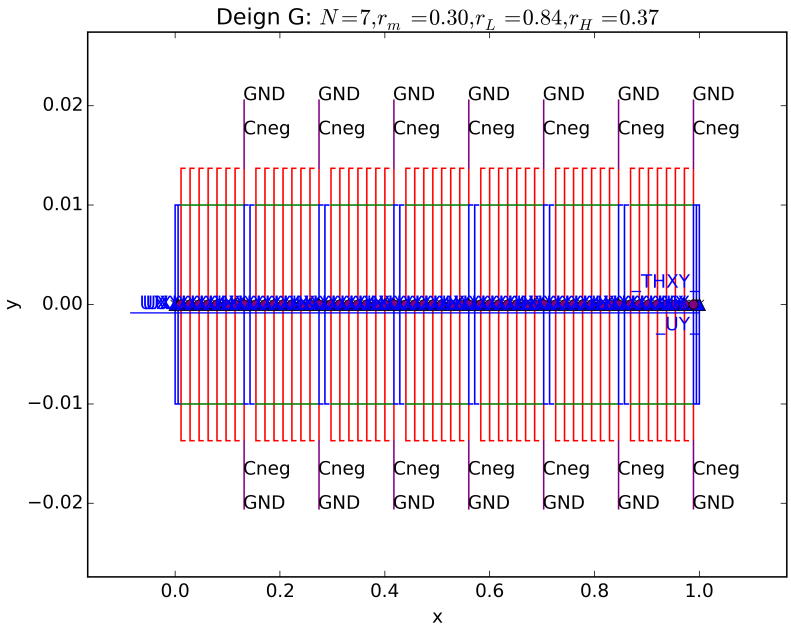

Figure F.12: Finite element mesh of the cantilever beam with configuration G.

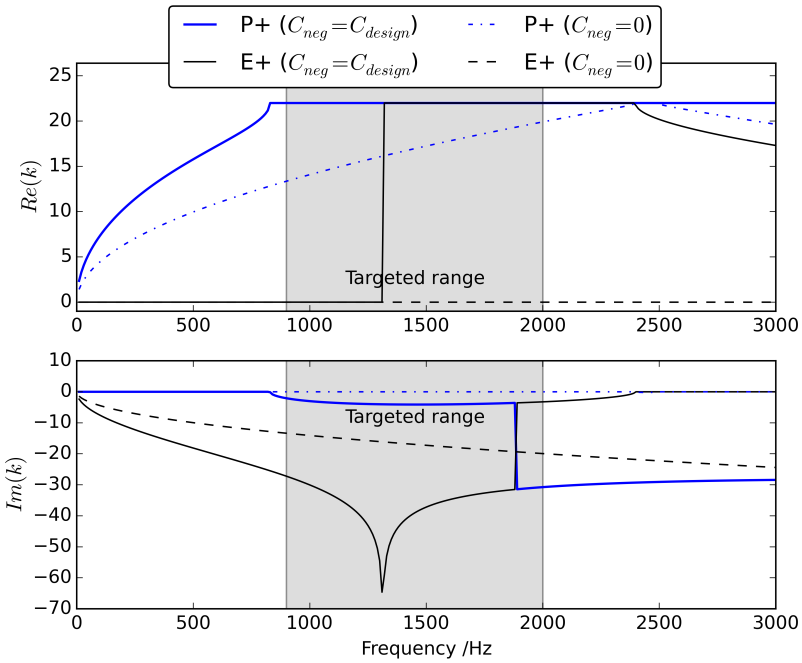

Figure F.13: Dispersion curves of the possitive-going waves when the designed negative capacitance is shunted to configuration G, in comparison to the open-circuit results.

Bibliography

[1] Shashank Priya and Daniel J. Inman, editors. *Energy Harvesting Technologies*. Springer US, Boston, MA, 2009.

[2] André Preumont. *Dynamics of Electromechanical and Piezoelectric Systems*. Springer Netherlands, 2006.

[3] Wikipedia. Piezoelectricity, 2016.

[4] Pierre Curie and Jacques Curie. Développement par compression de l'électricité polaire dans les cristaux hémièdres à faces inclinées. *Bulletin de la Société minérologique de France*, 3:90–93, 1880.

[5] Pierre Curie and Jacques Curie. Contractions et dilatations produites par des tensions dans les cristaux hémièdres à faces inclinées. *Comptes rendus*, 93:1137–1140, 1881.

[6] IEEE. *IEEE Standard on Piezoelectricity*. IEEE, 1988.

[7] Khaled S Ramadan, D Sameoto, and S Evoy. A review of piezoelectric polymers as functional materials for electromechanical transducers. *Smart Materials and Structures*, 23(3):033001, 2014.

[8] J Zhang, C Y Wang, and C Bowen. Piezoelectric effects and electromechanical theories at the nanoscale. *Nanoscale*, 6(22):13314–13327, 2014.

[9] André Preumont. Twelve lectures on structural dynamics. *Solid Mechanics and its Applications*, 198:1–319, 2013.

[10] Zi Guang Chen, Yuan Tai Hu, and Jia Shi Yang. Piezoelectric generator based on torsional modes for power harvesting from angular vibrations. *Applied Mathematics and Mechanics (English Edition)*, 28(6):779–784, 2007.

[11] M Sitti, D Campolo, J Yan, and R.S. Fearing. Development of PZT and PZN-PT based unimorph actuators for micromechanical flapping mechanisms. In *Proceedings 2001 ICRA. IEEE International Conference on Robotics and Automation (Cat. No.01CH37164)*, volume 4, pages 3839–3846. IEEE, 2001.

[12] Henry A. Sodano, Daniel J. Inman, and Gyuhae Park. A Review of Power Harvesting from Vibration Using Piezoelectric Materials. *The Shock and Vibration Digest*, 36(3):197–205, may 2004.

[13] B. Mokrani, G. Rodrigues, B. Ioan, R. Bastaits, and a. Preumont. Synchronized switch damping on inductor and negative capacitance. *Journal of Intelligent Material Systems and Structures*, 23(18):2065–2075, 2012.

[14] J G Smits and W Choi. The constituent equations of piezoelectric heterogeneous bimorphs. *IEEE transactions on ultrasonics, ferroelectrics, and frequency control*, 38(3):256–70, jan 1991.

[15] J.G. Smits and A Ballato. Dynamic behavior of piezoelectric bimorphs. In *Proceedings of IEEE Ultrasonics Symposium*, volume 2, pages 463–465. IEEE, 1993.

[16] S.R. Platt S.R. Platt, S. Farritor S. Farritor, and H. Haider H. Haider. On low-frequency electric power generation with PZT ceramics. *IEEE/ASME Transactions on Mechatronics*, 10(2):240–252, 2005.

[17] Marcus Neubauer, Robert Oleskiewicz, Karl Popp, and Tomasz Krzyzynski. Optimization of damping and absorbing performance of shunted piezo elements utilizing negative capacitance. *Journal of Sound and Vibration*, 298(1-2):84–107, nov 2006.

[18] N.W. Hagood and A. von Flotow. Damping of structural vibrations with piezoelectric materials and passive electrical networks. *Journal of Sound and Vibration*, 146 (2):243–268, apr 1991.

[19] Lei Zuo and Wen Cui. Dual-Functional Energy-Harvesting and Vibration Control: Electromagnetic Resonant Shunt Series Tuned Mass Dampers. *Journal of Vibration and Acoustics*, 135(5):051018, jun 2013.

[20] Lionel Petit, Elie Lefeuvre, Claude Richard, and Daniel Guyomar. A broadband semi passive piezoelectric technique for structural damping. In Kon-Well Wang, editor, *Proc. SPIE 5386, Smart Structures and Materials 2004: Damping and Isolation*, pages 414–425. International Society for Optics and Photonics, jul 2004.

[21] B Lossouarn, M Aucejo, and J-F Deü. Multimodal coupling of periodic lattices and application to rod vibration damping with a piezoelectric network. *Smart Materials and Structures*, 24(4):045018, apr 2015.

[22] Boris Lossouarn, Mathieu Aucejo, and Jean-François Deü. Multimodal vibration damping through a periodic array of piezoelectric patches connected to a passive network. In Wei-Hsin Liao, editor, *Smart Materials and Structures*, volume 9431, page 94311A. IOP Publishing, apr 2015.

[23] O Thomas, J Ducarne, and J-F Deü. Performance of piezoelectric shunts for vibration reduction. *Smart Materials and Structures*, 21(1):015008, jan 2012.

[24] Y. Fan, M. Collet, M. Ichchou, L. Li, O. Bareille, and Z. Dimitrijevic. Energy flow prediction in built-up structures through a hybrid finite element/wave and finite element approach. *Mechanical Systems and Signal Processing*, 66-67:137–158, jan 2016.

[25] Biao Zhou. *Study of Piezoelectric shunt Damping Applied to Mistuned Bladed Disks.* Phd thesis, Ecole Centrale de Lyon, 2012.

[26] Lin Li, Pengcheng Deng, and Yu Fan. Dynamic characteristics of a cyclic-periodic structure with a piezoelectric network. *Chinese Journal of Aeronautics*, 28(5):1426–1437, sep 2015.

[27] Yu Fan and Lin Li. Vibration Dissipation Characteristics of Symmetrical Piezoelectric Networks With Passive Branches. In *ASME Turbo Expo 2012: Turbine*

Technical Conference and Exposition, Volume 7: Structures and Dynamics, Parts A and B, pages 1263–1273. ASME, jun 2012.

[28] Qing Ming Wang and L. Eric Gross. Constitutive equations of symmetrical triple layer piezoelectric benders. *IEEE Transactions on Ultrasonics, Ferroelectrics, and Frequency Control*, 46(6):1343–1351, 1999.

[29] Amr El-Sayed, Ahmed Abo-Ismail, Moumen El-Melegy, Nur Hamzaid, and Noor Osman. Development of a Micro-Gripper Using Piezoelectric Bimorphs. *Sensors*, 13(5):5826–5840, may 2013.

[30] J.G. Smits and S.I. Dalke. The constituent equations of piezoelectric bimorphs. In *Proceedings., IEEE Ultrasonics Symposium*, volume 28, pages 781–784. IEEE, 1989.

[31] Jan G. Smits, Susan I. Dalke, and Thomas K. Cooney. The constituent equations of piezoelectric bimorphs. *Sensors and Actuators A: Physical*, 28(1):41–61, jun 1991.

[32] E. F. Crawley and E. H. Anderson. Detailed Models of Piezoceramic Actuation of Beams. *Journal of Intelligent Material Systems and Structures*, 1(1):4–25, 1990.

[33] Young S. Cho, Y. Eugene Pak, Chang S. Han, and Sung K. Ha. Five-port equivalent electric circuit of piezoelectric bimorph beam. *Sensors and Actuators, A: Physical*, 84(1):140–148, 2000.

[34] Sung Kyu Ha. Analysis of the asymmetric triple-layered piezoelectric bimorph using equivalent circuit models. *The Journal of the Acoustical Society of America*, 110 (2):856, 2001.

[35] A. Erturk and D. J. Inman. A Distributed Parameter Electromechanical Model for Cantilevered Piezoelectric Energy Harvesters. *Journal of Vibration and Acoustics*, 130(4):041002, aug 2008.

[36] A Erturk and D J Inman. An experimentally validated bimorph cantilever model for piezoelectric energy harvesting from base excitations. *Smart Materials and Structures*, 18(2):025009, feb 2009.

[37] J. Brufau-Penella and M. Puig-Vidal. Electromechanical Model of a Multi-Layer Piezoelectric Cantilever. In *7th. Int. Conf. on Thermal, Mechanical and Multi-physics Simulation and Experiments in Micro-Electronics and Micro-Systems*, pages 1–7. IEEE, 2006.

[38] C. Maurini, M. Porfiri, and J. Pouget. Numerical methods for modal analysis of stepped piezoelectric beams. *Journal of Sound and Vibration*, 298(4-5):918–933, 2006.

[39] Ruediger G. Ballas, H. F. Schlaak, and A. J. Schmid. The constituent equations of piezoelectric multilayer bending actuators in closed analytical form and experimental results. *Sensors and Actuators, A: Physical*, 130-131(SPEC. ISS.):91–98, 2006.

[40] Qing Ou, XiaoQi Chen, S Gutschmidt, A Wood, and N Leigh. A two-mass cantilever beam model for vibration energy harvesting applications. In *2010 IEEE International Conference on Automation Science and Engineering*. IEEE, aug 2010.

[41] Ayech Benjeddou and Jean-François Deü. A two-dimensional closed-form solution for the free-vibrations analysis of piezoelectric sandwich plates. *International Journal of Solids and Structures*, 39(6):1463–1486, mar 2002.

[42] Jean-François Deü and Ayech Benjeddou. Free-vibration analysis of laminated plates with embedded shear-mode piezoceramic layers. *International Journal of Solids and Structures*, 42(7):2059–2088, apr 2005.

[43] Francesco Dell'Isola and Stefano Vidoli. Distributed control of beams by electric transmission lines with PZT actuators. In Alex Hariz, Vijay K. Varadan, and Olaf Reinhold, editors, *Proceedings of SPIE*, volume 3241, pages 312–321, nov 1997.

[44] Silvio Alessandroni, Ugo Andreaus, Francesco Dell'Isola, and Maurizio Porfiri. Piezo-ElectroMechanical (PEM) Kirchhoff-Love plates. *European Journal of Mechanics, A/Solids*, 23(4):689–702, 2004.

[45] F. dell'Isola, E.G. Henneke, and M. Porfiri. Piezoelectromechanical structures: A survey of basic concepts and methodologies. *Proceedings SPIE Smart Structures and Materials, Smart Structures and Integrated Systems*, 5056:574–582, 2003.

[46] Corrado Maurini, Francesco Dell'Isola, and Dionisio Del Vescovo. Comparison of piezoelectronic networks acting as distributed vibration absorbers. *Mechanical Systems and Signal Processing*, 18:1243–1271, 2004.

[47] Stefano Vidoli and Francesco Dell'Isola. Vibration control in plates by uniformly distributed PZT actuators interconnected via electric networks. *European Journal of Mechanics - A/Solids*, 20(3):435–456, may 2001.

[48] Silvio Alessandroni, Francesco Dell'Isola, and Maurizio Porfiri. A revival of electric analogs for vibrating mechanical systems aimed to their efficient control by PZT actuators. *International Journal of Solids and Structures*, 39:5295–5324, 2002.

[49] A. Benjeddou. Advances in piezoelectric finite element modeling of adaptive structural elements: a survey. *Computers & Structures*, 76(1-3):347–363, jun 2000.

[50] A. Lazarus, O. Thomas, and J.-F. Deü. Finite element reduced order models for nonlinear vibrations of piezoelectric layered beams with applications to NEMS. *Finite Elements in Analysis and Design*, 49(1):35–51, feb 2012.

[51] O. Thomas, J.-F. Deü, and J. Ducarne. Vibrations of an elastic structure with shunted piezoelectric patches: efficient finite element formulation and electromechanical coupling coefficients. *International Journal for Numerical Methods in Engineering*, 80(2):235–268, oct 2009.

[52] M. Collet and K.A. Cunefare. Modal Synthesis and Dynamical Condensation Methods for Accurate Piezoelectric Systems Impedance Computation. *Journal of Intelligent Material Systems and Structures*, 19(11):1251–1269, apr 2008.

[53] Carlos C Pagani Jr and Marcelo a Trindade. Optimization of modal filters based on arrays of piezoelectric sensors. *Smart Materials and Structures*, 18(9):095046, sep 2009.

[54] Jichul Kim, Joon-Seok Hwang, and Seung Jo Kim. Design of Modal Transducers by Optimizing Spatial Distribution of Discrete Gain Weights. *AIAA Journal*, 39(10): 1969–1976, oct 2001.

[55] Seung Jo Kim, Chul Yong Yun, and Byung Joo Paek. Optimal design of a piezoelectric passive damper for vibrating plates. volume 3989, pages 512–519, apr 2000.

[56] O. Bareille, M. Kharrat, W. Zhou, and M.N. Ichchou. Distributed piezoelectric guided-T-wave generator, design and analysis. *Mechatronics*, 22(5):544–551, aug 2012.

[57] Bilal Mokrani. *Piezoelectric Shunt Damping of Rotationally Periodic Structures*. Phd thesis, Université libre de Bruxelles, 2015.

[58] Jie Yuan, Giuliano Allegri, Fabrizio Scarpa, Sophoclis Patsias, and Ramesh Rajasekaran. A novel hybrid Neumann expansion method for stochastic analysis of mistuned bladed discs. *Mechanical Systems and Signal Processing*, 72-73:241–253, 2016.

[59] Lin Li, Shunhua Yin, Xue Liu, and Jun Li. Enhanced electromechanical coupling of piezoelectric system for multimodal vibration. *Mechatronics*, 31:205–214, oct 2015.

[60] Warren P. Mason and Hans Baerwald. Piezoelectric Crystals and Their Applications to Ultrasonics. *Physics Today*, 4(5):23, 1951.

[61] DON A. BERLINCOURT, DANIEL R. CURRAN, and HANS JAFFE. Piezoelectric and Piezomagnetic Materials and Their Function in Transducers. In *Physical Acoustics*, pages 169–270. Elsevier, 1964.

[62] W. J. Toulis. Electromechanical Coupling and Composite Transducers. *The Journal of the Acoustical Society of America*, 35(1):74, 1963.

[63] Ralph S Woollett. Comments on "Electromechanical Coupling and Composite Transducers". *The Journal of the Acoustical Society of America*, 35(11):1837, 1963.

[64] S.H. Chang, N.N. Rogacheva, and C.C. Chou. Analysis of methods for determining electromechanical coupling coefficients of piezoelectric elements. *IEEE Transactions on Ultrasonics, Ferroelectrics and Frequency Control*, 42(4):630–640, 1995.

[65] Shi Chen, Yinhong Zhang, Shuyu Lin, and Zhiqiang Fu. Study on the electromechanical coupling coefficient of Rayleigh-type surface acoustic waves in semi-infinite piezoelectrics/non-piezoelectrics superlattices. *Ultrasonics*, 54(2):604–608, feb 2014.

[66] Li Fan, Shu-Yi Zhang, Kai Zheng, Wei Lin, and Hui-Dong Gao. Calculation of electromechanical coupling coefficient of Lamb waves in multilayered plates. *Ultrasonics*, 44 Suppl 1:e849–52, dec 2006.

[67] C M a Vasques. Improved passive shunt vibration control of smart piezo-elastic beams using modal piezoelectric transducers with shaped electrodes. *Smart Materials and Structures*, 21(12):125003, dec 2012.

[68] J. Ducarne, O. Thomas, and J.-F. Deü. Placement and dimension optimization of shunted piezoelectric patches for vibration reduction. *Journal of Sound and Vibration*, 331(14):3286–3303, jul 2012.

[69] Hongbiao Yu, K.W. Wang, and Jianhua Zhang. Piezoelectric networking with enhanced electromechanical coupling for vibration delocalization of mistuned periodic structures—Theory and experiment. *Journal of Sound and Vibration*, 295(1-2): 246–265, aug 2006.

[70] Y. Fan, M. Collet, M. Ichchou, L. Li, O. Bareille, and Z. Dimitrijevic. A wave-based design of semi-active piezoelectric composites for broadband vibration control. *Smart Materials and Structures*, 25(5):055032, may 2016.

[71] J Tang and K W Wang. Active-passive hybrid piezoelectric networks for vibration control: comparisons and improvement. *Smart Materials and Structures*, 10(4): 794–806, aug 2001.

[72] F. Tateo, M. Collet, M. Ouisse, and K. Cunefare. Design variables for optimizing adaptive metacomposite made of shunted piezoelectric patches distribution. *Journal of Vibration and Control*, aug 2014.

[73] B de Marneffe and A Preumont. Vibration damping with negative capacitance shunts: theory and experiment. *Smart Materials and Structures*, 17(3):035015, jun 2008.

[74] M Berardengo, S Manzoni, O Thomas, and C Giraud-Audine. A new electrical circuit with negative capacitances to enhance resistive shunt damping. *Proceedings of the ASME 2015 Conference on Smart Materials, Adaptive Structures and Intelligent Systems - SMASIS 2015*, (April 2016):ID 8836, 2015.

[75] D.J. Mead. Wave Propagation in Continuous Periodic Structures: Research Contributions from Southampton, 1964–1995. *Journal of Sound and Vibration*, 190(3): 495–524, feb 1996.

[76] X.Q. Wang, R.M.C. So, and K.T. Chan. Resonant beam vibration: A wave evolution analysis. *Journal of Sound and Vibration*, 291(3-5):681–705, apr 2006.

[77] RS Langley. Some perspectives on wave-mode duality in SEA. In *Proceedings of the IUTAM International Symposium on Statistical Energy Analysis*, pages 1–12. Kluwer Academic Publishers, jul 1997.

[78] D.J. Mead. Waves and Modes in Finite Beams: Application of the Phase-Closure Principle. *Journal of Sound and Vibration*, 171(5):695–702, apr 1994.

[79] Mira Mitra and S Gopalakrishnan. Guided wave based structural health monitoring: A review. *Smart Materials and Structures*, 25(5):053001, 2016.

[80] Zhongqing Su, Lin Ye, and Ye Lu. Guided Lamb waves for identification of damage in composite structures: A review. *Journal of Sound and Vibration*, 295(3-5):753–780, 2006.

[81] Mahmoud I. Hussein, Michael J. Leamy, and Massimo Ruzzene. Dynamics of Phononic Materials and Structures: Historical Origins, Recent Progress, and Future Outlook. *Applied Mechanics Reviews*, 66(4):040802, may 2014.

[82] H.G.D. Goyder and R.G. White. Vibrational power flow from machines into built-up structures, part I: Introduction and approximate analyses of beam and plate-like foundations. *Journal of Sound and Vibration*, 68(1):59–75, jan 1980.

[83] Yoshiyuki Waki. *On the application of finite element analysis to wave motion in one-dimensional waveguides*. Phd thesis, UNIVERSITY OF SOUTHAMPTON, 2007.

[84] D.J. Mead. A general theory of harmonic wave propagation in linear periodic systems with multiple coupling. *Journal of Sound and Vibration*, 27(2):235–260, mar 1973.

[85] M. Collet, M. Ouisse, M. Ruzzene, and M.N. Ichchou. Floquet–Bloch decomposition for the computation of dispersion of two-dimensional periodic, damped mechanical systems. *International Journal of Solids and Structures*, 48(20):2837–2848, oct 2011.

[86] H.G.D. Goyder and R.G. White. Vibrational power flow from machines into built-up structures, part II: Wave propagation and power flow in beam-stiffened plates. *Journal of Sound and Vibration*, 68(1):77–96, jan 1980.

[87] C. Droz, J.-P. Lainé, M.N. Ichchou, and G. Inquiété. A reduced formulation for the free-wave propagation analysis in composite structures. *Composite Structures*, 113: 134–144, jul 2014.

[88] C W Zhou, J.-P. Lainé, M.N. Ichchou, and A. M. Zine. Wave finite element method based on reduced model for periodic structures. *International Journal of Applied Mechanics*, 07(02):1550018, 2015.

[89] Tao Chen and Ligang Wang. Suppression of bending waves in a periodic beam with timoshenko beam theory. *Acta Mechanica Solida Sinica*, 26(2):177–188, apr 2013.

[90] Dianlong Yu, Jianyu Fang, Li Cai, Xiaoyun Han, and Jihong Wen. Triply coupled vibrational band gap in a periodic and nonsymmetrical axially loaded thin-walled Bernoulli-Euler beam including the warping effect. *Physics Letters, Section A: General, Atomic and Solid State Physics*, 373(38):3464–3469, 2009.

[91] Yan Gao, Michael J. Brennan, and Fusheng Sui. Control of flexural waves on a beam using distributed vibration neutralisers. *Journal of Sound and Vibration*, 330 (12):2758–2771, jun 2011.

[92] Yong Xiao, Brian R. Mace, Jihong Wen, and Xisen Wen. Formation and coupling of band gaps in a locally resonant elastic system comprising a string with attached resonators. *Physics Letters A*, 375(12):1485–1491, mar 2011.

[93] Y. Waki, B.R. Mace, and M.J. Brennan. Numerical issues concerning the wave and finite element method for free and forced vibrations of waveguides. *Journal of Sound and Vibration*, 327(1-2):92–108, oct 2009.

[94] D.J. Mead and S.M. Lee. Receptance methods and the dynamics of disordered one-dimensional lattices. *Journal of Sound and Vibration*, 92(3):427–445, feb 1984.

[95] D.J. Mead. Wave propagation and natural modes in periodic systems: I. Mono-coupled systems. *Journal of Sound and Vibration*, 40(1):1–18, may 1975.

[96] D.J. Mead. Wave propagation and natural modes in periodic systems: II. Multi-coupled systems, with and without damping. *Journal of Sound and Vibration*, 40 (1):19–39, may 1975.

[97] L Raghavan and a Srikantha Phani. Local resonance bandgaps in periodic media: theory and experiment. *The Journal of the Acoustical Society of America*, 134(3): 1950–9, sep 2013.

[98] W.X. Zhong and F.W. Williams. On the direct solution of wave propagation for repetitive structures. *Journal of Sound and Vibration*, 181(3):485–501, mar 1995.

[99] Changwei Zhou. *Wave and modal coupled approach for multi-scale analysis of periodic structures*. Phd thesis, Ecole Centrale de Lyon, 2014.

[100] C.W. Zhou, J.P. Lainé, M.N. Ichchou, and A.M. Zine. Numerical and experimental investigation on broadband wave propagation features in perforated plates. *Mechanical Systems and Signal Processing*, 75:556–575, jun 2016.

[101] C.W. Zhou, J.P. Lainé, M.N. Ichchou, and A.M. Zine. Multi-scale modelling for two-dimensional periodic structures using a combined mode/wave based approach. *Computers & Structures*, 154:145–162, jul 2015.

[102] D. Duhamel, B. R. Mace, and M. J. Brennan. Finite element analysis of the vibrations of waveguides and periodic structures. *Journal of Sound and Vibration*, 294 (1-2):205–220, jun 2006.

[103] J.-M. Mencik and M.N. Ichchou. A substructuring technique for finite element wave propagation in multi-layered systems. *Computer Methods in Applied Mechanics and Engineering*, 197(6-8):505–523, jan 2008.

[104] J.-M. Mencik. A model reduction strategy for computing the forced response of elastic waveguides using the wave finite element method. *Computer Methods in Applied Mechanics and Engineering*, 229-232:68–86, jul 2012.

[105] C. Droz, C. Zhou, M.N. Ichchou, and J.-P. Lainé. A hybrid wave-mode formulation for the vibro-acoustic analysis of 2D periodic structures. *Journal of Sound and Vibration*, 363:285–302, feb 2016.

[106] D.J. Mead. The forced vibration of one-dimensional multi-coupled periodic structures: An application to finite element analysis. *Journal of Sound and Vibration*, 319(1-2):282–304, jan 2009.

[107] L. Houillon, M.N. Ichchou, and L. Jezequel. Wave motion in thin-walled structures. *Journal of Sound and Vibration*, 281(3-5):483–507, mar 2005.

[108] J.-M. Mencik and M.N. Ichchou. Wave finite elements in guided elastodynamics with internal fluid. *International Journal of Solids and Structures*, 44(7-8):2148–2167, apr 2007.

[109] J.-M. Mencik and M.N. Ichchou. Multi-mode propagation and diffusion in structures through finite elements. *European Journal of Mechanics - A/Solids*, 24(5):877–898, sep 2005.

[110] T.L. Huang, M.N. Ichchou, O.A. Bareille, M. Collet, and M. Ouisse. Traveling wave control in thin-walled structures through shunted piezoelectric patches. *Mechanical Systems and Signal Processing*, 39(1-2):59–79, aug 2013.

[111] T. Huang, M. N. Ichchou, O. Bareille, M. Collet, and M. Ouisse. Multimodal wave propagation in smart composite structures with shunted piezoelectric patches. *Journal of Intelligent Material Systems and Structures*, 24(10):1155–1175, mar 2013.

[112] T. L. Huang, M. N. Ichchou, O. A. Bareille, M. Collet, and M. Ouisse. Multi-modal wave propagation in smart structures with shunted piezoelectric patches. *Computational Mechanics*, 52(3):721–739, feb 2013.

[113] A. Bocquillet, M.N. Ichchou, and L. Jezequel. Energetics of axisymmetric fluid-filled pipes up to high frequencies. *Journal of Fluids and Structures*, 17(4):491–510, mar 2003.

[114] Z P Liao. *Introduction to Wave Motion Theories in Engineering.* Science Press, 2002.

[115] Alexander H.-D. Cheng and Daisy T. Cheng. Heritage and early history of the boundary element method. *Engineering Analysis with Boundary Elements*, 29(3): 268–302, mar 2005.

[116] John L. Meek. Infinite elements. *Computing Systems in Engineering*, 5(1):103, feb 1994.

[117] Mi Zhao, Xiuli Du, Jingbo Liu, and Heng Liu. Explicit finite element artificial boundary scheme for transient scalar waves in two-dimensional unbounded waveguide. *International Journal for Numerical Methods in Engineering*, 87(11):1074–1104, sep 2011.

[118] Mi Zhao. *Study on the viscous-spring boundary and the transmitting boundary.* Master thess, Beijing University of Technology, 2004.

[119] Mi Zhao. *Stress-type time-domain artificial boundary condition for finite-element simulation of near-field wave motion and its engineering application.* Phd thesis, Beijing University of Technology, 2009.

[120] M Collet, M Ruzzene, and K A Cunefare. Generation of Lamb waves through surface mounted macro-fiber composite transducers. *Smart Materials and Structures*, 20(2): 025020, feb 2011.

[121] Jamil M. Renno and Brian R. Mace. Vibration modelling of structural networks using a hybrid finite element/wave and finite element approach. *Wave Motion*, 51 (4):566–580, jun 2014.

[122] Jamil M. Renno and Brian R. Mace. Calculation of reflection and transmission coefficients of joints using a hybrid finite element/wave and finite element approach. *Journal of Sound and Vibration*, 332(9):2149–2164, apr 2013.

[123] Shengbing Chen, Gang Wang, Jihong Wen, and Xisen Wen. Wave propagation and attenuation in plates with periodic arrays of shunted piezo-patches. *Journal of Sound and Vibration*, 332(6):1520–1532, mar 2013.

[124] Wenqiang Wang, Jidong Yu, and Zhiping Tang. General dispersion and dissipation relations in a one-dimensional viscoelastic lattice. *Physics Letters A*, 373(1):5–8, dec 2008.

[125] Robert L Forward. Electronic damping of vibrations in optical structures. *Applied Optics*, 18(5):690, 1979.

[126] G. Song, V. Sethi, and H.-N. Li. Vibration control of civil structures using piezoceramic smart materials: A review. *Engineering Structures*, 28(11):1513–1524, sep 2006.

[127] Melin Sahin, Fatih Mutlu Karadal, Yavuz Yaman, Omer Faruk Kircali, Volkan Nalbantoglu, Fatma Demet Ulker, and Tarkan Caliskan. Smart structures and their applications on active vibration control: Studies in the Department of Aerospace Engineering, METU. *Journal of Electroceramics*, 20:167–174, 2008.

[128] Jae-Hung Han, Junji Tani, and Jinhao Qiu. Active flutter suppression of a lifting surface using piezoelectric actuation and modern control theory. *Journal of Sound and Vibration*, 291(3-5):706–722, apr 2006.

[129] U. Aridogan and I. Basdogan. A review of active vibration and noise suppression of plate-like structures with piezoelectric transducers. *Journal of Intelligent Material Systems and Structures*, 26(12):1455–1476, 2015.

[130] Rabih Alkhatib and M. F. Golnaraghi. Active structural vibration control: a review. *Shock and Vibration Digest*, 35(5):367, 2003.

[131] M. a. Trindade and A. Benjeddou. Hybrid Active-Passive Damping Treatments Using Viscoelastic and Piezoelectric Materials: Review and Assessment. *Journal of Vibration and Control*, 8(6):699–745, jun 2002.

[132] Michael Strassberger and Heinz Waller. Active noise reduction by structural control using piezo-electric actuators. *Mechatronics*, 10(8):851–868, 2000.

[133] Shu-yau Wu. Piezoelectric shunts with a parallel R-L circuit for structural damping and vibration control. In Conor D. Johnson, editor, *Proc. SPIE 2720, Smart Structures and Materials 1996: Passive Damping and Isolation, 259*, pages 259–269, may 1996.

[134] Chul H. Park and Daniel J. Inman. Enhanced Piezoelectric Shunt Design. *Shock and Vibration*, 10(2):127–133, 2003.

[135] a J Fleming, S Behrens, and S O R Moheimani. Reducing the inductance requirements of piezoelectric shunt damping systems. *Smart Materials and Structures*, 12 (1):57–64, feb 2003.

[136] Giovanni Caruso. A critical analysis of electric shunt circuits employed in piezoelectric passive vibration damping. *Smart Materials and Structures*, 10(5):1059–1068, oct 2001.

[137] P Soltani, G Kerschen, G Tondreau, and a Deraemaeker. Piezoelectric vibration damping using resonant shunt circuits: an exact solution. *Smart Materials and Structures*, 23(12):125014, 2014.

[138] Tao Ni, Lei Zuo, and Ahsan Kareem. Assessment of Energy Potential and Vibration Mitigation of Regenerative Tuned Mass Dampers on Wind Excited Tall Buildings. In *Volume 1: 23rd Biennial Conference on Mechanical Vibration and Noise, Parts A and B*, pages 333–342. ASME, 2011.

[139] David J Warkentin and Nesbitt W Hagood. Nonlinear piezoelectric shunting for structural damping. *Smart Structures and Materials 1997: Smart Structures and Integrated Systems*, 3041(1):747–757, 1997.

[140] G. A. Lesieutre, G. K. Ottman, and H. F. Hofmann. Damping as a result of piezoelectric energy harvesting. *Journal of Sound and Vibration*, 269(3-5):991–1001, 2004.

[141] Shad Roundy, Paul K. Wright, and Jan Rabaey. A study of low level vibrations as a power source for wireless sensor nodes. *Computer Communications*, 26(11): 1131–1144, 2003.

[142] RS Langley and NS Bardell. A review of current analysis capabilities applicable to the high frequency vibration prediction of aerospace structures. *Aeronautical Journal*, (102):287–297, mar 1998.

[143] J. J. Hollkamp. Multimodal Passive Vibration Suppression with Piezoelectric Materials and Resonant Shunts. *Journal of Intelligent Material Systems and Structures*, 5(1):49–57, jan 1994.

[144] S.-Y. Wu. Method for Multiple Mode Piezoelectric Shunting with Single PZT Transducer for Vibration Control. *Journal of Intelligent Material Systems and Structures*, 9(12):991–998, dec 1998.

[145] Sam Behrens and S. O. Reza Moheimani. Current flowing multiple-mode piezoelectric shunt dampener. In Gregory S. Agnes, editor, *SPIE's 9th Annual International Symposium on Smart Structures and Materials*, pages 217–226. International Society for Optics and Photonics, jun 2002.

[146] Kim-Ho Ip and Ping-Cheung Tse. Optimal configuration of a piezoelectric patch for vibration control of isotropic rectangular plates. *Smart Materials and Structures*, 10(2):395–403, 2001.

[147] Ivan Giorgio, Antonio Culla, and Dionisio Del Vescovo. Multimode vibration control using several piezoelectric transducers shunted with a multiterminal network. *Archive of Applied Mechanics*, 79:859–879, 2009.

[148] Francesco Dell'Isola, Maurizio Porfiri, and Stefano Vidoli. Piezo-electromechanical (PEM) structures: Passive vibration control using distributed piezoelectric transducers. *Comptes Rendus - Mecanique*, 331(1):69–76, 2003.

[149] P. Bisegna, G. Caruso, and F. MacEri. Optimized electric networks for vibration damping of piezoactuated beams. *Journal of Sound and Vibration*, 289(4-5):908–937, 2006.

[150] F. Dell'Isola, C. Maurini, and M. Porfiri. Passive damping of beam vibrations through distributed electric networks and piezoelectric transducers: prototype design and experimental validation. *Smart Materials and Structures*, 299(13):299–308, 2004.

[151] S. Alessandroni, U. Andreaus, F. Dell'Isola, and M. Porfiri. A passive electric controller for multimodal vibrations of thin plates. *Computers and Structures*, 83: 1236–1250, 2005.

[152] Bilal Mokrani, Renaud Bastaits, Mihaita Horodinca, Iulian Romanescu, Ioanica Burda, Régis Viguié, and André Preumont. Parallel Piezoelectric Shunt Damping of Rotationally Periodic Structures. *Advances in Materials Science and Engineering*, 2015:1–12, 2015.

[153] Hongbiao Yu and K. W. Wang. Vibration Suppression of Mistuned Coupled-Blade-Disk Systems Using Piezoelectric Circuitry Network. *Journal of Vibration and Acoustics*, 131(2):021008, 2009.

[154] S S Mester and H. Benaroya. Periodic and Near-Periodic Structures. *Shock and Vibration*, 2(1):69–95, 1995.

[155] Christophe Pierre, Matthew P. Castanier, and Wan Joe Chen. Wave Localization in Multi-Coupled Periodic Structures: Application to Truss Beams. *Applied Mechanics Reviews*, 49(2):65, 1996.

[156] J. Tang and K. Wang. Vibration Delocalization of Nearly Periodic Strcutures Using Coupled Piezoelectric Networks. *Journal of Vibration and Acoustics*, 125(1):95–108, 2003.

[157] F. Tateo, M. Collet, M. Ouisse, M. Ichchou, K. Cunefare, and P. Abbe. Experimental characterization of a bi-dimensional array of negative capacitance piezo-patches for vibroacoustic control. *Journal of Intelligent Material Systems and Structures*, 26(8):952–964, may 2015.

[158] B. S. Beck, K. A. Cunefare, M. Ruzzene, and M. Collet. Experimental Analysis of a Cantilever Beam with a Shunted Piezoelectric Periodic Array. *Journal of Intelligent Material Systems and Structures*, 22(11):1177–1187, aug 2011.

[159] J Tang and K W Wang. Vibration control of rotationally periodic structures using passive piezoelectric shunt networks and active tuning. *American Society of Mechanical Engineers, Design Engineering Division (Publication) DE*, 97(July 1999): 39–45, 1998.

[160] R.A. Morgan and K.W. Wang. Active–passive piezoelectric absorbers for systems under multiple non-stationary harmonic excitations. *Journal of Sound and Vibration*, 255(4):685–700, aug 2002.

[161] C. L. Davis and G. A. Lesieutre. An actively tuned solid-state vibration absorber using capacitive shunting of piezoelectric stiffness. *Journal of Sound and Vibration*, 232(3):601–617, may 2000.

[162] Joseph J Hollkamp and T. F. Starchville. A Self-Tuning Piezoelectric Vibration Absorber. *Journal of Intelligent Material Systems and Structures*, 5(4):559–566, jul 1994.

[163] William W. Clark. Semi-active vibration control with piezoelectric materials as variable-stiffness actuators. pages 123–130, jun 1999.

[164] William W. Clark. Vibration Control with State-Switched Piezoelectric Materials. *Journal of Intelligent Material Systems and Structures*, 11(4):263–271, 2000.

[165] Claude Richard, Daniel Guyomar, David Audigier, and Gil Ching. Semi-passive damping using continuous switching of a piezoelectric device. In T. Tupper Hyde, editor, *1999 Symposium on Smart Structures and Materials*, pages 104–111. International Society for Optics and Photonics, jun 1999.

[166] Claude Richard, Daniel Guyomar, David Audigier, and Henri Bassaler. Enhanced semi-passive damping using continuous switching of a piezoelectric device on an inductor. In T. Tupper Hyde, editor, *Proc. SPIE 3989, Smart Structures and Materials 2000: Damping and Isolation*, pages 288–299. International Society for Optics and Photonics, apr 2000.

[167] M. Lallart, L. Yan, C. Richard, and D. Guyomar. Damping of periodic bending structures featuring nonlinearly interfaced piezoelectric elements. *Journal of Vibration and Control*, feb 2015.

[168] Y. Linjuan. *Broadband vibration control using nonlinearly interfaced piezoelectric elements*. Phd thesis, INSA de Lyon, 2013.

[169] Lawrence R Corr and William W Clark. Comparison of low-frequency piezoelectric switching shunt techniques for structural damping. *Smart Materials and Structures*, 11(3):370–376, jun 2002.

[170] Hongli Ji, Jinhao Qiu, Jun Cheng, and Daniel Inman. Application of a Negative Capacitance Circuit in Synchronized Switch Damping Techniques for Vibration Suppression. *Journal of Vibration and Acoustics*, 133(4):041015, aug 2011.

[171] a. Badel, G. Sebald, D Guyomar, M. Lallart, E. Lefeuvre, C. Richard, and J. Qiu. Piezoelectric vibration control by synchronized switching on adaptive voltage sources: Towards wideband semi-active damping. *The Journal of the Acoustical Society of America*, 119(5):2815, 2006.

[172] Mickaël Lallart, Linjuan Yan, Yi-Chieh Wu, and Daniel Guyomar. Electromechanical semi-passive nonlinear tuned mass damper for efficient vibration damping. *Journal of Sound and Vibration*, 332(22):5696–5709, oct 2013.

[173] Mickaël Lallart, Élie Lefeuvre, Claude Richard, and Daniel Guyomar. Self-powered circuit for broadband, multimodal piezoelectric vibration control. *Sensors and Actuators A: Physical*, 143(2):377–382, may 2008.

[174] Hui Shen, Hongli Ji, Jinhao Qiu, and Kongjun Zhu. A semi-passive vibration damping system powered by harvested energy. *International Journal of Applied Electromagnetics and Mechanics*, 31(4):219–233, 2009.

[175] Hui Shen, Jinhao Qiu, Hongli Ji, Kongjun Zhu, Marco Balsi, Ivan Giorgio, and Francesco Dell'Isola. A low-power circuit for piezoelectric vibration control by synchronized switching on voltage sources. *Sensors and Actuators A: Physical*, 161 (1-2):245–255, jun 2010.

[176] Dan Wu, Daniel Guyomar, and Claude Richard. A new global approach using a network of piezoelectric elements and energy redistribution for enhanced vibration damping of smart structure. *Proc. SPIE 8688, Active and Passive Smart Structures and Integrated Systems 2013*, 8688:86880V, 2013.

[177] Lawrence R. Corr and William W. Clark. A Novel Semi-Active Multi-Modal Vibration Control Law for a Piezoceramic Actuator. *Journal of Vibration and Acoustics*, 125(May 2001):214, 2003.

[178] D. Guyomar and A. Badel. Nonlinear semi-passive multimodal vibration damping: An efficient probabilistic approach. *Journal of Sound and Vibration*, 294(1-2):249–268, jun 2006.

[179] Hongli Ji, Jinhao Qiu, Kongjun Zhu, Yuansheng Chen, and Adrien Badel. Multimodal vibration control using a synchronized switch based on a displacement switching threshold. *Smart Materials and Structures*, 18(3):035016, mar 2009.

[180] a. Cherif, C. Richard, D. Guyomar, S. Belkhiat, and M. Meddad. Simulation of multimodal vibration damping of a plate structure using a modal SSDI-Max technique. *Journal of Intelligent Material Systems and Structures*, 23(6):675–689, apr 2012.

[181] J.-M. Mencik. New advances in the forced response computation of periodic structures using the wave finite element (WFE) method. *Computational Mechanics*, 54 (3):789–801, apr 2014.

[182] Y. Waki, B.R. Mace, and M.J. Brennan. Free and forced vibrations of a tyre using a wave/finite element approach. *Journal of Sound and Vibration*, 323(3-5):737–756, jun 2009.

[183] R-R. Craig and M C C Bampton. Coupling of Substructures for Dynamics Analyses. *AIAA Journal*, 6(7):1313, 1968.

[184] S. N. Hou. Review of modal synthesis techniques and a new approach. *Shock and vibration bulletin*, 40(4):25–39, 1969.

[185] Richard H. MacNeal. A hybrid method of component mode synthesis. *Computers & Structures*, 1(4):581–601, 1971.

[186] S. Rubin. Improved Component-Mode Representation for Structural Dynamic Analysis. *AIAA Journal*, 13(8):995–1006, 1975.

[187] Ji-Bao Qiu, Zu-Guang Ying, and L. H. Yam. New Modal Synthesis Technique Using Mixed Modes. *AIAA Journal*, 35(12):1869–1875, dec 1997.

[188] J.-M. Mencik. On the low- and mid-frequency forced response of elastic structures using wave finite elements with one-dimensional propagation. *Computers & Structures*, 88(11-12):674–689, jun 2010.

[189] W.J. Zhou and M.N. Ichchou. Wave propagation in mechanical waveguide with curved members using wave finite element solution. *Computer Methods in Applied Mechanics and Engineering*, 199(33-36):2099–2109, jul 2010.

[190] Ji Bao Qiu, F. W. Williams, and Ren Xi Qiu. A new exact substructure method using mixed modes. *Journal of Sound and Vibration*, 266(4):737–757, 2003.

[191] Shuhong Xiang, Jibao Qiu, and Dajun Wang. The recent progresses on modal analysis and dynamic sub-structure methods. *Advances in mechanics*, 34(3):289–303, jan 2004.

[192] A. De Kraker and D. H. Van Campen. Rubin's CMS reduction method for general state-space models. *Computers and Structures*, 58(3):597–606, 1996.

[193] J.-M. Mencik and D. Duhamel. A wave-based model reduction technique for the description of the dynamic behavior of periodic structures involving arbitrary-shaped substructures and large-sized finite element models. *Finite Elements in Analysis and Design*, 101:1–14, sep 2015.

[194] Yu.I. Bobrovnitskii. On the energy flow in evanescent waves. *Journal of Sound and Vibration*, 152(1):175–176, jan 1992.

[195] R.S. Langley. On the Modal Density and Energy Flow Characteristics of Periodic Structures. *Journal of Sound and Vibration*, 172(4):491–511, may 1994.

[196] a. Spadoni, M. Ruzzene, and K. Cunefare. Vibration and Wave Propagation Control of Plates with Periodic Arrays of Shunted Piezoelectric Patches. *Journal of Intelligent Material Systems and Structures*, 20(8):979–990, mar 2009.

[197] Yong Xiao, Jihong Wen, Dianlong Yu, and Xisen Wen. Flexural wave propagation in beams with periodically attached vibration absorbers: Band-gap behavior and band formation mechanisms. *Journal of Sound and Vibration*, 332(4):867–893, feb 2013.

[198] Dianlong Yu, Jihong Wen, Honggang Zhao, Yaozong Liu, and Xisen Wen. Vibration reduction by using the idea of phononic crystals in a pipe-conveying fluid. *Journal of Sound and Vibration*, 318(1-2):193–205, nov 2008.

[199] Gang Wang, Xisen Wen, Jihong Wen, and Yaozong Liu. Quasi-One-Dimensional Periodic Structure with Locally Resonant Band Gap. *Journal of Applied Mechanics*, 73(1):167, 2006.

[200] W.J. Zhou, M.N. Ichchou, and J.M. Mencik. Analysis of wave propagation in cylindrical pipes with local inhomogeneities. *Journal of Sound and Vibration*, 319 (1-2):335–354, jan 2009.

[201] Longxiang Dai, Shan Jiang, Ziyang Lian, Hongping Hu, and Xuedong Chen. Locally resonant band gaps achieved by equal frequency shunting circuits of piezoelectric rings in a periodic circular plate. *Journal of Sound and Vibration*, 337:150–160, feb 2015.

[202] Mickaël Lallart, Stéphanie Harari, Lionel Petit, Daniel Guyomar, Thibaut Richard, Claude Richard, and Luc Gaudiller. Blind switch damping (BSD): A self-adaptive semi-active damping technique. *Journal of Sound and Vibration*, 328(1-2):29–41, nov 2009.

[203] M. Collet, K.a. Cunefare, and M.N. Ichchou. Wave Motion Optimization in Periodically Distributed Shunted Piezocomposite Beam Structures. *Journal of Intelligent Material Systems and Structures*, 20(7):787–808, oct 2008.

[204] Bruce L. Davis, Andrew S. Tomchek, Edgar A. Flores, Liao Liu, and Mahmoud I. Hussein. Analysis of Periodicity Termination in Phononic Crystals. In *Proceedings of the ASME 2011 International Mechanical Engineering Congress & Exposition. Volume 8: Mechanics of Solids, Structures and Fluids; Vibration, Acoustics and Wave Propagation*, pages 973–977. ASME, jan 2011.

[205] Yong Xiao, Jihong Wen, Gang Wang, and Xisen Wen. Theoretical and Experimental Study of Locally Resonant and Bragg Band Gaps in Flexural Beams Carrying Periodic Arrays of Beam-Like Resonators. *Journal of Vibration and Acoustics*, 135 (4):041006, jun 2013.

[206] Yu.I. Bobrovnitskii. Author's Reply. *Journal of Sound and Vibration*, 161(2):357, feb 1993.

[207] U.J. Kurze. Comments On "On The Energy Flow In Evanescent Waves" 1992. *Journal of Sound and Vibration*, 161(2):355–356, feb 1993.

[208] L. Rouleau, J.-F Due, and A. Legay. Review of Reduction Methods Based on Modal Projection for Highly Damped Structures. (Wccm Xi):1–13, 2014.

[209] K. C. Park, C. A. Felippa, and U. A. Gumaste. A localized version of the method of Lagrange multipliers and its applications. *Computational Mechanics*, 24(6):476–490, jan 2000.

[210] Carlos A. Felippa. Error analysis of penalty function techniques for constraint definition in linear algebraic systems. *International Journal for Numerical Methods in Engineering*, 11(4):709–728, 1977.